Two examples of multi-scale numerical modelling combined with advanced X-ray based experiments : multi-scale imaging for reactive transport in porous media and X-ray beam induced current (XBIC)

Abdellatif Saadaldin

To cite this version:

Abdellatif Saadaldin. Two examples of multi-scale numerical modelling combined with advanced X-ray based experiments : multi-scale imaging for reactive transport in porous media and X-ray beam induced current (XBIC). Material chemistry. Université de Bordeaux, 2022. English. NNT : 2022BORD0238 . tel-04683902

HAL Id: tel-04683902
https://theses.hal.science/tel-04683902v1

Submitted on 2 Sep 2024

THÈSE PRÉSENTÉE

POUR OBTENIR LE GRADE DE

DOCTEUR DE

L'UNIVERSITÉ DE BORDEAUX

École doctorale des sciences chimiques

Physico-Chimie de la Matière Condensée

Par

Abdellatif SAADALDIN

Two examples of multi-scale numerical modelling combined with advanced X-ray based experiments: multi-scale imaging for reactive transport in porous media and X-ray beam induced current (XBIC)

Sous la direction de : Dr. Dominique BERNARD
(co-directeur : Prof. Yannick BERTHOUMIEU)

Soutenue le 29 Août 2022

Membres du jury :

Mme. CROGUENNEC Laurence	Directrice de recherche, ICMCB, France	Présidente
Mme. MARONE Federica	Directrice de recherche, Paul Scherrer Institute, Suisse	Rapporteur
M. BRUNO Giovanni	Full professor, BAM - Division 8.5 Micro NDE, Allemagne	Rapporteur
M. LASSEUX Didier	Directeur de recherche, I2M Dept TREFLE, France	Examinateur
M. ANDREASEN Jens	Full professor, Technical University of Denmark, Denmark	Examinateur
M. QATANANI Naji	Full professor, An-Najah National University, Palestine	Examinateur
M. BERTHOUMIEU Yannick	Professeur des universités, IMS Lab, France	Co-Directeur
M. BERNARD Dominique	Directeur de recherche, ICMCB, France	Directeur de thèse

Acknowledgments

الحمد لله الذي بنعمته تتم الصالحات

PRAISE IS TO ALLAH BY WHOSE GRACE GOOD DEEDS ARE COMPLETED

First of all, I would like to express my sincere gratitude to my supervisor Dr. Dominique BERNARD for all his guidance, support, encouragement and patience throughout these years. I would also like to thank him for giving me the opportunity to be part of this great and extraordinary project. I have learnt many exhilarating things and met so many amazing people who in different ways inspired and helped me to realise my dream.

The project MUMMERING (MUltiscale, Multimodal and Multidimensional imaging for EngineeRING) was funded by EU Horizon 2020 Marie Sklodowska-Curie Actions Innovative Training Network, Grant No. 765604; I show my gratitude towards the funding agency. Special thanks to everyone who was part of this network, for all the efforts and time they spent so we can have this unforgettable experience. By 'we' I mean, all the 15 early stage researchers (ESR) whom I would like to thank for their support and kindness.

I would like to thank all the jury members for agreeing to be there in the committee: Dr. Federica MARONE and Dr. Giovanni BRUNO for reviewing my thesis manuscript, Dr. Didier LASSEUX, Dr. Laurence CROGUENNEC, Dr. Jens ANDREASEN and Dr. Naji QATANANI for examining. Special thanks to my Co-supervisor Dr. Yannick BERTHOUMIEU.

I would like to extend my sincere thanks to my colleagues and all members in the research group 1, for the cherished time that we spent together in the ICMCB lab. I am also truly thankful for their prompt help whenever I needed it.

I would like to thank all my friends, the one newly added to the old ones in the list, for constantly motivating and pushing me to my greater heights even in the toughest moments. It is their kind help and support that have made my stay a wonderful one.

I would like to express immense gratitude to my parents for their support back home. I also want to mention my whole family, without whom I would never have become who I am today. Especially, my daughters Maha and Zaina for being my inspiration.

Finally, I want to dedicate this thesis to my beloved wife, Rana, for her love and support during this journey. Thank you for always being there for me.

Résumé du manuscrit de thèse

Cette thèse est constituée de deux exemples de modélisation numérique multi-échelle combinée à des expériences de rayons X synchrotron : (1) Imagerie et modélisation multi-échelle pour le transport réactif à l'échelle du pore, (2) Caractérisation multimodale des cellules solaires à couche mince en kestérite : résultats expérimentaux et interprétation numérique. Ces deux exemples ont été développés au sein d'un réseau de formation appelé MUMMERING (MUltiscale, Multimodal and Multidimensional imaging for EngineeRING). Ce fut une occasion extrêmement enrichissante et passionnante d'apprendre des choses exaltantes grâce à ce programme de formation.... Permettez-moi donc de commencer ma thèse en expliquant un peu ce qu'est MUMMERING avant de me plonger dans les détails scientifiques de ce travail. MUMMERING [1] est l'un des programmes du réseau de formation innovant (ITN) des actions Marie Sklodowska-Curie. Son objectif principal était de créer un outil de recherche qui englobe les différtents aspects des nouvelles modalités d'imagerie 3D qui se développent pour des applications dans le domaine de l'ingénierie des matériaux, et de créer un programme de doctorat qui forme 15 chercheurs débutants (ESR) dans tous les volets de l'imagerie 3D, de l'acquisition de données à la modélisation physique, en passant par la reconstruction et la segmentation. En tant que ITN, MUMMERING a également pour objectif de former une nouvelle génération d'ESR créatifs et innovants, capables de convertir les connaissances et les idées en produits et services pour un bénéfice économique et social, et de travailler en collaboration avec d'autres ESR du réseau pour résoudre des problèmes réels.

Les modèles et simulations multi-échelles sont des défis importants pour la science numérique dans de nombreux domaines de recherche. La plupart des phénomènes de la vie réelle impliquent une gamme étendue d'échelles spatiales et/ou temporelles, ainsi que l'interaction entre divers processus naturels. De plus, les méthodes d'imagerie multi-échelle forment un pont entre la compréhension à l'échelle atomique (obtenue par la microscopie électronique, la diffraction et la spectroscopie, la tomographie à l'échelle nanométrique) et les objets à l'échelle macro. La microscopie corrélative unifie les informations dérivées d'une variété de modalités d'imagerie obtenues par la variation d'énergie et les différentes interactions de la sonde avec le matériau. Les propriétés uniques du rayonnement synchrotron, à savoir un spectre continu, un flux et une luminance élevés et une grande cohérence, en font un outil essentiel dans les modalités d'imagerie à plusieurs échelles. Les spécialistes des matériaux utilisent généralement le rayonnement X synchrotron pour étudier la structure des matériaux à l'échelle du micromètre ou du nanomètre. En établissant un lien entre la structure des matériaux et leur comportement mécanique et physique, il est possible de concevoir des matériaux aux performances optimisées. La gamme d'applications des expériences de rayons X synchrotron est très large et couvre des secteurs aussi divers que l'industrie chimique (polymères), l'industrie des semi-conducteurs, la recherche géologique (et pétrolière), l'industrie agroalimentaire et les applications de fabrication avancée.

L'objectif principal de cette thèse était de développer une procédure d'imagerie et de modélisation multi-échelle pour le transport réactif dans les milieux poreux. En outre, un travail de collaboration intitulé "Multi-Modal Characterization of kesterite Thin-Film Solar Cells : Experimental results and numerical interpretation" initié avec Azat M. Slyamov (ESR 9) est devenu une partie essentielle de mon doctorat. Ce travail est le résultat de discussions continues au cours des ateliers et des réunions du projet MUMMERING. L'objectif principal de cette collaboration était de développer une approche multi-échelle basée sur les premiers principes pour simuler les expériences de courant induit par un faisceau de rayons X (XBIC). Ces deux exemples partagent la propriété d'être des expériences dépendantes des rayons X du synchrotron et le même objectif de développer des procédures d'imagerie et de modélisation multi-modales et multi-échelles.

Dans le premier exemple, l'imagerie et la modélisation multi-échelle du transport réactif à l'échelle du pore ont été envisagées. La modélisation du transport dans les milieux poreux nécessite de garder à l'esprit les aspects multi-échelles existants dans les structures des milieux poreux. Un milieu poreux est un matériau contenant du vide ; les filtres, les adsorbants, le papier d'impression, le bois, les matériaux composites et les tissus biologiques en sont des exemples, tout comme le sol et les chaussées, ainsi que les réservoirs de pétrole, de gaz et les réservoirs géothermiques [2]. Ces milieux poreux sont généralement très hétérogènes à l'échelle locale (échelle du pore) et il n'est généralement pas possible d'utiliser les modèles décrivant le transport à l'échelle du pore pour prédire et observer le transport à l'échelle globale (échelle macroscopique). Par exemple, dans un aquifère, à l'échelle du pore, l'écoulement monophasique est régi par l'équation de Stokes. Cependant, en raison du large éventail d'échelles impliquées, allant de l'échelle du pore (environ 100 µm) à l'échelle macroscopique (km), et de la géométrie complexe à l'échelle du pore, il est pratiquement impossible d'utiliser l'équation de Stokes pour décrire l'écoulement dans le système entier. Au lieu de cela, une approche continue est proposée pour décrire l'écoulement à l'échelle macroscopique par la loi de Darcy [3]. Dans cette approche, le milieu poreux est traité comme un continuum et l'écoulement est prédit sans information sur la configuration microscopique de la géométrie à l'échelle des pores. Le résultat du travail de Darcy est une loi empirique avec un domaine de validité limité. Par conséquent, de nombreux chercheurs ont tenté de dériver la loi de Darcy d'une manière générale en utilisant les informations sur l'échelle des pores au moyen de techniques de changement d'échelle [4], [5]. Le modèle macroscopique qui en résulte contient la propriété effective, le tenseur de perméabilité, qui peut être calculée en utilisant les informations à l'échelle du pore. Ensuite, plutôt que de traiter le problème en termes d'équations qui ne sont valables que dans les pores, nous pouvons utiliser les techniques de changement d'échelle pour dériver des équations macroscopiques qui sont valables partout et sont liées à la géométrie à l'échelle du pore par les propriétés effectives. Un problème central dans la recherche sur l'échelle des pores est la détermination de ces propriétés effectives qui décrivent le comportement d'un milieu poreux à l'échelle macroscopique, c'est-à-dire les propriétés qui sont pertinentes et peuvent être mesurées dans des expériences en laboratoire ou sur le terrain [6]. La technique de moyenne volumique est l'une des diverses méthodes théoriques fournissant une description rigoureuse de la procédure de changement d'échelle [5], [7]–[9]. Celle-ci est bien adaptée pour notre problème (transport réactif en milieu poreux) [9]–[13]. En général, la plupart des systèmes naturels sont hétérogènes et les propriétés effectives de transport dépendent fortement des détails géométriques [12]. La mesure de la géométrie tridimensionnelle (3D) peut être abordée de plusieurs façons. La microtomographie synchrotron est l'un des outils avancés de la science des matériaux qui fournit des images 3D du matériau étudié. Traditionnellement, les images 3D sont quantifiées par un nombre limité de paramètres (porosité, surface réactive, etc...), et ces paramètres sont les entrées utilisées dans les modèles. Comme alternative, l'ensemble des données 3D peut être utilisé comme entrée pour calculer les propriétés effectives [14]–[17]. Cela favorise la transition vers une prochaine génération de modèles plus précis, qui incluent l'hétérogénéité de la microstructure.

Pour calculer les propriétés effectives, l'image 3D décrivant la géométrie locale doit être suffisamment grande pour être représentative. Par représentatif, nous entendons que les propriétés effectives ne changeront pas pour des images plus grandes. Ce volume minimal requis est communément appelé volume élémentaire représentatif (VER) [18]. Les outils d'imagerie modernes fournissent de très grandes images 3D (géométries décrites par des milliards de voxels), et l'utilisation de ces images 3D entières est un défi. Il convient donc d'accorder une attention particulière à l'utilisation de la mémoire et au temps de calcul. Un aspect important de la simulation numérique est la discrétisation de l'espace. La méthode la plus simple et la plus courante consiste à utiliser une grille cartésienne régulière (uniforme) (grille de voxels). Les inconvénients des grilles régulières sont les exigences en matière d'effort de calcul et de taille de mémoire. Par conséquent, une discrétisation spatiale adaptée est nécessaire pour résoudre ce problème.

Pour les problèmes que nous considérons, les réactions hétérogènes sont dominantes, ce qui signifie que la partie réactive de l'interface fluide-solide doit être décrite précisément à l'échelle locale. D'autre part, la distribution spatiale globale du solide doit également être caractérisée avec précision car elle détermine la représentativité des propriétés moyennes de transport. Les techniques d'imagerie multi-échelle peuvent fournir une image basse résolution (LR), correspondant à un large champ de vision, qui peut être utilisée comme entrée pour le calcul des propriétés de transport moyennes et des images haute résolution

(HR) qui décrivent l'interface fluide-solide en détail. Pour la modélisation numérique, nous avons besoin de l'image LR de tout le domaine de calcul, et des informations HR des zones ayant un fort effet sur le transport, par exemple, les zones où des réactions importantes ont lieu. L'acquisition d'une image HR de tout le domaine de calcul n'est pas réaliste, et, si une valeur moyenne n'est pas suffisante pour la modélisation (surface réactive effective), nous avons besoin d'un moyen d'incorporer dans un modèle multi-échelle les informations HR et LR. Dans ce travail, nous utilisons un maillage cartésien non uniforme (NUCM) résultant d'une double approche : d'abord, un grossissement de la grille visant à améliorer les aspects calculatoires, et ensuite un affinement local de la géométrie de l'interface visant à améliorer la précision des résultats. Dans l'approche multi-échelle que nous proposons, les images LR (pertinentes à l'échelle globale) et HR (pertinentes à l'échelle locale) sont prises en compte dans le processus d'affinement.

Le deuxième exemple concerne la caractérisation multimodale des cellules solaires à couche mince en kesterite : résultats expérimentaux et interprétation numérique. La microscopie à rayons X à balayage basée sur le synchrotron est une technique puissante pour l'étude à haute résolution spatiale des matériaux des cellules solaires : [19], [20]. La grande flexibilité des lignes de faisceaux pour intégrer différentes modalités d'étude et le développement de l'optique à rayons X permettent d'obtenir et de corréler de manière unique des informations sur les différentes propriétés des matériaux à l'échelle nanométrique [21]–[24]. Les techniques analytiques, telles que la fluorescence X (XRF), la diffraction des rayons X et le XBIC, appliquées simultanément, peuvent fournir des informations spatialement corrélées entre la composition chimique et les propriétés électriques de l'échantillon (analyse non destructive) [25]–[30]. Cependant, ces informations ne sont souvent pas suffisantes pour comprendre les limites des dispositifs de collecte d'énergie. L'architecture complexe des cellules solaires de nouvelle génération comprenant plusieurs couches rend difficile la détermination des mécanismes fondamentaux affectant les performances électriques. Une modélisation de premier principe du signal XBIC est nécessaire pour obtenir une meilleure compréhension des corrélations entre les propriétés des matériaux et les performances électriques du dispositif. Par conséquent, nous complétons les données expérimentales avec un modèle numérique multi-échelle du signal XBIC basé sur les premiers principes. L'équation de Poisson et les équations de continuité pour les électrons et les trous, ainsi que le modèle bidimensionnel (2D) de dérive-diffusion, combinés aux profils de génération basés sur la simulation Monte-Carlo, sont résolus dans le domaine de calcul 2D construit à partir des données XRF.

Pour résumer, au cours de ce projet de doctorat, nous avons développé une procédure d'imagerie et de modélisation multi-échelle pour le transport réactif dans les milieux poreux, et un modèle numérique 2D pour simuler l'expérience XBIC pour les dispositifs de cellules solaires. L'expérience d'imagerie multi-échelle a été réalisée pendant mon détachement à l'Institut Paul Scherrer (PSI) dans le cadre du projet MUMMERING. Les volumes 3D obtenus ont été utilisés dans les applications de la procédure d'imagerie et de modélisation multi-échelle proposée pour le transport réactif dans les milieux poreux. L'expérience XBIC a été réalisée par des chercheurs de l'Université technique du Danemark (DTU) à NanoMAX, une ligne de faisceau de nanosondes à rayons X durs de l'installation synchrotron MAX IV à Lund (Suède). Les simulations de Monte-Carlo ont été réalisées en collaboration avec Michael Stuckelberger du Deutsches Elektronen-Synchrotron (DESY).

Après une introduction, nous exposons brièvement quelques éléments concernant le rayonnement synchrotron, qui est central pour notre travail. Puis les chapitres suivants présentent les deux exemples de modélisation numérique multi-échelle combinée à des expériences de rayonnement X synchrotron.

Dans le chapitre deux, dans un premier temps les bases de l'imagerie microtomographique 3D et l'expérience d'imagerie multi-échelle que nous avons réalisé sont présentées. Nous exposons ensuite la formulation mathématique du problème de la diffusion réactive dans les milieux poreux. Le modèle résultant que nous devons résoudre est présenté avec sa discrétisation numérique basée sur la méthode des volumes finis centrés sur les cellules. Dans un second temps, la nouvelle approche de grossissement de la grille est présentée avec la discrétisation spatiale. Ensuite, nous traitons des différentes stratégies de raffinement local du maillage (LMR). Enfin, nous présentons les résultats et discutons des conséquences de l'approche d'imagerie et de modélisation multi-échelle sur la précision des propriétés effectives calculées et la réduction du coût de calcul.

Une expérience d'imagerie multi-échelle a été réalisée à la ligne de faisceau TOMCAT dans le cadre du projet MUMMERING. Quatre matériaux poreux différents ont été considérés avec une complexité de structure variable. Pour chaque échantillon, un total de huit acquisitions a été réalisé à différentes résolutions. La figure 1 illustre le protocole de l'expérience d'imagerie multi-échelle avec des coupes transversales de l'échantillon de grès de Fontainebleau. Pour chaque échantillon, un balayage complet de l'ensemble de l'échantillon a été réalisé avec différents grossissements : 2x et 4x, ce qui a permis d'obtenir des volumes 3D pour les échantillons complets avec (1600×1600×962) et (2560×2560×2160) voxels, respectivement. Avec un grossissement de 10x, deux régions ont été définies pour effectuer une microtomographie locale, ce qui a donné des volumes 3D de (2560×2560×2160) voxels. À l'intérieur de l'une des régions de grossissement 10x, deux autres microtomographies locales ont été réalisées avec un grossissement 20x, donnant lieu à des volumes 3D de (2560×2560×2160) voxels.

La figure 2 illustre l'approche de grossissement de la grille développée. Cette approche nous permet d'avoir une grille grossière loin des interfaces fluide-solide. En fixant la taille des cellules près des interfaces et en agrégeant 2 × 2 cellules actives (ACs) en 2D et 2 × 2 × 2 ACs en 3D ailleurs, nous obtenons le premier niveau de la grille grossière. En répétant la même procédure, on obtient la grille grossière finale.

Le NUCM est composé de AC de différentes tailles. Cela nécessite des procédures de communication des données à travers les interfaces non concordantes pour répondre aux

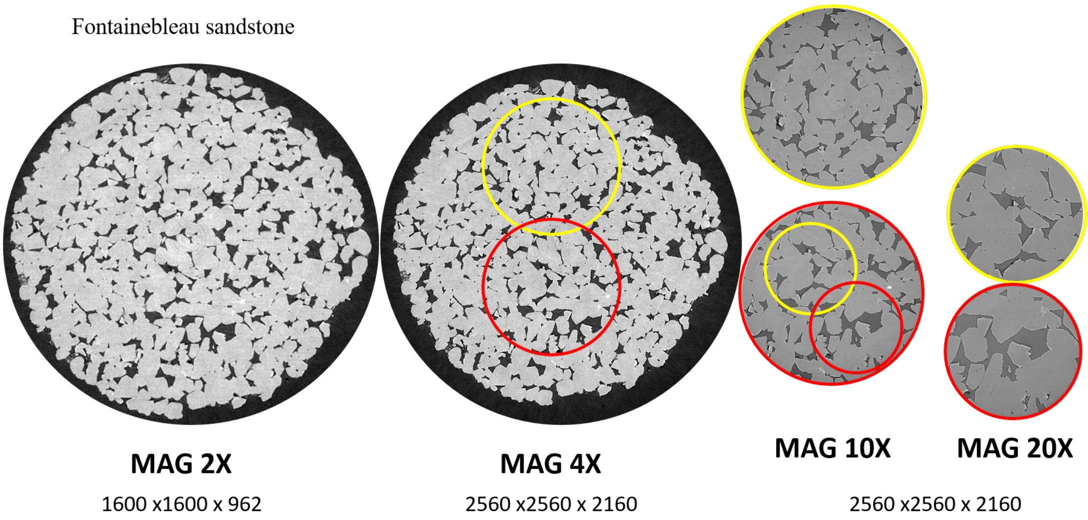

Figure 1: Coupes transversales du grès de Fontainebleau avec une approche d'imagerie multi-échelle.

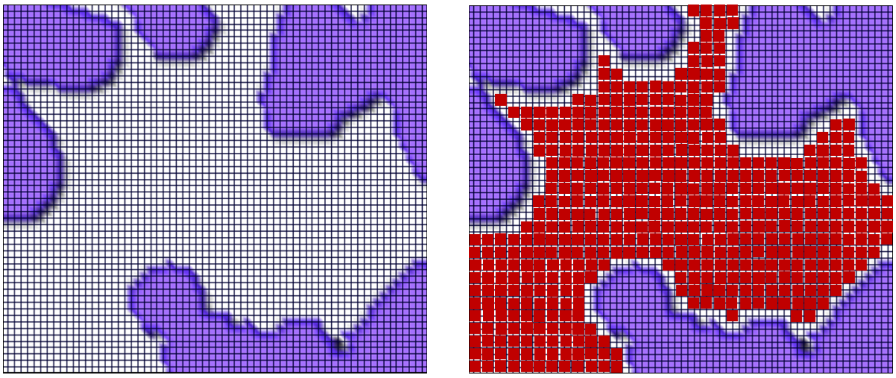

(a) Original grid. (b) First level of the coarse grid.

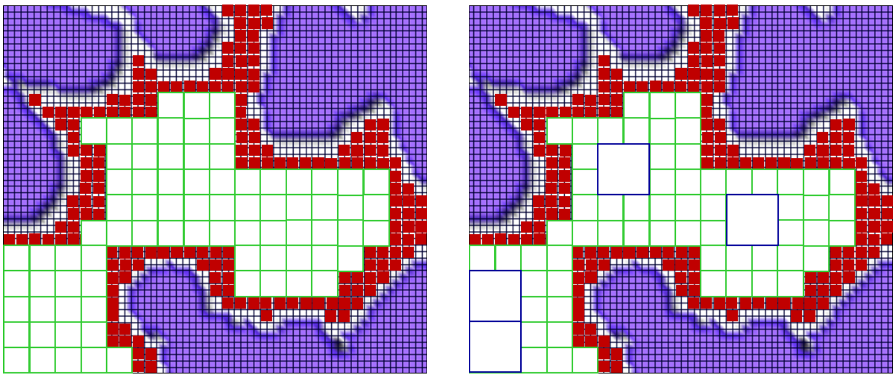

(c) Second level of the coarse grid. (d) Final level of the coarse grid.

Figure 2: Grossissement de la grille pour un exemple en 2D.

exigences des schémas de discrétisation. La discrétisation spatiale développée est basée sur l'interpolation barycentrique. Elle a été utilisée à la fois dans les étapes de grossissement et d'affinement.

L'approche d'imagerie et de modélisation multi-échelle développée a été testée et ses avantages ont été étudiés. Trois géométries ont été considérées :

- Une géométrie simple sans zone réeactive

- La même géométrie avec des parties réactives ajoutées
- Des volumes 3D extraits des volumes Sic-Diamonds

En utilisant la première géométrie, les tests suivants ont été effectués pour étudier les effets de :

- Affinement global du maillage sur D_{eff} avec les différents niveaux d'interpolation décrits dans la section 2.3.5.
- Changement de la résolution sur D_{eff} et le temps CPU.
- Approche du grossissement de la grille sur D_{eff} et le temps CPU.

Dans le troisième test, les résultats ont été comparés au cas uniforme et les avantages de l'application de l'approche développée ont été discutés (voir figure 3).

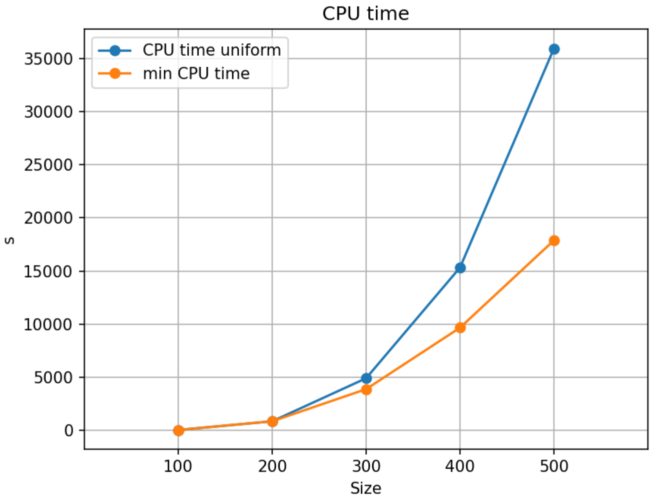

Figure 3: L'effet de l'approche du grossissement de la grille sur le temps CPU pour les volumes 3D de différentes résolutions en comparaison avec le cas uniforme.

La deuxième géométrie a été utilisée pour étudier les effets sur l'ensemble complet des propriétés effectives, c'est-à-dire D_{eff} et le vecteur U. De plus, elle a été utilisée pour la mise en œuvre du LMR proposé avec une approche d'imagerie multi-échelle et plusieurs régions critiques ont été testées. Enfin, une tentative d'application de l'approche développée sur un ensemble de données réelles a été réalisée en utilisant la troisième géométrie.

Dans le chapitre trois, nous commençons par présenter le travail de collaboration dans le deuxième exemple sous la forme d'un article publié dans le journal Faraday Discussions. Dans un second temps, nous présentons les bases de la physique des semi-conducteurs et décrivons le modèle que nous avons choisi pour notre problème. Ensuite, nous traitons des approches de modélisation numérique utilisées pour discrétiser et résoudre les équations différentielles partielles non linéaires couplées afin de simuler l'expérience XBIC. Enfin, nous présentons quelques résultats supplémentaires et discutons des facteurs possibles limitant les performances du dispositif considéré sur la base des résultats de la simulation.

Un échantillon à base de CZTS (cuivre zinc étain sulfure) a été considéré dans l'expérience. La figure 4 montre les images XRF des éléments constituant l'échantillon et le signal XBIC correspondant. Comme les mesures ont été effectuées simultanément, aucun recalage des images XRF et XBIC n'est nécessaire et une corrélation par pixel entre les images peut être effectuée. Les inhomogénéités de composition les plus importantes dans la couche de CZTS sont mises en évidence dans les images par des flèches blanches. Elles sont associées à des densités projetées relativement plus faibles de tous les éléments composant la couche. Une zone plus notable avec une composition chimique inhomogène est marquée par la boîte blanche. La zone correspondante dans l'image XRF du Cd indique des précipités de CdS résultant du dépôt par bain chimique. Il n'est cependant pas clair si le précipité de CdS résulte de l'absence de la couche de ZnO déposée sur le dessus. Quoi qu'il en soit, les images XRF de In et Sn montrent une variation de la composition des éléments constituant la couche d'ITO qui suit la topologie du précipité de CdS. Globalement, l'image XBIC dans la zone située sous la boîte blanche montre une diminution du courant associée aux défauts électroniques causés par la structure perturbée de la couche.

Un domaine de calcul 2D a été généré à partir des données XRF, et une approche de simulation numérique 2D en volumes finis a été utilisée. En conjonction avec les équations de continuité pour les électrons et les trous couplées à une simulation de Monte Carlo (MC) pour l'interaction rayons X/matériau, l'équation de Poisson a été résolue pour simuler l'expérience XBIC.

Nous avons développé un simulateur basé sur la méthode des volumes finis centrés sur les cellules combinées au schéma de Scharfetter Gummel. Le simulateur a été conçu pour prendre en compte :

- La structure réelle de la couche dans les simulations en utilisant le domaine de calcul 2D construit à partir des données XRF.
- Les simulations de Monte-Carlo dans le calcul des profils de génération 2D.

Le simulateur développé a été comparé au logiciel Sesame, montrant un bon accord pour les cas simples. Des analyses de sensibilité en 2D ont été réalisées pour étudier certains défauts qui apparaissent lors de la corrélation des données XRF avec les résultats expérimentaux du XBIC. Dans la section 3.2, nous avons étudié l'effet du type de contact et les effets de l'absence de couche de ZnO sur les performances du dispositif. Dans les résultats supplémentaires, les défauts de composition inhomogène ont été abordés en étudiant les effets des paramètres de la couche absorbante (CZTS) sur le signal XBIC à l'échelle nanométrique.

À notre connaissance, ce travail peut être considéré comme la première tentative de simulation des mesures XBIC pour une géométrie d'échantillon réaliste à l'échelle nanométrique.

Pour conclure, nous avons présenté deux exemples de modélisation numérique multi-échelle combinée à des expériences de rayons X synchrotron : (1) Imagerie et modélisation

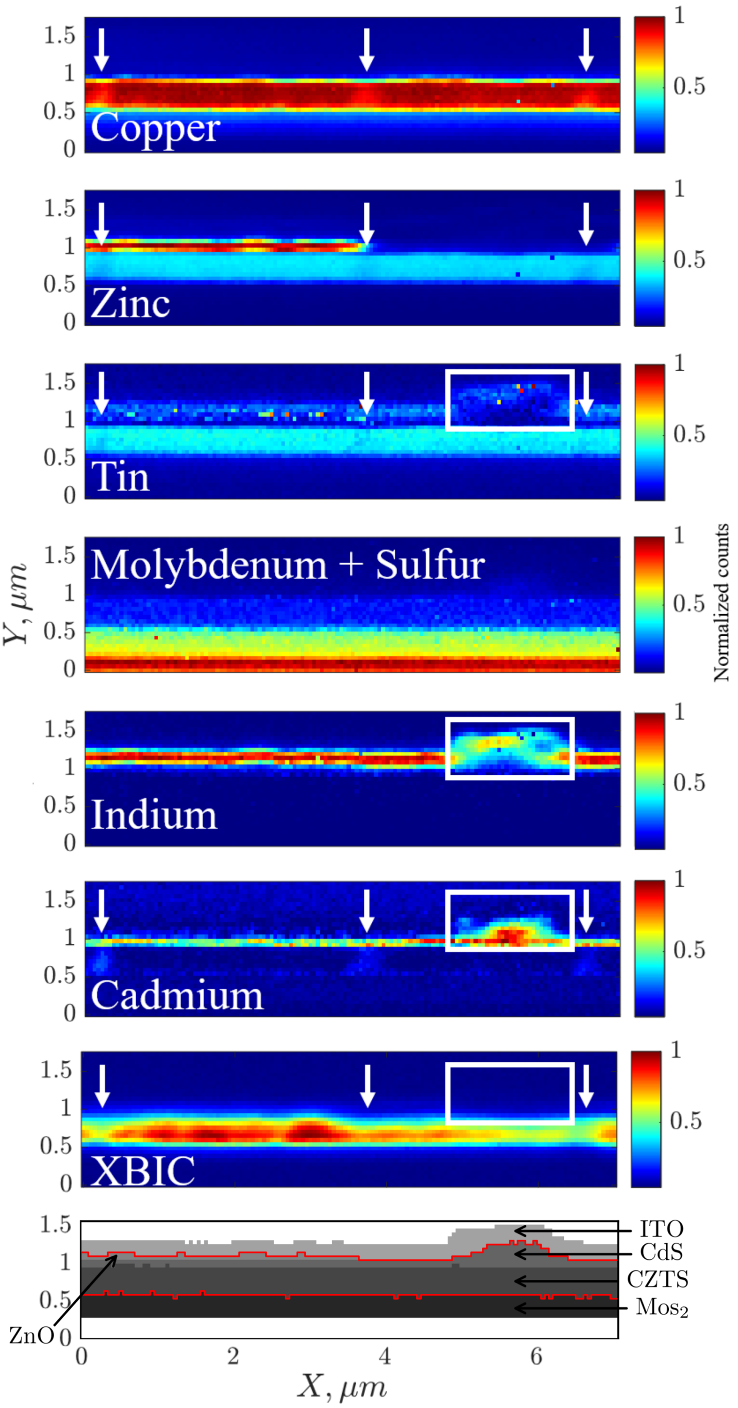

Figure 4: Images XRF des principaux éléments constituant l'échantillon ainsi que le signal XBIC résultant de la spécification de la structure en couches avec le domaine de calcul entre les lignes rouges. Les flèches blanches mettent en évidence les zones associées aux variations de composition de la couche CZTS et la boîte blanche indique la zone avec une distribution inhomogène des éléments des couches CdS et ITO, ainsi que l'absence de la couche ZnO.

multi-échelle pour le transport réactif à l'échelle du pore, (2) Caractérisation multimodale des cellules solaires à couche mince en kesterite : résultats expérimentaux et interprétation numérique. Nous avons montré l'importance des techniques d'imagerie multi-échelle dans l'approximation des propriétés effectives et les avantages de les combiner avec des procédures de modélisation numérique multi-échelle. En outre, nous avons illustré les avantages de la combinaison de la modélisation numérique multi-échelle avec les expériences XBIC pour relier les défauts locaux aux performances globales.

Dans le premier exemple, l'approche d'imagerie et de modélisation multi-échelle proposée a été mise en œuvre avec succès et divers cas d'essai de volume 3D synthétisé et réel ont été présentés. L'approche proposée de grossissement de la grille et la discrétisation spatiale ont permis d'améliorer les aspects calculatoires du problème et de maintenir une grande précision globale des résultats. En utilisant l'approche d'imagerie multi-échelle dans l'étape d'affinement du maillage local, nous avons pu améliorer la qualité des résultats lors du calcul des propriétés effectives. Des recherches supplémentaires sont nécessaires pour identifier les régions critiques à l'étape d'affinement du maillage local.

Dans le second exemple, nous avons développé un simulateur de dispositif 2D basé sur les premiers principes, conçu pour traiter les structures réelles de dispositifs 2D et pour combiner la simulation Monte-Carlo afin de simuler les expériences XBIC. La microscopie à rayons X à balayage corrélatif est un outil puissant pour l'étude de matériaux fonctionnels tels que les cellules solaires, fournissant une caractérisation corrélative à résolution spatiale de la composition chimique et des performances électriques à l'échelle nanométrique. Les cartes XRF combinées et corrélées avec les mesures XBIC permettent de visualiser les inhomogénéités dans toutes les couches du dispositif et de les corréler avec l'efficacité de conversion de charge locale. Ensuite, les défauts électroniques identifiés à partir de cette combinaison peuvent être expliqués en utilisant le simulateur développé.

Pour terminer, dans ce travail, nous avons démontré à l'aide de deux exemples les avantages et les bénéfices de la combinaison entre la modélisation numérique multi-échelle et les expériences de rayons X synchrotron. Les outils d'imagerie avancés fournissent de très grands volumes de données qui doivent être traités. Le développement d'outils numériques multi-échelles est d'une grande importance pour analyser et extraire efficacement des informations précieuses de ces volumes. D'autre part, la comparaison directe entre les résultats expérimentaux et les résultats de simulation permet de faire un pas en avant dans la compréhension de la fonctionnalité des matériaux avancés.

Contents

Introduction

This thesis consists of two examples of multi-scale numerical modelling combined with synchrotron X-ray experiments: (1) Multi-scale imaging and modelling for reactive transport at the pore scale, (2) Multi-modal characterization of Kesterite thin-film solar cells: experimental results and numerical interpretation. These two examples developed within a training network called MUMMERING (MUltiscale, Multimodal and Multidimensional imaging for EngineeRING). It was an extremely pleasurable and exciting opportunity to learn exhilarating things through this training program.. So, let me begin my thesis by explaining a bit about MUMMERING before I delve into the scientific details of this work. MUMMERING [1] is one of the Marie Sklodowska-Curie Actions Innovative Training Network (ITN) programs. ***The overarching goal of it was to create a research tool that encompasses the wealth of new 3D imaging modalities that are surging forward for applications in materials engineering, and to create a doctoral programme that trains 15 early stage researchers (ESRs)***[*] in all aspects of 3D imaging from data acquisition, over reconstruction and segmentation to physical modelling. As an ITN, MUMMERING also aimed to train a new generation of creative and innovative ESRs who are able, to convert knowledge and ideas into products and services for economic and social benefit, and to work collaboratively with other ESRs in the network to solve real world problems.

Multi-scale models and simulations are important challenges for computational science in many domains of research. Most real-life phenomena involve an extended range of spatial or temporal scales, as well as the interaction between various natural processes. Moreover, ***multi-scale imaging methods form the bridge between the atomic scale understanding gained from electron microscopy, diffraction and spectroscopy, through nanoscale tomography and all the way up to macro-scale objects. Correlative microscopy unifies information derived from a variety of imaging modalities obtained through energy variation and different probe interactions with material.***[*]Unique properties of synchrotron radiation, which are continuous spectrum, high flux and brightness, and high coherence, make it an essential tool in multi-scale imaging modalities. Material scientists typically use synchrotron X-ray to probe the structure of materials at the micrometre to nanometre scales. By relating the structure of materials to their mechanical-physical behaviour, materials with opti-

---

[*] Part of MUMMERING proposal [1]

mized performance can be engineered. The range of applications of synchrotron X-ray experiments is very large and covers sectors as diverse as chemical (polymer) industry, semiconductor industry, geology (and oil) research, agro-food industry and advanced manufacturing applications.

The main objective of this PhD was to develop a multi-scale imaging and modelling procedure for reactive transport in porous media. Furthermore, a collaborative work titled "Multi-Modal Characterization of Kesterite Thin-Film Solar Cells: Experimental results and numerical interpretation" initiated with ESR 9 (Azat M. Slyamov) became an essential part of my PhD. This work resulted from the continuous discussions during the workshops and meetings in MUMMERING project. The main objective of the collaborative work was to develop a multi-scale approach based on first-principles to simulate X-ray beam induced current (XBIC) experiments. Indeed, these two different examples are sharing the property of being synchrotron X-ray dependent experiments and the same objective of developing multi-modal multi-scale imaging and modelling procedures.

In the first example, multi-scale imaging and modelling for reactive transport (transport with reaction at the interfaces; heterogeneous reaction) at the pore scale was considered. Modelling transport in porous media requires keeping in mind multi-scale aspects existent in porous media structures. A porous medium is a material containing voids; examples are filters, adsorbents, print paper, wood, composite materials, and biological tissues, as well as soil and pavement, and oil, gas, and geothermal reservoirs [2]. Such porous media are typically highly heterogeneous at local scale (pore scale) and using the models describing the transport at the pore scale to predict and observe the transport at the global scale (macroscopic scale) is usually not feasible. For instance, in an aquifer, at the pore scale, the single-phase flow is governed by the Stokes equation. However, due to the large range of scales involved, span from the pore scale (about 100 µm) to the macroscopic scale (km), and to the complex geometry at the pore scale, it is practically impossible to use Stokes equation to describe the flow in the entire system. Instead, the continuum approach is proposed to describe the flow in the macroscopic scale by Darcy's law [3]. In this approach, the porous media is treated as a continuum and the flow is predicted without information on the microscopic configuration of the pore scale geometry. The results of Darcy's work is an empirical law with limited range of validity. Therefore, many researchers attempted to derive Darcy's law in a general way using the pore scale information by means of change of scale techniques [4], [5]. The resulting macroscopic model contains the effective property, the permeability tensor, which can be computed using the information at the pore scale. Then, rather than attack the problem in terms of equations that are only valid in the pores, we can use the change of scale techniques to derive macroscopic equations that are valid everywhere and are linked to the pore scale geometry through the effective properties. A central problem in pore scale research is the determination of such effective properties that describe the behaviour of a porous medium on macroscopic scales, i.e., the properties that are relevant and can be measured in laboratory or field experiments [6]. The volume averaging technique is one of the various theoretical methods providing a rigorous description of change of scale procedure [5], [7]–[9], and it is well developed for our targeted problem (reactive transport in porous media) [9]–[13]. In general, most natural systems are heterogeneous and the effective transport properties are highly dependent on the geometrical details [12]. Measurement of three-dimensional (3D) geometry can be approached in a number of ways. Synchrotron microtomography is one of the advanced tool in material science providing 3D images of the material under investigation. Traditionally, 3D images are quantified through a limited number of parameters (porosity, reactive surface area, etc...), and these parameters are the input used in the models. As an alternative, the entire 3D data set can be used as the input to compute the effective properties [14]–[17]. This supports transition towards a next generation of more accurate models, which include the microstructure heterogeneity.

To compute the effective properties, the 3D image describing the local geometry should be large enough to be representative. By representative we mean that the effective properties will not change for larger images. This minimal required volume is commonly called the representative elementary volume (REV) [18]. Modern imaging tools are providing very large 3D images (geometries described by up to billions of voxels), and using these entire 3D images is challenging. Therefore, special care for the memory usage and computational time should be taken into account. One important aspect in numerical simulation is the space discretization, the simplest and commonly way is using regular (uniform) Cartesian grid (voxel grid). The disadvantages of the regular grids are the requirements for computational effort and memory size. Therefore, adapted space discretization is needed to solve that problem.

For the problems we consider, heterogeneous reactions are dominant, meaning that the reactive part of the fluid-solid interface must be precisely described at the local scale. On the other hand, the global spatial distribution of the solid must also be precisely characterized because it determines the representativeness of the average transport properties. Multi-scale imaging techniques can provide a low-resolution (LR) image, corresponding to a large field of view that can be used as input for computing the average transport properties and high-resolution (HR) images that describe the fluid-solid interface in details. For numerical modelling, we need the LR image of all the computation domain, and HR information of the zones having a strong effect on the transport, for instance, zones where significant reactions take place. Acquiring a HR image of the full computation domain is not realistic, and, if an average value is not sufficient for modelling (effective reactive surface), we need a way to incorporate in a multi-scale model both HR and LR information. In this work, we use a non-uniform Cartesian grid resulting from a twofold approach: first, a grid coarsening aiming in improving the computational aspects, and second a local refinement of the interface geometry aiming in improving the accuracy of the results. In the multi-scale approach, we propose, both LR (relevant to the global scale) and HR (relevant to the local scale) images are taken into account through the refinement process.

The second example concerns the multi-modal characterization of Kesterite thin-film solar cells: experimental results and numerical interpretation. Synchrotron based scanning X-ray microscopy is a powerful technique for spatially resolved high-resolution investigation of solar cell materials [19], [20]. The high flexibility of beamlines to incorporate different study modalities and the development of X-ray optics allows obtaining and uniquely correlating information about different properties of materials at the nanoscale [21]–[24]. Analytical techniques, such as X-ray fluorescence (XRF), X-ray diffraction and XBIC applied simultaneously can provide spatially correlated information between chemical composition and electrical properties of the specimen without destroying it [25]–[30]. However, such information is often not sufficient to understand limitations of energy harvesting devices. The complex architecture of the new generation solar cells comprising multiple layers makes it hard to determine the fundamental mechanisms affecting electrical performance. First-principles modelling of the XBIC signal is required to obtain a deeper understanding of the correlations between material properties and the electrical performance of the device. Therefore, we support the experimental data with a multi-scale numerical model of the XBIC signal based on first-principles. Poisson's equation and the continuity equations for electrons and holes along with the two-dimensional (2D) drift-diffusion model, combined with generation profiles based on Monte-Carlo simulation are solved within the 2D computation domain constructed from the XRF data.

In a nutshell, during this PhD project, we developed a multi-scale imaging and modelling procedure for reactive transport in porous media, and a 2D numerical model to simulate XBIC experiment for solar cell devices. The multi-scale imaging experiment was carried out during my secondment at Paul Scherrer Institute (PSI) under the framework of MUMMERING project. The resulted 3D volumes were used in the applications of the proposed multi-scale imaging and modelling procedure for reactive transport in porous media. The XBIC experiment was performed by researchers from Technical University of Denmark (DTU) at NanoMAX, a hard X-ray nano-probe beamline of the MAX IV synchrotron facility in Lund (Sweden). The Monte-Carlo simulations were performed in collaboration with Michael Stuckelberger from Deutsches Elektronen-Synchrotron (DESY).

After this introduction, we briefly expose some elements concerning synchrotron radiation as it is a central tool for our work. Then the following chapters present the two examples of multi-scale numerical modelling combined with synchrotron X-ray experiments.

In chapter two, we start by presenting the basics of 3D microtomography imaging and the multi-scale imaging experiment we performed. Then we expose the mathematical formulation of the reactive diffusion problem in porous media. The resulting model that we need to solve is presented with its numerical discretization based on the cell centred finite volume method. Thereafter, the novel grid coarsening approach is presented along with the spatial discretization. Then, we discuss the different strategies for local mesh refinement (LMR). Finally, we present the results and discuss the consequences of the multi-scale imaging and modelling approach on the precision of the computed effective properties and the reduction of the computation cost.

In chapter three, we begin by introducing the collaborative work in the second example in the form of a paper accepted for publication in Faraday Discussions journal. Thereafter, we present the basics of semiconductor physics and describe the model we chose for our problem. Then, we discuss the numerical modelling approaches used for discretizing and solving the non-linear coupled partial differential equations to simulate the XBIC experiment. Finally, we present some supplementary results and discuss the possible factors limiting the performance of the device under consideration based on the simulation results.

At the end, we draw some general conclusions, expose the limitations and the difficulties of the selected approaches that we experienced, and discuss the possible developments of our works.

Chapter 1

Synchrotron X-ray

1.1 History of Synchrotron X-ray

Since their discovery X-rays have been used to image the bulk of materials which are non-transparent for visible light. Figure 1.1 shows one of the first X-ray images taken by Wilhelm Röntgen, after his great discovery in 1895 for new invisible radiation of unknown nature, which he called X-ray [31]. Due to interactions with the electrons in the material, X-ray penetrating an object is attenuated. This attenuation depends on the energy of the X-ray, the thickness, the density and the atomic number of the investigated material.

Figure 1.1: A print of the left hand of Anna Bertha Ludwig Röntgen.

In 1909, it was shown by Barkla and Sadler that many elements, when subject to a suitable beam of X-rays, emit a homogeneous beam of secondary X-rays of penetrating power characteristic of the radiating element [32]. X-rays are electromagnetic radiation that transfer energy in discrete packets (photons) and, interact in different ways with matter. They are mainly interacting with the electrons located at particular shells in the atom. When X-rays hit a material some photons transfer their energy to one of the core shell electrons and ionizes the atom. The electron is either moved to one of the higher shells or ejected from the atom. De-excitation is happening by filling the vacancy with an electron from a higher shell and produces X-ray fluorescence (XRF) or an Auger electron. In this case, we say that the X-rays are absorbed by the material. Absorption is not the only way by which X-rays interact with materials; they also scatter, refract and reflect.

Using the X-ray tubes to generate X-rays, great and remarkable results were obtained. These results were restricted due to the limitations of X-ray tubes in focusing or making the rays parallel. In 1947, at the General Electric Research Laboratory in Schenectady, New York, undesirable radiations were observed in the 70 MeV synchrotron [33]. This radiations cause the charged particles in accelerator (synchrotron) to lose energy. Synchrotrons were originally designed to be used in nuclear physics research and, the observed radiations have been named after them as synchrotron radiation. Diran Tomboulian and Paul Hartman performed the first experiments to investigate the possible applications of synchrotron X-rays at Cornell synchrotron in 1956 [34]. Five years later, was the birth of the Synchrotron Ultraviolet Radiation Facility (SURF I) at the National Bureau of Standards in the United States. It is the first facility designed for regular users of synchrotron radiation and is considered as a first-generation synchrotron radiation sources [35]. In 1973, The first international symposium for synchrotron radiation users took place at Daresbury Laboratory and provided early impetus for the development of the world's first dedicated X-rays synchrotron radiation source. This was a second-generation source whose primary source of radiation is the lattice dipoles. With electron storage ring of 2 GeV the first second-generation synchrotron source started its operation in 1981 at Synchrotron Radiation Source (SRS), Daresbury [36]. The European Synchrotron Radiation Facility (ESRF) was the first collaborative synchrotron radiation facility in Europe. In 1988, eleven European countries joined forces to build the world's most performing and bright third-generation light source [37]. The first third-generation facility ESRF with 6 GeV electron storage ring completed and began experiments in 1994. Three years later, the Swiss Parliament approved the Swiss Light Source (SLS) project at Paul Scherrer Institute. The SLS is designed to produce a maximum brilliance in the vacuum ultraviolet and soft X-ray regions and it is started operation in 2001 [38]. One of the most recent fourth-generation facility is MAX IV synchrotron in Lund, Sweden. The inauguration of MAX IV took place on 21st June 2016, with two electron storage rings at 3 GeV and 1.5 GeV, and optimized for the hard X-ray and soft X-ray/ultraviolet spectral ranges, respectively [39].

Beyond this, a fourth-generation of synchrotron radiation facilities is coming of age in the first decade of the twenty-first century, which will be defined by a greatly improved performance, especially with regards to the coherence and brilliance of the x-rays, using so-called energy recovery linacs (ERLs), and free electron lasers (FELs) [40].

1.2 The principle

Synchrotron radiation is created by accelerating free particles in high vacuum. When electrons or other charged particles moving at relativistic speeds are forced by magnetic fields to follow curved trajectories they are accelerated and then they emit electromagnetic radiation in the direction of their motion [41].

In the first-generation of synchrotron radiation sources, electrons were accelerated in a circular orbit (storage ring) and the X-ray beam produced was tangent to the curved trajectory of the electrons. In the second-generation sources, a polyhedral path was used in which electrons travel in straight lines before changing its direction under the effect of bending magnets. This allows localization of the individual radiation sources to be used in beamlines placed around the path. Moreover, the radius of the individual bends can be made smaller to produce X-rays of a higher energy and intensity. In each turn the electrons lose part of their energy, emitting synchrotron radiations. A radio frequency (RF) accelerator is placed in the section between the bending magnets to compensate the loss in energy of the electrons by electric field. In the third-generation synchrotron sources, insertion devices are installed in the straight sections between the two bending magnets. High magnetic field devices known as wigglers and undulators are the components of the insertion devices that provide much more brilliant radiation [42]. Figure 1.2 shows the gain in brightness achieved by the new synchrotron radiation sources, as a function of time. By brightness (brilliance), we mean the amount of power per unit frequency, surface area and solid angle.

Figure 1.3 shows schematic representation of a synchrotron radiation facility. Firstly, electrons are accelerated using the linear accelerator (linc) until their energy reaches several millions of electron volts (MeV). Then, they are injected to the booster ring and accelerated until the desired value (energies of several GeV), before their periodic injection into the storage ring. In the storage ring, the electrons are circulating in close path and their energies are maintained by the use of an array of magnets. The ring is a structure consisting of arced sections containing bending magnets, and straight sections used for insertion devices. The lattice of magnets in an insertion device forces the particles to execute small oscillations which produce intense beams of radiation. Then, the bending magnet is used to deflect the electrons around the arced sections causing another emission of synchrotron radiations. The beamlines run off tangentially to the storage ring, along the axes of the insertion devices and tangentially at bending magnets. In the beamline, the radiations pass through a number of optical elements, such as a monochromator, focusing device, etc., so that a beam of radiation with the desired properties is delivered to the sample [40].

Since many beamlines and monochromator can be set up at a storage ring, many experimental setups can be planned in the experimental hutch depending on the research interest. In this thesis, two different setups were considered in our examples of multi-scale numerical models: 3D microtomography imaging and X-ray beam-induced current

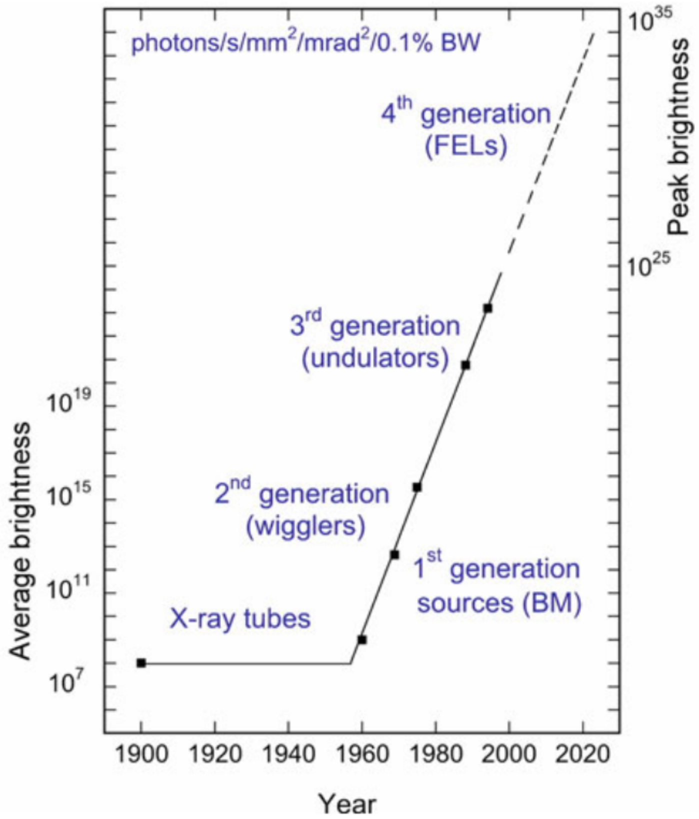

Figure 1.2: Evolution of the average brightness of different generations of synchrotrons (after [41], Fig. 1.4).

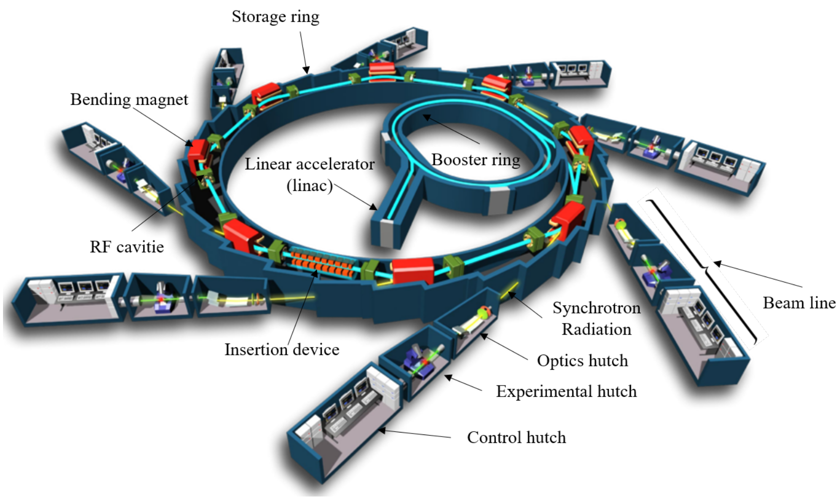

Figure 1.3: Schematic representation of a synchrotron radiation facility (Source: EPSIM 3D/JF Santarelli, Synchrotron Soleil).

(XBIC) setups.

Using the first setup, 3D microtomography imaging, a multi-scale imaging experiment was performed at TOMCAT beamline from the Swiss Light Source (SLS). The resulted multi-scale 3D images were used as inputs for the developed multi-scale model in the first example. Detailed description of the experimental setup and the multi-scale model is presented in chapter 2. The microtomography imaging is a full-field technique in which, the X-ray beam is more extended or comparable to the field-of-view (FOV) of interest.

While in the second setup, XBIC, a highly focused X-ray beam is used to scan the desired field-of-view. In this scanning-base technique, a wide variety of modalities can be obtained from different interactions between X-ray and the studied material. X-ray fluorescence (XRF) combined with XBIC measurements is collected to provide a correlative study of electrical performance and chemical composition. The experiment was performed at the NanoMAX beamline which is a part of the MAX IV synchrotron facility. The first-principles model developed to simulate the XBIC measurements is presented in chapter 3 along with the experimental setup.

Chapter 2

Multi-scale imaging and modelling for reactive diffusion at the pore scale

2.1 Introduction

In this chapter, we focused our attention on reactive transport in porous media. This phenomenon appears in a wide variety of scientific and engineering domains, including chemical reaction engineering, soil mechanics, electrochemical systems, oil industry, storage of nuclear waste, groundwater hydrology, and biophysical and biological systems [43]. Due to their inherently multi-scale nature, such systems can be modelled from a macroscale (Darcy scale) perspective or a microscale (pore scale) perspective. The validity and the accuracy of each model is largely dependent on the applications. In most cases, a multi-scale modelling is required for understanding the multi-physics of the system [44]–[50]. The combination between microscale and macroscale is achieved by means of upscaling techniques such as homogenization [51], singular perturbation technique [52], thermodynamically constrained averaging theory [53] or volume averaging [9]. In the volume averaging method, the model is derived by spatially smoothing the governing equations at the pore scale. The resulting macroscopic model contains the effective properties that can be evaluated by solving auxiliary problems, the closure problems, in representative volumes of the pore scale structure [54]–[56]. To be representative, the volumes should be large enough to capture all the global features. On the other hand, they should have high spatial resolution to precisely describe the fluid/solid interface at the pore scale.

X-ray computed tomography (CT), in particular synchrotron microtomography, is a powerful tool for detecting the microscale pore structure and it has been applied to many natural and synthetic porous media [16], [57], [58]. With high resolution (HR) images more details of the pore structure can be revealed and more accurate description of the volume can be obtained. However, in most cases, the obtained HR 3D volumes are non-representative because they correspond to a small field-of-view. On the other hand, the low resolution (LR) images provide large field-of-view and are able to capture the global microscale pore structure, but they are losing the accuracy and are not able to detect pores with size smaller than the scanning resolution. As reported in the literature, the scanning resolution has significant effect on the computed effective properties for different porous materials [59]–[63]. There is an inevitable trade-off between image resolution and the sample size that should be taken into account in the approximation process. To overcome this limitation, a detailed 3D volume with different resolutions or different imaging techniques should be used. Nevertheless, the combination of these multi-scale images into a single 3D volume is challenging. A multi-scale image fusion of X-ray microtomography and SEM (scanning electron microscope) techniques was proposed in [64] to compute the effective properties. The fusion process used was computationally expensive and the resulted 3D volumes might not be accurate enough for complex structures. Still, they reported a good agreement with the experimental results. In [65], a multi-scale imaging and modelling workflow to compute transport properties of rocks with wide pore size distributions was proposed. Following similar approach as in [66], they used a dry/wet micro CT imaging technique in order to reveal sub-resolution porous regions coupled with backscattered electrons (BSE) images and the resulted 3D porosity maps were utilized into a multi-scale pore network model. In [67], they used four different voxel resolution (4.4 µm, 6.2 µm, 8.3 µm, 10.2 µm) for scanning the same physical field of view in order to study the effect of voxel resolution on different porous materials. They also introduced a numerical coarsening scheme which was used to coarsen a high voxel resolution image (4.4 µm) to lower resolutions images. The HR image was coarsened by mapping the coarser grid onto the original binarized HR image to reduce the computational power and time used in the calculation of the effective properties. Acquiring a HR image of a sample large enough to be representative is time consuming and exhausting as multiple 3D images are concatenated and correlated to build the full 3D volume. In most cases, it is not realistic and it is even useless as the HR images are only needed for some critical regions as in the zones having strong effects on the transport process. In this work, we try to use information contained in both HR and LR images in a multi-scale model by using a non-uniform Cartesian grid resulting from a twofold approach: first, a grid coarsening aiming in improving the computational aspects, and second, a local refinement of the interface geometry aiming in improving the accuracy of the results. In our multi-scale approach, both LR (relevant to the global scale) and HR (relevant to the local scale) images are taken into account through the refinement process.

Identifying the critical regions is not a straightforward procedure. In general, a first solution of the model at the LR images is required and then the HR information are injected where it is needed. At the scanning step, this information is lacking and choosing where to acquire the HR images should be made without it. Some critical regions might be located in the acquired HR images, but, the rest of them might not be. Hence, the refinement step requires being able to inject HR information at any location in the LR grid. Using the LR and HR images of the same zone of the sample, a statistical model can be built to represent the LR-HR change of scale. Then, this model can be used to complement LR images with HR information. This can be achieved by means of superresolution techniques. The multi-scale imaging experiment presented in section 2.2 was performed having in mind that the resulting multi-scale 3D volumes will be used in the development of superresolution approach in collaboration with SUPREMATIM (SUPerREsolution of 3d MATerials IMages) project [68].

The objective of this work was to develop a multi-scale imaging and modelling procedure for reactive transport in porous media. To handle the fluid flow, we first considered the computation of the effective permeability tensor. The classical methods developed in house use the finite volume method with staggered grid at uniform Cartesian grid [15]. Applying the same method with the proposed non-uniform grid was very complicated due to the large number of configuration generated from using the staggered grid structure. So, as a first step to look for a proof of concept, the case of diffusion reaction was considered instead to test the proposed multi-scale imaging and modelling approach.

This chapter is arranged as following: In section 2.2, the multi-scale imaging experiment along with the resulting 3D volumes are presented. In section 2.3, we start with a brief description of the reactive diffusion problem and of the change of scale procedure using the volume averaging method. Thereafter, the discretization of the problem using the cell centred finite volume on uniform Cartesian grid is given. Then, the proposed grid coarsening approach and local mesh refinement along with the spatial discretization are presented. Finally, in section 2.4, we present the results and discussions on the consequences of the multi-scale imaging and modelling approach on the precision of the computed effective properties and the reduction of the computation cost.

2.2 Multi-Scale Imaging Approach

The macroscopic properties of solid microscopically heterogeneous materials such as metals, ceramics, composite materials, porous or granular media, etc. depend on local properties as well as on the local geometrical organization of their constituents. X-ray microtomography imaging is a powerful tool for investigating the internal structure of such materials with wide range of spatial resolutions.

In this section, we first introduce briefly the basics of 3D microtomography imaging (for more detailed description on this technique, the readers are kindly referred to [42]). Then, the multi-scale imaging experiment performed at TOMCAT beamline is presented.

2.2.1 3D microtomography imaging

X-ray microtomography is a non-destructive characterization method that allows to expose the internal geometry of a material. The term tomography denotes imaging by sections or sectioning that uses any kind of penetrating wave. The term micro simply describes the scale reached by the technique.

X-ray microtomography can be performed using different X-ray sources namely lab-based X-ray tubes and synchrotron radiations out of which synchrotron based X-ray provides the largest number of experimental options for tomography. Among the existing modalities, we only considered absorption (attenuation) microtomography technique.

Absorption microtomography is based on the detection of X-ray radiation attenuated by an object. The attenuated X-ray beam is recorded by a detection system, in which it is converted into visible light by a scintillator. The resulting visible image is then projected onto a CCD (Charge-coupled device) camera, from which a digital image is read out into a computer where it is stored and further processed [42]. The produced image is called a tomogram (radiograph) and it contains all the in-depth information integrated along the projected direction. To obtain a complete 3D image representing the local attenuation distribution in the object, radiographic projections should be taken for many angular positions. Then, the resulted set of projections are used for reconstructing the 3D image.

With the assumption that the acquisition system is able to provide a set of projections along straight lines (rays), parallel beam geometry as for synchrotron sources, we can compute the intensity of the transmitted beam along each straight line using the Beer-Lambert law as follows:

$$I_1 = I_0 e^{-\int\limits_{path} \mu(l)dl} \tag{2.1}$$

where I_1 is the intensity of the transmitted beam, I_0 is the intensity of the emitted beam and μ is the linear attenuation coefficient. With calibration procedures, we assume that both I_1 and I_0 are measured by the acquisition system, then the projection of μ along a ray is expressed as follows:

$$\ln\left(\frac{I_0}{I_1}\right) = \int\limits_{path} \mu(l)dl \tag{2.2}$$

Taking into account each rays along a line of the detector for all angular positions will generate a sinogram which is mathematically known as the Radon transform of function μ. The inverse Radon transform then is used to obtain a reconstructed 2D image of μ from the projection data.

Unfortunately, there is no exact implementation of the inverse Radon transform. Approximation techniques should be used in the inversion process which are usually called tomographic reconstruction methods. The two widely used reconstruction approaches are: filtered backprojection [69] and the algebraic reconstruction methods [70]. A mathematical formulation of these algorithms can be found in [42].

2.2.2 TOMCAT beam line Experiment

During my first year, I did a three weeks secondment at Paul Scherrer Institute (PSI) in Switzerland. At the beamline TOMCAT from the Swiss Light Source (SLS), I learned about synchrotron microtomography and multi-scale imaging. We had the attribution of 24 hours for doing multi-scale imaging experiments on different type of materials.

The beamline for TOmographic Microscopy and Coherent rAdiology experimenTs (TOMCAT) is offering cutting-edge technology and scientific expertise for exploiting the distinctive peculiarities of synchrotron radiation for fast, non-destructive, high resolution, quantitative investigations on a large variety of samples. Absorption-based and phase contrast imaging are routinely performed in an energy range of 8-45 keV [71]. Figure 2.1 illustrates the standard experimental setup for absorption-based 3D microtomography.

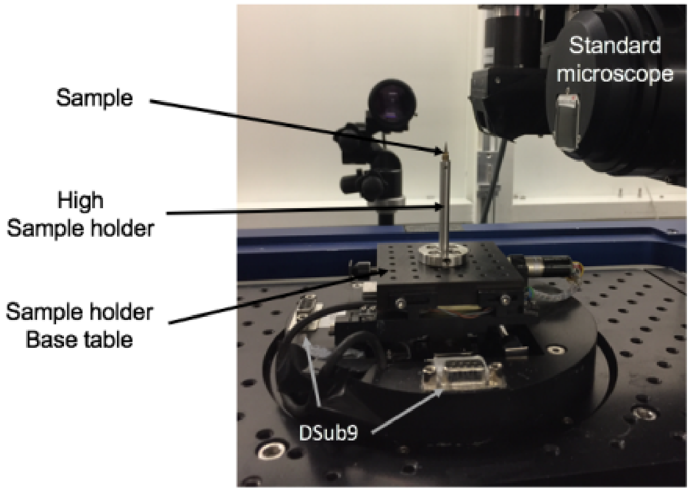

Figure 2.1: TOMCAT beamline Experimental setup.

Different combinations of scintillators, microscopes and cameras are available at TOMCAT in order to obtain optimal image quality for a given experimental setup. The standard high resolution microscope (Microscope 1) is based on diffraction-limited optics and, thanks to its interchangeable (motorized) objectives, the field of view can easily vary from 0.4×0.3 mm^2 up to 13.3×11.2 mm^2 with pixel sizes ranging from 0.16×0.16 µm^2 up to

5.2×5.2 µm^2. Table 2.1 summarizes the several imaging options (field of view and pixel size) available. With the advantage of the advanced rotating stage and the sample holder, we were able to perform multi-scale imaging experiments for different type of materials since the sample can be centred with 0.1 µm reproducibility.

Objective	Magnification	Field of View (mm2)	Pixel Size (µm2)
PLAPO1.25x	1.25	13.3 x 11.2	5.2 x 5.2
PLAPO2x	2	8.3 x 7.0	3.25 x 3.25
UPLAPO4x	4	4.2 x 3.5	1.63 x 1.63
UPLAPO10x	10	1.7 x 1.4	0.65 x 0.65
UPLAPO20x	20	0.8 x 0.7	0.33 x 0.33
UPLAPO40x	40	0.4 x 0.3	0.16 x 0.16

Table 2.1: Specifications of the different objectives available for Microscope 1.

Figure 2.2 shows the samples used in the experiments. They were chosen to give different levels of complexity in the internal structure. Fontainebleau sandstone is an example of a simple natural porous medium with pure mineral composition mainly consisting in quartz. The SiC–Diamond (silicon carbide-Diamond) sample is a synthesized composite obtained by microwave sintering, see [72]. It is composed of silicon carbide and diamond, and it is an example of two solids phase material. The third sample is a North Sea reservoir rock which is another example of sandstone with more complex and heterogeneous structure consisting of clay, quartz, feldspar and carbonate cement. The last sample being the most complex one is a carbonate (CaCO3) containing a wide range of pore size which makes the use of multi-scale imaging techniques essential.

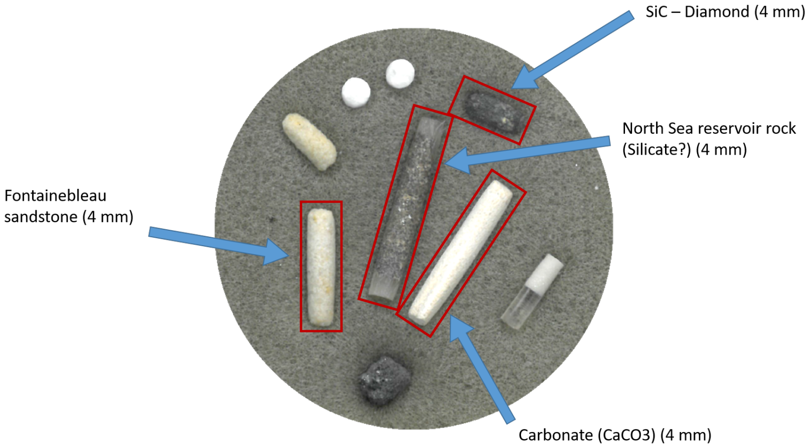

Figure 2.2: Samples used for the multi-scale imaging experiments (red boxes).

For each sample, full scan for the entire sample had been taken with different magnifications; 2x and 4x, resulting in 3D volumes for the full samples with (1600×1600×962) and (2560×2560×2160) voxels, respectively. With magnification 10x two regions were defined to perform local microtomography resulting in 3D volumes with (2560×2560×2160) voxels. Inside one of the regions of magnification 10x, two other local microtomography were performed with magnification 20x resulting in 3D volumes with (2560×2560×2160) voxels. Figure 2.3 illustrates the multi-scale imaging experiment protocol with cross-sections of Fontainebleau sandstone sample.

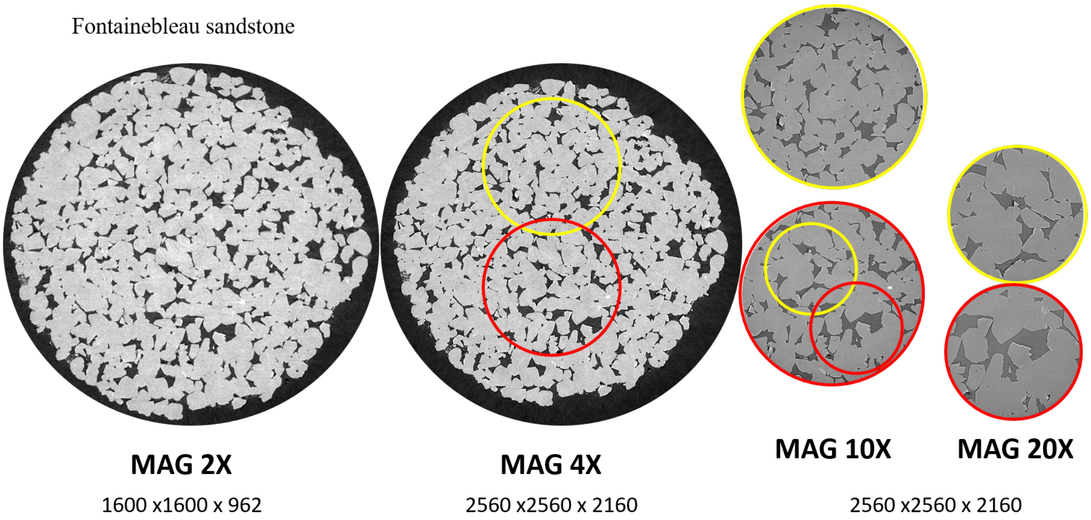

Figure 2.3: Cross sections of Fontainebleau sandstone with a multi-scale imaging approach.

Acquiring 3D volumes in two regions in magnifications 10x and 20x was done keeping in mind that the acquired data will be used by our colleagues in SUPREMATIM (SUPerREsolution of 3d MATerials IMages) project [68]. This project aims to develop new superresolution methods guided by HR local sub images of real 3D material data. The selected mathematical methods are based on local and global Generalized Gaussian Mixture Models as well as Student-t Mixture Models in conjunction with variational methods. Using both LR and HR information in the same region the statistical model will be built and then will be used to inject HR information where it's needed. So, one HR region will be used to develop the model and the other one will be used for validation. The Fontainebleau sandstone and SiC-Diamond data sets were used as an application for PCA reduced Gaussian Mixture models in [73] and for Wasserstein patch prior for superresolution of 2D and 3D images in [74].

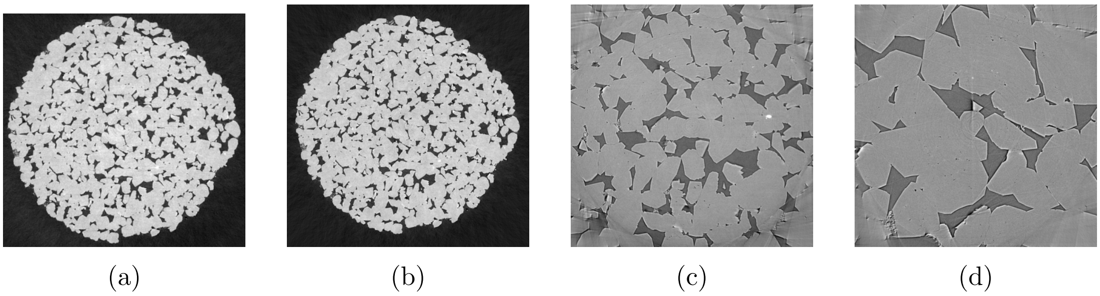
(a) (b) (c) (d)

Figure 2.4: Fontainebleau sandstone cross sections with different resolutions, a) 2x MAG with pixel size of 3.25 µm, b) 4x MAG with pixel size of 1.63 µm, c) 10x MAG with pixel size of 0.65 µm, d) 20x MAG with pixel size of 0.33 µm.

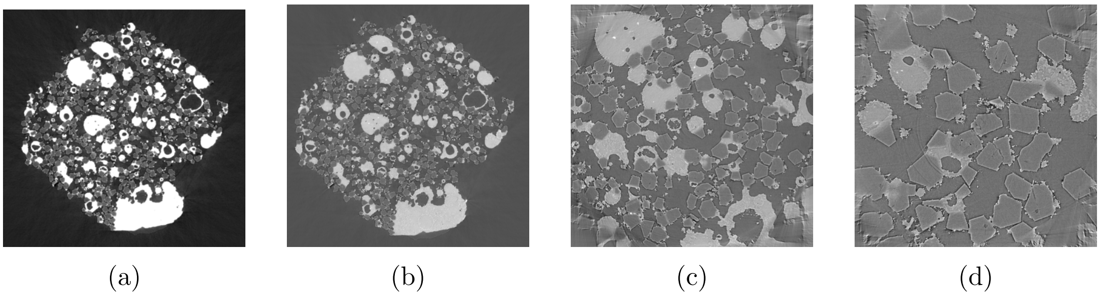
(a) (b) (c) (d)

Figure 2.5: SiC–Diamond cross sections with different resolutions, a) 2x MAG with pixel size of 3.25 µm, b) 4x MAG with pixel size of 1.63 µm, c) 10x MAG with pixel size of 0.65 µm, d) 20x MAG with pixel size of 0.33 µm.

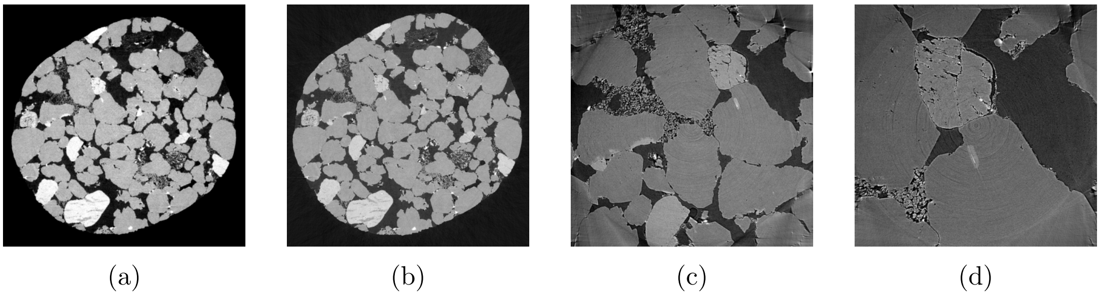
(a) (b) (c) (d)

Figure 2.6: North Sea reservoir rock cross sections with different resolutions, a) 2x MAG with pixel size of 3.25 µm, b) 4x MAG with pixel size of 1.63 µm, c) 10x MAG with pixel size of 0.65 µm, d) 20x MAG with pixel size of 0.33 µm.

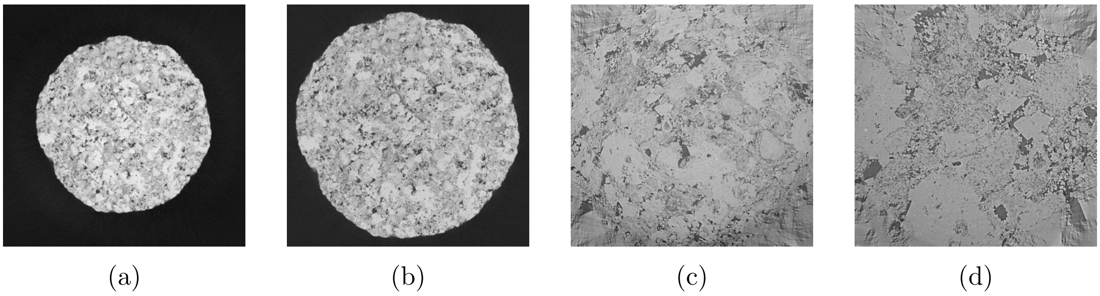
(a) (b) (c) (d)

Figure 2.7: Carbonate (CaCO3) cross sections with different resolutions , a) 2x MAG with pixel size of 3.25 µm, b) 4x MAG with pixel size of 1.63 µm, c) 10x MAG with pixel size of 0.65 µm, d) 20x MAG with pixel size of 0.33 µm.

Figures 2.4, 2.5, 2.6 and 2.7 illustrate cross sections of the 3D volumes of Fontainebleau sandstone, SiC–Diamond, North Sea reservoir rock and carbonate (CaCO3), respectively, with different magnifications (MAG). From these figures, we can observe various levels of complexity among the selected materials. The Fontainebleau sandstone is the simplest one with almost homogeneous structure. The SiC–Diamond sample shows two distinguished solid phases which can be segmented, generally speaking, easily. In the North Sea reservoir rock sample, we can observe almost four solid phases which makes the segmentation of such sample challenging. The carbonate sample being the most complex one with almost dense structure with MAG 2x and 4x while the sub-micron pores size are visible with MAG 10x and 20x. Such pores have significant effects on the effective properties of these types of materials.

The resulting data sets contain 3D images of real materials with very good quality images and different resolutions. With the artefacts and problems associated with the acquisition process, these data sets are of great interest for different applications. These artefacts and problems are ring artefacts, phase contrast effect, intensity gradients and registration problem. Due to the lack of time and being out-of-the-scope of this thesis, these artefacts will not be discussed any further. Nevertheless, the phase contrast effect was discussed by ESR 11 of the MUMMERING ITN (Elise O. Brenne) and the Fontainebleau sandstone set was investigated in [75].

The main goal for this experiment was obtaining multi-scale 3D images to be used in: (i) the development of superresolution techniques for real 3D materials under the framework of SUPREMATIM project, (ii) the local mesh refinement step when computing the effective properties for reactive transport in porous media.

2.2.3 Summary of section 2.2

A multi-scale imaging experiment was performed at TOMCAT beamline in the framework of the MUMMERING project. Four different porous materials were considered with varied structure complexity. For each sample, a total of eight acquisitions were performed with different resolutions. The acquired data sets were used in the development of superresolution techniques for real 3D materials under the framework of SUPREMATIM project.

2.3 Numerical Modelling

In this section, we start with a brief description of the reactive diffusion problem and of the change of scale procedure using the volume averaging method. Thereafter, the discretization of the problem using the cell centred finite volume on uniform Cartesian grid is given. Then, the proposed non-uniform Cartesian mesh (NUCM) resulting from the grid coarsening approach and local mesh refinement are presented along with the spatial discretization. Finally, the computation of the effective properties with different interpolation levels are presented.

2.3.1 Local equations and change of scale

At the local scale, the governing equations are defined and applying the change of scale by volume averaging approach led to the equation at the macroscopic scale. The effective properties appearing in this equation can be computed from the solution of the closure problems stated at the local scale.

The pore scale configuration is illustrated on Figure 2.8. The solid phase (S) is composed of two materials; $\mathrm{S_R}$, a rigid solid able to react in contact with the fluid phase (F) and $\mathrm{S_I}$, the inert part of S. The fluid-solid interface $\mathrm{A_{fs}}$ is divided into two components, $\mathrm{A_{fsr}}$ corresponding to the interface with $\mathrm{S_R}$, and $\mathrm{A_{fsi}}$ corresponding to the interface with $\mathrm{S_I}$. The equation that governs the transport by diffusion reaction at the local scale for the compound a, is given by:

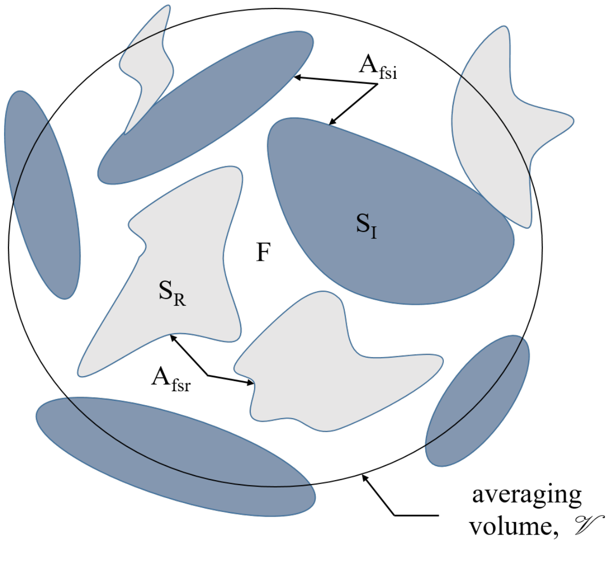

Figure 2.8: Local scale averaging volume and the notations used.

$$\frac{\partial C}{\partial t} = \nabla \cdot (D \nabla C), \quad \text{in the F phase} \tag{2.3}$$

where C is the concentration of the transported compound a (mol m^{-3}), t is the time (s) and D is the bulk diffusion coefficient (m^2 s^{-1}). In equation (2.3), we assumed that the homogeneous reactions are negligible.

On the fluid-solid interface, we consider a first order reaction expressed by:

$$-n_{\mathrm{fs}} \cdot (D \nabla C) = k(C - C^{*}), \quad \text{at } \mathrm{A_{fs}} \tag{2.4}$$

where n_{fs} is the unit vector normal to $\mathrm{A_{fs}}$ and oriented from the fluid to the solid, k is the reaction rate (m s^{-1}) and C^{*} is the concentration of equilibrium (mol m^{-3}). The reaction rate k is null on $\mathrm{A_{fsi}}$ and is equal to k_{R} on $\mathrm{A_{fsr}}$.

Using H as a reference length (m) and D, we can put the system of equations (2.3) and (2.4) under dimensionless form. The dimensionless variables used are:

$$X' = \frac{X}{H}; \quad t' = \frac{Dt}{H^2}; \quad C' = CH^3; \quad k' = \frac{kH}{D} \tag{2.5}$$

Omitting the apostrophe ($'$) to note the dimensionless variables, equations (2.3) and (2.4) in dimensionless form are rewritten as follows:

$$\frac{\partial C}{\partial t} = \nabla \cdot \nabla C, \quad \text{in the F phase} \tag{2.6}$$

$$-n_{\mathrm{fs}} \cdot (\nabla C) = k(C - C^{*}), \quad \text{at } \mathrm{A_{fs}} \tag{2.7}$$

Applying the change of scale by volume averaging approach and following the steps presented in [9], the macroscopic diffusion reaction equation is given as follows:

$$\varepsilon \frac{\partial \langle C \rangle^f}{\partial t} = \nabla \cdot \left[\varepsilon D_{\mathrm{eff}} \cdot \nabla \langle C \rangle^f\right] + \nabla \cdot \left[\varepsilon k_R U(\langle C \rangle^f - C^{*})\right] - \varepsilon k_R \frac{\mathrm{A_{fsr}}}{V_f}(\langle C \rangle^f - C^{*}) \tag{2.8}$$

For detailed mathematical developments on how to obtain this result, we refer the reader to appendix A. In the upscaling procedure, we defined an averaging domain $\mathscr{V}$ including the fluid and solid domains V_f and V_s and the fluid solid interface A_{fs} from which we defined the porosity by the volume fraction of the F phase as follows:

$$\varepsilon = \frac{V_f}{\mathscr{V}} \tag{2.9}$$

Equation 2.8 is describing the diffusion at the macroscopic scale with $\langle C \rangle^f$ being the intrinsic average concentration. It is containing the effective diffusivity tensor D_{eff} and the effective parameter vector U. These parameters depend on the solution of the following closure problems which have to be solved at the local scale:

$$\nabla^2 \mathbf{B} = 0 \tag{2.10}$$

$$-n_{\mathrm{fs}} \cdot \nabla \mathbf{B} = n_{\mathrm{fs}}, \quad \text{at} \quad \mathrm{A_{fs}} \tag{2.11}$$

$$\mathbf{B}(r + l_i) = \mathbf{B}(r), \quad i = 1, 2, 3 \tag{2.12}$$

with

$$\langle \mathbf{B} \rangle^f = 0 \tag{2.13}$$

and

$$\nabla^2 s^* = -\frac{\mathrm{A}_{\mathrm{fsr}}}{V_f} \tag{2.14}$$

$$-n_{\mathrm{fs}} \cdot \nabla s^* = 1, \quad \text{at} \quad \mathrm{A}_{\mathrm{fsr}} \tag{2.15}$$

$$s^*(r + l_i) = s^*(r), \quad i = 1, 2, 3 \tag{2.16}$$

with

$$\langle s^* \rangle^f = 0 \tag{2.17}$$

Equations (2.12) and (2.16) represent periodic boundary conditions where r is the position vector and l_i is the lattice vector. The vector $\mathbf{B}$ and the scalar s^* mainly take into account the effects of the micro-geometry on diffusion. Using these closure variables, we can compute the effective parameters as follows:

$$D_{\mathrm{eff}} = I + \frac{1}{V_f} \int\limits_{\mathrm{A}_{\mathrm{fs}}} (n_{\mathrm{fs}} \mathbf{B}) dA \tag{2.18}$$

and

$$U = \frac{1}{V_f} \int\limits_{\mathrm{A}_{\mathrm{fs}}} (n_{\mathrm{fs}} s^*) dA \tag{2.19}$$

In general, the second term on the right-hand side of the macroscopic equation 2.8 is negligible for the case of diffusion and can be important when convective transport is important [9], [46]. In this work, these formula were used to study the effect of the proposed multi-scale imaging and modelling approach on the effective parameters values and on the computation time.

In this subsection, the information at the pore scale was used to derive the equation at the macroscopic scale. The resulting closure problems need to be solved at the pore scale in order to compute the effective properties. In the next subsections, we present how to solve these problems numerically using the finite volume method on both uniform and the proposed non-uniform Cartesian mesh.

2.3.2 Numerical model

To compute the effective diffusion tensor D_{eff}, we need to solve the closure problem (2.10)-(2.13), where the vector $\mathbf{B}$ is given by:

$$\mathbf{B} = \begin{bmatrix} B_x \\ B_y \\ B_z \end{bmatrix} \tag{2.20}$$

Hence, we can rewrite the closure problem for $\mathbf{B}$ in terms of three scalar problems as follows:

$$\nabla^2 B_\zeta = 0 \tag{2.21}$$

$$-n_{\mathrm{fs}} \cdot \nabla B_\zeta = n_\zeta, \quad \text{at} \quad \mathrm{A}_{\mathrm{fs}} \tag{2.22}$$

$$B_\zeta(r + l_i) = B_\zeta(r), \quad i = 1, 2, 3 \tag{2.23}$$

with:

$$\langle B_\zeta \rangle^f = 0 \tag{2.24}$$

where the subscript ζ correspond to the three directions of space X, Y, and Z. Furthermore, to compute the vector U we need to solve another scalar problem for s^* (2.14)-(2.17). So, we have to solve four scalar problems of the following form:

$$\nabla^2 u = v \tag{2.25}$$

$$-n_{\mathrm{fs}} \cdot \nabla u = b, \quad \text{at} \quad \mathrm{A}_{\mathrm{fs}} \tag{2.26}$$

$$u(r + l_i) = u(r), \quad i = 1, 2, 3 \tag{2.27}$$

with:

$$\langle u \rangle^f = 0 \tag{2.28}$$

where u corresponds to a component of vector $\mathbf{B}$ or to s^*, v is a volume source term and b a surface source term. The first equation is describing the diffusive transport within the fluid phase with the volume source term v, the second one is the reaction at the fluid/solid interface (b can be variable depending on the nature of the considered solid phase), the third one indicates that u is periodic in all directions at the limits of the averaging domain and the last one points that the intrinsic average of u should be equal to zero. Therefore, we need to solve four similar problems with the same matrix and different second members.

2.3.3 Cell centred finite volume method on uniform Cartesian mesh

Considering the nature of the computation domain, 3D volumes from microtomography imaging are voxelized, using the finite volume method appears as relevant. Due to the nature of the problem we used the cell centred finite volume method to discretize the diffusion equation. The computation domain is discretized into set of control volumes (active cells). Each active cell (AC) is a parallelepiped of dimensions $dx \times dy \times dz$ with the same ratios $\frac{dy}{dx}$ and $\frac{dz}{dx}$ for all the ACs.

In the cell centred finite volume scheme the local unknowns are localized at the centre of each AC. We start by the integration of equation (2.25) over an arbitrary control volume:

$$\int_{CV} (\nabla^2 u) d\Omega = \int_{CV} v d\Omega \tag{2.29}$$

where CV is the control volume associated to the local unknown. Here, it is the volume of the AC. Using the Gauss' divergence theorem, the first term of equation (3.92) can be transformed in a surface integral giving:

$$\oint_{\Gamma_{CV}} (\nabla u \cdot n) d\Gamma = \int_{CV} v d\Omega \tag{2.30}$$

where Γ_{CV} is the boundary of the control volume and n is the vector normal to Γ_{CV} oriented towards the outside of the AC. Using the notations of Figure 2.9, we can split the surface integral in (2.30) into the sum of the surface integrals over the interfaces between the CV and its neighbours. Using the midpoint rule to approximate the surface and volume integrals, we obtain:

$$\sum_{i=1}^{6} (\nabla u \cdot n)_{c\Gamma_i} \Gamma_i = v_{CV} V_{CV} \tag{2.31}$$

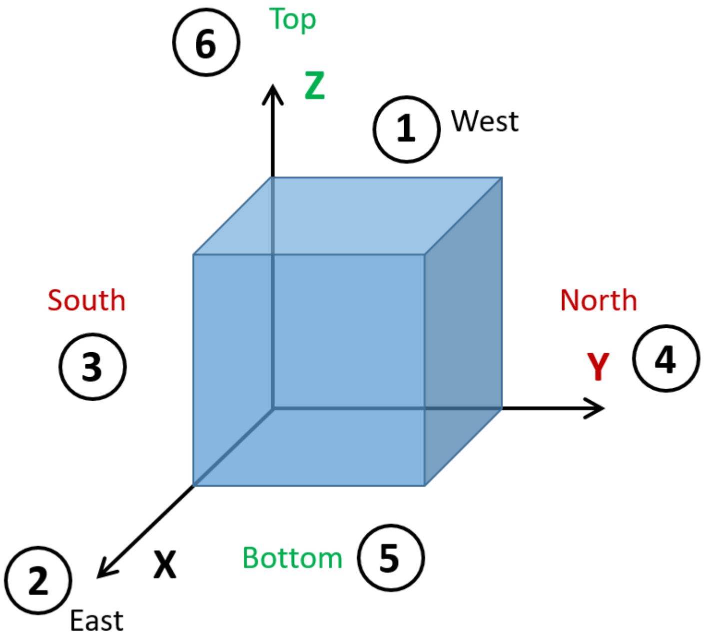

Figure 2.9: Notations for CV faces and surrounding neighbours.

Where Γ_i is the area of the face i, $(\nabla u \cdot n)_{c\Gamma_i}$ is the value at the centre of face i of the gradient component normal to this face, v_{CV} is the value of the source term in the AC and V_{CV} is the volume of the AC. When the face i is at the fluid/solid interface, the term $(\nabla u \cdot n)_{c\Gamma_i}$ is given by the boundary condition (2.26) ($n = n_{\text{fs}}$). In the other cases, an approximation of this term must be used based on the values of the unknowns in the neighbourhood (eventually taking into account the periodicity). When the anisotropic Cartesian grid is uniform, the approximation is obtained as the difference of the unknowns at the centres of the cells sharing face i divided by their distance and taking into account the direction of n. We end up to solve the linear system in the form:

$$\alpha_{CV} u_{CV} + \sum_{i=1}^{6} \alpha_i u_i = v_{CV} V_{CV} - \sum_{i=1}^{6} \beta_i (\nabla u \cdot n_{fs})_{c\Gamma_i} \Gamma_i \tag{2.32}$$

where:

$$\alpha_{CV} = - \sum_{i=1}^{6} \alpha_i \tag{2.33}$$

$$\alpha_i = \begin{cases} 0 & \text{, if } \quad \Gamma_{CV_i} \in A_{fs} \\ \dfrac{\Gamma_i}{d_i} & \text{, if } \quad \Gamma_{CV_i} \notin A_{fs} \end{cases} \tag{2.34}$$

$$\beta_i = \begin{cases} 1 & \text{, if } \quad \Gamma_{CV_i} \in A_{fs} \\ 0 & \text{, if } \quad \Gamma_{CV_i} \notin A_{fs} \end{cases} \tag{2.35}$$

Here u_{CV} is the value of the unknown at the centre of the AC, u_i is the value of the unknown at the centre of the neighbour AC$_i$, Γ_{CV_i} is the face i of the AC and d_i is the distance between u_{CV} and u_i.

Applying equation (2.32) for each AC will generate a linear system in the form:

$$M u^* = -G \tag{2.36}$$

where M is the Na × Na matrix built using the left-hand side of equation (2.32), Na being the number of ACs. u^* is the vector of real unknowns and G is the vector composed of the volumic source terms and the fluid-solid interface flux terms.

2.3.4 Non-uniform Cartesian mesh (NUCM)

In the previous section, a uniform Cartesian mesh was used to discretize the fluid phase into a number of ACs supporting one unknown localized at their centres. These ACs are identical with dimensions $dx \times dy \times dz$ which are equivalent to the scanning voxels size. For large 3D volumes this number is very massive resulting in computationally demanding problems. In general, reducing the number of ACs will reduce the CPU time. Nevertheless, this reduction process should be done efficiently without affecting the final results.

We know from equation (2.18) that to compute D_{eff} we need to integrate the components of $\mathbf{B}$ over the fluid-solid interfaces. It means that the final result depends on the ACs located at these interfaces and reducing the number of ACs away from them might not have a major effect. Our grid coarsening approach allows us to have coarse grid away from the fluid-solid interfaces. By fixing the cells size near the interfaces and aggregating 2×2 ACs in 2D and $2 \times 2 \times 2$ ACs in 3D elsewhere, we get the first level of the coarse grid. Repeating the same procedure will lead to the final coarse grid. Figure 2.10 illustrates this approach in a 2D example.

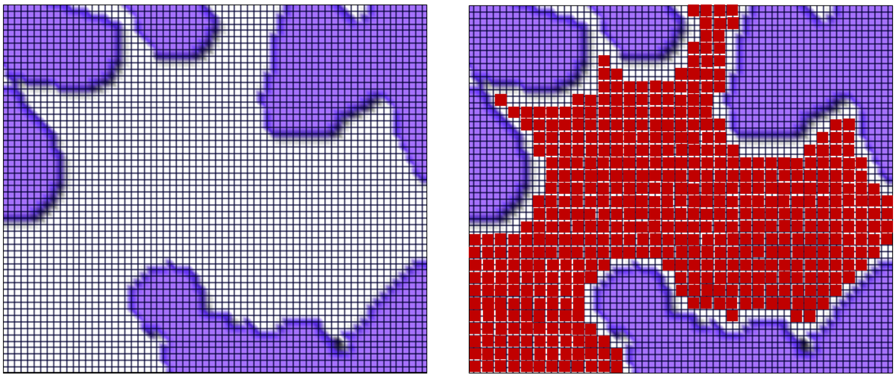

(a) Original grid. (b) First level of the coarse grid.

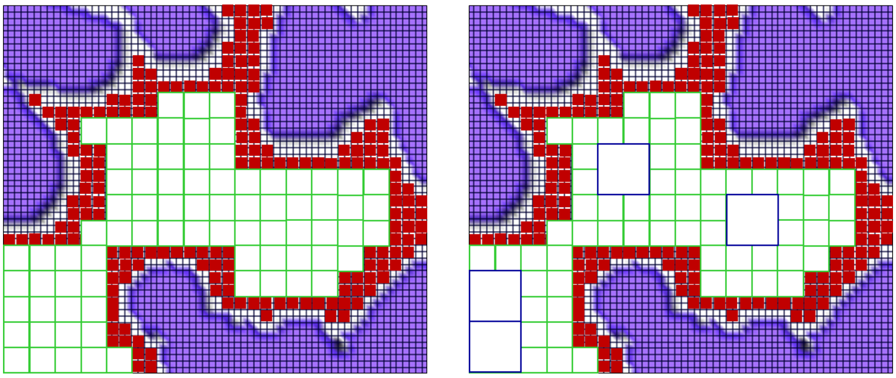

(c) Second level of the coarse grid. (d) Final level of the coarse grid.

Figure 2.10: Grid coarsening for a 2D example.

The proposed NUCM is resulting from a twofold approach: first, a grid coarsening, and second, a local mesh refinement. In the local mesh refinement step, the HR information are injected where it is needed at the fluid-solid interfaces which aims to improve the accuracy of the results. The NUCM is composed of ACs of different sizes. This requires procedures for communication of data across the non-matching interfaces to accommodate the requirements of discretization stencils. In the next subsections, we will describe the grid coarsening approach and the local mesh refinement in details, as well as the spatial discretization needed at the coarse-fine grid interfaces.

2.3.4.1 Grid coarsening approach

We start with the initial 3D volume with identical voxels size related to the scanning resolution. The segmentation process gives labelled 3D images with each voxel assigned to one of the phases detected within the studied material. The labelled 3D images will be partitioned in two regions: the active region (value = 1), corresponding to the active phases where the considered transport is taking place, and the inactive region (value = 0) corresponding to the inactive phases and defining the internal boundary of the active region.

A NUCM is composed of ACs of different levels (L). An AC of level L comprises S voxels that were aggregated to form it ($S = 2^{3(L-1)}$). At the beginning of the process, all the ACs in the active region are composed of one single voxel of dimensions $dx \times dy \times dz$ and they are in the same level ($L = 1$).

The basic rules for the grid coarsening approach to form the NUCM are:

- Coarsening is forbidden for AC sharing at least one face with an internal boundary (fluid-solid interfaces) or an external boundary and these ACs will stay at level $L = 1$.
- Local coarsening is done by aggregation of (2 x 2 x 2) AC of level L to form a single AC of level $L + 1$.
- An AC of level L can only share faces with AC of level equal to $L - 1$, L or $L + 1$.

The NUCM is described by the byte array Mail(N_x, N_y, N_z) built above the 3D volume, where N_x, N_y and N_z are the dimensions of the 3D volume. Each voxel of Mail has a value equal to 0 (the voxel is in the inactive region) or L, where L is the level of the AC to which the voxel belongs. The NUCM is built iteratively from level 1 to L_{max}, where L_{max} is the largest mesh level reached during the building process. The value of L_{max} can be determined automatically from the coarsening process or given by the user as an input parameter.

At level L, the global mesh is composed of ACs of levels 1 to $L - 1$ that are fixed, and of the ACs of level L that might be aggregated to create new ACs of level $L + 1$. As a benefit from the previous iteration, the domain defining these ACs is divided in a series of connected components (CC) and the local coarsening from level L to level $L + 1$ is performed independently on each CC.

The way we aggregate the ACs of level L will result in a series of CC of level $L + 1$. Using the CC will minimize the considered domains and it is a simple way to perform the local coarsening in a local system of coordinates that can be transposed easily to the global coordinates. At the beginning of the process, we consider that at level $L = 1$ all the ACs belong to the same CC.

The idea is to initiate the coarsening at the centres of the largest regions to have the largest CC centred there. For that, for each CC of level L, we perform the coarsening process in two steps. In the first step, we compute the distance map of the CC and determine the AC with the largest value. Then, we test the 8 possible aggregates comprising the AC and check whether the AC can be aggregated with 7 neighbours to create an AC of level $L+1$. If yes, we select the aggregate with the maximum average distance to create an AC of level $L+1$ and to create the first CC of level $L+1$. The expansion of this CC is done by using a region growing algorithm. We create a chain made of the ACs on the boundary of the CC and for each element in the chain we test the 6 possible aggregates of level L in contact with a face. If the test is positive, we create a new AC of level $L+1$ and add it to the chain. This process is repeated until the chain is empty. The CC created in this first step is almost always the largest one. The number of ACs to be tested after this step is generally very large and applying the same procedure is CPU time consuming for a limited benefit. Indeed, the remaining ACs are situated in regions of small extension and initiating the coarsening at the centres is not providing better results in terms of final number of aggregated AC.

At the end of first step, we update the distance map for the remaining ACs of level L. In the second step, we loop over the remaining ACs of level L in the CC. If the value of the distance map larger than 1, we test whether this AC can be aggregated with 7 neighbours to build an AC of level $L+1$. If yes, a new CC of level $L+1$ is created and increased by a region growing algorithm as in the first step. Before checking the next CC, the distance map is modified by giving the value -1 to all the AC in contact with a face of an AC belonging to the new CC of level L+1.

The modification of the distance map after each creation of new CC of level $L+1$ is necessary to prevent the situation shown in Figure 2.11. This situation is forbidden by the basic rules since the AC of level L can only share faces with AC of level equal to $L-1$, L or $L+1$.

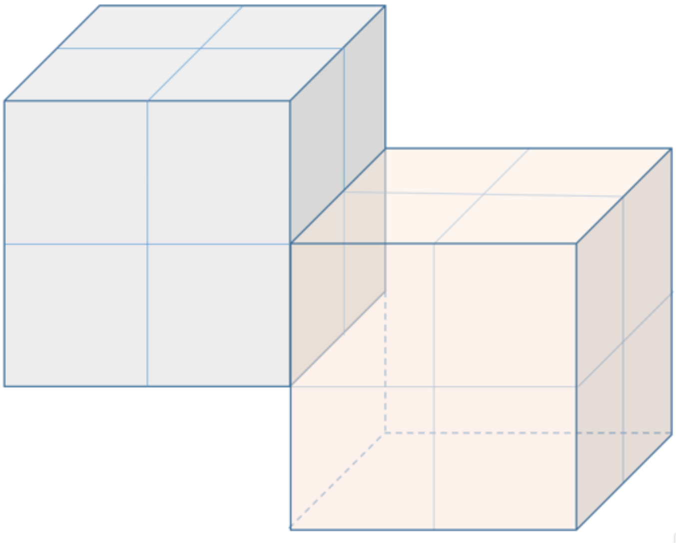

Figure 2.11: An example of forbidden situation in the NUCM.

The NUCM is composed of ACs of different levels and a specific spatial discretization is needed at the coarse-fine grid interfaces. A tailored structure is developed by introducing ghost unknowns to allow communications between the ACs at different levels.

2.3.4.2 Local mesh refinement (LMR) using Multi-Scale imaging approach

In the problems we are interested in, only certain regions of the physical domain are critical and a finer grid is needed only there. An alternative way to improve the results is by local mesh refinement (LMR), in which sequences of nested finer grids are applied in the critical region(s). To define these regions, prior knowledge is needed, which we generally do not have for our problems. In adaptive mesh refinement (AMR), a first approximation of the solution on the coarse mesh is required to identify the regions that need finer grid and then LMR is applied.

At the time a solution has been built on the NUCM, a LMR is applied at the critical regions. Usually, the grid in the critical regions is refined by just dividing the ACs into smaller ones by specific ratio. The fluid-solid interfaces in this case are not changed and are kept fixed related to the initial scanning resolution.

In the proposed multi-scale imaging approach, multi 3D volumes with different resolutions are obtained. LR 3D images correspond to a large field of view relevant for the transport at the global scale and HR images describe the fluid-solid interfaces more precisely. The LR images are used to construct the first approximation on the NUCM. Then, the HR images are used to replace the LR critical regions information with HR ones in the LMR step.

At the LMR step, we first apply global modifications to the NUCM resulting from the grid coarsening approach. We subsample the NUCM by a factor of 2 and increase the actual level for each AC by 1. Then, for each critical region a parallelepiped sub volume from the HR images is used to modify the geometry. After that, all the ACs at the fluid-solid interfaces where we have geometrical changes are set to level 1. At the end of this step, all the voxels on the interface within the refined region have a level equal to 1 or 2. Then, two verification tests are applied to check that: (1) all the ACs of level 2 have four sub-voxels in contact with the solid phase, (2) for all faces of an AC in contact with the solid phase, we have two ACs of the same level in the direction of the normal vector from the solid to the fluid phase. This is done to preserve the coarsening rules presented in section 2.3.4.1 and to facilitate the application of the interpolation levels presented in section 2.3.5.

Before using the HR images we need to decide where the LR critical regions are located. The criterion for defining these regions depends on the nature of the physical problems. In many problems, physical quantities like sharp density gradients or large charge distributions may provide indicators for that. In this work, we performed two empirical tests to study the possible choices for identifying the critical regions. These tests are presented in section 2.4.5.

2.3.4.3 Spatial Discretization

At coarse-fine interfaces, it is no longer possible to use the uniform discretization as described in section 2.3.3. In this section, we present the modifications and the spatial discretization needed for the NUCM resulting from the grid coarsening approach and local mesh refinement. Starting from equation (2.31) to compute $(\nabla u \cdot n)_{c\Gamma_i}$ we consider three cases:

- Case one : the AC of level L is sharing a face with an AC of the same level. Here we use the same discretization as in section 2.3.3.
- Case two : the AC of level L is sharing a face with an AC of level $L + 1$. One direct neighbour will be missing to complete the discretization stencil. To overcome this problem, a ghost unknown will be introduced in the larger neighbour by interpolation.
- Case three: the AC of level L is sharing a face with an AC of level $L-1$ and here the AC missing gradients are evaluated by the arithmetic average of the adjacent smaller ACs gradients to enforce the flux matching and the continuity of the gradient across the interface.

Case 1: the AC of level L is sharing a face with an AC of the same level

In this case, the same discretization as in section 2.3.3 will be used.

Case 2: the AC of level L is sharing a face with an AC of level $L + 1$

The fine cell AC$_i$ at level l with dimensions $dx_l \times dy_l \times dz_l$ has the unknown u_i localized at the centre. For simplicity, keeping in mind the notation in Figure 2.9, we assume having face 1 (West) at the coarse-fine interface, the other faces are treated in analogue way in cases where they are located at the coarse-fine interface. The West neighbour AC$_j$ at level $l+1$ with dimensions $dx_{l+1} \times dy_{l+1} \times dz_{l+1}$ has the unknown u_j localized at the centre. We have to consider four subcases defined by the location of the AC$_i$ on the face of its larger neighbour AC$_j$. Figure 2.12 illustrates the numbering of the different parts of a large face shared with smaller ACs. Looking to the shared face from the centre of the larger active cell, number one is the part situated at the upper left corner and numbering is continued turning in the clock wise direction.

Case 2.1: we consider the face 1 (West) of AC$_i$ in contact with part 1 of the face 2 (East) of the larger AC$_j$. A direct West unknown is missing to complete the discretization stencil. A ghost unknown u_{j1} is introduced and localized at the centre of the fine grid ghost cell positions in AC$_j$. We represent u_{j1} in terms of the available real unknowns at nearby ACs centres. First, a barycentric interpolation at u_j and the two most adjacent ACs centres except u_i is used to approximate u_n located at the intersection of the line

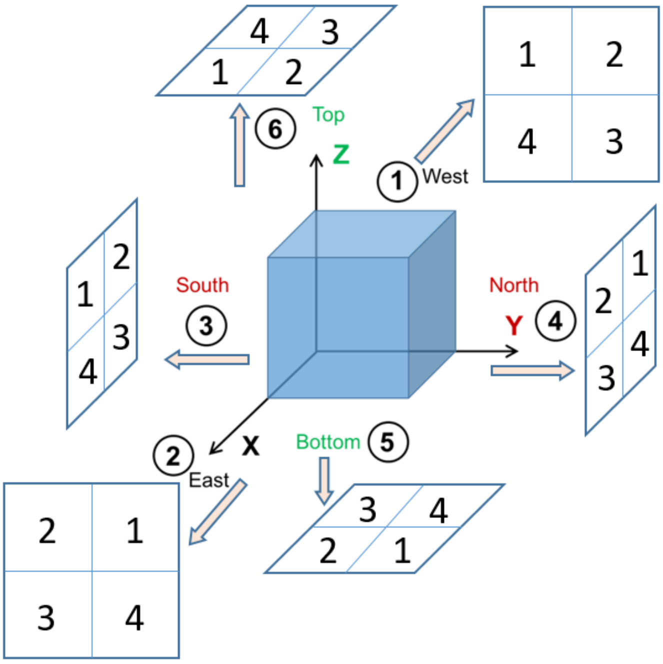

Figure 2.12: The numbering of the different parts of a large face shared with smaller ACs.

joining the centre of the AC$_i$ and the centre of face 1 of AC$_i$ with the triangular plane. Then, a linear interpolation at u_i and u_n is used to approximate u_{j1}. To compute u_n, we use along with u_j the unknowns located at the centres of AC$_k$ and AC$_h$ where AC$_k$ with the unknown u_k is sharing face 4 (North) of AC$_j$ and AC$_h$ with the unknown u_h is sharing face 6 (Top) of AC$_j$. There is three possible different levels for each of them (l, $l+1$, $l+2$) and this generates 3^2 subcases with additional two cases depending on the location of AC$_j$ related to its larger neighbour of level $l+2$.

Case 2.1.1: As can be seen from Figure 2.13, AC$_k$ is of level l and shares the part 2 of face 4 (North) of AC$_j$, AC$_h$ is of level l and shares the part 2 of face 6 (Top) of AC$_j$. For simplicity, we used localized coordinates at the centre of face 2 of AC$_j$ to drive the interpolation relations, see Figure 2.13. The location of the points involved in the interpolation are summarized in Table 2.2. The barycentric interpolation for u_n is defined as follows:

$$u_n = \lambda_j u_j + \lambda_k u_k + \lambda_h u_h \tag{2.37}$$

where:

$$\lambda_j = \frac{area(p_n, p_k, p_h)}{area(p_j, p_k, p_h)}$$
$$\lambda_k = \frac{area(p_j, p_n, p_h)}{area(p_j, p_k, p_h)}$$
$$\lambda_h = \frac{area(p_j, p_k, p_n)}{area(p_j, p_k, p_h)}$$

	X	Y	Z
p_i	$\frac{1}{2}$	$\frac{1}{2}$	$\frac{1}{2}$
p_j	-1	0	0
p_k	$-\frac{1}{2}$	$\frac{3}{2}$	$\frac{1}{2}$
p_h	$-\frac{1}{2}$	$\frac{1}{2}$	$\frac{3}{2}$
p_n	$-\frac{3}{4}$	$\frac{1}{2}$	$\frac{1}{2}$
p_{j1}	$-\frac{1}{2}$	$\frac{1}{2}$	$\frac{1}{2}$

Table 2.2: The points involved in the interpolation case 2.1.1.

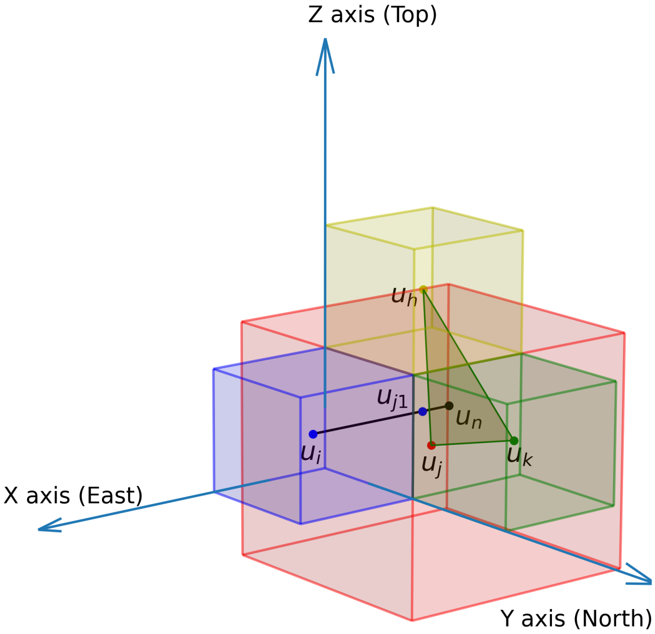

Figure 2.13: Case 2.1.1 schematic diagram.

Here $area(p_n, p_k, p_h)$ is the area of the triangle composed of the point p_n, p_k and p_h and it is computed as follows:

$$area(p_n, p_k, p_h) = \frac{\|\overrightarrow{p_n p_k} \times \overrightarrow{p_n p_h}\|}{2} \tag{2.38}$$

In a similar way, we can compute u_{j1} by:

$$u_{j1} = \lambda_i u_i + (1 - \lambda_i) u_n \tag{2.39}$$

where:

$$\lambda_i = \frac{dis_x(p_{j1}, p_n)}{dis_x(p_i, p_n)} \tag{2.40}$$

where dis_x is the distance between the two points in the X direction.

Applying equation (2.37) we have:

$$u_n = \frac{2u_j + u_k + u_h}{4} \tag{2.41}$$

and using equation (2.39) we get:

$$u_{j1} = \frac{u_i + 4u_n}{5} = \frac{u_i + 2u_j + u_k + u_h}{5} \tag{2.42}$$

Finally, the term $(\nabla u \cdot n)_{c\Gamma_1} \Gamma_1$ is approximated as:

$$(\nabla u \cdot n)_{c\Gamma_1} \Gamma_1 = \frac{u_{j1} - u_i}{dx_l} dy_l dz_l \tag{2.43}$$

Table 2.3 summarizes the formulas used to approximate the ghost unknown for the different subcases. Detailed derivation can be found in Appendix B.

Case	u_{j1}	Case	u_{j1}
Case 2.1.2	$\frac{2u_i+3u_j+2u_k+u_h}{8}$	Case 2.1.7	$\frac{4u_i+3u_j+2u_k+u_h}{10}$
Case 2.1.3	$\frac{4u_i+10u_j+4u_k+u_h}{14}$	Case 2.1.8	$\frac{4u_i+5u_j+u_k+4u_h}{14}$
Case 2.1.4	$\frac{2u_i+3u_j+u_k+2u_h}{8}$	Case 2.1.9	$\frac{4u_i+3u_j+u_k+2u_h}{10}$
Case 2.1.5	$\frac{2u_i+2u_j+u_k+u_h}{6}$	Case 2.1.10	$\frac{4u_i+4u_j+u_k+u_h}{10}$
Case 2.1.6	$\frac{4u_i+4u_j+u_k+u_h}{10}$	Case 2.1.11	$\frac{4u_i+2u_j+u_k+u_h}{8}$

Table 2.3: The formulas used for the ghost unknown in the subcases of Case 2.1.

Case 2.2: We consider the face 1 (West) of AC$_i$ in contact with part 2 of the face 2 (East) of the larger AC$_j$. A direct West unknown is missing to complete the discretization stencil. A ghost unknown u_{j2} is introduced and localized at the centre of the fine grid ghost cell positions in AC$_j$. Similar to Case 2.1, we used first barycentric interpolation at u_j, AC$_k$ and AC$_h$ to approximate u_n. In this case, AC$_k$ with the unknown u_k is sharing face 3 (South) of AC$_j$ and AC$_h$ with the unknown u_h is sharing face 6 (Top) of AC$_j$. Then, a linear interpolation at u_i and u_n is used to approximate u_{j2}. There are 11 possible subcases with similar relations as in Case 2.1.

Case 2.3: We consider the face 1 (West) of AC$_i$ in contact with part 3 of the face 2 (East) of the larger AC$_j$. A direct West unknown is missing to complete the discretization stencil. A ghost unknown u_{j2} is introduced and localized at the centre of the fine grid ghost cell positions in AC$_j$. Similar to Case 2.1, we used first barycentric interpolation at u_j, AC$_k$ and AC$_h$ to approximate u_n. In this case, AC$_k$ with the unknown u_k is sharing face 3 (South) of AC$_j$ and AC$_h$ with the unknown u_h is sharing face 5 (Bottom) of AC$_j$. Then, a linear interpolation at u_i and u_n is used to approximate u_{j3}. There are 11 possible subcases with similar relations as in Case 2.1.

Case 2.4 We consider the face 1 (West) of AC$_i$ in contact with part 4 of the face 2 (East) of the larger AC$_j$. A direct West unknown is missing to complete the discretization stencil. A ghost unknown u_{j2} is introduced and localized at the centre of the fine grid ghost cell positions in AC$_j$. Similar to Case 2.1, we used first barycentric interpolation at u_j, AC$_k$ and AC$_h$ to approximate u_n. In this case, AC$_k$ with the unknown u_k is sharing face 4 (North) of AC$_j$ and AC$_h$ with the unknown u_h is sharing face 5 (Bottom) of AC$_j$. Then, a linear interpolation at u_i and u_n is used to approximate u_{j2}. There are 11 possible subcases with similar relations as in Case 2.1.

Case 3: the AC of level L is sharing a face with an AC of level $L-1$

Special care should be taken into account when the control volume is around a coarse cell adjacent to the coarse-fine interface. We can approximate the missing unknown by simply averaging the adjacent fine unknown neighbours there. However, this method will fail to generate a stable system. This is because of the resulting flux being discontinuous across the coarse-fine interface. To overcome this problem, we need to enforce the flux matching and the continuity of the gradient across the interface.

The coarse cell AC$_i$ at level $l+1$ with dimensions $dx_{l+1} \times dy_{l+1} \times dz_{l+1}$ has the unknown u_i localized at the centre. As in case 2 we will assume having the face 1 (West) at the coarse-fine interface. The West neighbours AC$_{j_m}$ $(m = 1, 2, 3, 4)$ at level l with dimensions $dx_l \times dy_l \times dz_l$ have the unknowns u_{j_m} stored at their centres, see Figure 2.14. AC$_i$ is an East neighbour for the AC$_{j_m}$ and using equation (2.43) we can approximate the gradient components normal to this face pointed form AC$_{j_m}$ to AC$_i$ as follows:

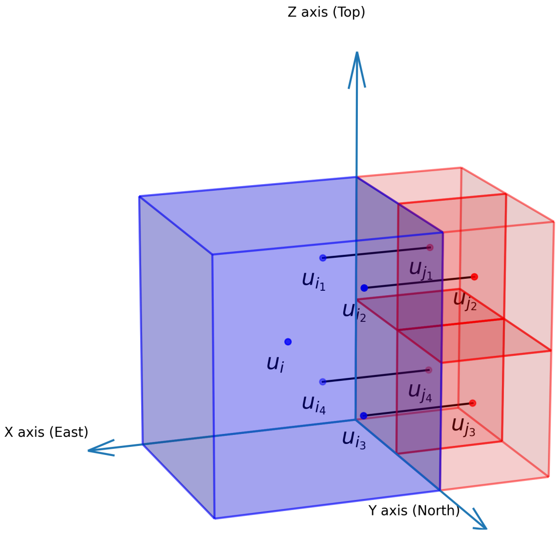

Figure 2.14: Case 3 schematic diagram.

$$(\nabla u_{j_m} \cdot n)_{c\Gamma_2} = \frac{u_{i_m} - u_{j_m}}{dx_l}, \quad m = 1, 2, 3, 4 \tag{2.44}$$

Where u_{i_m} are the ghost unknowns as defined in equation (2.39). To enforce the continuity of the flux, the AC$_i$ gradient is taken as the arithmetic average of the AC$_{j_m}$ gradients as follows:

$$(\nabla u_i \cdot n)_{c\Gamma_1} = -\frac{1}{4} \sum_{m=1}^{4} (\nabla u_{j_m} \cdot n)_{c\Gamma_2} \tag{2.45}$$

and with $dx_l = \dfrac{dx_{l+1}}{2}$ the total flux across face 1 will be equal to,

$$(\nabla u_i \cdot n)_{c\Gamma_1}\Gamma_1 = \frac{1}{2}\sum_{m=1}^{4} \frac{u_{j_m} - u_{i_m}}{dx_{l+1}} dy_{l+1} dz_{l+1} \tag{2.46}$$

As mentioned earlier, the same treatment is done for the other faces taking into account the change of direction.

The discretization of equation (2.25) using the spatial discretization will result in Na algebraic equations of the form:

$$\sum_{i=1}^{nr_i} c_i u_i + \sum_{i=1}^{ng_i} c_{g_i} u_{g_i} = -\sum_{i=1}^{nb_i} G_i \tag{2.47}$$

where Na is the number of ACs, nr_i, ng_i and nb_i are the number of real unknowns, the number of ghost unknowns and the number of faces at the fluid-solid interface participating in the relation associated to the AC$_i$, respectively, u_i are the real unknowns localized at the centres of the ACs, u_{g_i} are the ghost unknowns as defined in this section and G_i the term coming from the boundary condition if the AC$_i$ is on the fluid-solid interface. By writing the ghost unknowns in terms of the real ones, we can rewrite the linear system in the following form,

$$M_{NUCM} U = -G \tag{2.48}$$

where M_{NUCM} is the Nun × Nun matrix built using the right-hand side of equation (2.47), Nun is the number of unknowns, U is the vector of unknowns and G is the vector composed of the volumic source terms and the fluid-solid interface flux terms.

2.3.5 Computing the effective diffusion tensor D_{eff}

After solving the linear system 2.36 or (2.48) for each component of the vector **B**, we can compute the D_{eff} using the following formula:

$$D_{\text{eff}} = I + \frac{1}{V_f}\int_{\mathrm{A_{fs}}} (n_{\text{fs}}\mathbf{B}) dA \tag{2.49}$$

using the outer product or the tensor product of n_{fs} and **B**, we can rewrite equation (2.49) in matrix form as follows:

$$\begin{bmatrix} D_{xx} & D_{xy} & D_{xz} \\ D_{yx} & D_{yy} & D_{yz} \\ D_{zx} & D_{zy} & D_{zz} \end{bmatrix} = \begin{bmatrix} 1 & 0 & 0 \\ 0 & 1 & 0 \\ 0 & 0 & 1 \end{bmatrix} + \frac{1}{V_f}\int_{A_{fs}} \begin{bmatrix} n_x B_x & n_x B_y & n_x B_z \\ n_y B_x & n_y B_y & n_y B_z \\ n_z B_x & n_z B_y & n_z B_z \end{bmatrix} \tag{2.50}$$

Here we have used n_x, n_y and n_z to represent the components of the unit vector n_{fs}. Starting with the first component, we have:

$$D_{xx} = 1 + \frac{1}{V_f} \int\limits_{\mathrm{A_{fs}}} n_x B_x dA \tag{2.51}$$

by splitting the integral into the sum of the integrals over the interfaces between the active cells at the fluid-solid interface (AC_{fs}) and its solid face boundaries we have:

$$D_{xx} = 1 + \frac{1}{V_f} \sum_{AC_{\mathrm{fs}}} \int\limits_{AC_{\mathrm{fs}}} n_x B_x dA \tag{2.52}$$

in the same way we did for equation (2.30), taking into account the notations of Figure 2.9, we can split the integral in (2.52) into the sum of the integrals over the interfaces between the AC_{fs} and its boundary neighbours. And using the midpoint rule to approximate the integrals, we obtain:

$$D_{xx} = 1 + \frac{1}{V_f} \sum_{AC_{\mathrm{fs}}} (n_x B_x)_{\mathrm{c}\Gamma_i} \Gamma_i \tag{2.53}$$

where $(n_x B_x)_{\mathrm{c}\Gamma_i}$ is the value at the centre of face i of the B_x component in the x direction.

In the cell centred finite volume method the unknowns are localized at the centres of ACs and an approximation is needed to compute $B_{x_{\mathrm{c}\Gamma_i}}$ at the centre of the face i. Different levels of interpolation can be used to approximate this value.

The simplest way is to approximate it by the value localized at the centre of the AC at the fluid-solid interface:

$$B_{x_{\mathrm{c}\Gamma_i}} = B_{x_{AC}}, \qquad i = 1, 2, 3, 4, 5, 6 \tag{2.54}$$

where $B_{x_{AC}}$ is the value at the centre of the AC and we will refer to this approximation as Level.0. With a coarse grid this is a poor approximation and the alternative is using higher interpolation levels.

Level.1.1

Another way to approximate this value is using the boundary condition (2.22). For any component of the vector $\mathbf{B}$, the boundary condition is given by:

$$-n_x \frac{\partial B_\zeta}{\partial x} - n_y \frac{\partial B_\zeta}{\partial y} - n_z \frac{\partial B_\zeta}{\partial z} = n_\zeta \tag{2.55}$$

Assuming the boundary neighbour share the face 1 (West) with the AC and the unit vector n_{fs} normal to this face has the following components ($n_x = -1$, $n_y = 0$ and $n_z = 0$), equation (2.55) reduces to:

$$\frac{\partial B_x}{\partial x} = -1 \tag{2.56}$$

using the forward difference formula to approximate the derivative at the interface, we obtain:

$$\frac{B_{x_{AC}} - B_{x_{c\Gamma_1}}}{\frac{dx_1}{2}} = -1 \tag{2.57}$$

and the value of B_x at the centre of face 1 is equal to:

$$B_{x_{c\Gamma_1}} = B_{x_{AC}} + \frac{dx_1}{2} \tag{2.58}$$

In the same way, we can approximate $B_{x_{c\Gamma_2}}$ for the boundary neighbour sharing the face 2 (East) with the AC by:

$$B_{x_{c\Gamma_2}} = B_{x_{AC}} - \frac{dx_2}{2} \tag{2.59}$$

On the other hand, the boundary neighbour share the face i ($i = 3, 4, 5, 6$) with the AC has a unit vector n_{fs} with zero component in the X direction ($n_x = 0$) and the value of $B_{x_{c\Gamma_i}}$ is:

$$B_{x_{c\Gamma_i}} = B_{x_{AC}}, \qquad i = 3, 4, 5, 6 \tag{2.60}$$

In a similar way, we can approximate $B_{\zeta_{c\Gamma_i}}$ with $\dfrac{\partial B_\zeta}{\partial \zeta} = -1$ in the direction ζ and zero in the other directions.

Level.1.2

Here, we are using linear extrapolation at the AC on the fluid-solid interface and the relative AC$_j$. Assuming the boundary neighbour share the face 1 (West) with the AC and the (East) neighbour is the relative AC$_j$, the value at the centre of face 1 at the fluid-solid interface will be equal to:

$$B_{x_{c\Gamma_1}} = \frac{3B_{x_{AC}} - B_{x_{ACj}}}{2} \tag{2.61}$$

In the same way, we can approximate the value at the centre of the other faces.

Level.2

Here, we are using a quadratic interpolation at the AC on the fluid-solid interface and the relative AC$_j$ with the information coming from the boundary condition (2.22). Similar to Level.1.1 the value of the gradient equal -1 in the same directions of the component of B and 0 in the other directions. Assuming the case for the component B_x, the value of B_x at the centre of face 1 (West) will be equal to:

$$B_{x_{c\Gamma_1}} = \frac{9B_{x_{AC}} - B_{x_{ACj}} + 3dx}{8} \tag{2.62}$$

and we can approximate the value of $B_{x_{c\Gamma_2}}$ for the boundary neighbour sharing the face

2 (East) with the AC$_i$ by:

$$B_{x_{c\Gamma_2}} = \frac{9B_{x_{AC}} - B_{x_{ACj}} - 3dx}{8} \tag{2.63}$$

for the boundary neighbour sharing the face i ($i = 3, 4, 5, 6$) with the AC$_i$ the value of $B_{x_{c\Gamma_i}}$ will be equal to:

$$B_{x_{c\Gamma_i}} = \frac{9B_{x_{AC}} - B_{x_{ACj}}}{8}, \qquad i = 3, 4, 5, 6 \tag{2.64}$$

With the value on the interface, we can compute the effective diffusivity as the integral over the fluid-solid interfaces of $n_{\mathrm{fs}}B$.

2.3.6 Sparse matrix

In section 2.3.5 we said that " After solving the linear system ... ", in fact, solving the linear system is very challenging. A linear system in the form (2.36) or (2.48) need to be solved for each component of the vector B and solved for the scalar s^*. Usually, Na × Na is very large number and storing the whole matrix in the memory is not realistic and resourcefully demanding. To put in perspective how huge the matrix M is, we assume a volume discretized in 100 × 100 × 100 cubic voxel with the number of ACs is equal to ($Na = 155920$). Storing each element with 32 bit size will require at least $155920 \times 155920 \times 32 \approx 97\ GB$ of random-access memory (RAM). This is a huge amount of resources, and even with nowadays technology storing the whole matrix is not really feasible especially for larger volumes. The good news is that we do not need to store the whole matrix M. The matrix M is a sparse matrix since most of its elements are zeros.

There are many ways to store sparse matrix and the widely used storage format are COO (Coordinate list) and CSR (Compressed Sparse Row) or CSC (Compressed Sparse Column). In COO format only the non-zeros are stored by defining three arrays of length NNZ, where NNZ is the number of non- zeros in the matrix, (rowM(NNZ), colM(NNZ), valM(NNZ)). For each non-zero the row and column index of that matrix element are stored in the rowM and colM arrays. The value of the non-zero matrix element is placed in the corresponding location of the valM array. This is an extremely easy data structure to generate and it used to build and construct our matrix M. On the other hand, it is not too efficient on matrix-vector products for the iterative solution of linear systems. Hence, we change the data structure to CSC format which is more efficient for arithmetic operations, column slicing, and matrix-vector products. CSC format compresses the column index of COO from NNZ to column index + 1 (rowM(NNZ), colM(Na+1), valM(NNZ)). Where valM and rowM store the non-zero values and the row indices correspond to these values, and colM holds the index in valM and rowM where the given row starts and the last element is always NNZ.

When the sparse linear system is large using the direct method to solve it is not a good choice any more. The iterative methods in this situation are more appropriate for the solution. They usually require less memory, less computational effort and in general they are easier to program. The choice of the iterative method is not trivial. Since, the convergence behaviour of the iterative methods depends on the structure of the matrix of the linear system under consideration. For our matrix M we used the BiConjugate gradient method with diagonal scaling and it gave a good convergence rate.

The matrix M is symmetric and positive definite. It is converging quite fast with the BiConjugate gradient method with diagonal scaling. On the other hand, the matrix M_{NUCM} is not symmetric; introducing the ghost unknowns with the interpolation method proposed in 2.3.4.3 breaks the symmetry of the matrix and this will cause the system to have lower convergence rate.

In fact, solving non-symmetric large sparse linear systems is an active research area and it is in great importance for many applications. For the scope of this thesis, we restrict ourself to the BiConjugate gradient method with diagonal scaling since it gives a quite good results keeping in mind that an improvement can be done in this area.

Having non-symmetric system will raise the following question, is the creation of CC of level $L+1$ as described in 2.3.4.1 always reducing the CPU time? Indeed, the grid coarsening approach will reduce the number of real unknowns, but this will not mean that we will always benefit from that in terms of reducing the CPU time. For that, the creation of new CC should be controlled.

For a CC of N AC of level $L+1$, the number of real unknowns is equal to N. Each of these AC is an aggregate of 8 AC of level L corresponding to $8N$ real unknowns. The creation of this new CC of level $L+1$ decreases the number of real unknowns by $7N$. On the other hand, we will introduce 4 ghost unknowns for each face at the interface with AC of level L. Assuming M faces at the interfaces, the number of introduced ghost unknowns will be equal to $4M$. Introducing the ghost unknowns will increase the complexity of the linear system and in return will increase the CPU time. To make sure that we will always benefit from creating new CC, we should have the advantages from reducing the number of real unknowns much larger than the disadvantages from increasing the number of ghost unknowns. We can simply say that the number of real unknowns decrease should be much larger than the number of ghost unknowns increase ($7N >> 4M$). For that, we introduce the parameter $\tau = \dfrac{N}{M}$ and it supposed to be much larger than $\dfrac{4}{7}$, if not, we reject the new CC of level $L+1$.

2.3.7 Summary of section 2.3

In this section, the proposed multi-scale imaging and modelling approach was presented.

The choices we made were:

- The reactive diffusion problem was considered to test the proposed approach.

- The cell centred finite volume method was used in the discretization of the problem.
- The novel grid coarsening approach aiming to reduce the computational time was based on grouping the voxels away from the fluid-solid interfaces.
- The local mesh refinement step was based on injecting the HR information in the LR critical regions.
- The developed spatial discretization was based on barycentric interpolation. It was used in both coarsening and refinement steps.
- The BiConjugate gradient method with diagonal scaling was used in solving the resulted linear systems.

2.4 Results and discussion

In this section, the effects of global mesh refinement, change of resolution and the proposed grid coarsening approach on the effective properties and CPU time are presented. We first considered a rather simple geometry without reactive parts for which the effects on D_{eff} were investigated. Then, a reactive part was introduced in the centre of the previous geometry to study the effects on the complete set of effective properties i.e D_{eff} and the vector U. With this geometry different critical regions were selected based on the properties of the solution of the scalar s^*. Finally, a 3D volumes extracted from the Sic-Diamonds volumes was considered and the implementation of the proposed approach was tested.

So in total three geometries are considered. In the last period of our work we have been confronted with a serious technical problem: The HPC server crashed making the computations with large data impossible. Because of time constraints, it has not been possible to install the different codes on a new server, and consequently, the results presented for the last two geometries are only preliminary results.

Chemists usually use a face-centred cubic (FCC) unit cell to describe the lattice structure in crystalline metals. In FCC arrangement of atoms, the unit cell consists of eight atoms at the corners of a cube and one atom at the centre of each of the faces of the cube. We used the same principle to generate our first porous media to test the proposed multi-scale imaging and modelling approach. Figure 2.15a represents the FCC used in our computation with slight random perturbations of the sphere radius. This represents a periodic unit cell defined analytically, i.e. the spheres positions and radius are exactly known allowing discretization with any resolution. As an example, the cubic domain visible in blue is discretized in 100 × 100 × 100 cubic voxels. Figure 2.15b shows the discretized solid phase while, Figure 2.15c shows the discretized fluid phase.

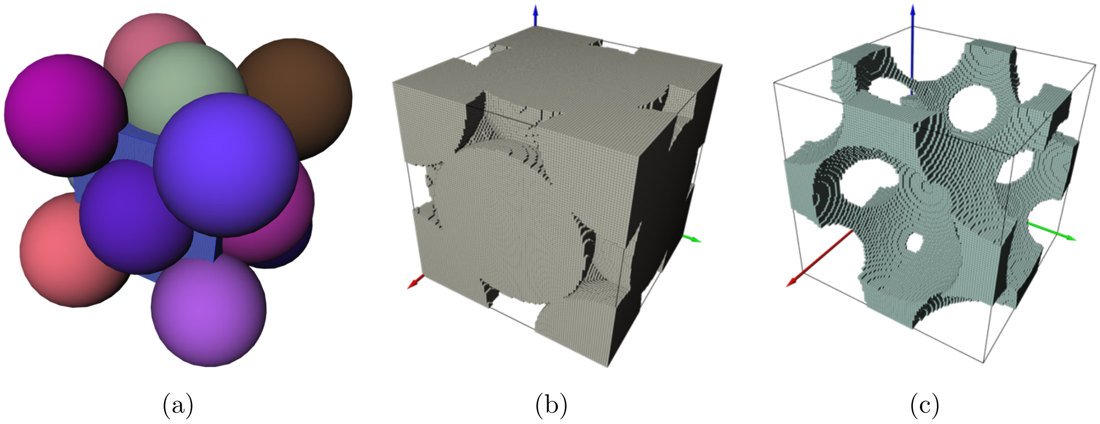
(a) (b) (c)

Figure 2.15: a) FCC with slight random perturbations of the sphere radius , b) the discretized solid phase, c) the uniform discretized fluid phase.

Using in house program that imitate the effect of changing the scanning resolution discrete images of any resolution can be generated. By change of resolution we mean, scanning the same object with different magnifications. A series of 3D volumes for FCC sample with different resolutions was generated using magnifications factors 2, 3, 4 and 5. The obtained 3D volumes were of size of 200^3, 300^3, 400^3 and 500^3 cubic voxels, respectively.

Figure 2.16 illustrates the difference between global mesh refinement and change of resolution. By global mesh refinement we mean that the domain is globally discretized with smaller mesh size (voxel size). It is usually used to reduce the error resulting from the domain discretization. Figure 2.16a shows a section of the initial geometry discretized with 100^3 cubic voxels. Figure 2.16b shows a section of the initial geometry with global refinement of factor 2 discretized with 200^3 cubic voxels. While, Figure 2.16c shows a section of the geometry with scanning magnification 2 discretized with 200^3 cubic voxels.

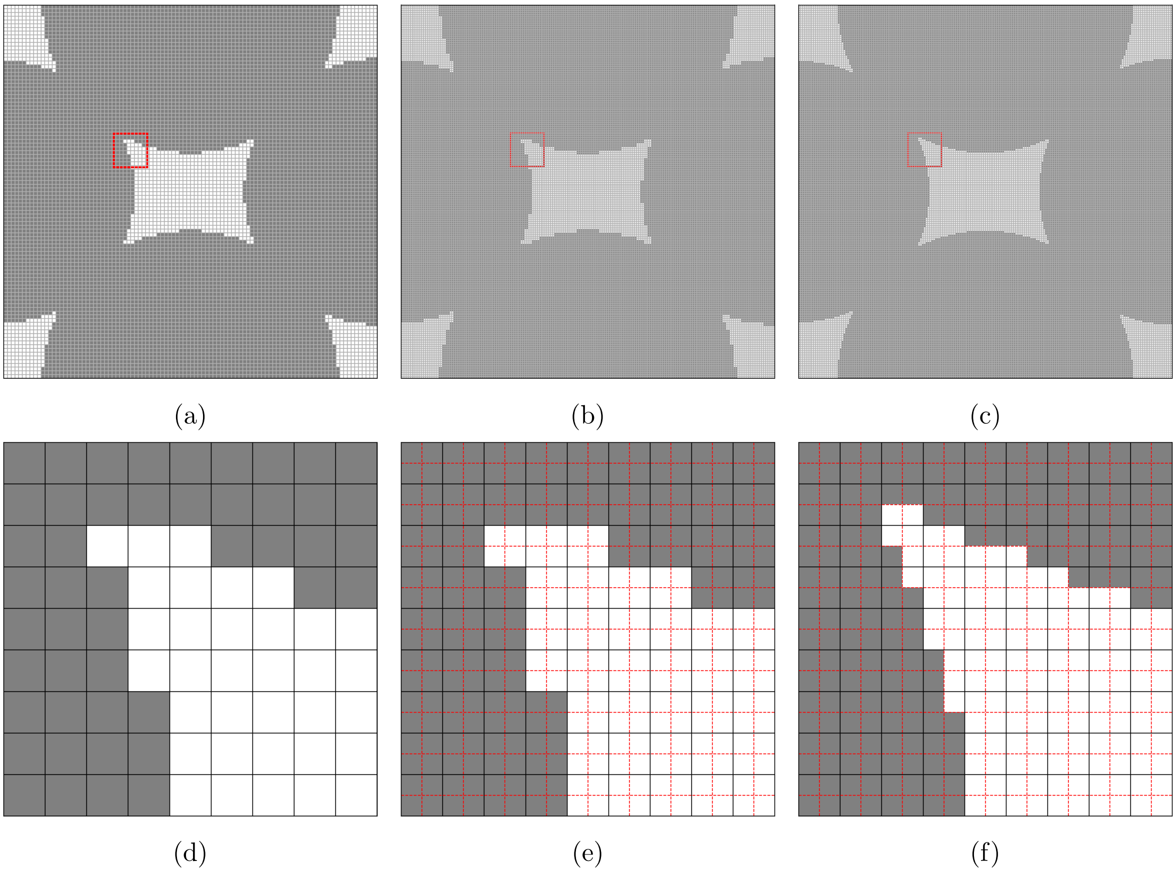
(a) (b) (c)

(d) (e) (f)

Figure 2.16: a) Section of the initial geometry discretized with 100^3 cubic voxels, b) Global mesh refinement of (a) with factor 2, c) The same section as in (a) with scanning magnification 2, (d-f) zoom of the area within the red box in (a-c), respectively.

Figures 2.16(d-f) show a zoom of the area within the red box in the sections (see Figures 2.16(a-c)). The black mesh (grid) represents the pixel size relevant to the initial geometry discretization. Whereas, the dash red mesh represents the pixel size correspond to the discretization with 200^2 pixels. From Figure 2.16e, we can clearly see that we only refine the domain without changing the geometry in the global mesh refinement. However, in Figure 2.16f, we can see the effect of changing the resolution on the fluid-solid interfaces. With the HR images more precise description of the fluid-solid interfaces were obtained.

In the next subsection the effects of the global mesh refinement and the interpolation level used to compute D_{eff} (see section 2.3.5) are investigated.

2.4.1 The effect of global mesh refinement on D_{eff}

In the global mesh refinement procedure the initial geometry is discretized with different size of cubic voxels. A series of global mesh refinement with factors 2, 3, 4, 5 and 6 were done to study the effect of global mesh refinement with the different interpolation levels described in section 2.3.5 when computing D_{eff}. The uniform discretization of the fluid phase is used to compute D_{eff} using the cell centred finite volume method as described in section 2.3.3. Figure 2.17 illustrates these effects on the diagonal components of the D_{eff} tensor.

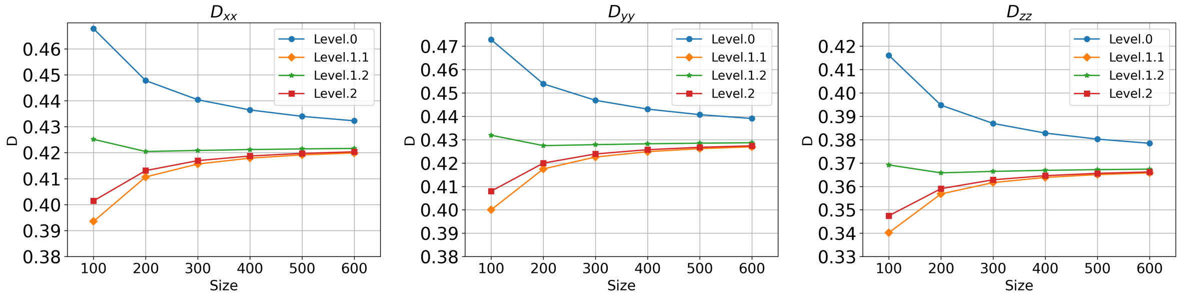

(a) (b) (c)

Figure 2.17: The effect of global mesh refinement on the different interpolation levels when computing D_{eff}. a) D_{xx} , b) D_{yy}, c) D_{zz}.

From Figure 2.17 we can see that decreasing the voxels size (increasing the number of voxels discretizing the same volume) will affect the components of D_{eff} in different ways depending on the interpolation level. Level.0 overestimates the D_{eff} components on a coarse grid and decreases towards the convergence limit with the global mesh refinement. On the other hand, Level.1.1 and Level.2 underestimate the values and increase toward the limits. For Level.1.2, it gives a very good approximation for the components of D_{eff} even with the coarse mesh and the effect of the global mesh refinement is limited. Since D_{eff} is a global property, using linear extrapolation to approximate the values at the centre of the faces was very suitable to compute D_{eff}. For that, Level.1.2 was used in the computation of D_{eff} and the vector U in the next subsections.

2.4.2 The effect of change of resolution on D_{eff}

In the previous subsection, the initial FCC 3D volume discretized in $100 \times 100 \times 100$ cubic voxels was fixed and we only applied a series of global mesh refinement. Using interpolation Level.1.2 in the computation of D_{eff} shows that the results are depending only on the initial 3D volume resolution and the effect of the global mesh refinement is limited. In this subsection, the effects of change of resolution on D_{eff} and CPU time are presented. Using the uniform discretized fluid phase with different magnifications the D_{eff} was computed and the results are presented in Figure 2.18.

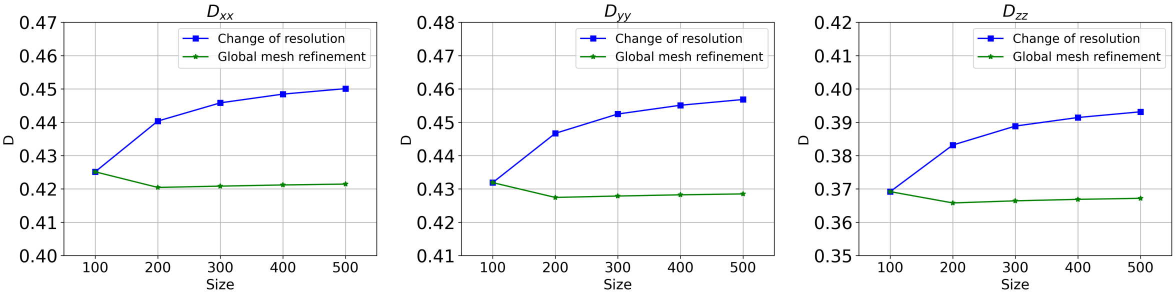

(a) (b) (c)

Figure 2.18: The effects of global mesh refinement and change of resolution on D_{eff}. a) D_{xx} , b) D_{yy}, c) D_{zz}.

From Figure 2.18 we can clearly see that increasing the resolution increases the D_{eff} components in X, Y and Z directions. In the higher resolution 3D volumes we have more precise details for the fluid-solid interfaces which influences the values of D_{eff}. Moreover, D_{eff} is strongly related to the porosity of the volume, Figure 2.19 shows the relation between D_{eff} and the porosity of the 3D volumes at different resolutions. Decreasing the porosity by 0.05% increases D_{eff} components by 2%. In comparison with the global mesh refinement, the change of resolution has significant effect on the computed values of the effective properties.

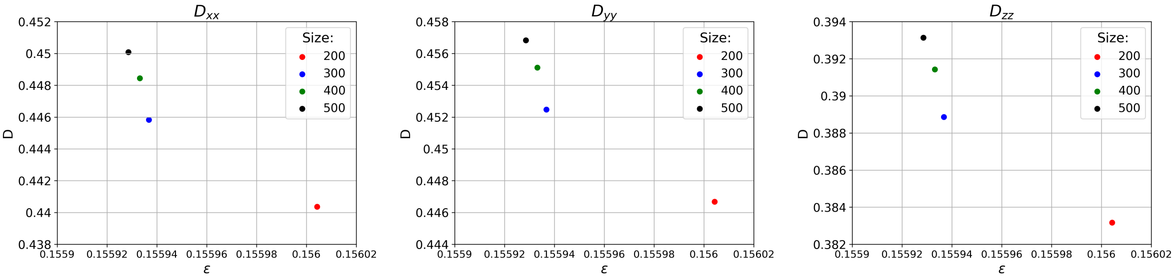

(a) (b) (c)

Figure 2.19: The effects of porosity on D_{eff}. a) D_{xx} , b) D_{yy}, c) D_{zz}.

Increasing the number of voxels hugely increases the memory usage and the computation time. Figure 2.20 illustrates the effect of change of resolution on the CPU time. Increasing the number of voxels by factor of 5 causes the CPU time to increase by a factor of 700. The CPU time is significantly increased.

In the next subsection, the effects of the proposed grid coarsening approach on the D_{eff} and CPU time are investigated.

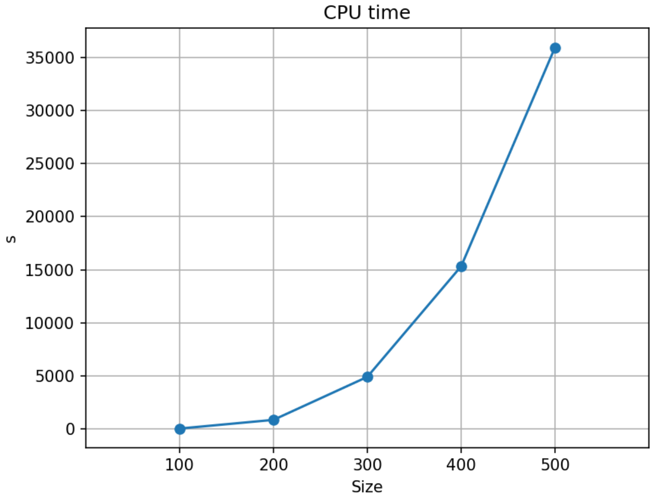

Figure 2.20: The effect of change of resolution on the CPU time.

2.4.3 The effect of the grid coarsening approach on D_{eff} and CPU time

Using the FCC 3D volumes with different resolutions as described in section 2.4.2 we studied the effect of the grid coarsening approach on D_{eff} and CPU time. The developed grid coarsening approach was used to generate the NUCM with different L_{max}. Then, the finite volume method along with the spatial discretization (see section 2.3.4.3) were used to solve the closure problem. Figures 2.21(a-c) illustrate a zoom at the centre of the section presented in Figure 2.16a With L_{max} is equal to 1,2 and 3, respectively. When ($L_{max} = 1$) the resulting mesh is equivalent to the uniform one. Figure 2.21d shows 3D sub volume of the same region with L_{max} equals 3.

Figure 2.22 illustrates the effect of changing the largest mesh level L_{max} when building the NUCM on D_{eff} components. When ($L_{max} = 1$) the results are equivalent to the uniform case presented in Figure 2.18. Increasing L_{max} has negligible effect in comparison with the effect of change of the resolution. Using the barycentric interpolation with locally first-order accuracy in the spatial discretization at coarse-fine interfaces was able to maintain higher global accuracy.

Figure 2.23 shows the effect of changing L_{max} on the CPU time for the 3D volumes of different resolutions. Different values of the parameter τ were used to force the initial grid to reach the required L_{max}. In the zoomed region in Figure 2.23, we can see that, for small 3D volumes (100, 200), even if the grid coarsening approach reduces the number of the real unknowns, the CPU time is increasing. This is due to the fact that we increased the complexity of the matrix M which in return reduced the convergence rate of the BiConjugate gradient method. For larger 3D volumes (300, 400, 500), the grid coarsening approach reduced the CPU time. Table 2.4 shows the relative CPU time for the 3D volumes of different resolutions. Even for larger volumes the grid coarsening approach is not always beneficial in terms of CPU time, a trade-off between reducing the number of

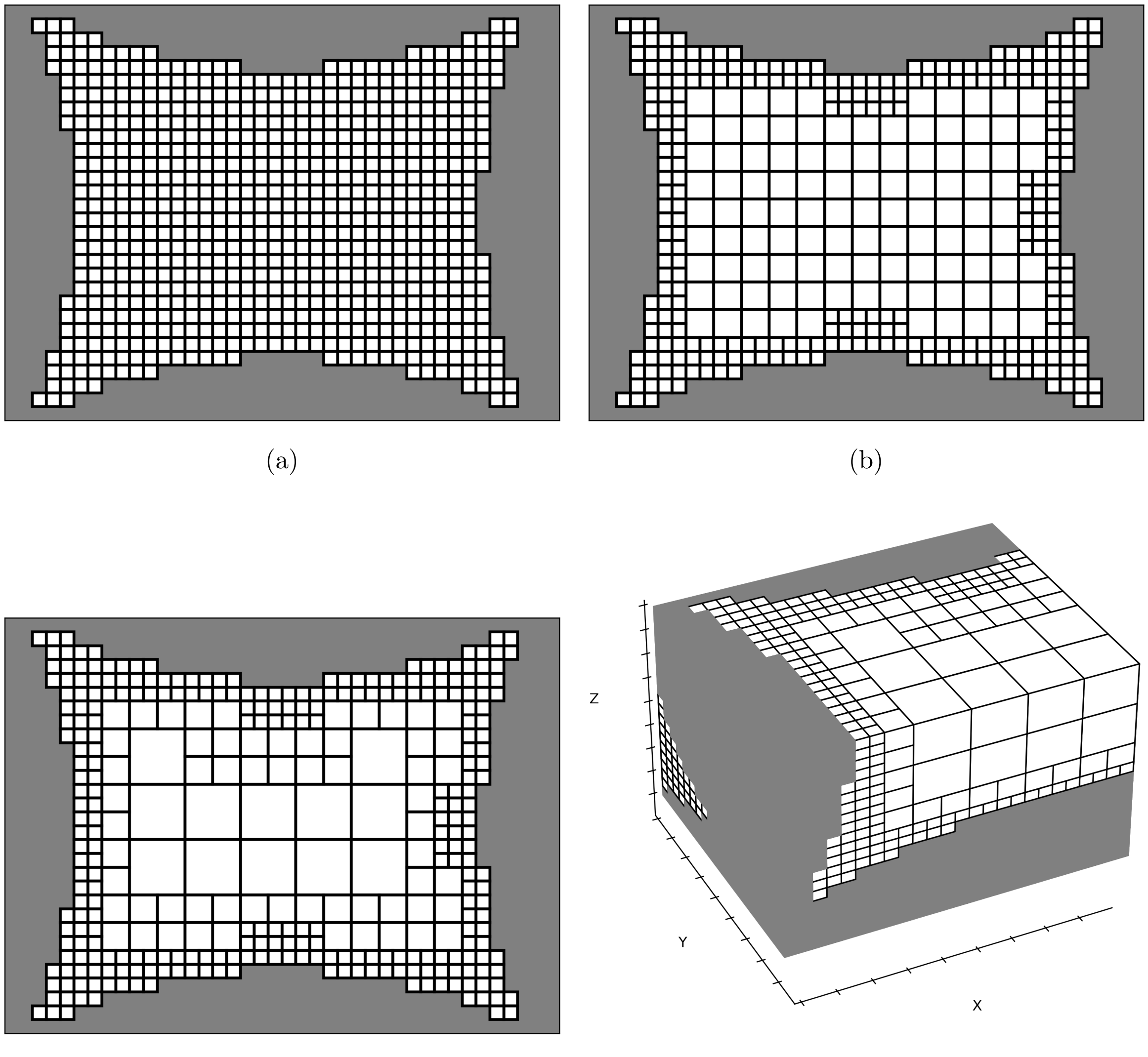

(a) (b)

(c) (d)

Figure 2.21: Sections of the NUCM 100^3 zoomed at the center of the section 2.16a with different L_{max}. a) $L_{max} = 1$, b) $L_{max} = 2$, c) $L_{max} = 3$, d) 3D sub volume of (c).

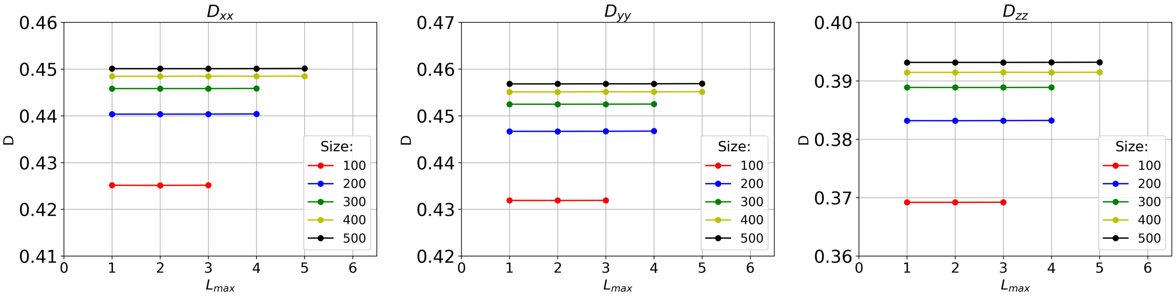

(a) (b) (c)

Figure 2.22: The effect of grid coarsening approach on D_{eff}. a) D_{xx} , b) D_{yy}, c) D_{zz}.

real unknowns and increasing the complexity of the matrix should be taken into account.

Figure 2.24 shows the effect of the grid coarsening approach on the CPU time for the 3D volumes of different resolutions in comparison with the uniform case. According to the minimum relative CPU time (highlighted red) in Table 2.4, we chose L_{max} in the grid coarsening approach. We can see that using the grid coarsening approach is reducing the

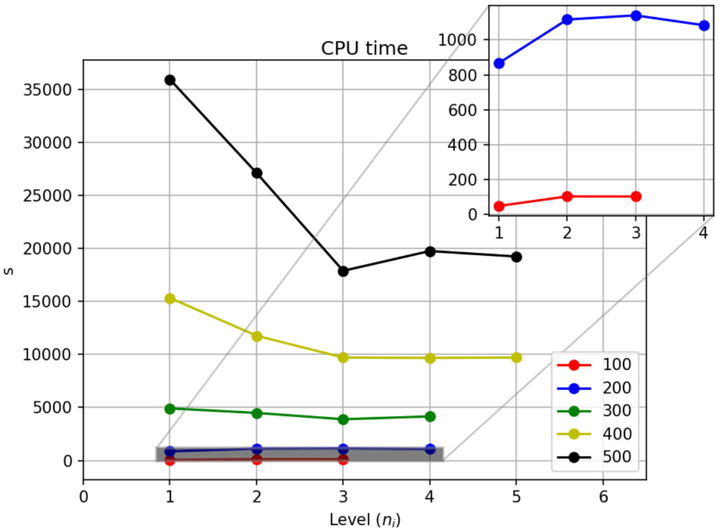

Figure 2.23: The effect of changing L_{max} on the CPU time for the different resolution 3D volumes.

Size	L_{max}	CPU Time (s)	Relative CPU Time (%)	Size	L_{max}	CPU Time (s)	Relative CPU Time (%)
100	1	49.6	0	400	1	15326.3	0
	2	104.1	109.8		2	11764.6	-23.2
	3	103.7	109.0		3	9704.0	-36.6
200	1	867.3	0		4	9669.5	-36.9
	2	1116.4	28.7		5	9704.0	-36.6
	3	1140.1	31.4	500	1	35925.8	0
	4	1083.8	24.9		2	27108.8	-24.5
300	1	4913.8	0		3	17880.5	-50.2
	2	4484.6	-8.7		4	19746.2	-45.0
	3	3888.9	-20.8		5	19229.6	-46.4
	4	4156.3	-15.4	-	-	-	-

Table 2.4: Relative CPU time for the 3D volumes of different resolutions with different L_{max}. Where the relative CPU time is the difference between the time of L_{max} and the time of $L_{max} = 1$ divided by the time of $L_{max} = 1$. The red cells correspond to the minimum relative CPU time.

CPU time up to 50%, depending on the size of the initial 3D volume and on L_{max} reached by the process. In this example, we obtained the maximum benefit of the proposed NUMC with $L_{max} = 3$.

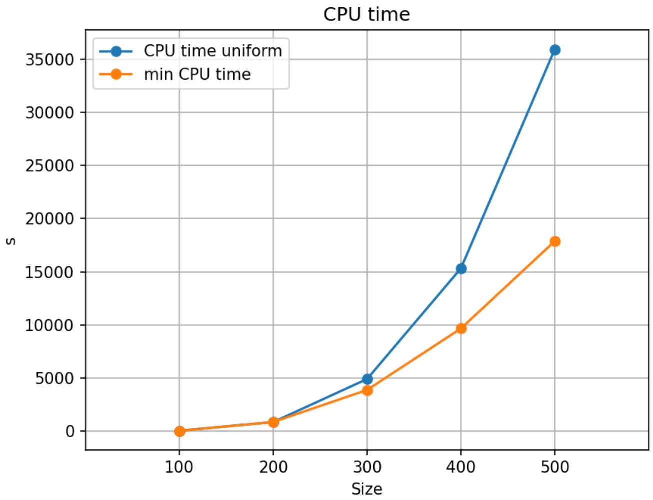

Figure 2.24: The effect of the grid coarsening approach on the CPU time for the 3D volumes of different resolutions in comparison with the uniform case.

2.4.4 The second geometry

In the same way as in subsection 2.4.1, we used the principle of FCC to generate new set of samples with sizes 100^3, 200^3 and 400^3 to mimic the change of resolution effects. In the centre of the new sample, the solid phase has been modified adding smaller spheres that are tagged as reactive part as showed in Figures 2.25 and 2.26.

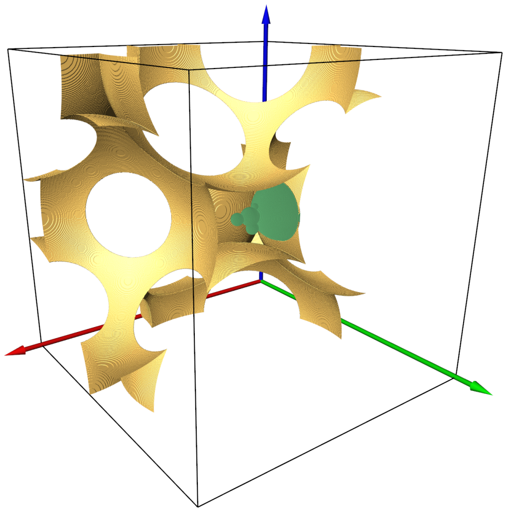

Figure 2.25: Isosurface of FCC with the reactive part (green) in the centre of the sample.

From Figure 2.26 we can see clearly the effect of changing the resolution on the interfaces of the reactive and inert parts. The effective diffusivity tensor, the vector U, and the macroscopic reactive source have been computed for the 3D volumes of different resolutions and the results are illustrated in Figure 2.27. The proposed NUCM was used in all the computations.

Figure 2.27 shows that increasing the resolution and the quality of the fluid-solid interfaces is increasing the values of D_{eff} components in all directions. On the other hand,

(a) (b) (c)

Figure 2.26: Sections with different resolutions. Black = fluid, grey = inert solid, white = reactive solid, a) Size 100, b) Size 200, c) Size 400.

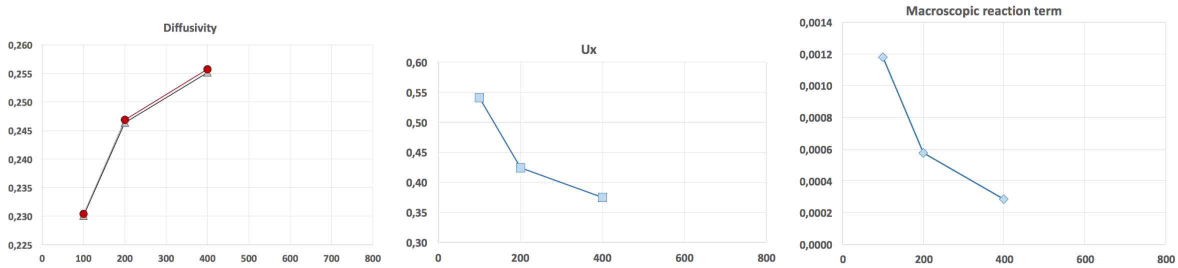

(a) (b) (c)

Figure 2.27: a) Diagonal terms of the diffusivity tensor, b) Component U_x of the vector U, c) Macroscopic reaction term.

the values of the component U_x and the macroscopic reactive source are decreasing with the change of resolutions.

With this geometry different critical regions were selected based on the properties of the solution of the scalar s^*

2.4.5 Identification of the critical regions; Some empirical results

When we compute D_{eff}, computations only involve the values of **B** at the fluid-solid interfaces. Taking that into account, we first tried to use these values in our criterion for defining the LR critical regions. We assumed that these regions correspond to the zones where the component of **B** in any direction has the larger absolute value. Using this criterion in the LMR step appeared as insufficient, no improvement of the results being obtained with the refined meshes.

In the second geometry different critical regions based on the properties of the solution of the scalar s^* were selected. In this test, we considered the case with the volume of 200^3 as the LR image and the volume of 400^3 as the HR image. From Figure 2.27, we observed that when changing the scanning resolution from 2 to 4 (size 200^3 to 400^3) the value of the averaged diffusivity was increased by 3.6% while, the value of U_x and the reactive source term were decreased by -11.7% and -50.4%, respectively. This was due to the change of resolution effects. These values were used as reference for the LMR tests.

The trivial choice for the critical regions was the geometry of the reactive part. The LR critical region with the NUCM of size 200 is illustrated in Figure 2.28a, where the inert part is in purple, the reactive part is in red, ACs of level 1 are in light blue and ACs of level 2 are in light green. In the LMR step, first, we increased the level for each AC by 1 and subsample the NUCM by factor of 2 , then we replace the fluid-solid interfaces in the LR critical region with the HR ones as illustrated in Figure 2.28b, where the inert part is in purple, the reactive part is in red, ACs of level 1 are in blue, ACs of level 2 are in light blue and ACs of level 3 are in light green.

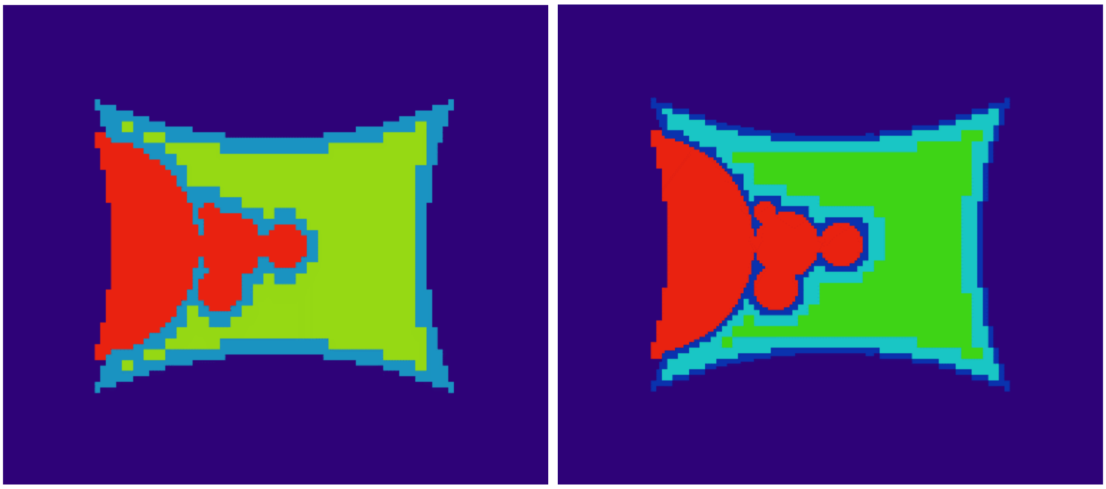
(a) (b)

Figure 2.28: a) Section of the NUCM 200^3 zoomed at the critical region , b) Section of the subsampled NUCM with factor 2 (400^3) with local refining of the reactive interface.

With the proposed critical regions, which we called **first local refining** (Ref1), the value of the averaged D_{eff} is decreased by 0.03%, the value of U_x is increased by 0.4% and the value of the macroscopic reactive source is decreased by 49.7% when applying LMR.

The LMR with the criterion Ref1 give very good approximation of the macroscopic reactive term but, have almost no effect on D_{eff} and U in comparison with the reference values. The reactive term is only determined by the geometry, if the discretization of the reactive interface is improved, we improve the approximation. The small difference is due to the difference in porosity. D_{eff} and U are obtained by solving a partial differential problem on the complete volume. As seen in the first tests, a local refining of the geometry is not noticeably improving the computed effective properties.

In the closure problem for the scalar s^*, we have a volume source term in all the fluid domain, and a localized source term on the reactive interface. Comparing the computed values of s^* for the 200^3 volume with the 400^3 one, we noticed that the larger values are localized in the corner of the sections and that they decrease from 200^3 to 400^3, see Figure 2.29.

To better characterize the difference between the solution of s^* for 200^3 and 400^3 volumes, we computed a projection of the solution for 400^3 volume on the mesh used for 200^3 volume. Figure 2.30 illustrate the 3D rendering of the regions with the largest

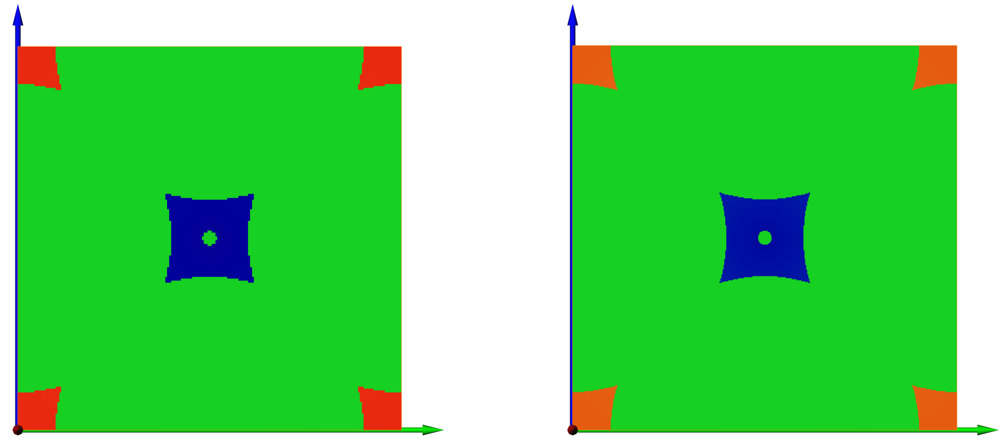

(a) (b)

Figure 2.29: Section in the plane YZ for the computed fields s^*, with colour map (blue=-230, red=+180). a) size 200^3 , b) size 400^3.

absolute difference.

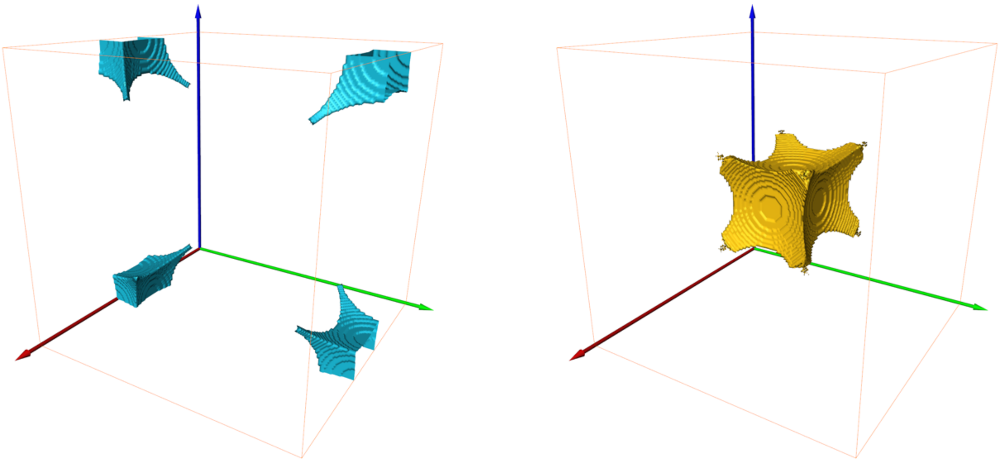

(a) (b)

Figure 2.30: 3D rendering of the regions with the largest absolute difference. a) difference $<$ -10 , b) difference $>$ 10.

The zones where larger values of s^* are localized correspond to the zones in blue on Figure 2.30. From Figure 2.31 we can see that these zones are connected to the centre by the smaller links (one link indicated by the white arrow) and, the discretization of these zones had been improved by the change of resolution.

To test this hypothesis, a series of refining had been done as follows:

- Second local refining (Ref2): Eight points situated in the middle of the smaller links previously identified (white arrow Figure 2.31) are selected, and the fluid zone is refined within a cube of 20^3 voxels centred on these points.
- Third local refining (Ref3): The same points as in Ref2 but, with cubes of 30^3 voxels

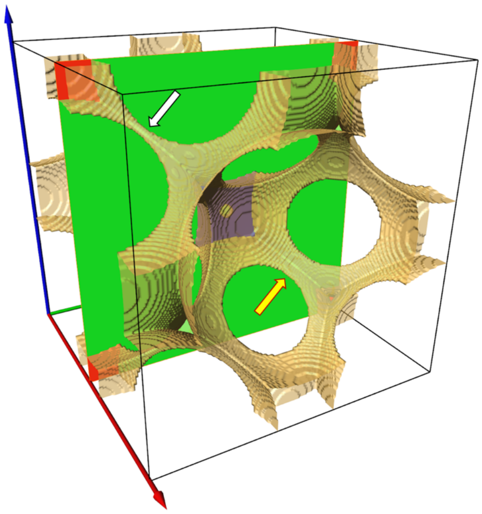

Figure 2.31: Computed fields s^* for the 200 volume, section in the plane YZ same as in Figure 2.29a with isosurface corresponding to the fluid-solid interface.

- Fourth local refining (Ref4): Eight new points were added corresponding to the links directly connected to the central zone (yellow arrow Figure 2.31), and the fluid zone is refined within a cube of 20^3 voxels centred on all points.
- Fifth local refining (Ref5): The same points as in Ref4 but, with cubes of 30^3 voxels.
- Sixth local refining (Ref6): The same points as in Ref4 but, with cubes of 40^3 voxels.

Table 2.5 summarizes the effect of applying the proposed series of refinements and the results are illustrated in Figure 2.32. With Ref2 we start to have good tendency, the diffusivity is increasing and the component U_x is decreasing. Increasing the cubes size in Ref3 have limited effects. Introducing the new points corresponding to the links directly connected to the central zone in Ref4 gives good improvements to the results. Finally, using cubes of 30^3 and 40^3 voxels in Ref5 and Ref6 give very good results.

Method	Averaged deffusivity	U_x	Reactive source
Change of resolution	3.6%	-11.7%	-50.4%
Ref1	-0.02%	0.43%	-49.7%
Ref2	0.62%	-4.91%	-49.7%
Ref3	0.81%	-5.16%	-49.7%
Ref4	1.48%	-7.12%	-49.7%
Ref5	2.12%	-8.65%	-49.7%
Ref6	2.35%	-9.48%	-49.7%

Table 2.5: The effect of the different method of refinement.

The effective properties, D_{eff} and the vector U, are global properties and, they depend on the entire 3D volume. The series of LMR indicates that the critical regions depend

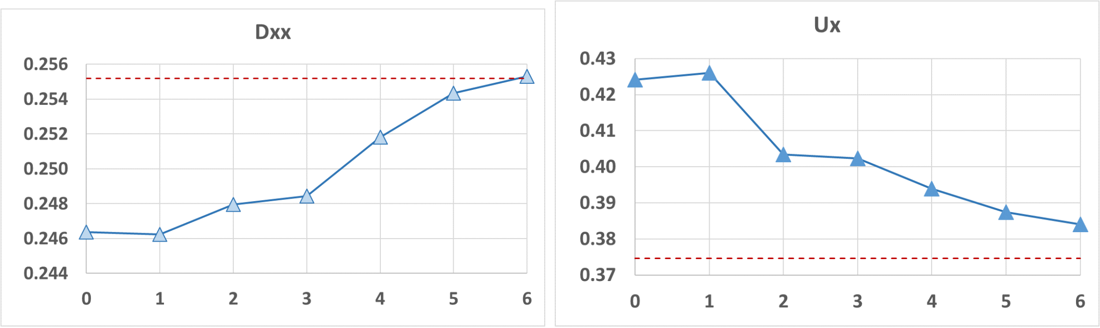

(a)

(b)

Figure 2.32: The effect of the different refinement methods on: a) Component D_{xx} of the diffusivity tensor, b) Component U_x of the vector U.

on the transport in the 3D volume. These tests were an empirical attempt to analyse the possible choices for the critical regions. Moreover, they are considered as a proof of concept to the preposed LMR with multi-scale imaging approach. We were able to successfully implement the preposed approach as shown by these tests. To facilitate the implementation of the LMR step, a well defined criterion is needed to identify the critical regions.

2.4.6 Application to a real 3D volume

Using the real 3D volumes acquired in the multi-scale imaging experiment presented in section 2.2.2 is challenging. The 3D images are virtually free of the artefacts known from laboratory tomography, such as e.g. beam hardening or excessive noise, thanks to the monochromaticity and parallelity of the synchrotron beam. Nevertheless, by imperfect detector elements or by defects on the scintillator, ring artefacts are appearing in the reconstructed 3D images acquired with magnifications 2x and 4x. Registration of 3D volumes with different magnifications is challenging, due to the difference in contrast between the 3D volumes, especially in the higher magnifications 10x and 20x (due to asymmetric local tomography acquisitions). Moreover, different scintillators were used with magnifications 2x and 4x, causing the ring artefacts to appear in different sections. Various methods can be used to deal with these artefacts [76]–[78], we even proposed new method for correcting these artefacts in collaboration with BAM institute (Bundesanstalt für Materialforschung und -prüfung). Due to lack of time we were not able to address suitable corrections to the entire set of the 3D volumes.

For that, we only considered the SiC–Diamond 3D volume acquired with a magnification of 4x to test the effect of change of resolution on the effective properties. Figure 2.33 illustrates two sections of the considered sample. Avoiding large ring artefacts, we have been able to extract two sub volumes of 600^3 voxels. Two sections are illustrated in Figure 2.34.

Image treatment and post-processing were done using in house codes. Simple segmentation algorithm was used, by a simple thresholding to approximate the SiC, diamonds

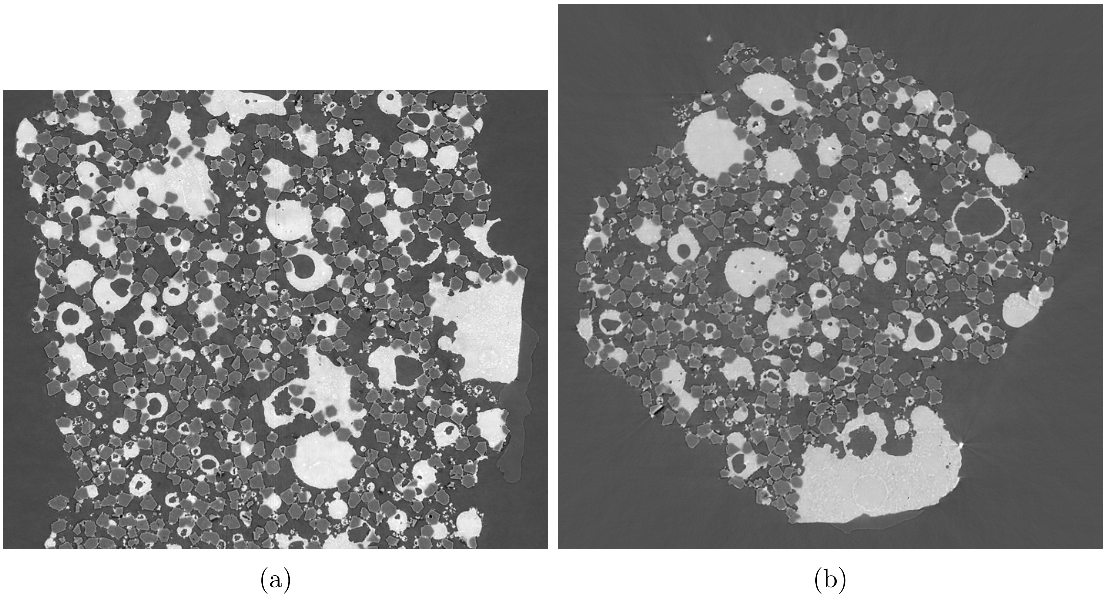
(a)
(b)

Figure 2.33: Sections of the 3D image of the considered sample: a) X=1280, b) Z=1084.

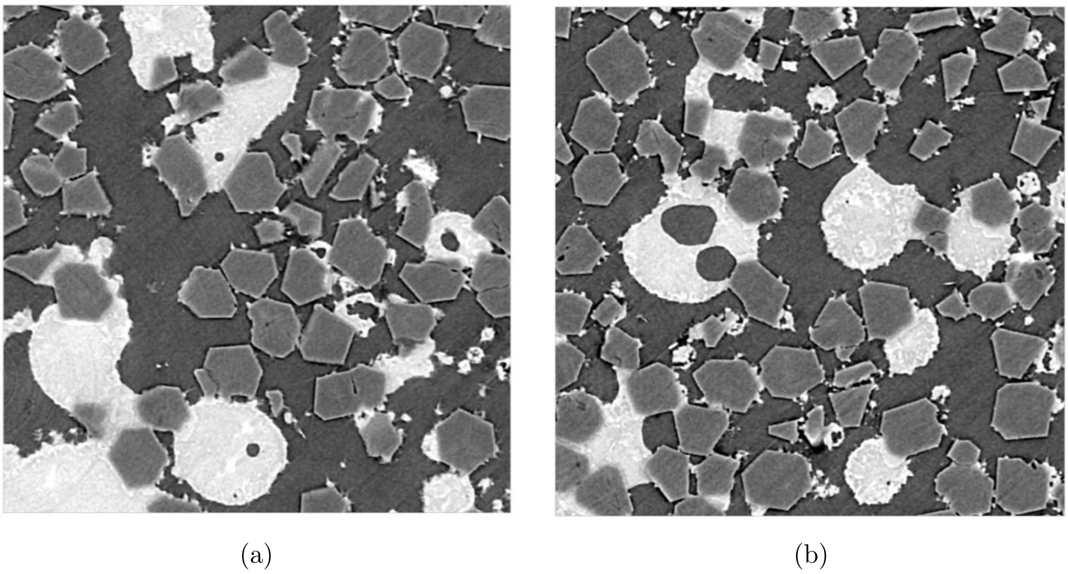
(a)
(b)

Figure 2.34: Sections Z=300 of the two extracted sub-volumes. a) first sub-volume, b) second sub-volume

and the pores. To facilitate the thresholding, filtering by anisotropic diffusion was used to improve the definition of the histogram. Figure 2.35 illustrates the effect of the anisotropic diffusion filter on the images and the corresponding histograms.

To study the effect of change of resolution on the effective properties, the initial grey scale image of the first sub-volume was downscaled to generate images of 300^3 and 150^3. The same post-processing was applied to the samples, sections of the resulting segmented sub-volumes are shown in Figure 2.36.

The segmented images in Figure 2.36 represent the labelled 3D images used in the grid coarsening process with SiC in white, Diamond in gray and the pores in black. With the assumption that SiC represents the reactive part and Diamond represents the inert part, Figure 2.37a illustrates a section of the NUCM results from the grid coarsening process

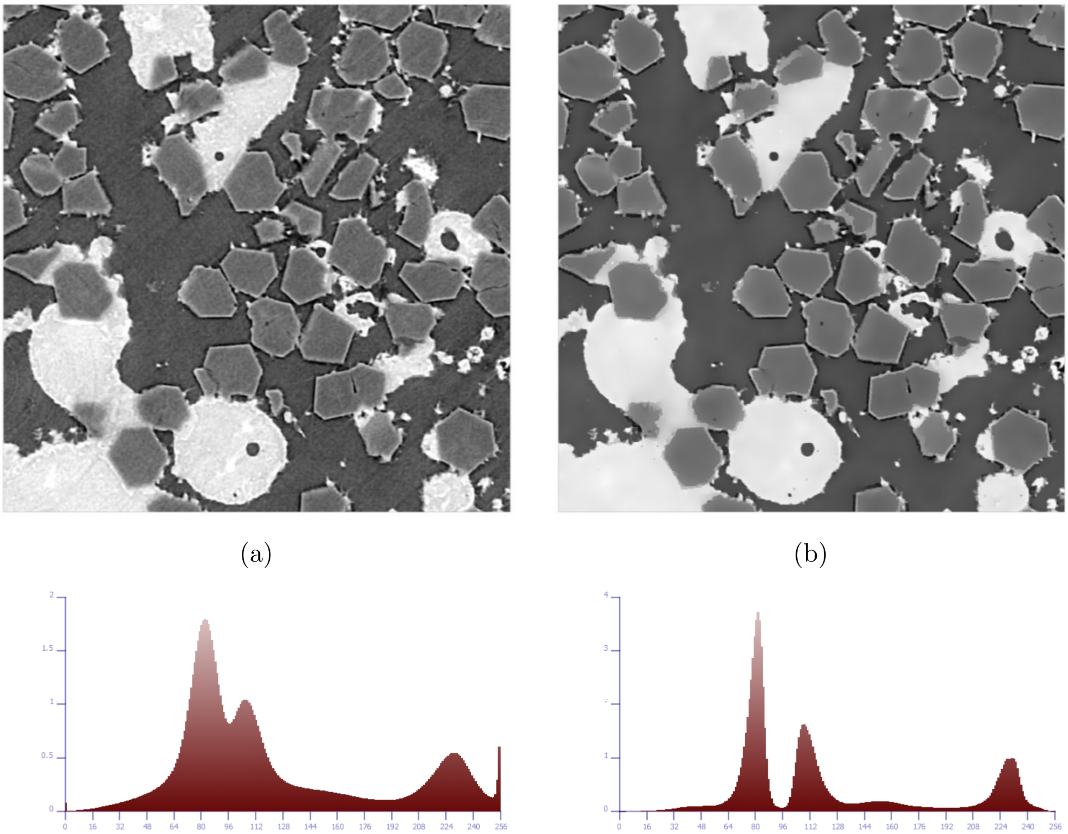

(a) (b)

(c) (d)

Figure 2.35: a) Section Z=300 of the extracted first sub-volume before application of the anisotropic diffusion filter, b) Section Z=300 of the extracted first sub-volume after application of the anisotropic diffusion filter, c) Histogram before application of the anisotropic diffusion filter, d) Histogram after application of the anisotropic diffusion filter.

with L_{max} equal 4 and Figure 2.37b shows the corresponding labelled section.

The effect of change of resolution on D_{eff} components, illustrated in Figure 2.38, is limited due to the downscaling process. Further corrections and post-processing for the real 3D volumes are needed. Nevertheless, the applications of the proposed multi-scale imaging and modelling approach for real 3D volumes are demonstrated.

Working with real data is problematic. We mentioned in section 2.2 that the SiC-Diamond sample was selected as an example of two solids phase material which can be segmented easily. In fact, due to the phase contrast artefact the segmentation of this sample was challenging. The objective of this part was to develop multi-scale imaging and modelling procedures for reactive transport in porous media. These preliminary results give a proof of concept and validate the proposed procedures. Moreover, they show that the applicability of the developed procedures is not limited to synthetic samples, but is also applicable for real data sets.

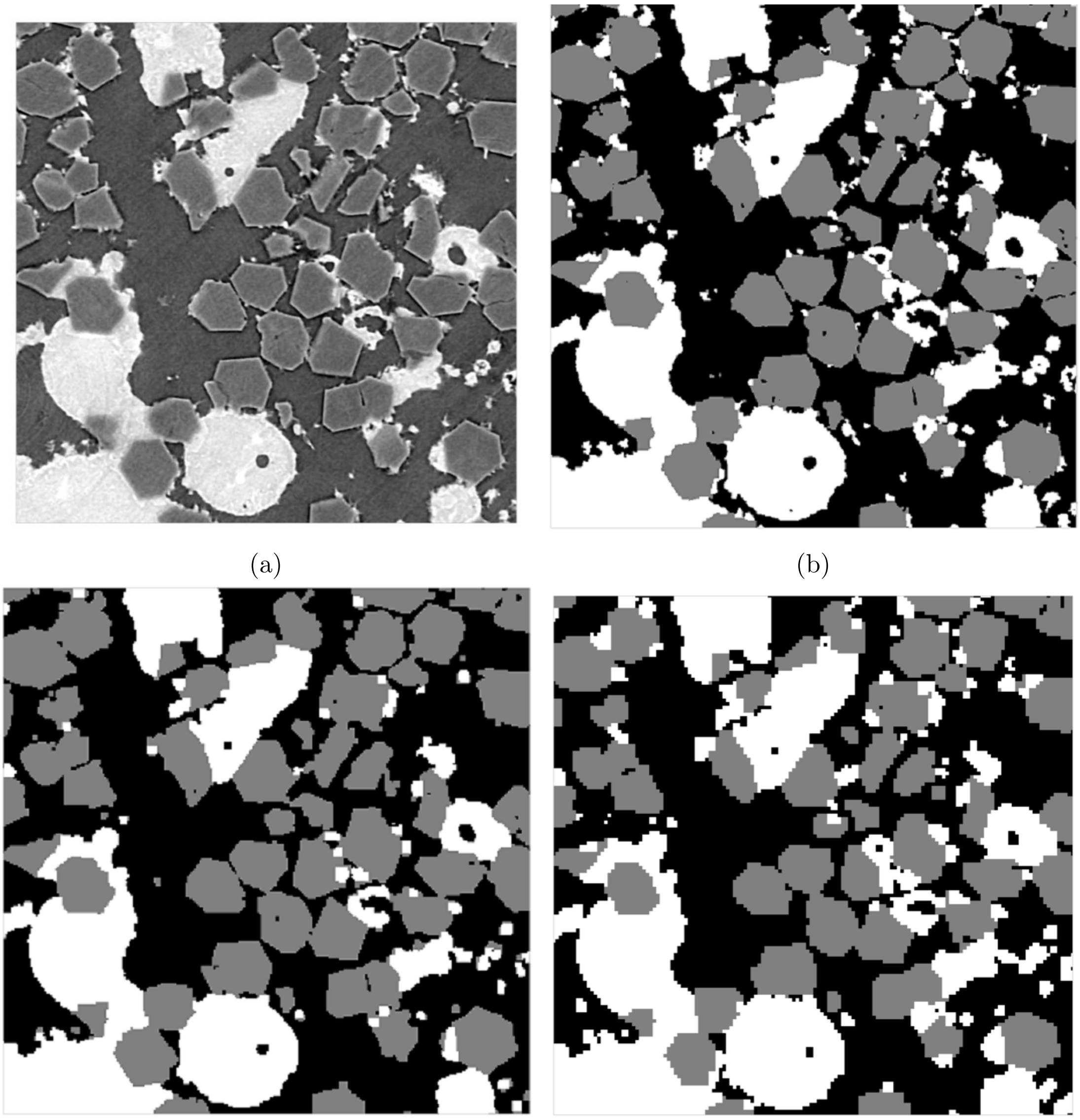

(a) (b)

(c) (d)

Figure 2.36: a) Section Z=300 of the extracted first sub-volume before application of the anisotropic diffusion filter, b) Section Z=300 of the extracted first sub-volume after segmentation, c) Section Z=150 of the segmented volume after sub-sampling by a factor 2, d) section Z=75 of the segmented volume after sub-sampling by a factor 4.

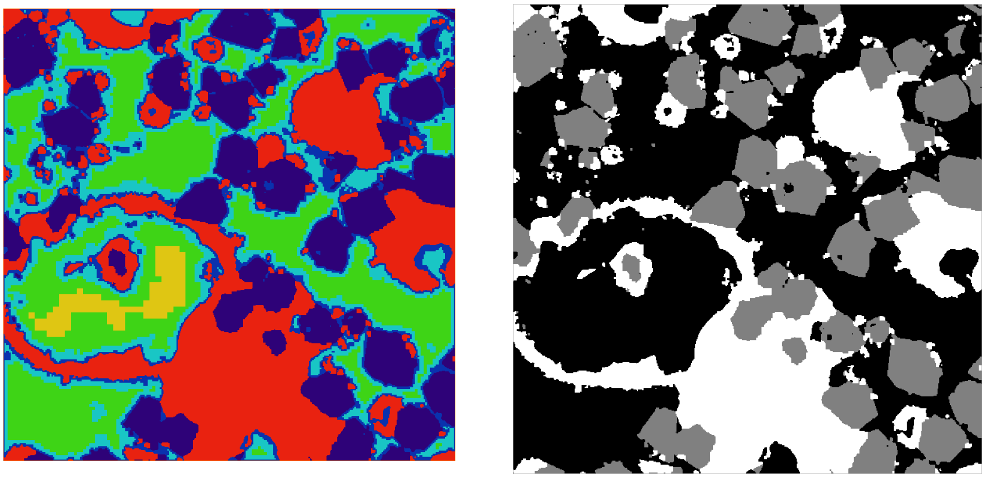

(a) (b)

Figure 2.37: Section Z=64 of the first sub-volume. a) The NUCM, where the inert part is in purple, the reactive part is in red, ACs of level 1 are in blue, ACs of level 2 are in light blue, ACs of level 3 are in green and ACs of level 4 are in yellow, b) The segmented image, where the inert part is in gray, the reactive part is in white and the pores in black.

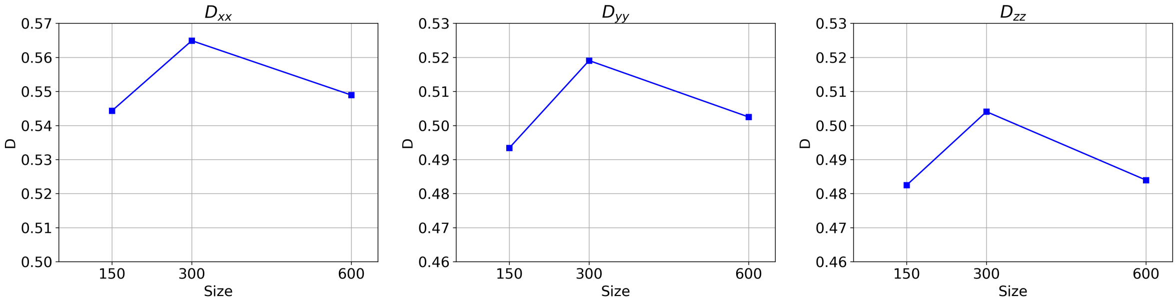

(a) (b) (c)

Figure 2.38: The effect of change of resolution on D_{eff}. a) D_{xx} , b) D_{yy}, c) D_{zz}.

2.4.7 Summary of section 2.4

In this section, the developed multi-scale imaging and modelling approach was tested and its benefits were investigated. Three geometries were considered:

- A simple geometry without reactive parts
- The same geometry with reactive parts added
- A 3D volumes extracted from the Sic-Diamonds volumes

Using the first geometry the following tests were performed to study the effects of:

- Global mesh refinement on D_{eff} along with the different interpolation levels described in section 2.3.5.
- Change of resolution on D_{eff} and CPU time.
- Grid coarsening approach on D_{eff} and CPU time.

In the third test the results were compared to the uniform case and the benefits from applying the developed approach were discussed.

The second geometry was used to study the effects on the complete set of effective properties i.e D_{eff} and the vector U. Moreover, it was used for the implementation of the proposed LMR with multi-scale imaging approach and several critical regions were tested.

Finally, an attempt of applying the developed approach on real data set was performed using the third geometry.

2.5 Summary of chapter 2

In this chapter we presented the multi-scale imaging and modelling approach for reactive diffusion in porous media. The proposed approach consists of two steps, grid coarsening and local mesh refinement steps. The novel grid coarsening approach is aiming to reduce the computation time by aggregating the voxels away from the interfaces. At TOMCAT beamline, the multi-scale imaging experiment was performed. In the local mesh refinement step, both LR images and HR images were used to improve the accuracy of the results.

The spatial discretization needed in both steps was based on barycentric interpolation. The resulted linear system was solved using the BiConjugate gradient method with diagonal scaling.

Finally, using synthesized and real data sets different tests were performed to test and investigate the benefits of the developed multi-scale imaging and modelling approach.

2.6 Conclusions

In this chapter we presented the first example of multi-scale numerical modelling combined with synchrotron X-ray experiments. The importance of the multi-scale imaging approach when approximating the effective properties has been presented as well as the advantage of combining it with multi-scale numerical simulations to improve the computational time of the approximations.

We developed a multi-scale imaging and modelling approach for reactive diffusion problems in porous media. This work was a proof of concept for the validity and the effectivity of the proposed NUCM. Several tests were performed using synthesized and real data sets to demonstrate the effects and benefits of the proposed approach. The novel grid coarsening approach was able to reduce the CPU time up to 50% for large volumes in comparison with the uniform mesh. Moreover, the proposed spatial discretization used at the NUCM with its first-order accuracy was able to maintain higher global accuracy. The proposed local mesh refinement using the multi-scale imaging technique was implemented successfully. LR images corresponding to a large field of view were used as input for computing the first approximation on the NUCM. Then, the HR images are used to replace the LR critical regions information with HR ones in the LMR step.

The proposed NUCM can be applied to various type of reactive transport problem in porous media. Nevertheless, a suitable spatial discretization should be developed at the coarse-fine interfaces taken into account the targeted problem. The use of the NUCM will significantly decrease the computation time when approximating the effective properties.

The obtained data sets from the multi-scale imaging experiment are of great interest for different applications. In general, when developing new approaches synthesized or artificial samples are used in the testing and validation processes. This data sets with its variety and complexity give real samples to test the effectiveness of these developed approaches. Examples of such approaches are; superresolution techniques, reconstruction and segmentation algorithms and the presented work in this thesis. Due to the lack of time and the scope of this work the use of this data sets was limited to only an attempt to test the proposed approach on a real data set.

Finally, this work was a proof of concept with preliminary results. Future tests will be done to further investigate the effects and benefits of proposed approach taking into account the specificities of the real data sets. Moreover, to facilitate the implementation of the LMR step a well defined criterion to identify the critical regions will be investigated.

Chapter 3

Modelling and simulation of X-ray beam induced current (XBIC) experiment

3.1 Introduction

In recent decades, the need of renewable energy sources with simple production and at low cost is highly urgent [79]. Attention has increasingly focused on photovoltaic (PV) systems especially on thin film solar cells. In principle, the thinner the layers, the less amount of material is used, thus the cost of the device will be reduced. Nevertheless, thin film device fabrication is complex requiring proper control over the entire process sequence and advanced characterization methods [80], [81].

One of the emerging thin-film PV technologies is based on kesterite crystal structures such as Cu_2ZnSnS_4 (copper zinc tin sulfide - CZTS). The fact that it is composed of earth-abundant and environmental friendly elements makes it a very good candidate for low cost thin-film solar cells. Another advantage of CZTS is that it is a p-type semiconductor with direct band gap energy between 1.2 eV and 1.6 eV, and an absorption coefficient greater than 10^4 cm^{-1} in the visible light spectrum. This fact gives CZTS the condition of being a serious alternative for application as absorber layer in thin-film solar cells [82]. The device architecture of CZTS solar cells is borrowed from the highly successful $Cu(In,Ga)Se_2$ (CIGS) device architecture, with CIGS replaced by CZTS. CIGS solar cells have more than 40 years of research and development allowing them to reach a maximum efficiency of 22.6% [83]. While, for our newly and non-optimized material, the maximum reported efficiency is only 12%, which is relatively far from the theoretical conversion efficiency limit of 32.2% [84] . Therefore, advanced characterization techniques are needed to investigate the possible factors limiting the performance of such devices and to enlarge the knowledge to overcome these limitations.

The ability to observe at nanoscale the influence of defects on the local performance of a fully functional CZTS device can be crucial for understanding the spatial correlations between charge-transport mechanism and defects in the structure of the device. Synchrotron-based hard X-ray microscopes are able to provide X-ray spot sizes down to the nanometer scale and very long penetration depths. Multiple analytical techniques can be applied simultaneously to enable a direct correlation between the electrical performance and the chemical structure, by combining X-ray beam induced current (XBIC) measurements with X-ray fluorescence (XRF) [29], [30], [85]–[88].

The principle of XBIC is similar to that of electron beam induced current (EBIC) in a scanning electron microscope [89]: a current measuring device connected to the solar-cell electrodes evaluates the X-ray beam induced current. The focused X-ray beam, on one point of the sample, generates excess carriers that will diffuse inside the sample, with parts of them reaching the edge of the space-charge region (SCR) of the p-n junction. The electric field inside the SCR, and gradients in the electrochemical potentials of holes and electrons, i.e. in their quasi-Fermi levels, are the driving forces behind separation of electrons and holes toward their respective contacts. This leads to an appearance of current in an external circuit giving rise to the photo-current. By scanning the sample with the X-ray beam, a two-dimensional map of collected photocurrent in the device is constructed [90]–[92].

The complex architecture of the new generation solar cells comprising multiple layers makes it hard to determine the fundamental mechanisms impacting electrical performance. First-principles modelling of the XBIC signal is a possible way to obtain a deeper understanding of the correlations between material properties and the electrical performance of the device. XBIC experiments on a semiconductor device combined with the modelling has been performed for a single nanowire with 1D numerical simulation carried out using Comsol Multiphysics software [93], and for a single-junction, CdTe/CdS solar cell with a model in PyCDTS, a python-based solver for carrier and defect transport [94], [95]. In the mentioned previous works, 1D virtual sample was considered and drift-diffusion model was used with constant generation rate to simulate the XBIC experiment. To our best knowledge, the model presented in this thesis can be considered as the first attempt to simulate XBIC measurements for a realistic sample geometry at the nanoscale. The developed python-based 2D device simulator is based on drift-diffusion model combined with 2D generation profiles resulting from Monte-Carlo simulation. Furthermore, the simulator is taking into account the real layer structure in the simulations by using 2D computation domain constructed from the XRF data.

This work is the result of a collaboration with researchers from Technical University of Denmark (DTU). One goal of MUMMERING was to create collaborative works in subjects related to X-ray imaging modalities between the ESRs. This work initiated from the continuous discussions during the workshops and meetings in MUMMERING project and more specifically with ESR 9 (Azat M. Slyamov). The XBIC experiment was performed by the researchers from DTU and the Monte-Carlo simulations were performed in collaboration with Michael Stuckelberger from DESY. Section 3.2 consists of a paper accepted in

Faraday Discussions journal titled "Multi-Modal Characterization of Kesterite Thin-Film Solar Cells: Experimental results and numerical interpretation" presented here under the format of submission [96]. We chose to present the experimental and main simulation results in the form of our accepted paper to provide a concrete overview of this work. My main contribution was the development of a python-based 2D device simulator designed to handle 2D real device structures and to combine Monte-Carlo simulation in order to simulate XBIC experiments. In addition to that, I also ran several computational tests investigating the effects of material parameters, performing sensitivity analysis, obtaining the final results, participating in discussions and in physical interpretations of the obtained results.

To simulate XBIC measurement, one needs to understand the underlying physics of the device under experiment. Thin-film solar cells are basically multilayer of semiconductor materials. In section 3.3, we present the basics of semiconductor physics and the choices we made for the first-principles model we used in our simulator. Then, the discretization methods and schemes utilized in our simulator are presented in section 3.4. Finally, in section 3.5 we give supplementary results to the simulation results presented in section 3.2.

3.2 Multi-Modal Characterization of Kesterite Thin-Film Solar Cells: Experimental results and numerical interpretation

Faraday Discussions

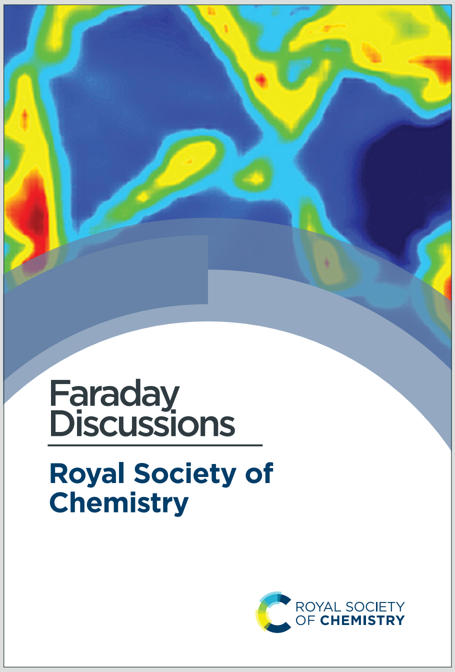

This article can be cited before page numbers have been issued, to do this please use: A. Saadaldin, A. Slyamov, M. E. Stuckelberger, P. S. Jørgensen, C. Rein, M. Mar Lucas, T. Ramos, A. Rodriguez-Fernandez, D. Bernard and J. W. Andreasen, *Faraday Discuss.*, 2022, DOI: 10.1039/D2FD00044J.

ROYAL SOCIETY OF CHEMISTRY

www.rsc.org/faraday_d

Multi-Modal Characterization of Kesterite Thin-Film Solar Cells: Experimental results and numerical interpretation

View Article Online
DOI: 10.1039/D2FD00044J

Abdellatif Saadaldin,[1,*] Azat M. Slyamov,[2,*] Michael E. Stuckelberger,[3,†] Peter S. Jørgensen,[2] Christian Rein,[2]
Mariana Mar Lucas,[2] Tiago Ramos,[2] Angel Rodriguez-Fernandez,[4] Dominique Bernard,[1] and Jens W. Andreasen[2]
[1] *CNRS, Univ. Bordeaux, Bordeaux INP, ICMCB, UMR 5026, F-33600 Pessac, France*
[2] *Technical Univ. of Denmark, DTU Energy, 310, Fysikvej, DK-2800 Kgs. Lyngby, Denmark*
[3] *Center for X-ray and Nano Science CXNS, Deutsches Elektronen-Synchrotron DESY, Notkestr. 85, 22607 Hamburg, Germany*
[4] *MAX IV Laboratory, Lund University, Box 118, 221 00 Lund, Sweden*

(Dated: March 11, 2022)

We report a multi-modal study of electrical, chemical and structural properties of a kesterite thin-film solar cell by combining the spatially-resolved X-ray beam induced current and fluorescence imaging techniques for the evaluation of a fully functional device in cross-section geometry. Data allowed correlating chemical composition, defects at interfaces and inhomogeneous deposition of the layers with the local charge-collection efficiency of the device. We support our observations with Monte-Carlo simulations of high-energy X-ray interactions with the semiconductor device, and finite-volume modeling of the charge-collection efficiency.

I. INTRODUCTION

The growing energy demand is currently being addressed with a focus on climate change mitigation, and the development of renewable energy sources [1]. Among these, solar energy has the potential of becoming a multi-terawatt technology [2, 3]. In 2017, crystalline silicon-based photo-voltaic (PV) technology had around 95% of the solar market share due to the well-established silicon industry, relatively high efficiency and stability of the devices. However, silicon solar modules' production is not efficient in terms of energy and material consumption [4–6]. To become a commercially viable alternative to silicon-based technology, the new generations of solar cells have to be competitive in terms of stability, up-scaling and energy-payback time [7]. Thin-film PV is currently being investigated as a promising candidate that could satisfy the requirements mentioned above.

One of the emerging thin-film PV technologies is based on kesterite crystal structures such as Cu_2ZnSnS_4 (copper zinc tin sulfide - CZTS). The advantage of kesterite solar cells is that they can be produced in a low-cost manner, mostly made of abundant and non-toxic elements. The high absorption coefficient of CZTS associated with its direct band gap, allows reducing the thickness of the absorber layer to few hundred nanometers, making the technology extremely resource-efficient. However, the most recent studies on laboratory scale CZTS solar cells have shown efficiencies just above 10% which is far behind the predicted theoretical limit of 28% for this type of material [8]. The possible factors limiting the performance are the presence of undesired phases in the composition of the CZTS absorber layer and defects at the interface of the device layers [9, 10]. The ability to observe at the nanoscale the influence of these defects on the local performance of a fully functional CZTS device can bring crucial information for understanding spatial correlations between charge-transport mechanism and defects in the structure of the device.

Synchrotron-based scanning X-ray microscopy is a powerful technique for spatially resolved high-resolution investigation of solar-cell materials [11, 12]. The high flexibility of beamlines to incorporate different modalities and the advancement of X-ray optics allow obtaining and uniquely correlating information about different properties of materials at the nanoscale [13–16]. Analytical techniques, such as X-ray fluorescence (XRF), X-ray diffraction, ptychography and X-ray beam induced current (XBIC) applied simultaneously can provide spatially correlated information between chemical composition and electrical properties of the specimen without destroying it [17–22]. However, such information is often not sufficient to understand limitations of energy-harvesting devices. The complex architecture of the new generation solar cells comprising multiple layers makes it hard to determine the fundamental mechanisms impacting electrical performance. First-principles modeling of the XBIC signal is required to obtain a deeper understanding of the correlations between material properties and the electrical performance of the device. Therefore, XBIC experiments on a semiconductor device combined with the modeling has been performed for a single nanowire with 1D numerical simulation carried out using Comsol Multiphysics software [23], and for a single-junction, CdTe/CdS solar cell with 2D drift-diffusion modeling [24, 25].

In this paper, we present the results of the multi-modal study of a CZTS solar cell in cross-section by employing combined measurements of scanning X-ray analytical techniques for a correlative investigation of structural, chemical and electrical properties of a fully functional device at the nanoscale. We support experimental data with the finite volume modeling of the XBIC signal by solving Poisson's equation and the continuity equations

---

[*] These two authors contributed equally
[†] Corresponding author: michael.stuckelberger@desy.de

for electrons and holes within the 2D computation domain constructed from the XRF data.

II. EXPERIMENTAL

A. CZTS solar cell preparation

The solar cell was obtained by deposition of a Mo bilayer on a soda-lime glass substrate before pulsed-laser deposition of CZTS precursors. For good adhesion to the substrate, the first 200 nm thick Mo layer was deposited under 1.3×10^{-2} mbar pressure. For a lower sheet resistance, the second 300 nm Mo layer was deposited under 3.9×10^{-3} mbar pressure. CZTS precursors were deposited under high vacuum (5×10^{-6} mbar) from a sintered target with overall CZTS stoichiometry (2.5 cm diameter, 2CuS:ZnS:SnS, Testbourne Ltd), resulting in an ultra-thin absorber layer (less than 450 nm). Annealing was performed at 560 °C. On top of the absorber layer, a 60 nm CdS buffer layer was deposited by chemical bath deposition. After that, a 50 nm intrinsic ZnO (i−ZnO) window layer and a 200 nm indium tin oxide (ITO) layer were sputtered by an RF magnetron, followed by 100 nm MgF anti-reflection coating. A more detailed description of the solar cell fabrication has been reported earlier [26].

A multi-modal study of a single device put constraints on the sample configuration. In contrast to the common approach of plane-view measurements, the measurements presented hereafter were taken on a cross-section following a similar experiment design as in reference [27]: XBIC and XRF measurements of a thin lamella in a cross-section of the sample allow observing the collection of charge carriers in the absorber layer on the one hand, and the elemental distribution on the other hand. A 1 µm thick lamella was chosen to match the approximate CZTS grain size determined from preliminary experiment on comparable devices [28, 29]. Furthermore, the thin sample cross-section allows X-rays to be transmitted and recorded in the far-field regime to derive differential phase contrast (DPC) using a pixel array detector [30].

The investigated CZTS thin-film solar cell was previously characterized by Raman spectroscopy, X-ray diffraction, time-resolved photoluminescence, 3D X-ray Diffraction [29] and resonant ptychographic tomography [28]. Fig. 1 (left) shows the device architecture alongside an SEM image of the sample (right) used in the experiment, consisting of a cross-section lamella of ca. 1 µm thickness derived from the solar cell using a focused ion beam (FIB) technique. The lamella was extracted from the best-performing subcell of a device that was sized on the order of 1 cm^2. The entire lamella was scanned, and a region containing both homogeneous and defective parts was selected for further analysis.

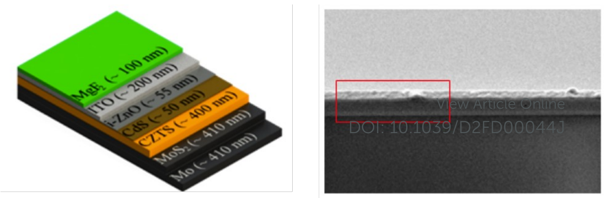

FIG. 1: Solar-cell device architecture (left) and SEM image (right) of the cross-section lamella used in the experiment. The red box indicates the area raster-scanned by the focused X-ray beam.

B. Analytical techniques

Upon irradiation with X-ray photons whose energy exceeds the electron-binding energy, core-level electrons are excited to a higher state or ejected. Excited atoms relax to the ground state by filling the resulting vacancies with electrons from one of the higher states. Such transitions are accompanied by the emission of fluorescent photons of energies that are characteristic of given types of atoms in the specimen. Two-dimensional maps of constituent elements can be derived by scanning the specimen and recording the energy of emitted fluorescent photons. The energy spectrum of fluorescent photons at every scanning position is composed of individual peaks directly related to the abundance of atoms of constituent elements [31].

The principle of XBIC is similar to that of electron beam induced current (EBIC) in a scanning electron microscope: a current-measuring device connected to the solar-cell electrodes evaluates the X-ray beam induced current. Excess carriers generated by the X-ray beam will diffuse inside the sample, with part of it reaching the edge of the space-charge region (SCR) of the p-n junction. The electric field inside the SCR separates electron-hole pairs that give rise to the photo-current in an external circuit. By scanning the X-ray beam, a two-dimensional map of collected photo-current in the device is constructed [11, 32, 33].

C. Measurements

The experiment was performed at the NanoMAX, a hard X-ray nanoprobe beamline of the MAX IV synchrotron facility in Lund, Sweden [14]. The measurements were carried out under ambient conditions with a 10.4 keV coherent monochromatic X-ray beam. The X-ray energy was chosen to yield fluorescent photons corresponding to K and L transitions of the elements constituting the sample. The beam was focused by Kirkpatrick-Baez (KB) mirrors to the spot size of 80 nm × 80 nm on the sample. A piezo stage was used to move the sample with 50 nm step size in the plane perpendicular to the beam propagation. An Amptek energy-dispersive fluorescence detector was placed 2 cm away from the sample

View Article Online
DOI: 10.1039/D2FD00044J

under approximately 30° relative to the scanning plane to collect fluorescence photons. A photon counting Dectris Pilatus 100k pixel-array detector was located 4 m downstream from the sample to record the diffraction signal of transmitted photons. An optical chopper was placed upstream of the sample to modulate the incident X-ray beam with a chopping frequency of 617 Hz. The P and N terminals of the solar cell were connected to the MFLI lock-in amplifier from Zurich Instruments.

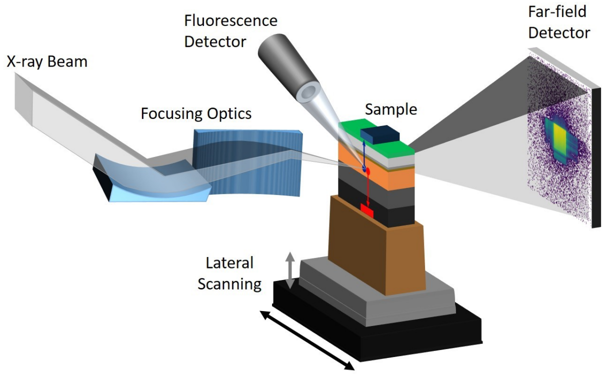

FIG. 2: Schematic of the experimental setup. Incoming X-rays are focused using KB-mirrors down to 80 nm × 80 nm. The sample is raster scanned in the lateral plane. A far-field detector measures the diffraction signal of the transmitted beam, and an energy-dispersive fluorescence detector collects fluorescence photons. The X-ray beam induced current in the semiconductor device is amplified and measured at every scan position.

III. NUMERICAL MODELING

In this work, a 2D computation domain was generated from the XRF data, and a 2D finite-volume numerical simulation approach was used. In conjunction with the continuity equations for electrons and holes coupled with a Monte Carlo (MC) simulation for the X-ray/material interaction, Poisson's equation was solved to simulate the XBIC experiment. Simulations were performed on a regular grid defined from the measurements step size (50 nm) and taking into account a beam limited to one point. These simplifications were made to be as close as possible to the experiment assuming that the physical processes included in the numerical model were more relevant than the real intensity profile of the experimental beam, the consideration of which would have been beyond the scope of this work.

A. Electron-hole-pair generation from X-ray beam

X-ray propagation and interaction with matter are often described using analytical models. This approach might not be sufficient for modeling complex phenomena, and Monte Carlo-based numerical simulations might be more suitable. In general, a Monte Carlo simulation employs known probability distributions of various interactions of X-ray photons with matter to model their propagation within the interaction volume and associated change of their state. We utilized a personalized version of Penelope [34], to simulate the generation of electron-hole pairs in the multi-layered solar cell upon the incidence of the pencil X-ray beam. The resulting profiles of the generation rate G were then used in the modeling of the XBIC signal.

B. Numerical model

The basic equations to be solved in modeling semiconductor devices are Poisson's equation and the electrons and holes continuity equation. In steady state, they are expressed as

$$\nabla \cdot (\varepsilon_r \varepsilon_0 \nabla \psi) = q(n - p + N_{\mathrm{A}} - N_{\mathrm{D}}), \tag{1}$$

$$\nabla \cdot J_n = -q(G - R), \tag{2}$$

$$\nabla \cdot J_p = q(G - R), \tag{3}$$

where ε_r, ε_0 denote the relative and vacuum permittivity, ψ the electrostatic potential, q the elementary charge, n, p the electron and hole densities, N_{A}, N_{D} the ionized acceptor and donor densities, and J_n, J_p the electron- and hole-current densities. The Shockley-Read-Hall recombination rate R is given by

$$R = \frac{np - n_{\mathrm{i}}^2}{\tau_p (n + n_{\mathrm{t}}) + \tau_n (p + p_{\mathrm{t}})}, \tag{4}$$

where n_{i} is the intrinsic carrier density, τ_p, τ_n are the hole and electron lifetimes, and n_{t}, p_{t} are the electron and hole concentrations when the quasi Fermi-level matches the trap energy. Using the drift-diffusion model, we expressed the current densities as

$$J_n = q\mu_n \left(-n \nabla \psi_n + V_{\mathrm{T}} \nabla n\right), \tag{5}$$

$$J_p = q\mu_p \left(-p \nabla \psi_p - V_{\mathrm{T}} \nabla p\right), \tag{6}$$

where μ_n, μ_p are the electron and hole mobilities, $\psi_n = q\psi + \dfrac{\chi}{q} + V_{\mathrm{T}} \ln N_{\mathrm{C}}$, $\psi_p = q\psi + \dfrac{\chi}{q} + \dfrac{E_{\mathrm{g}}}{q} + V_{\mathrm{T}} \ln N_{\mathrm{V}}$ are the effective potentials for electrons and holes, χ is the electron affinity, E_{g} is the energy gap, N_{C}, N_{V} are the effective densities of state in the conduction and valence bands, and $V_{\mathrm{T}} = \dfrac{kT}{q}$ is the thermal potential with the Boltzmann constant k and the temperature T. In equations (5) and (6), we used the so-called Einstein relation [35]. Moreover, since we assumed having only non-degenerate semiconductors, the Boltzmann approximations were used in our simulations to compute the density of carriers as follows:

$$n = N_{\mathrm{C}} \exp\left(\frac{q\psi + \chi - q\varphi_n}{kT}\right), \tag{7}$$

$$p = N_{\mathrm{V}} \exp\left(\frac{q\varphi_p - q\psi - \chi - E_{\mathrm{g}}}{kT}\right), \tag{8}$$

where φ_n and φ_p are the quasi-Fermi potentials for electrons and holes, respectively.

The choice of boundary conditions will effect the solution of the set of partial differential equations. In our simulations, we considered two types of contacts: Ohmic and Schottky contacts. For ideal Ohmic contacts, the space charge vanishes at the contact and the interface recombination velocities for electrons and holes (S_n, S_p) are assumed to be infinite. This will impose the Dirichlet boundary conditions for n and p at the contact. The Dirichlet boundary conditions for the electrostatic potential at Ohmic contacts is given by the sum of the externally applied bias V_0 and the built-in potential ψ_{bi}. The physics of Schottky contacts is complex and we used simplified models. We assumed that the Fermi level in the semiconductor is lined up with the Fermi level of the metal and that the electrostatic potential at the boundary is proportional to the electron barrier height Φ_{B_n}. The carrier concentrations at Schottky contacts depend in general on the current density at the contact, which implies that they depend on S_n, S_p, and Φ_{B_n}.

Due to the different orders of magnitude of the dependent variables (ψ, n, p) and to avoid numerical overflow, rewriting the equations in dimensionless form is necessary. The scaling factors used in the simulations are summarized in Tab. I.

Quantity	Expression	Value
Concentrations	M_0	10^{25} m^{-3}
Potentials	$V_t = \dfrac{kT}{q}$	0.02585 V
Length	$l = \sqrt{\dfrac{\epsilon_0 kT}{q^2 M_0}}$	3.78×10^{-10} m
Energy	kT	0.02585 eV
Mobility	μ_0	10^{-4} m^2 V^{-1} s^{-1}
Time	$\dfrac{l^2}{\mu_0 V_t}$	5.53×10^{-14} s
Gen., Rec. rates	$\dfrac{V_t M_0 \mu_0}{l^2}$	1.81×10^{38} m^{-3} s^{-1}
Current density	$-\dfrac{kT M_0 \mu_0}{l}$	1.10×10^{10} A m^{-2}
Velocity	$\dfrac{\mu_0 V_t}{l}$	6.84×10^{3} m s^{-1}

TABLE I: Quantities used to scale variables to dimensionless form.

The finite volume method was used to discretize the linearized Poisson's equation and the continuity equations. A suitable approximation for the current expressions using the Scharfetter Gummel scheme [36] was implemented. The derived coupled nonlinear system was solved using Gummel's algorithm [37]. Current densities were calculated from the resulting solution, and the total current (XBIC signal) was calculated by integrating the local current density over the contact.

IV. RESULTS AND DISCUSSION

A. Experimental results

Fig. 3 shows XRF images of elements constituting the sample and the corresponding XBIC signal. As measurements were performed simultaneously, no registration of XRF and XBIC images is necessary and per pixel based correlation between images can be performed. The most prominent compositional inhomogeneities within the CZTS layer are highlighted in the images with white arrows. They are associated with relatively lower projected densities of all elements composing the layer (except for S and Mo, which could not be reliably differentiated from each other [38]). This can be attributed to reduced thickness due to sample preparation or voids between CZTS grains filled with CdS [28]. Both factors will result in reduced charge-collection efficiency that is correlated with the relative decrease of the XBIC signal in these regions. A more notable area with inhomogeneous chemical composition is marked with the white box. The corresponding area in the XRF image of Cd indicates CdS precipitates resulting from the chemical bath deposition. It is, however, unclear whether the CdS precipitate resulted in the absence of the ZnO layer deposited on top. Regardless, the XRF images of In and Sn show a variation in composition of elements constituting the ITO layer that follows the topology of the CdS precipitate. Overall, the XBIC image in the area below the white box shows a decreased current associated with the electronic defects caused by the disturbed layer structure.

B. Construction of the computation domain

Individual XRF maps of elements constituting the CZTS sample under consideration were used to construct the computational domain. Image pixels were assigned to one of the materials according to the nominal architecture of the device presented in Fig. 1. From the XRF data, the geometry had been obtained through the following process: We started from the bottom of the image: Mo will correspond to the pixels having an intensity in

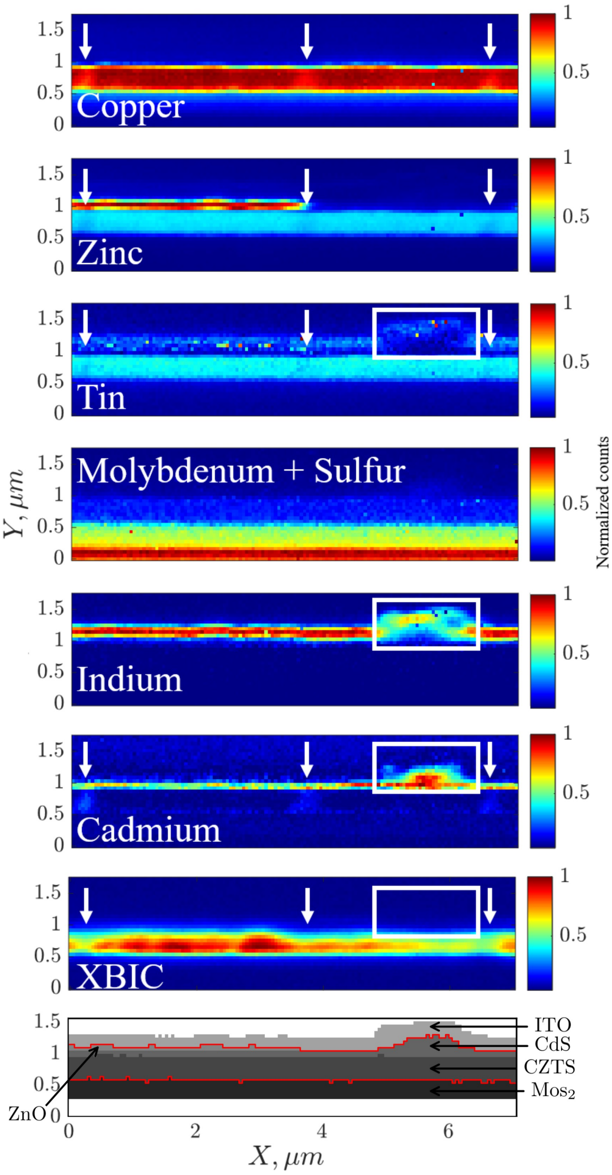

FIG. 3: XRF images of the main elements constituting the sample together with the XBIC signal resulting in the specification of the layered structure with the computation domain between red lines. The white arrows highlight the areas associated with composition variations in the CZTS layer and the white box indicates the area with inhomogeneous distribution of elements from CdS and ITO layers, as well as the absence of the ZnO layer.

the MoS image larger than ξ_1, MoS_2 to the pixels not yet defined and having an intensity in the MoS image larger than ξ_2, CZTS to the pixels not yet defined and having an intensity in the Cu image larger than ξ_3, CdS to the pixels not yet defined and having an intensity in the Cd image larger than ξ_4, etc. The threshold values ξ_i were selected manually by combining the six chemical images and examining the interfaces between the different layers. After cleaning the geometry defined from the chemical data, we obtained the grey level image shown as the lowest panel of Fig. 3. The correlation with the ptychographic reconstruction of the phase contrast from far-field diffraction data corroborate the segmentation. At the lower part of the sample, the MoS_2 layer was considered as the electrode, and the boundary condition was applied at the interface with the CZTS layer. At the upper part, the ITO layer was considered as the electrode, and the boundary condition was applied at the interface with the ZnO and CdS layers. The resulting computation domain was then composed of the three layers encompassed by a red line in Fig. 3. On the lateral boundaries, we imposed periodicity, and on the upper and lower boundaries, electrical contact with the electrodes.

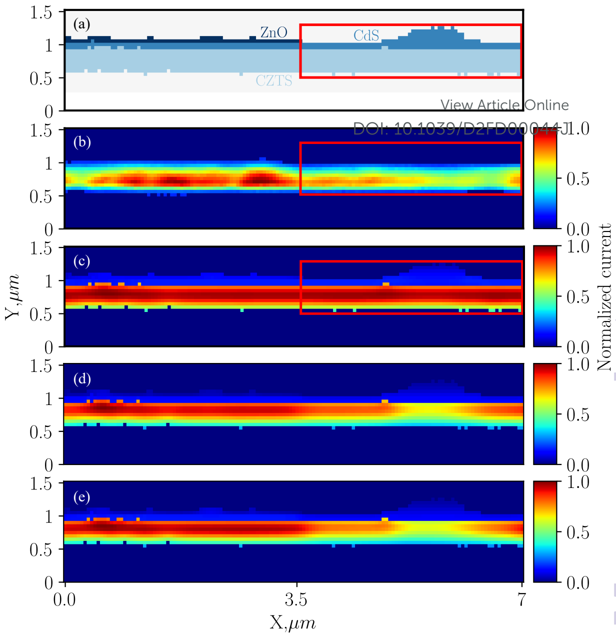

FIG. 4: (a) The computation domain based on the XRF measurements shown in Fig. 3, (b) the experimental results, and simulation results from applying Ohmic boundary conditions (c), ideal Schottky contact boundary conditions with the material parameters listed in Tab. II (d), and Schottky contact boundary conditions with work function equal to 5.3 eV for the MoS_2 layer and barrier height equal to 0.5 eV at the CdS contact (e).

C. 2D Simulations

The computation domain shown in Fig. 4(a) is discretized into 1435 computation cells with 50 nm × 50 nm

View Article Online
DOI: 10.1039/D2FD00044J

Parameter	Description	Unit	CZTS	CdS	ZnO
N_C	Effective density of state in conduction band	m^{-3}	2.2×10^{24}	2.2×10^{24}	2.2×10^{24}
N_V	Effective density of state in valence band	m^{-3}	1.8×10^{25}	1.8×10^{25}	1.8×10^{25}
E_g	Energy gap	eV	1.4	2.4	3.3
χ	Electron affinity	eV	4.7	4.5	4.5
ε_r	Relative permittivity	–	10	10	9
μ_n	Electron mobility	$\mathrm{m}^2\mathrm{V}^{-1}\mathrm{s}^{-1}$	10^{-2}	10^{-2}	10^{-2}
μ_p	Hole mobility	$\mathrm{m}^2\mathrm{V}^{-1}\mathrm{s}^{-1}$	2.5×10^{-3}	2.5×10^{-3}	2.5×10^{-3}
τ_n	Electron lifetime	s	2×10^{-8}	10^{-12}	10^{-12}
τ_p	Hole lifetime	s	10^{-5}	5×10^{-13}	10^{-7}
N_D	Ionized donor density	m^{-3}	0	10^{22}	10^{23}
N_A	Ionized acceptor density	m^{-3}	3×10^{22}	0	0
S_n	Interface recombination velocities for electron	ms^{-1}	10^5	10^5	10^5
S_p	Interface recombination velocities for hole	ms^{-1}	10^5	10^5	10^5
Φ_{B_p}/Φ_{B_n}	Electrons barrier height	eV	-1.2	0.2	0.2

TABLE II: Material parameters used for the 2D simulation reference.

size, equivalent to the measurement grid. For each cell, a generation profile was derived from the Monte-Carlo simulation of a pencil beam with an energy of 10.4 keV interacting with the material associated with each layer. The continuity equations, along with Poisson's equation were solved for the entire domain for each generation profile, and the resulting total current was stored to construct a 2D map of the XBIC signal. Two types of boundary conditions are considered: Ohmic and Schottky contacts. At an Ohmic contact we assume a perfect contact, meaning that there is nothing blocking the carriers from one material to another. Fig. 4(c) shows the result of applying Ohmic boundary conditions. From Fig. 4(b) we can clearly see the effect of the lacking ZnO layer at the right-hand side of the domain (red box) on the experimental data, which is not the case for the simulation results in Fig. 4(c).

At a Schottky contact we assumed having a potential barrier formed at the interface that impedes the transfer of carriers from one material to another. The barrier height of an ideal Schottky contact for an n-type semiconductor is given by the difference between the contact work function and the electron affinity as follows:

$$\Phi_{B_n} = \phi_M - \chi, \tag{9}$$

and for a p-type semiconductor the barrier height is given by the difference between the contact work function, the electron affinity and the energy gap as follows:

$$\Phi_{B_p} = \phi_M - \chi - E_\mathrm{g}. \tag{10}$$

After trying different combinations of Ohmic and Schottky boundary conditions, we chose to apply the Schottky boundary condition at the top of ZnO or CdS, and at the bottom of the CZTS region. At the front contact (top of ZnO or CdS) we have an ITO layer with work function $\phi_M = 4.7\,\mathrm{eV}$ [39], and at the back contact (bottom of CZTS) we have a MoS_2 layer. Estimating the work function of MoS_2 is challenging and we first used the value $\phi_M = 5\,\mathrm{eV}$ in our simulation which is approximately equal to the work function of Mo [40]. The material parameters for each layer used in the simulation are listed in Tab. II. These parameters were taken from the literature [41–44]. Fig. 4(d) shows the simulation results when applying ideal Schottky contact boundary conditions. We start seeing the effect of the lacking ZnO layer on the simulation results on the right-hand side of the domain. In order to match the experimental results, we did a 2D sensitivity analysis to study the effect of the barrier height at the contact on the simulation results.

D. 2D sensitivity analysis

In the 2D sensitivity analysis, the results presented in Fig. 4(d) are used as a simulation reference. We studied the effect of the barrier height at the top contact of CdS and at the bottom contact of CZTS.

According to [39], ITO forms an ideal Schottky contact to ZnO. From Fig. 3, in the white box, we can see inhomogeneities in the distribution of the elements forming the ITO layer (indium and tin). Therefore, the assumption of an ideal Schottky contact with the CdS layer is an oversimplification as it neglects the existence of surface and interface states. Moreover, Dharmadasa

View Article Online
DOI: 10.1039/D2FD00044J

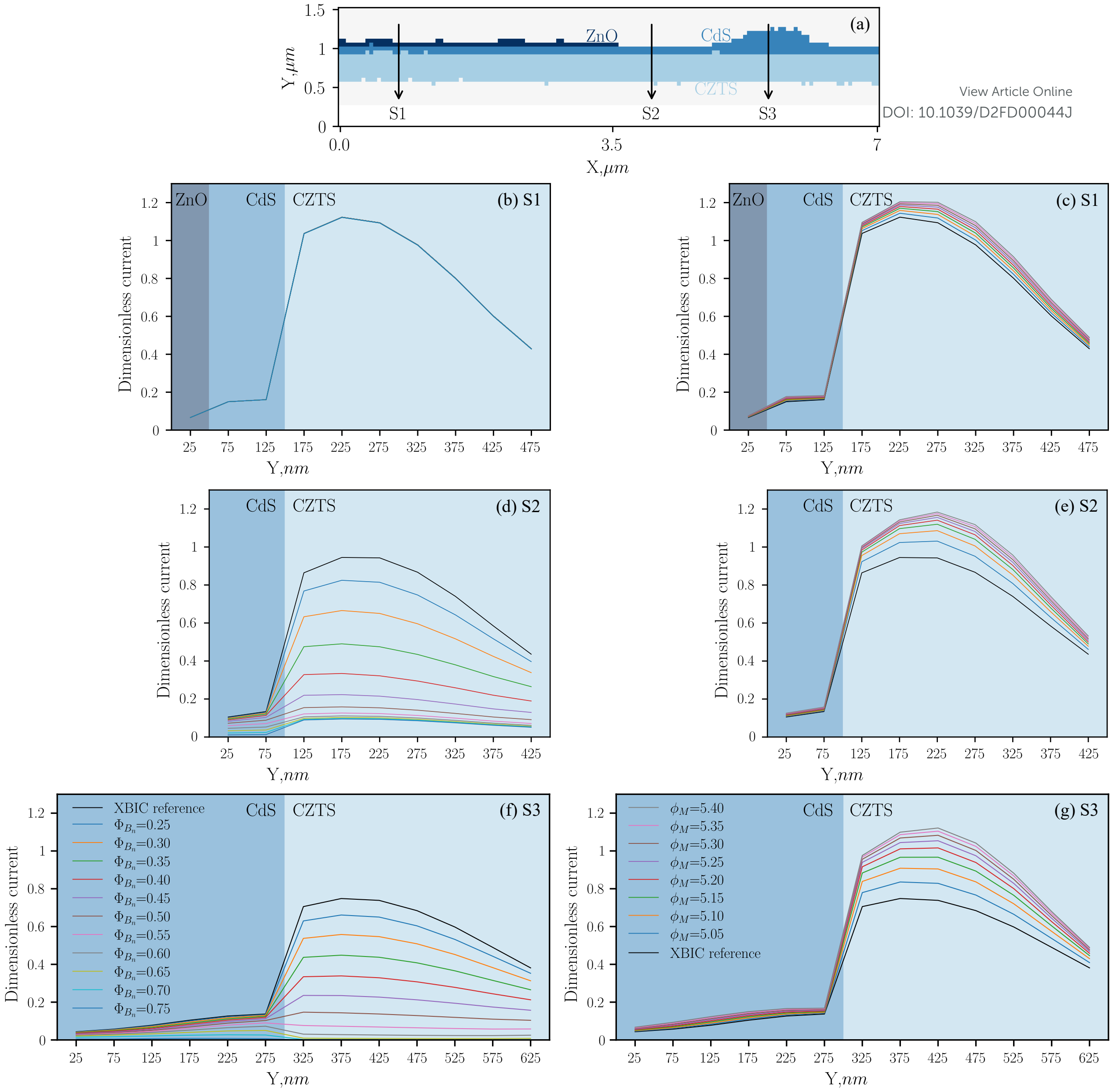

FIG. 5: (a) The computation domain with three distinct layer configurations S1, S2 and S3. (b–g) The 2D sensitivity analysis was done using the material parameters listed in Tab. II. The effects of changing the barrier height Φ_{B_n} at the CdS contact along S1, S2 and S3 are shown in (b,d,f), and the effects of changing the work function ϕ_M of MoS_2 along S1, S2 and S3 in (c,e,g), respectively. The legends displayed in (f) and (g) refer to (b,d,f) and (c,e,g), respectively. All curves overlap in (b).

[45] reported that the Schottky barrier formation at the CdS contact is found to be governed by Fermi level pinning, depending on the contact and the fabrication process rather than on the work function of the contact. At the bottom contact of CZTS, the work function of MoS_2 is varying from 5.15 eV to 5.39 eV depending on the thickness of the layer [46].

Three different layer configurations are used to present the 2D sensitivity analysis as line profiles. These configurations, noted S1, S2 and S3, are localized in Fig. 5(a). In S1 we have the complete layer structure ZnO/CdS/CZTS, in S2 and S3 the ZnO layer is missing, and S3 is on the CdS defect. The effects of changing the barrier height from 0.25 eV to 0.75 eV at the CdS

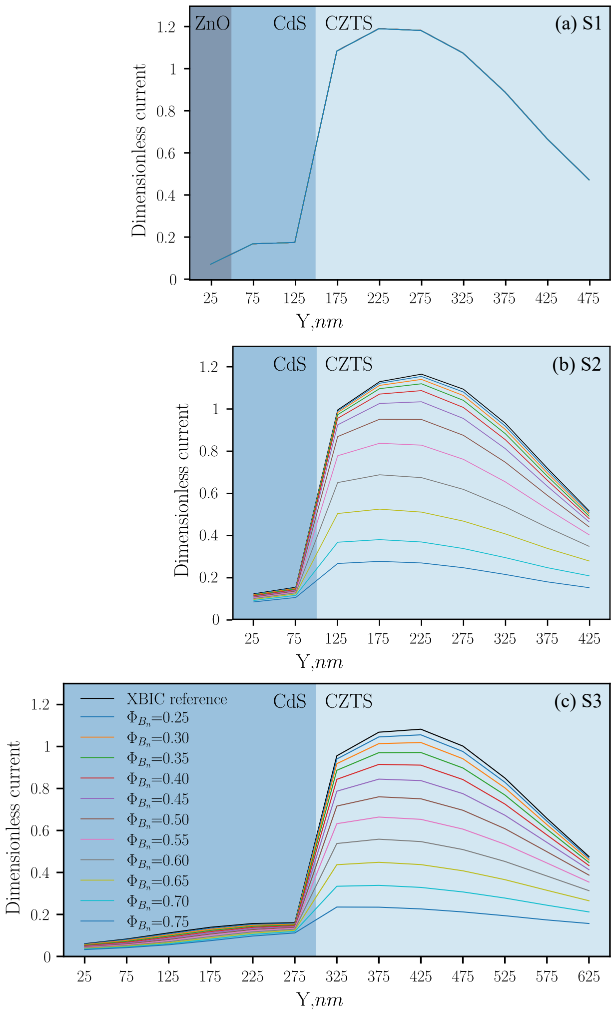

FIG. 6: The 2D sensitivity analysis was performed with the updated simulation reference to evaluate the effects of changing the barrier height at the CdS contact along S1 (a), S2 (b), and S3 (c). The legend displayed in panel (c) refers to all panels. All curves overlap in panel (a).

contact are presented in Fig. 5(b,d,f) along S1, S2 and S3, respectively. Along S1 changing the barrier height at the CdS contact has no effect on the XBIC signal. On the other hand, increasing the barrier height at the CdS contact is decreasing the XBIC signal along S2 and S3. The presence of the ZnO layer with barrier height equal to 0.2 eV is essential for the performance of the device under consideration.

Figures 5(c,e,g) show the effects of changing the work function of MoS_2 from 5.05 eV to 5.4 eV on the XBIC signal along S1, S2 and S3, respectively. The XBIC peak in the CZTS layer shifts upwards with increasing the work function of MoS_2 along S1, S2 and S3. Therefore, the presence of the interfacial MoS_2 layer with a work function higher than the one in Mo is beneficial for the performance of the device under consideration. This result is in good agreement with the result of [47], and in [40] they found similar behaviour for CZTSe devices.

From Fig. 5 we see clearly that increasing the barrier height for electrons at the CdS contact will reduce the XBIC peak at the right-hand side of the domain. Moreover, decreasing the barrier height for holes by increasing the work function of MoS_2 will increase the XBIC peak for the entire domain. These two parameters need to be tuned in order to match the experimental results. With a thickness around 400 nm the work function of MoS_2 will equal approximately 5.3 eV [46]. We updated our XBIC simulation reference with this value and restudied the effects of changing the barrier height at the CdS contact (see Fig. 6) and found the same trend as in Fig. 5.

From Fig. 6 we chose the value of 0.5 eV as the barrier height at the CdS contact to generate the simulation results illustrated in Fig. 4(e). This value was found to have the best match to the experimental results and to reproduce the effect of the absence of the ZnO layer at the right-hand side of the domain. This suggests that the XBIC loss at the red box in Fig. 4(b) was caused by the high barrier height at the CdS contact and the losses increase with the electronic defects in the white box in Fig. 3.

E. Analysis

Figure 7(a) shows the computation domain with the positions at which we chose to analyse the experimental and simulation results. P1 represents the white arrow in Fig. 3 where we have inhomogeneities within the CZTS layer. P2 indicates the region where we have the maximum XBIC signal. In P3 and P4 the ZnO layer is missing, and P4 is on the CdS defect.

Figures 7(b–d) represent the line profiles from the experimental and simulation results along P1, P2, P3 and P4, respectively. From these figures we can observe that the experimental XBIC peak is almost at the center of the absorber layer (CZTS), while in the simulation result, the XBIC peak is shifted towards the CZTS/CdS interface. In spite of that, we can see a good agreement between the experimental and simulation results in the absorber layer. In general, it is very hard to avoid the presence of the secondary phases in CZTS based solar cells [9], and the experimental peak shift might be due to the presence of such a phase near the heterointerface. Due to the experiment's resolution limitations and 2D configuration it was difficult to deduce such a phase from the XRF data in our sample. Moreover, we can see a sharp loss of the charge collection (XBIC signal) in the simulation results near the heterointerface. One reason for that is the limited accuracy of the interface definition: construction of the domain from the XRF data is challenging due to the experimental resolution, and the spread of hot and thermalized charge carriers between the layers is not accounted for. Furthermore, a simple model at the het-

View Article Online
DOI: 10.1039/D2FD00044J

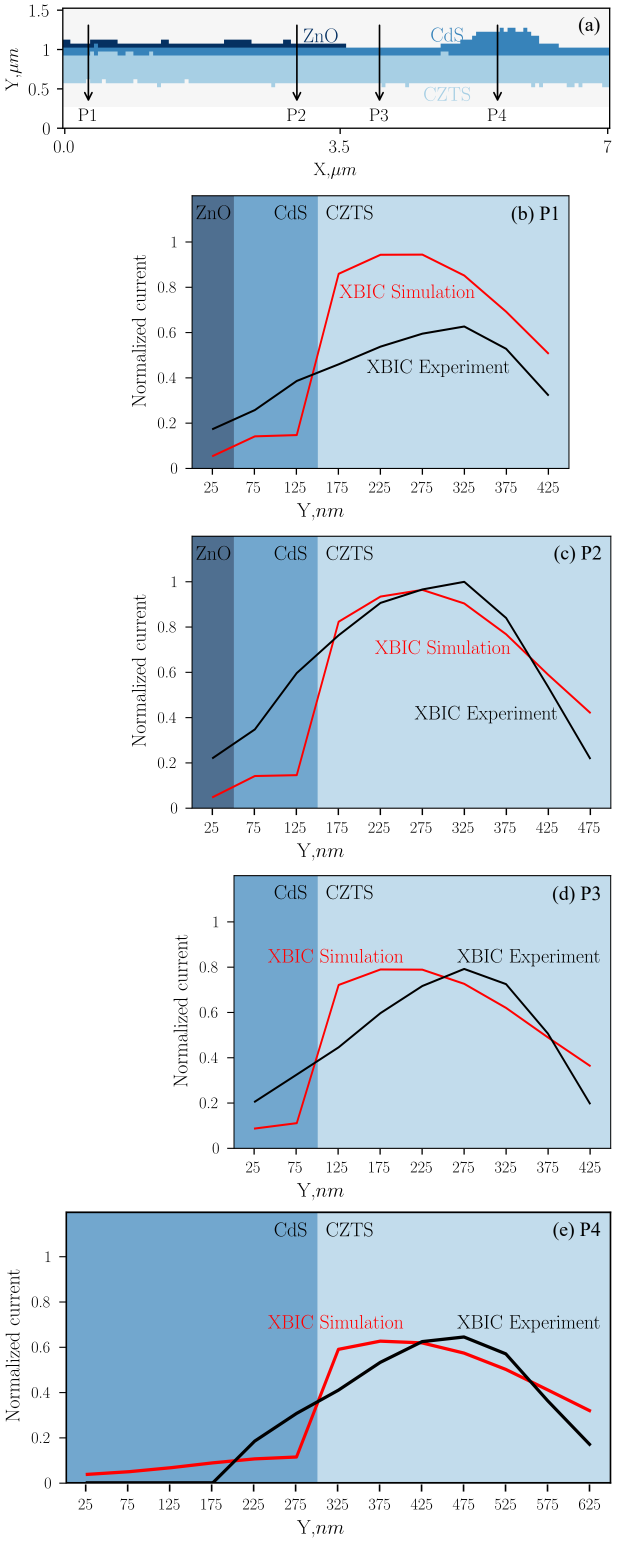

FIG. 7: The computation domain (a) with the location of line profiles from the experimental and simulated data along P1, P2, P3 and P4 shown in (b–e).

erointerface was used in our simulation considering the effective potentials for electrons and holes.

With the assumptions that ITO is an ideal Schottky contact to ZnO layer with a barrier height equal to 0.2 eV, and a barrier height equal to 0.5 eV at the CdS/ITO interface, we were able to simulate the effect of the absence of the ZnO layer on the right-hand side of the domain, see Fig. 6(c). The results of Fig. 6(c–d) show that increasing the CdS thickness will increase the charge-carrier loss in the absorber layer.

In our simulation, we assumed homogeneous layers with constant parameters. From Fig. 7(b), we can see a lower current in the experimental result than the simulation. This is related to the fact that P1 is lying in one of the regions with an inhomogeneous distribution of the absorber layer contents. We can see the correlation between the diffusion of Cd in the absorber layer and the XBIC signal highlighted by white arrows in Fig. 3.

V. CONCLUSIONS

Correlative scanning X-ray microscopy is a powerful tool for *in situ* and *operando* studies of functional materials such as solar cells, providing a spatially-resolved correlative characterization of the chemical composition and electrical performance at the nanoscale. From the analysis of the acquired data from different modalities, we see a significant potential of applying correlative scanning X-ray microscopy to new generations of solar cells. XRF maps allow us to visualize inhomogeneities in all the device layers and correlate them with local charge conversion efficiency obtained from XBIC measurements.

The conventional approach of modeling the performance of solar cells considers the nominal architecture of the device. However, structural variations resulting, e.g., from the inhomogeneous deposition of layers during fabrication, as well as various defects occurring in real devices are not considered. We presented a framework in which material parameters can be associated with the local electrical performance based on the actual structure of the device. The framework consists of constructing a computational domain from X-ray fluorescence data (and phase-contrast images, if needed) used for first-principles modeling of the XBIC signal. The model can then be used to interpret some aspects of the experimentally measured XBIC signal. Our approach shows that electronic defects can be identified by XBIC, correlated with compositional and structural inhomogeneities from XRF and phase contrast, and explained by simulations.

To address some limitations of the current implementation, new developments will be required: The recorded data from a 2D projection of a micron-thick cross-section lamella does not allow the unambiguous assignment of chemical and morphological inhomogeneities on the scale of grains and grain boundaries. To achieve this, the data will have to be extended to 3D by tomographic acquisition and accompanying extension of the model to 3D.

This is not trivial because of the added experimental complexity and because neither XRF or XBIC signals are simple line integrals of the beam path. However, it is feasible to mill out a pillar that is a functional solar cell [48] and have it electrically connected during 3D scanning microscopy measurements [49, 50]. Algebraic iterative reconstruction algorithms may be applied to reconstruct the volumetric response of a non-linear beam-matter interaction [51, 52]. To realize a better representation of the typically nano-structured 3^{rd} generation solar-cell devices, some more challenging requirements should ideally be met: the material properties need to be determined at the scale of the measurements and model, as they cannot be assumed to be representative of homogeneous materials. Furthermore, our simplistic approach includes Monte Carlo simulations for each material separately, which will necessarily lead to incorrect generation profiles at interfaces. We hope that these considerations will stimulate a constructive discussion on how to best overcome the challenges to make optimum use of the boosted brilliance at next-generation storage rings [53].

CREDIT AUTHORSHIP CONTRIBUTION STATEMENT

Abdellatif Saadaldin: Formal Analysis, Methodology, Software, Validation, Visualization, Writing – original draft, Writing – review & editing. **Azat M. Slyamov:** Investigation, Methodology, Validation, Visualization, Writing – original draft. **Michael E. Stuckelberger:** Conceptualization, Formal Analysis, Funding acquisition, Investigation, Methodology, Project administration, Supervision, Validation, Visualization, Writing – original draft, Writing – review & editing. **Peter S. Jørgensen:** Investigation, Methodology. **Christian Rein:** Investigation. **Mariana Mar Lucas:** Investigation. **Tiago Ramos:** Investigation. **Angel Rodriguez-Fernandez:** Investigation. **Dominique Bernard:** Conceptualization, Formal Analysis, Funding acquisition, Methodology, Project administration, Supervision, Validation, Visualization, Writing – original draft, Writing – review & editing. **Jens W. Andreasen:** Conceptualization, Formal Analysis, Funding acquisition, Investigation, Methodology, Project administration, Supervision, Validation, Visualization, Writing – original draft, Writing – review & editing.

ACKNOWLEDGEMENT

The authors acknowledge the staff of NanoMAX, hard X-ray nanoprobe beamline of the MAX IV synchrotron facility, for support with the multi-modal scanning nanoprobe experiment. Stela Canulescu, Sara Engberg, Andrea Crovetto, and Prof. Jørgen Schou are acknowledged for providing the investigated solar cell. This study was funded by EU Horizon 2020 Marie Skłodowska-Curie Actions Innovative Training Network: MUltiscale, Multimodal and Multidimensional imaging for EngineeRING (MUMMERING), Grant No. 765604. The research leading to these results has received funding from Deutsches Elektronen-Synchrotron DESY.

[1] P. A. Owusu and S. Asumadu-Sarkodie, A review of renewable energy sources, sustainability issues and climate change mitigation, Cogent Engineering **3**, 10.1080/23311916.2016.1167990 (2016).
[2] M. Z. Jacobson and M. A. Delucchi, Providing all global energy with wind, water, and solar power, Part I: Technologies, energy resources, quantities and areas of infrastructure, and materials, Energy Policy **39**, 1154 (2011).
[3] M. A. Delucchi and M. Z. Jacobson, Providing all global energy with wind, water, and solar power, Part II: Reliability, system and transmission costs, and policies, Energy Policy **39**, 1170 (2011).
[4] B. G. Gribov and K. V. Zinov'ev, Preparation of high-purity silicon for solar cells (2003).
[5] C. Battaglia, A. Cuevas, and S. De Wolf, High-efficiency crystalline silicon solar cells: status and perspectives, Energy & Environmental Science **9**, 1552 (2016).
[6] L. C. Andreani, A. Bozzola, P. Kowalczewski, M. Liscidini, and L. Redorici, Silicon solar cells: toward the efficiency limits, Advances in Physics: X **4**, 1548305 (2019).
[7] L. El Chaar, L. A. Lamont, and N. El Zein, Review of photovoltaic technologies (2011).
[8] M. Green, E. Dunlop, J. Hohl-Ebinger, M. Yoshita, N. Kopidakis, and X. Hao, Solar cell efficiency tables (version 57), Progress in photovoltaics: research and applications **29**, 3 (2021).
[9] T. J. Huang, X. Yin, G. Qi, and H. Gong, CZTS-based materials and interfaces and their effects on the performance of thin film solar cells, physica status solidi (RRL)–Rapid Research Letters **8**, 735 (2014).
[10] M. Kumar, A. Dubey, N. Adhikari, S. Venkatesan, and Q. Qiao, Strategic review of secondary phases, defects and defect-complexes in kesterite CZTS–Se solar cells, Energy & Environmental Science **8**, 3134 (2015).
[11] M. Stuckelberger, B. West, T. Nietzold, B. Lai, J. M. Maser, V. Rose, and M. I. Bertoni, Review: Engineering solar cells based on correlative X-ray microscopy, Journal of Materials Research **32**, 1825 (2017).
[12] M. E. Stuckelberger, T. Nietzold, B. West, R. Farshchi, D. Poplavskyy, J. Bailey, B. Lai, J. M. Maser, and M. I. Bertoni, Defect activation and annihilation in CIGS solar cells: an operando x-ray microscopy study, J. Phys.: Energy **2**, 25001 (2020).
[13] R. P. Winarski, M. V. Holt, V. Rose, P. Fuesz, D. Carbaugh, C. Benson, D. Shu, D. Kline, G. Brian Stephenson, I. McNulty, and J. Maser, A hard X-ray nanoprobe beamline for nanoscale microscopy, Journal of Synchrotron Radiation **19**, 1056 (2012).

[14] U. Johansson, U. Vogt, and A. Mikkelsen, Nanomax: a hard x-ray nanoprobe beamline at max iv, in *X-Ray Nanoimaging: Instruments and Methods*, Vol. 8851 (International Society for Optics and Photonics, 2013) p. 88510L.

[15] G. Martínez-Criado, J. Villanova, R. Tucoulou, D. Salomon, J.-P. Suuronen, S. Labouré, C. Guilloud, V. Valls, R. Barrett, E. Gagliardini, *et al.*, Id16b: a hard x-ray nanoprobe beamline at the esrf for nano-analysis, Journal of synchrotron radiation **23**, 344 (2016).

[16] A. Schropp, R. Döhrmann, S. Botta, D. Brückner, M. Kahnt, M. Lyubomirskiy, C. Ossig, M. Scholz, M. Seyrich, M. E. Stuckelberger, *et al.*, Ptynami: ptychographic nano-analytical microscope, Journal of applied crystallography **53**, 957 (2020).

[17] M. Trushin, O. Vyvenko, W. Seifert, M. Kittler, I. Zizak, A. Erko, M. Seibt, and C. Rudolf, Combined XBIC/μ-XRF/μ-XAS/DLTS investigation of chemical character and electrical properties of Cu and Ni precipitates in silicon, in *Physica Status Solidi (C) Current Topics in Solid State Physics*, Vol. 6 (2009) pp. 1868–1873.

[18] C. Ossig, T. Nietzold, B. West, M. Bertoni, G. Falkenberg, C. G. Schroer, and M. E. Stuckelberger, X-ray Beam Induced Current Measurements for Multi-Modal X-ray Microscopy of Solar Cells, Journal of Visualized Experiments **2019**, 10.3791/60001 (2019).

[19] A. Ulvestad, S. O. Hruszkewycz, M. V. Holt, M. O. Hill, I. Calvo-Almazán, S. Maddali, X. Huang, H. Yan, E. Nazaretski, Y. S. Chu, L. J. Lauhon, N. Rodkey, M. I. Bertoni, and M. E. Stuckelberger, Multimodal x-ray imaging of grain-level properties and performance in a polycrystalline solar cell, Journal of Synchrotron Radiation **26**, 1316 (2019).

[20] I. Calvo-Almazán, A. P. Ulvestad, E. Colegrove, T. Ablekim, M. V. Holt, M. O. Hill, S. Maddali, L. J. Lauhon, M. I. Bertoni, X. Huang, H. Yan, E. Nazaretski, Y. S. Chu, S. O. Hruszkewycz, and M. E. Stuckelberger, Strain mapping of CdTe grains in photovoltaic devices, IEEE Journal of Photovoltaics **9**, 1790 (2019).

[21] C. Ossig, C. Strelow, J. Flügge, A. Kolditz, J. Siebels, J. Garrevoet, K. Spiers, M. Seyrich, D. Brückner, N. Pyrlik, J. Hagemann, F. Seiboth, A. Schropp, R. Carron, G. Falkenberg, A. Mews, C. G. Schroer, T. Kipp, and M. E. Stuckelberger, Multi-modal X-ray microscopy measurements of a Cu(In,Ga)Se$_2$ solar cell, Materials **14**, 228 (2021).

[22] C. Ossig, C. Strelow, J. Flügge, A. Kolditz, J. Siebels, J. Garrevoet, K. Spiers, M. Seyrich, D. Brückner, N. Pyrlik, *et al.*, Four-fold multi-modal x-ray microscopy measurements of a cu (in, ga) se2 solar cell, Materials **14**, 228 (2021).

[23] L. Chayanun, G. Otnes, A. Troian, S. Hammarberg, D. Salomon, M. T. Borgström, and J. Wallentin, Nanoscale mapping of carrier collection in single nanowire solar cells using X-ray beam induced current, Journal of Synchrotron Radiation **26**, 102 (2019).

[24] N. M. Kumar, A. R. Shaik, T. Walker, T. Nietzold, B. Lai, E. Colegrove, M. Stuckelberger, and M. Bertoni, Mapping current collection in cross section: The case of copper- doped cdte solar cells, in *2020 47th IEEE Photovoltaic Specialists Conference (PVSC)* (2020) pp. 2178–2180.

[25] T. Walker, M. E. Stuckelberger, T. Nietzold, N. Mohan-Kumar, C. Ossig, M. Kahnt, F. Wittwer, B. Lai, D. Salomon, E. Colegrove, and M. I. Bertoni, The nanoscale distribution of copper and its influence on charge collection in CdTe solar cells, Nano Energy **91**, 106595 (2022).

[26] A. Cazzaniga, A. Crovetto, C. Yan, K. Sun, X. Hao, J. Ramis Estelrich, S. Canulescu, E. Stamate, N. Pryds, O. Hansen, and J. Schou, Ultra-thin Cu2ZnSnS4 solar cell by pulsed laser deposition, Solar Energy Materials and Solar Cells **166**, 91 (2017).

[27] M. Stuckelberger, B. West, S. Husein, H. Guthrey, M. Al-Jassim, R. Chakraborty, T. Buonassisi, J. M. Maser, B. Lai, B. Stripe, V. Rose, and M. Bertoni, Latest developments in the x-ray based characterization of thin-film solar cells, Proc. Photovoltaic Specialist Conference (PVSC) , 1 (2015).

[28] G. Fevola, P. S. Jørgensen, M. Verezhak, A. Slyamov, A. Crovetto, Z. I. Balogh, C. Rein, S. Canulescu, and J. W. Andreasen, Resonant x-ray ptychographic nanotomography of kesterite solar cells, Physical Review Research **2**, 013378 (2020).

[29] M. M. Lucas, T. Ramos, P. S. Jørgensen, S. Canulescu, P. Kenesei, J. Wright, H. F. Poulsen, and J. W. Andreasen, Non-destructive determination of phase, size, and strain of individual grains in polycrystalline photovoltaic materials, Journal of Alloys and Compounds **887**, 161364 (2021).

[30] A. Menzel, C. M. Kewish, P. Kraft, B. Henrich, K. Jefimovs, J. Vila-Comamala, C. David, M. Dierolf, P. Thibault, F. Pfeiffer, and O. Bunk, Scanning transmission X-ray microscopy with a fast framing pixel detector, Ultramicroscopy **110**, 1143 (2010).

[31] C. Ziska, C. Ossig, N. Pyrlik, R. Carron, E. Avancini, G. Fevola, A. Kolditz, J. Siebels, T. Kipp, Z. Cai, *et al.*, Quantifying the elemental distribution in solar cells from x-ray fluorescence measurements with multiple detector modules, in *2020 47th IEEE Photovoltaic Specialists Conference (PVSC)* (IEEE, 2020) pp. 1085–1092.

[32] O. Vyvenko, T. Buonassisi, A. Istratov, H. Hieslmair, A. Thompson, R. Schindler, and E. Weber, X-ray beam induced current—a synchrotron radiation based technique for the in situ analysis of recombination properties and chemical nature of metal clusters in silicon, Journal of Applied Physics **91**, 3614 (2002).

[33] T. Buonassisi, M. Heuer, O. Vyvenko, A. Istratov, E. Weber, Z. Cai, B. Lai, T. Ciszek, and R. Schindler, Applications of synchrotron radiation x-ray techniques on the analysis of the behavior of transition metals in solar cells and single-crystalline silicon with extended defects, Physica B: Physics of Condensed Matter **340-342**, 1137 (2003).

[34] F. Salvat, J. M. Fernández-Varea, and J. Sempau, PENELOPE-2006: A code system for Monte Carlo simulation of electron and photon transport, in *Workshop proceedings*, Vol. 4 (Nuclear Energy Agency, Organization for Economic Co-operation and Development, 2006).

[35] J. A. Nelson, *The physics of solar cells* (World Scientific Publishing Company, 2003).

[36] D. Scharfetter and H. Gummel, Large-signal analysis of a silicon Read diode oscillator, IEEE Transactions on Electron Devices **16**, 64 (1969).

[37] H. K. Gummel, A Self-Consistent Iterative Scheme for One-Dimensional Steady State Transistor Calculations, IEEE Transactions on Electron Devices **11**, 455 (1964).

[38] J. B. Ghasemi, M. K. Rofouei, and N. Amiri, Multivariate curve resolution alternating least squares in the quanti-

View Article Online
DOI: 10.1039/D2FD00044J

tative determination of sulfur using overlapped S(Kα)-Mo(Lα) emission peaks by wavelength dispersive X-ray fluorescence spectrometry, X-Ray Spectrometry **44**, 75 (2015).

[39] A. O. M. Alzahrani, M. S. Abdel-wahab, M. Alayash, and M. S. Aida, Metals and ITO Contact Nature on ZnO and NiO Thin Films, Brazilian Journal of Physics **51**, 1159 (2021).

[40] D. Cozza, C. M. Ruiz, D. Duche, J. J. Simon, and L. Escoubas, Modeling the Back Contact of Cu2ZnSnSe4 Solar Cells, IEEE Journal of Photovoltaics **6**, 1292 (2016).

[41] A. Crovetto, M. L. Palsgaard, T. Gunst, T. Markussen, K. Stokbro, M. Brandbyge, and O. Hansen, Interface band gap narrowing behind open circuit voltage losses in Cu2ZnSnS4 solar cells, Applied Physics Letters **110**, 10.1063/1.4976830 (2017), arXiv:1702.04229.

[42] A. Cherouana and R. Labbani, Study of CZTS and CZTSSe solar cells for buffer layers selection, Applied Surface Science **424**, 251 (2017).

[43] A. Benmir and M. S. Aida, Simulation of a thin film solar cell based on copper zinc tin sulfo-selenide Cu2ZnSn(S,Se)4, Superlattices and Microstructures **91**, 70 (2016).

[44] A. Kumar and A. D. Thakur, Role of contact work function, back surface field, and conduction band offset in Cu2ZnSnS4 solar cell, Japanese Journal of Applied Physics **57**, 10.7567/JJAP.57.08RC05 (2018).

[45] I. M. Dharmadasa, Recent developments and progress on electrical contacts to CdTe , CdS and ZnSe with special reference to BARRIER contacts to CdTe, Progress in crystal growth and characterization of materials **36**, 249 (1998).

[46] S. Choi, Z. Shaolin, and W. Yang, Layer-number-dependent work function of MoS2 nanoflakes, Journal of the Korean Physical Society **64**, 1550 (2014).

[47] A. R. Latrous, R. Mahamdi, B. N. Touafek, and M. Pasquinelli, Performance Enhancement in CZTS Solar Cells by SCAPS-1D Software, International Journal of Thin Films Science and Technology **10**, 59 (2021).

[48] H. F. Dam, T. R. Andersen, E. B. L. Pedersen, K. T. S. Thydén, M. Helgesen, J. E. Carlé, P. S. Jørgensen, J. Reinhardt, R. R. Søndergaard, M. Jørgensen, E. Bundgaard, F. C. Krebs, and J. W. Andreasen, Enabling flexible polymer tandem solar cells by 3d ptychographic imaging, Advanced Energy Materials **5**, 1400736 (2015).

[49] P. Parkinson, Y.-H. Lee, L. Fu, S. Breuer, H. H. Tan, and C. Jagadish, Three-dimensional in situ photocurrent mapping for nanowire photovoltaics, Nano Letters **13**, 1405 (2013).

[50] L. Chayanun, L. Hrachowina, A. Björling, M. T. Borgström, and J. Wallentin, Direct three-dimensional imaging of an x-ray nanofocus using a single 60 nm diameter nanowire device, Nano Letters **20**, 8326 (2020).

[51] K. W. Bossers, R. Valadian, S. Zanoni, R. Smeets, N. Friederichs, J. Garrevoet, F. Meirer, and B. M. Weckhuysen, Correlated x-ray ptychography and fluorescence nano-tomography on the fragmentation behavior of an individual catalyst particle during the early stages of olefin polymerization, Journal of the American Chemical Society **142**, 3691 (2020).

[52] J. Becher, D. F. Sanchez, D. E. Doronkin, D. Zengel, D. M. Meira, S. Pascarelli, J.-D. Grunwaldt, and T. L. Sheppard, Chemical gradients in automotive cu-ssz-13 catalysts for no$_x$ removal revealed by operando x-ray spectrotomography, Nature Catalysis **4**, 46 (2021).

[53] M. E. Stuckelberger, Multimodal scanning x-ray microscopy at nanoprobe endstations of fourth-generation synchrotrons, Spectroscopy **34**, 42 (2019).

3.3 Basics of Semiconductor Physics

To get an essential knowledge of semiconductor physics, we need to answer two fundamental questions: (1) how many charge carriers do we have, i.e. how many electrons and holes will be contributing to the current? and, (2) how these charge carriers are created and how do they move?

Our goals in this section are to provide basic and understandable answers to these questions, summarizing the principles and assumptions we used for formulating the problem and presenting it in an easy and simple way. For more, details the reader can refer to [97]–[100].

3.3.1 Semiconductor material

Semiconductors are a group of materials having conductivities between those of metals and insulators. In crystalline solids, when atoms are placed next to each other, the structure of their discrete energy levels will be transformed into energy band structure of allowed and forbidden energies. This energy band splitting and the formation of allowed and forbidden bands is the energy band theory of crystalline materials. We will use this energy band model for explanations and formulation of the problem. Figure 3.1a describes the energy band diagram of intrinsic semiconductor with the two allowed energy bands shown. There are two energy bands namely the lower band (the valence band) and the upper band (the conduction band), and each energy band consist of discrete energy levels. At absolute zero degrees, electrons (black circles) are at the lowest energy state, so that all states in the valence band are full and all states in the conduction band are empty. The band gap energy (E_g) is the difference between the energies at the top edge of the valence band (E_V) and the bottom edge of the conduction band (E_C) which is the width of the forbidden energy band. In this case, the semiconductor acts like an insulator since there are no free electrons in the conduction band to participate in conducting the current. As the temperature increases ($T > 0$ K), a few valence band electrons may gain enough thermal energy to break the covalent bond and jump into the conduction band. Leaving behind a positively charged “empty state” (white circles) called a hole which is free to move in the valence band (see Figure 3.1b).

Going back to our main question, we need to know the number of free electrons in the conduction band and free holes in the valence band that will be available for conduction. With the help of quantum mechanics theory (we will not go into details), we can answer this question. In general, due to the uncertainty principle it is more convenient to deal with electron and hole densities instead of number. The electron density in the conduction band is given by the density of allowed quantum states at energy level times the probability that a state is occupied by an electron. Integrating over the entire conduction band energies we have the total electron concentration at thermal equilibrium.

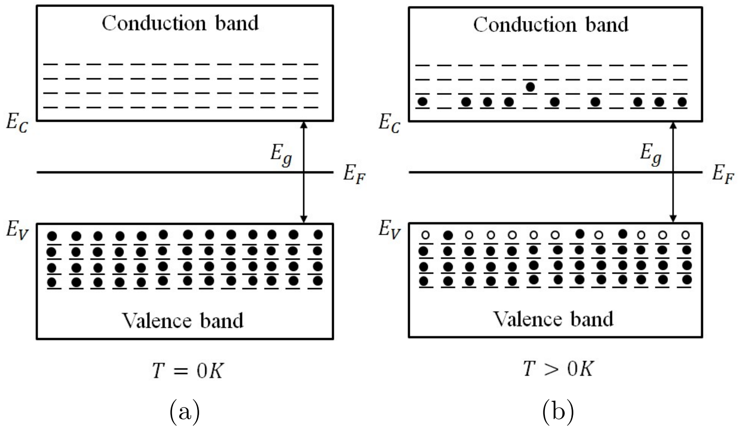

Figure 3.1: Band diagram of intrinsic semiconductor: a) $T = 0$ K, b) $T > 0$ K.

$$n = \int_{E_C}^{\infty} g_c(E_l) f_F(E_l, E_F) dE_l \tag{3.1}$$

where $g_c(E_l)$ is the density of quantum states in the conduction band, $f_F(E_l, E_F)$ is the Fermi-Dirac probability function and E_F is the energy below which all states are filled with electrons and above which all states are empty at $T = 0$ K, and called the Fermi energy or Fermi level. For an intrinsic semiconductor, the Fermi level generally lies very close to, but not exactly at, the middle of the band gap (see Figures 3.1a and 3.1b). Unfortunately, the integral in (3.1) does not have a closed form expression. But, with the help of Boltzmann statistics and assuming that $(E_l - E_F) \gg kT$, the Fermi probability function reduces to the Boltzmann approximation, which is:

$$f_F(E_l, E_F) = \frac{1}{1 + e^{\left(\dfrac{E_l - E_F}{kT}\right)}} \approx e^{-\left(\dfrac{E_l - E_F}{kT}\right)} \tag{3.2}$$

where k is Boltzmann's constant and T is the absolute temperature. Applying the Boltzmann approximation to Equation (3.1), the electron concentration in the conduction band at thermal equilibrium can be written as:

$$n = N_C e^{\left(\dfrac{E_F - E_C}{kT}\right)} \tag{3.3}$$

where N_C is the effective densities of state for electrons.

Similarly, the hole density in the valence band is given by the density of allowed quantum states at energy level times the probability that a state is not occupied by an electron. Integrating over the entire valence band energies we have the total hole concentration at thermal equilibrium:

$$p = \int_{-\infty}^{E_V} g_v(E_l)(1 - f_F(E_l, E_F)) dE_l \tag{3.4}$$

where $g_v(E_l)$ is the density of quantum states in the valence band. With the help of Boltzmann statistics and assuming that $(E_F - E_l) \gg kT$, the thermal equilibrium hole concentration in the valence band can be written as:

$$p = N_V e^{\left(\dfrac{E_V - E_F}{kT}\right)} \tag{3.5}$$

where N_V is the effective densities of state for holes.

At finite temperatures thermal generation occurs, which results in creation of electron hole pairs. This process is balanced by recombination of the electrons in the conduction band with holes in the valence band. At thermal equilibrium, for intrinsic semiconductors, the electron density is equal to the hole density and equal to the intrinsic carrier density n_i:

$$np = n_i^2 = N_C N_V e^{\left(\dfrac{-E_g}{kT}\right)} \tag{3.6}$$

So far, we answered our first question and determined the electron and hole densities at the conduction and valence bands respectively. In general, the conductivity of an intrinsic semiconductor at room temperature is very small and not efficient for applications. One way to improve the electrical properties of semiconductors is by adding a specific dopant or impurity atoms to the crystal structure. This doping process can greatly change the electrical characteristics of the semiconductor.

3.3.2 Doping

When electrons and holes generated by impurity are much more numerous than the thermally generated ones, the semiconductor is called extrinsic semiconductor. Introducing impurity atoms will add new energy levels for electrons and holes. Depending on the dopant concentration, the added energy levels may be localized within the forbidden energy level (band gap) giving a non-degenerate semiconductor. For heavily doped semiconductor, the distance between the impurity atoms decreases and atoms will interact. This will cause the single discrete energy level to split into a band of energies, which may overlap the bottom of the conduction band or the top of the valence band. When the concentration of dopant exceeds the density of states N_C or N_V, we have a degenerate semiconductor.

In degenerate semiconductors, the Fermi level is located in the conduction or valence band. So, the assumption that $(E_l - E_F) \gg kT$ or $(E_F - E_l) \gg kT$ is invalid any more and we need to use the value of Fermi-Dirac integral in equation (3.1) to compute the carrier densities. In our model, we assume that the semiconductors are non-degenerate and hence the Boltzmann approximation holds.

3.3.2.1 n-type material

Adding donor impurity atoms to a semiconductor will increase the density of electrons in the material. Allowed levels between E_F and E_C are introduced by replacing some atoms in the crystal lattice with impurity atoms. From equation (3.3) the density of electrons and the position of Fermi level are related, so increasing the electrons density will change the position of Fermi level from the intrinsic case (E_{Fi}) and pull it up close to the bottom of the conduction band see Figure 3.2a. As the electron concentration is greater than the hole concentration the semiconductor is called n-type. At room temperature, most of the donor atoms, if not all, donate an electron to the conduction band, leaving behind an empty state (positively charged) and we can assume that the donor states (E_d) are completely ionized. Figure 3.2c shows the band diagram for an n-type non-degenerate semiconductor in complete ionization conditions.

At thermal equilibrium, the semiconductor is electrically neutral. This can be expressed as the net density charge being equal to zero. Keeping in mind that the product of n and p is always a constant for a given semiconductor material at a given temperature, we then have:

$$n - p - N_D = 0 \tag{3.7}$$

and

$$np = n_i \tag{3.8}$$

where N_D is the ionized donor density. Solving (3.7) and (3.8) for n, we have:

$$n = \frac{N_D + \sqrt{N_D^2 + 4n_i^2}}{2} \tag{3.9}$$

In the case where $N_D \gg n_i$, the majority carrier electron concentration in an n-type semiconductor is given by:

$$n \approx N_D \tag{3.10}$$

and the minority carrier hole concentration in an n-type semiconductor is given by:

$$p = \frac{n_i^2}{N_D} \tag{3.11}$$

3.3.2.2 p-type material

In the same manner, doping a semiconductor to increase the density of holes will give a p-type material. Introducing an acceptor atoms to the lattice structure will add an empty states between E_V and E_F and pull down the Fermi level close to the top of the valence band, see Figure 3.2b. For typical acceptor atoms, the ionization energy is few meV and it is relatively small compared to the band gap energy. At room temperature, some valence electrons may gain enough energy to jump to the acceptor empty states leaving behind a hole in the valence band. We assume that all the acceptor states (E_a)

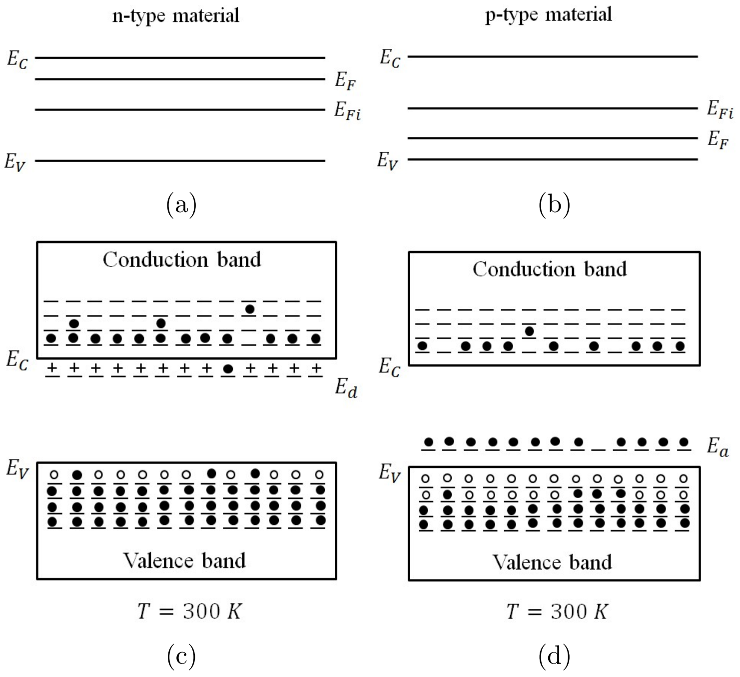

Figure 3.2: Band diagram of doped semiconductor: a) n-type material, b) p-type material,c) Ionized donor states, d) Ionized acceptor states.

are filled by an electron so as to have complete ionization. Figure 3.2d shows the band diagram of a p-type non-degenerate semiconductor in complete ionization conditions.

At thermal equilibrium, the charge neutrality condition holds. We then have

$$n - p + N_A = 0 \tag{3.12}$$

where N_A is the ionized acceptor density. Solving (3.12) and (3.8) for p, we have:

$$p = \frac{N_A + \sqrt{N_A^2 + 4n_i^2}}{2} \tag{3.13}$$

In the case where $N_A \gg n_i$, then the majority carrier hole concentration in a p-type semiconductor is given by:

$$p \approx N_A \tag{3.14}$$

and the minority carrier electron concentration in a p-type semiconductor is given by:

$$n = \frac{n_i^2}{N_A} \tag{3.15}$$

3.3.3 p-n Junction

The position of the Fermi level is significant when analysing a p-n junction. Putting a p-type material in contact with n-type material will force the electrons in the system to flow into the lower energy states. The diffusion of electrons from n-type into the p-type will continue until thermal equilibrium is reached. At thermal equilibrium the position of Fermi level will be the same for the two materials. In the same way, holes will diffuse from p-type into n-type. This diffusion will leave positively charged donor atoms in the n region and negatively charged acceptor atoms in the p region. Since the donor and acceptor atoms have fixed charge, this will induce an electric field in the region near the metallurgical junction and in the direction from the positive to the negative charge. This depleted region from mobile charges is called the depletion region and also referred to as the space charge region (SCR). The electrons and holes are swept out of the space charge region and a barrier for farther diffusion is created by the electric field.

3.3.3.1 Homojunction

We have discussed the basic p-n junction structure and the formation of the space charge region. Doping a material with different type of dopant to give p-type and n-type regions will formulate p-n homojunction. Since we have the same material in both regions, it is convenient to rewrite the electrons and holes densities in terms of the intrinsic carrier density n_i and the intrinsic Fermi level E_{Fi}. We then have:

$$n = n_i e^{\left(\dfrac{E_F - E_{Fi}}{kT}\right)} \tag{3.16}$$

$$p = n_i e^{\left(\dfrac{E_{Fi} - E_F}{kT}\right)} \tag{3.17}$$

where n and p are the electron and hole densities at thermal equilibrium respectively. At thermal equilibrium, there is no current and no external excitation is applied. The Fermi energy level is constant throughout the entire system and the electron and hole current densities are equal to zero. The differential form of Gauss's law expresses the local change of the electric field due to the volumetric charge density:

$$\nabla \cdot (\varepsilon E) = \rho \tag{3.18}$$

where ε is the electric permittivity, $\rho = q(p - n + N_D - N_A)$ is the charge density and E is the electric field given by:

$$E = -\nabla\psi \tag{3.19}$$

where ψ is the electrostatic potential. Combining equations (3.18) and (3.19), the Poisson's equation in semiconductor is given by:

$$\nabla \cdot (\varepsilon\nabla\psi) = q(n - p - C) \tag{3.20}$$

where $C = N_D - N_A$ and q is the elementary charge of electron. In p-n homojunction, we assume that the intrinsic Fermi level E_{Fi} is position independent on material parameters, but the energy value of this intrinsic level depends on the electrostatic potential. Hence, we can take this energy level as reference level for electrostatic potential:

$$E_{Fi} = -q\psi \tag{3.21}$$

Without loss of generality, we can set $E_F = 0$. Equation (3.20) along with (3.21), (3.16) and (3.17) give the non-linear Poisson equation for semiconductor device under thermodynamic equilibrium conditions and is given by:

$$\nabla \cdot (\varepsilon \nabla \psi) = q(n_i e^{\left(\frac{-q\psi}{kT}\right)} - n_i e^{\left(\frac{q\psi}{kT}\right)} - C) \tag{3.22}$$

3.3.3.2 Heterojunction

In devices with position dependent parameters where we have different materials (heterostructure) the intrinsic Fermi level can not be used as reference level for the electrostatic potential. Instead, we define a reference level such that the conduction band edge energy can be written as the difference between the electrostatic potential and the electron affinity (χ):

$$E_C = -q\psi - \chi \tag{3.23}$$

In similar manner the valence band edge can be written as:

$$E_V = -q\psi - \chi - E_g \tag{3.24}$$

Hence, the electron and hole densities can be written as:

$$n = N_C e^{\left(\frac{q\psi + \chi + E_F}{kT}\right)} \tag{3.25}$$

$$p = N_V e^{\left(\frac{-E_F - q\psi - \chi - E_g}{kT}\right)} \tag{3.26}$$

In the same way as in homojunction we assume that $E_F = 0$, so that the non-linear Poisson equation for heterostructure semiconductor device under thermodynamic equilibrium conditions is given by:

$$\nabla \cdot (\varepsilon \nabla \psi) = q(N_C e^{\left(\frac{q\psi + \chi}{kT}\right)} - N_V e^{\left(\frac{-q\psi - \chi - E_g}{kT}\right)} - C) \tag{3.27}$$

3.3.4 Semiconductor devices under illumination

In the previous sections our discussion was limited to semiconductors under the thermal equilibrium conditions. Hence, no current flows in the system. If, for example, a semiconductor device was exposed to a source of light with energy higher than the band gap energy, some valence band electrons may gain enough energy to jump into the conduction band creating an electron-hole pair. These excess carriers violate the thermal equilibrium and current flows in short circuit conditions.

3.3.4.1 Generation and Recombination rates

Generation (G) is an electronic excitation event which increases the number of free carriers available to carry charge. Recombination (R) is an electronic relaxation event which reduces the number of free carriers [97]. One may think that these events happen only due to external excitation. In fact, at thermodynamic equilibrium conditions these processes occur continually through the lattice vibrational kinetic energy. Since, at thermal equilibrium, for fixed temperature the product of electron and hole densities must be equal to the intrinsic carrier density. The rate in which an electron is promoted to a higher energy level due to thermal energy (thermal generation) is equivalent to the rate at which an electron relaxes to a lower energy level releasing thermal energy (thermal recombination).

An external excitation such as sunlight, electron beam and x-ray beam (a flux of photons), can generate electron-hole pairs creating a non-equilibrium condition. A continuous generation will not cause a continual increase of the carrier concentrations. The system will attend to restore the equilibrium conditions by recombination processes. These processes include contributions from Shocley-Read-Hall (SRH), radiative and Auger recombinations.

3.3.4.1.1 X-ray Generation rate

X-ray propagation and interaction with matter are often described using analytical models. This approach might not be sufficient for modelling more complex phenomena, and Monte Carlo-based numerical simulations might be more suitable. In general, a Monte Carlo simulation employs known probability distributions of various interactions of X-ray photons with matter to model their propagation within the interaction volume and associated change of their state. In this work, a personalized version of Penelope was used to simulate the generation of electron-hole pairs in the multi-layered solar cell upon the incidence of the localized X-ray beam [101]. The resulting profiles of the generation rate G were then used in the modelling of the XBIC signal.

3.3.4.1.2 Shocley-Read-Hall Recombination

So far, the most important recombination processes in real semiconductors are those which involve defect or trap states in the band gap [97]. The single-level recombination can be described by two processes: electron capture and hole capture. The net transition rate can be described by the Shockley-Read-Hall statistics [100] as:

$$R = \frac{np - n_i^2}{\tau_p(n + n_t) + \tau_n(p + p_t)} \tag{3.28}$$

where τ_n, τ_p are the electron and hole lifetimes, respectively and n_t, p_t are the electron and hole concentrations of the trap state that are given by:

$$n_t = N_C e^{\left(\dfrac{E_t - E_c}{kT}\right)}, \quad p_t = N_V e^{\left(\dfrac{E_v - E_t}{kT}\right)} \tag{3.29}$$

where E_t is the energy of the trap level. Only the E_t near the mid-gap are effective recombination centres. Considering only these traps, we can rewrite (3.28) as:

$$R = \frac{np - n_i^2}{\tau_p(n + n_i) + \tau_n(p + n_i)} \tag{3.30}$$

The carrier lifetimes from a single defect level with density N_t can be described for electron by:

$$\tau_n = \frac{1}{\sigma_n v_n N_t} \tag{3.31}$$

and for hole by:

$$\tau_p = \frac{1}{\sigma_p v_p N_t} \tag{3.32}$$

where σ_n, σ_p are the electron and hole capture cross-sections, respectively, and v_n, v_p are the thermal velocity of the electron and hole, respectively.

3.3.4.2 Carrier densities at nonequilibrium condition

The external excitation will generate electron-hole pairs, so the semiconductor is no longer in thermal equilibrium conditions and the Fermi level is no longer strictly defined. The electron and hole distributions are now governed by general distribution function instead of Fermi-Dirac probability function in (3.1). One of the great simplifications in semiconductor physics assumes that if the distributions disturbance is not too great or not changing too quickly, the populations of electrons and holes each relax to achieve a state of quasi-thermal equilibrium [97]. In other words, we can simply say that the Fermi level is split into two different quasi-Fermi levels: one for electrons E_{F_n} and another for holes E_{F_p}. Using these two energy levels, we can describe the electrons and holes distributions under non-equilibrium conditions as follows:

$$n = N_C e^{\left(\dfrac{q\psi + \chi - q\varphi_n}{kT}\right)} \tag{3.33}$$

$$p = N_V e^{\left(\dfrac{q\varphi_p - q\psi - \chi - E_g}{kT}\right)} \tag{3.34}$$

where φ_n and φ_p are quasi-Fermi potential for electron and hole, respectively, and they are given by:

$$\varphi_n = -\frac{1}{q} E_{F_n} \tag{3.35}$$

$$\varphi_p = -\frac{1}{q} E_{F_p} \tag{3.36}$$

3.3.4.3 Carrier Transport in Semiconductor: Drift-Diffusion model

There are various existing models for carrier transport in semiconductor. In quantum models the electrons are represented by their wave functions which are solutions of Schrödinger's equation. In many cases of semiconductor devices, quantum effects are negligible, and a semi-classical or classical description of transport is sufficient [102]. The Boltzmann transport equation is the stating point for driving the classical and semi-classical models. In this work, we used the classical models for describing the carrier transport equations. The most commonly used classical model is the drift-diffusion model since the derivation of the current equations from Boltzmann equation is an extremely large task. We used purely phenomenological derivation of the current equations by defining two main sources of current, drift current and diffusion current.

At the atomic scale, the electrons in semiconductor move randomly in all directions by the thermal energy. This movement will not last forever since the semiconductor crystal is full of objects with which the electrons collide and lose their energy. The random motion of electrons lead to an average net displacement equal to zero. On the other hand, if these electrons experience an electric field E, they will accelerate, on the microscopic scale, with a constant velocity v_{d_n} on the opposite direction of the electric field. This velocity, called the drift velocity, is proportional to the applied electric field and is given by:

$$v_{d_n} = -\mu_n E \tag{3.37}$$

where μ_n is the electron mobility. The resulting drift current density is equal to the product of the charge per electron, the electron concentration and the drift velocity, and it is given by:

$$J_n^{drift} = -qnv_{d_n} = q\mu_n nE \tag{3.38}$$

In the same way, we can define the drift current density for hole, the only difference is that, as the hole is a positively charged particle it will accelerate in the same direction as the applied electric field. The drift current density for hole is given by:

$$J_p^{drift} = qpv_{d_p} = q\mu_p pE \tag{3.39}$$

where v_{d_p} is the drift velocity for hole and μ_p is the hole mobility.

There is a second mechanism, in addition to drift, that can induce a current in semiconductor. Whenever there exists a gradient of carrier concentration, a process of diffusion occurs by which the carriers migrate from the region of high concentration toward the region of low concentration. This current is called the diffusion current. The diffusion of electrons from a region of high concentration to a region of low concentration produces a flux of electrons flowing in a specific direction. The resulting current will be in the opposite direction as electrons have negative charge. The diffusion current is proportional to the density gradient of the electrons concentration and is given by:

$$J_n^{diff} = qD_n \nabla n \tag{3.40}$$

where D_n is the electron diffusion coefficient. On the other hand, the diffusion current generated by the movement of holes from a region of high concentration to a region of low concentration will be in the same direction of the holes flux. The hole diffusion current density is proportional to the hole density gradient and is given by:

$$J_p^{diff} = -qD_p \nabla p \tag{3.41}$$

where D_p is the electron diffusion coefficient.

So far, we treated the drift and diffusion currents separately. But when both an electric field and a concentration gradient are present, we write the total current density for electrons and holes as a combination of both currents as follows:

$$J_n = q\mu_n nE + qD_n \nabla n \tag{3.42}$$

$$J_p = q\mu_p pE - qD_p \nabla p \tag{3.43}$$

where J_n and J_p are the electron and hole current densities, respectively. Moreover, the total current density J will be equal to the summation of electron and hole current densities.

$$J = J_n + J_p \tag{3.44}$$

In heterostructure device, the drift curent will not be only due to the electric field, but also due to the variation of material properties. So, we will use the effective electric fields of electrons and holes, E_n and E_p, respectively. They are equal to the gradients of the sum of the electrostatic potential, the electron affinity, the band gap and the effective densities of state for electrons and holes [97]:

$$E_n = -\nabla \left(\psi + \frac{\chi}{q} + \frac{KT}{q} \log(N_C) \right) \tag{3.45}$$

$$E_p = -\nabla \left(\psi + \frac{\chi}{q} + \frac{E_g}{q} - \frac{KT}{q} \log(N_V) \right) \tag{3.46}$$

where ψ is the electrostatic potential defined in (3.23). Hence, the drift-diffusion model for heterostructure devices can be written as:

$$J_n = -q\mu_n n\nabla\left(\psi + \frac{\chi}{q} + \frac{KT}{q}\log(N_C)\right) + qD_n\nabla n \tag{3.47}$$

$$J_p = -q\mu_p p\nabla\left(\psi + \frac{\chi}{q} + \frac{E_g}{q} - \frac{KT}{q}\log(N_V)\right) - qD_p\nabla p \tag{3.48}$$

Another useful form of the drift-diffusion model that arise as a result of the derivations of Boltzmann's equations, describes the current densities in terms of the quasi-Fermi potential for electron and hole, and it is given by:

$$J_n = -q\mu_n n\nabla\varphi_n \tag{3.49}$$

$$J_p = -q\mu_p p\nabla\varphi_p \tag{3.50}$$

3.3.4.4 Continuity equations for electron and hole

We treated the generation, the recombination, the drift current and diffusion current individually. But, in reality, these phenomena happen simultaneously. We will consider a differential volume as shown in Figure 3.3 to derive the continuity equation for electron. The net increase in the number of electrons per unit time within the differential volume element due to the x-component of electrons current density is the sum of the net flow into the volume, the carrier generation and recombination in the volume, that is:

$$\frac{\partial n}{\partial t}dxdydz = \left[\frac{J_n(x)}{-q} - \frac{J_n(x+dx)}{-q}\right]dydz + (G-R)dxdydz \tag{3.51}$$

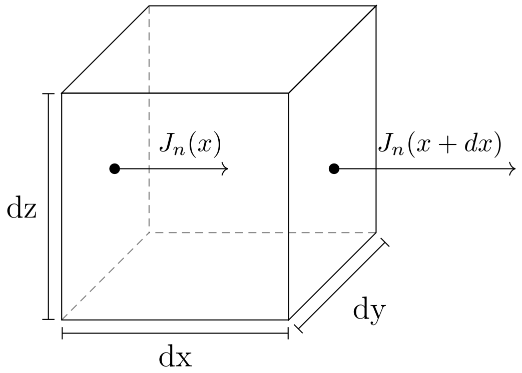

Figure 3.3: Differential volume.

Using the Taylor's expansion of $J_n(x+dx)$ and dividing both sides of the equation (3.51) by the differential volume, we obtain the net increase in the electron concentration per unit time as follows:

$$\frac{\partial n}{\partial t} = \frac{1}{q}\frac{\partial J_n}{\partial x} + (G-R) \tag{3.52}$$

The continuity equation for electron (3.52) can be generalized to two and three dimensions using the divergence of the current density vector as:

$$\frac{\partial n}{\partial t} = \frac{1}{q}\nabla \cdot J_n + (G - R) \tag{3.53}$$

Similarly, the continuity equation for hole is given by:

$$\frac{\partial p}{\partial t} = -\frac{1}{q}\nabla \cdot J_p + (G - R) \tag{3.54}$$

3.3.5 Formulation of the problem

In the previous subsections, the basics and first principles of semiconductor physics were presented. In the coming subsections, we sum up and present the system of equations that needs to be solved in modelling the semiconductor devices. The choice of boundary conditions will affect the solution of the set of partial differential equations. In this work, we consider two types of boundary conditions: Ohmic and Schottky boundary conditions.

3.3.5.1 System of equations

The basic equations to be solved in modelling semiconductor devices are: Poisson's equation and the continuity equations for electrons and holes. They are expressed in the steady states as:

$$\nabla \cdot (\varepsilon_r \varepsilon_0 \nabla \psi) = q(n - p + N_A - N_D) \tag{3.55}$$

$$\nabla \cdot J_n = -q(G - R) \tag{3.56}$$

$$\nabla \cdot J_p = q(G - R) \tag{3.57}$$

where $\varepsilon_r, \varepsilon_0$ are the relative and vacuum permittivity, respectively. The current density resulting from the flow of electrons and holes are given by the Drift-Diffusion model as following:

$$J_n = q\mu_n \left(-n\nabla\psi_n + V_t \nabla n\right) \tag{3.58}$$

$$J_p = q\mu_p \left(-p\nabla\psi_p - V_t \nabla p\right) \tag{3.59}$$

where $\psi_n = \psi + \frac{\chi}{q} + V_t \ln(N_C)$, $\psi_p = \psi + \frac{\chi}{q} + \frac{E_g}{q} - V_t \ln(N_V)$ and $V_t = \frac{kT}{q}$.

Equations (3.55), (3.56) and (3.57), together with the relations (3.58) and (3.59), form a system of equations for the three dependent variables ψ, n, and p. For analytical purposes, it is often helpful to use other variables than n and p in the basic equations. The current relations can be expressed in terms of the quasi-Fermi potentials as:

$$J_n = -q\mu_n e^{\left(\frac{\psi_n - \varphi_n}{V_t}\right)} \nabla\varphi_n \tag{3.60}$$

$$J_p = -q\mu_p e^{\left(\frac{\varphi_p - \psi_p}{V_t}\right)} \nabla\varphi_p \tag{3.61}$$

defining another set of variables in the same way as Slotboom [103] did and as following:

$$u = e^{\left(-\frac{\varphi_n}{V_t}\right)}, \quad v = e^{\left(\frac{\varphi_p}{V_t}\right)} \tag{3.62}$$

Hence, the carrier concentrations can be written as:

$$n = ue^{\left(\frac{\psi_n}{V_t}\right)} \tag{3.63}$$

$$p = ve^{\left(\frac{-\psi_p}{V_t}\right)} \tag{3.64}$$

Moreover, the steady state equations become:

$$\nabla.(\varepsilon_r\varepsilon_0\nabla\psi) = q(ue^{\left(\frac{\psi_n}{V_t}\right)} - ve^{\left(-\frac{\psi_p}{V_t}\right)} - C) \tag{3.65}$$

$$\nabla \cdot \left(q\mu_n V_t e^{\left(\frac{\psi_n}{V_t}\right)} \nabla u \right) = -q(G - R) \tag{3.66}$$

$$\nabla \cdot \left(-q\mu_p V_t e^{\left(-\frac{\psi_p}{V_t}\right)} \nabla v \right) = q(G - R) \tag{3.67}$$

The set of dependent variables ψ, u and v, simplifies and facilitates the mathematical analysis of the problem, while the set ψ, n and p is generally the best choice of the dependent variables for numerical simulations.

3.3.5.2 Boundary conditions

To have a complete model, we need boundary conditions. The choice of these conditions will affect the solution of the set of partial differential equations. It depends on the type of electrical contacts at the boundary. In our simulations, we assumed having two types of contacts: Ohmic and Schottky contacts.

3.3.5.2.1 Ohmic contacts

For ideal Ohmic contact, the space charge is vanishing at the contact and the surface recombination is assumed to be infinite. This will impose Dirichlet boundary conditions for n and p at the contact

$$n_0 = \frac{N_D + \sqrt{N_D^2 + 4n_i^2}}{2} \approx N_D \tag{3.68}$$

$$p_0 = \frac{n_i^2}{n_0} \tag{3.69}$$

for n-type material, and

$$p_0 = \frac{N_A + \sqrt{N_A^2 + 4n_i^2}}{2} \approx N_A \tag{3.70}$$

$$n_0 = \frac{n_i^2}{p_0} \tag{3.71}$$

for p-type material, where n_0 and p_0 are the concentrations of electron and hole at the contact.

The Dirichlet boundary conditions for the electrostatic potential at Ohmic contact is given by the sum of the external applied bias V_0 and the built-in potential ψ_{bi}:

$$\psi_0 = \psi_{bi} + V_0 \tag{3.72}$$

where ψ_0 is the electrostatic potential at contact. For calculation of the built-in potential, we assumed a homogeneously doped semiconductor and no external forces. Then the Laplacian of the electrostatic potential is identically zero and equation (3.27) reduces to:

$$N_C e^{\left(\frac{q\psi_{bi} + \chi}{kT}\right)} - N_V e^{\left(\frac{-q\psi_{bi} - \chi - E_g}{kT}\right)} - C = 0 \tag{3.73}$$

For n-type material we have:

$$N_C e^{\left(\frac{q\psi_{bi} + \chi}{kT}\right)} - \frac{n_i^2}{N_C e^{\left(\frac{q\psi_{bi} + \chi}{kT}\right)}} - C = 0 \tag{3.74}$$

solving (3.74) for ψ_{bi} we get:

$$\psi_{bi} = V_t \ln\left(\frac{N_D + \sqrt{N_D^2 + 4n_i^2}}{2N_C}\right) - \frac{\chi}{q} \tag{3.75}$$

in the same fashion, for p-type material, we get:

$$\psi_{bi} = V_t \ln\left(\frac{N_A + \sqrt{N_A^2 + 4n_i^2}}{2N_V}\right) - \frac{\chi}{q} - \frac{E_g}{q} \tag{3.76}$$

3.3.5.2.2 Schottky contacts

The physics of Schottky contacts is extremely complex and the models used for simulation are highly simplified. We assume that the Fermi level in the semiconductor is lined up with the Fermi level of the metal, and that electrostatic potential at the boundary is proportional to the metal work function. Hence, the Dirichlet boundary conditions for the electrostatic potential is given by:

$$\psi_0 = -\frac{\phi_M}{q} + V_0 \tag{3.77}$$

where ϕ_M is the metal work function. The boundary values for n and p at a Schottky contact depend on the current densities at the contact. From the thermionic emission and diffusion theories, we have the following boundary conditions:

$$J_n \cdot \nu = -qS_n \left(n - n_{eq}\right) \tag{3.78}$$

$$J_p \cdot \nu = \quad qS_n \left(p - p_{eq}\right) \tag{3.79}$$

where ν is the outward unit normal, S_n and S_p are the surface recombination velocities for electrons and holes at the contact and n_{eq} and p_{eq} are the electron and hole concentrations in thermodynamic equilibrium at the contact.

3.3.6 Summary of section 3.3

After briefly presenting the basics of semiconductor physics, we made the following choices for the first-principles model we used in our simulator for the XBIC signal:

- The system to be solved is composed of Poisson's equation plus the continuity equations for electrons and holes with the drift-diffusion model.
- The generation profile is based on Monte-Carlo simulations.
- We only have non-degenerate semiconductors implying that Boltzmann's approximation can be used to compute the carriers concentrations.
- The recompensation term only comes from Shockley-Read-Hall processes.
- The model at the heterointerface simply considers the effective potentials for electrons and holes.

3.4 Numerical Modelling

Due to the great different orders of magnitude existing between the dependent variables (ψ, n, p) and to avoid numerical overflow, rewriting the equations in dimensionless form is necessary. The scaling factors used in the simulations are obtained following [104] and are summarized in table 3.1. In this section, we only use the scaled quantities for the numerical derivation and discretization.

We start this section by putting the model in dimensionless form. Then we describe the discretization methods used in our python-based simulator. Poisson's equation linearization and Scharfetter Gummel scheme are presented. For solving the system of non-linear equations, we utilized Gummel's method combined with the lagging approach.

Quantity	Expression	Value
Concentrations	M_0	$10^{25}\, m^{-3}$
Potentials	$V_t = \dfrac{kT}{q}$	$0.02585\, V$
Length	$l = \sqrt{\dfrac{\epsilon_0 kT}{q^2 M_0}}$	$3.78 \times 10^{-10}\, m$
Energy	kT	$0.02585\, eV$
Mobility	μ_0	$10^{-4}\, m^2 V^{-1} s^{-1}$
Time	$\dfrac{l^2}{\mu_0 V_t}$	$5.53 \times 10^{-14}\, s$
Gen., Rec. rates	$\dfrac{V_t M_0 \mu_0}{l^2}$	$1.81 \times 10^{38}\, m^{-3} s^{-1}$
Current density	$-\dfrac{kT M_0 \mu_0}{l}$	$-1.10 \times 10^{10}\, Am^{-2}$
Velocity	$\dfrac{\mu_0 V_t}{l}$	$6.84 \times 10^{3}\, ms^{-1}$

Table 3.1: Quantities used to scale variables to dimensionless form.

3.4.1 Numerical model

Rewriting equations (3.55-3.59) in terms of the scaled quantities, and using the same notations as the unscaled ones, we obtain:

$$\nabla \cdot (\varepsilon_r \nabla \psi) = n - p + N_A - N_D \tag{3.80}$$

$$\nabla \cdot J_n = (G - R) \tag{3.81}$$

$$\nabla \cdot J_p = -(G - R) \tag{3.82}$$

$$J_n = \mu_n \left(n \nabla \psi_n - \nabla n\right) \tag{3.83}$$

$$J_p = \mu_p \left(p \nabla \psi_p + \nabla p\right) \tag{3.84}$$

where $\psi_n = \psi + \chi + \ln(N_C)$ and $\psi_p = \psi + \chi + E_g - \ln(N_V)$.

As we mentioned earlier, writing the set of equations using Slotboom [103] variables will facilitate the mathematical analysis, so rewriting equations (3.65-3.67) in dimensionless form is needed. Using the same notations as the unscaled quantities, we have:

$$\nabla.(\varepsilon_r \nabla \psi) = u e^{\psi_n} - v e^{-\psi_p} - C \tag{3.85}$$

$$\nabla \cdot \left(-\mu_n e^{\psi_n} \nabla u\right) = (G - R) \tag{3.86}$$

$$\nabla \cdot \left(\mu_p e^{-\psi_p} \nabla v\right) = -(G - R) \tag{3.87}$$

3.4.2 Poisson's equation linearization and Discretization

The non-linear Poisson's equation (3.85) is linearized using the fixed-point method assuming u and v are known. We assume that:

$$\psi^{l+1} = \psi^l + \delta \tag{3.88}$$

where ψ^l is the potential value from the previous iteration and δ is a perturbation on ψ^l. Equation (3.85) is linearized as:

$$\nabla \cdot (\varepsilon_r \nabla(\psi^l + \delta)) = u^l e^{(\psi_n^l + \delta)} - v^l e^{-(\psi_p^l + \delta)} - C \tag{3.89}$$

where $\psi_n^l = \psi^l + \chi + \ln(N_C)$ and $\psi_p^l = \psi^l + \chi + E_g - \ln(N_V)$. Assuming δ is small enough to permit the terms of second and higher order in Taylor's expansion to be neglected, we have:

$$e^{(\psi_n^l + \delta)} \approx e^{\psi_n^l}(1 + \delta), \quad e^{-(\psi_p^l + \delta)} \approx e^{-\psi_p^l}(1 - \delta)$$

and equation (3.89) becomes:

$$\nabla \cdot (\varepsilon_r \nabla(\psi^l + \delta)) = (u^l e^{\psi_n^l} - v^l e^{-\psi_p^l})\delta + u^l e^{\psi_n^l} - v^l e^{-\psi_p^l} - C \tag{3.90}$$

Rewriting equation (3.90) in terms of our main variables (ψ, n, p) using the equations (3.63), (3.64) and (3.88), we get:

$$\nabla \cdot (\varepsilon_r \nabla \psi^{l+1}) - (n^l - p^l)\psi^{l+1} = -(n^l - p^l)\psi^l + n^l - p^l - C \tag{3.91}$$

where n^l and p^l are the electron and hole densities from the previous iteration. Poisson's equation (3.91) had been discretized using the finite volume method. By integration over an arbitrary control volume (CV) and applying the Gauss divergence theorem, we obtain:

$$\oint_{\partial CV} \varepsilon_r \nabla \psi^{l+1} \cdot v dS - \int_{CV} (n^l - p^l)\psi^{l+1} dV = -\int_{CV} (n^l - p^l)\psi^l dV + \int_{CV} (n^l - p^l - C) dV \quad (3.92)$$

where v denotes the outward pointing normal and ∂CV is the surface of the CV. The surface integral in the equation (3.92) is split into the sum of line integrals over the planar interfaces between the control volume CV and its neighbours. According to Figure 3.4, we have:

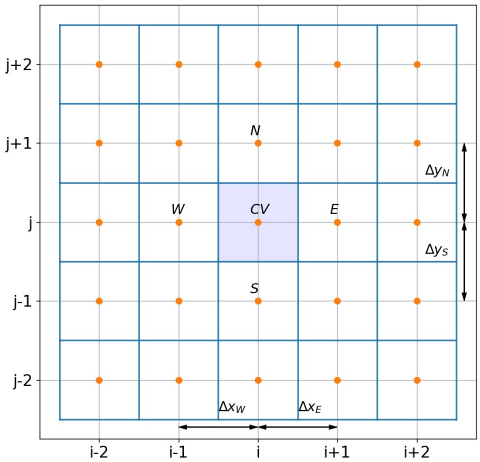

Figure 3.4: Control volume CV with its surrounding neighbours.

$$\oint_{\partial CV} \varepsilon_r \nabla \psi^{l+1} \cdot v dS = \int_e \varepsilon_r \frac{\partial \psi^{l+1}}{\partial x} dy_e - \int_w \varepsilon_r \frac{\partial \psi^{l+1}}{\partial x} dy_w + \int_n \varepsilon_r \frac{\partial \psi^{l+1}}{\partial y} dx_n - \int_s \varepsilon_r \frac{\partial \psi^{l+1}}{\partial y} dx_s \quad (3.93)$$

where e, w, n and s refer to the locations of the control volume interfaces with respect to the east, west, north and south neighbours, respectively. Using the midpoint rule to approximate the line integral, we obtain:

$$\oint_{\partial CV} \varepsilon_r \nabla \psi^{l+1} \cdot v dS = (\varepsilon_r \frac{\partial \psi^{l+1}}{\partial x})_e \Delta y_e - (\varepsilon_r \frac{\partial \psi^{l+1}}{\partial x})_w \Delta y_w + (\varepsilon_r \frac{\partial \psi^{l+1}}{\partial y})_n \Delta x_n - (\varepsilon_r \frac{\partial \psi^{l+1}}{\partial y})_s \Delta x_s \quad (3.94)$$

where Δy_e, Δy_w, Δx_n and Δx_s are the length of the east, west, north and south interface, respectively. Applying the central difference formula to approximate gradients at the CV

interfaces, we get:

$$\oint_{\partial CV} \varepsilon_r \nabla \psi^{l+1} \cdot v dS = (\varepsilon_r)_e \left(\frac{\psi_E^{l+1} - \psi_{CV}^{l+1}}{\Delta x_E} \right) \Delta y_e - (\varepsilon_r)_w \left(\frac{\psi_{CV}^{l+1} - \psi_W^{l+1}}{\Delta x_W} \right) \Delta y_w + (\varepsilon_r)_n \left(\frac{\psi_N^{l+1} - \psi_{CV}^{l+1}}{\Delta y_N} \right) \Delta x_n - (\varepsilon_r)_s \left(\frac{\psi_{CV}^{l+1} - \psi_S^{l+1}}{\Delta y_S} \right) \Delta x_s \tag{3.95}$$

where Δx_E, Δx_W, Δy_N Δy_S are the distance between CV and its east, west, north and south neighbours, ψ_E^{l+1}, ψ_{CV}^{l+1}, ψ_W^{l+1}, ψ_N^{l+1}, ψ_S^{l+1} are the nodal values of ψ^{l+1} and $(\varepsilon_r)_e$, $(\varepsilon_r)_w$, $(\varepsilon_r)_n$, $(\varepsilon_r)_s$ are the relative permittivity coefficient evaluated at the interfaces of the control volume. The interface values of ε_r were defined by requiring continuity of the ψ^{l+1} at the control volume interfaces and it is given by the harmonic mean of ε_r at the control volume and the adjacent neighbour.

Employing the midpoint rule to approximate the volume integrals in the equation (3.92) and adding equation (3.95) to it, we get:

$$\alpha_{CV} \psi_{CV}^{l+1} + \sum_i \alpha_i \psi_i^{l+1} = F; \qquad i = E, W, N, S \tag{3.96}$$

where

$$\begin{aligned}
\alpha_E &= (\varepsilon_r)_e \frac{\Delta y_e}{\Delta x_E} \\
\alpha_W &= (\varepsilon_r)_w \frac{\Delta y_w}{\Delta x_W} \\
\alpha_N &= (\varepsilon_r)_n \frac{\Delta x_n}{\Delta y_N} \\
\alpha_S &= (\varepsilon_r)_s \frac{\Delta x_s}{\Delta y_S} \\
\alpha_{CV} &= -(\Delta x \Delta y (n^l + p^l) + \sum_i \alpha_i); \qquad i = E, W, N, S \\
F &= \Delta x \Delta y (n^l - p^l - C - \psi^l (n^l + p^l))
\end{aligned}$$

3.4.3 Discretizing the continuity equations using the Scharfetter Gummel scheme

Now we consider the discretization of the electron and hole continuity equations (3.86) and (3.87). Just as Poisson's equation, we used the finite volume method for discretization of the continuity equations. Starting with electron continuity equation (3.86), it is convenient to rewrite the second-order equation as a first-order equation to facilitate the discretization process. By introducing the flux J_n, we obtain:

$$\nabla \cdot J_n = (G - R) \tag{3.97}$$

with

$$J_n = -\mu_n e^{\psi_n} \nabla u \tag{3.98}$$

Integrating equation (3.97) over an arbitrary control volume CV and applying the Gauss divergence theorem, we obtain:

$$\oint\limits_{\partial CV} J_n \cdot v dS = \int\limits_{CV} (G - R) dV \tag{3.99}$$

The surface and volume integrals in the equation (3.99) are approximated in the same way as in Poisson's equation,

$$-\Delta y_w (J_n)_w + \Delta y_e (J_n)_e - \Delta x_s (J_n)_s + \Delta x_n (J_n)_n = (G - R)\Delta x \Delta y \tag{3.100}$$

where $(J_n)_w, (J_n)_e, (J_n)_s$ and $(J_n)_n$ are the current density components evaluated at the interfaces of the control volume, these fluxes need to be expressed in terms of our set of unknowns, namely the nodal values of the electrostatic potential and electron density.

The electrostatic potential exhibits an exponential layer due to the discontinuities or exponential layers in the doping profile. The electron and hole densities exhibit similar behavior. In the approximation of the surface integrals in Poisson's equation, we assume implicitly that the electrostatic potential is approximated by a piece-wise linear function. It is inappropriate to make the same assumption for the electron and hole densities which will lead under certain conditions into large oscillations. In 1969, a numerically stable scheme was proposed by Scharfetter and Gummel [105]. They treated the continuity equations as differential equations in n and p with J_n, J_P, μ_n, μ_p and the electric field assumed piece-wise constant between mesh points.

Considering the interval $CV < x < E$ along the line $y = y_j$ it follows that:

$$(J_n)_e = (-\mu_n e^{\psi_n} \nabla u)_e \tag{3.101}$$

with:

$$u(CV) = u_{CV}, \quad u(E) = u_E \tag{3.102}$$

Integrating from CV to E, we obtain:

$$(J_n)_e = \frac{-(\mu_n)_e (u_E - u_{CV})}{\displaystyle\int_{CV}^{E} e^{-\psi_n} dx} \tag{3.103}$$

Using a quadrature rule to approximate the integral, same as in[106], [107]:

$$\int_{CV}^{E} e^{a(x)} dx = \begin{cases} \Delta x_E \dfrac{e^{a(E)} - e^{a(CV)}}{a(E) - a(CV)} & \text{, if} \quad a(E) \neq a(CV) \\ \Delta x_E e^{a(CV)} & \text{, if} \quad a(E) = a(CV) \end{cases} \tag{3.104}$$

Replacing the integral in equation (3.103) considering the first case, we obtain:

$$(J_n)_e = \frac{(\mu_n)_e}{\Delta x_E}\left[\frac{(\psi_{n_E} - \psi_{n_{CV}})(u_E - u_{CV})}{e^{-\psi_{n_E}} - e^{-\psi_{n_{CV}}}}\right] \tag{3.105}$$

Moreover, using equation (3.63) we can rewrite the equation (3.105) in terms of electron concentration:

$$(J_n)_e = \frac{(\mu_n)_e}{\Delta x_E}\left[-\frac{(\psi_{n_E} - \psi_{n_{CV}})}{e^{\left(\psi_{n_E} - \psi_{n_{CV}}\right)} - 1} n_E + \frac{(\psi_{n_{CV}} - \psi_{n_E})}{e^{\left(\psi_{n_{CV}} - \psi_{n_E}\right)} - 1} n_{CV}\right] \tag{3.106}$$

Rewriting the equation (3.106) with the help of Bernoulli function, we can combine the two cases as follows:

$$(J_n)_e = -\frac{(\mu_n)_e}{\Delta x_E}\left[B\left(\psi_{n_E} - \psi_{n_{CV}}\right) n_E - B\left(\psi_{n_{CV}} - \psi_{n_E}\right) n_{CV}\right] \tag{3.107}$$

where:

$$B(x) = \frac{x}{e^x - 1}, \quad B(0) = 1 \tag{3.108}$$

In similar manner, we can approximate the current densities at the interfaces for rest of the neighbours as follows:

$$(J_n)_w = -\frac{(\mu_n)_w}{\Delta x_W}\left[B\left(\psi_{n_{CV}} - \psi_{n_W}\right) n_{CV} - B\left(\psi_{n_W} - \psi_{n_{CV}}\right) n_W\right] \tag{3.109}$$

$$(J_n)_n = -\frac{(\mu_n)_n}{\Delta y_N}\left[B\left(\psi_{n_N} - \psi_{n_{CV}}\right) n_N - B\left(\psi_{n_{CV}} - \psi_{n_N}\right) n_{CV}\right] \tag{3.110}$$

$$(J_n)_s = -\frac{(\mu_n)_s}{\Delta y_S}\left[B\left(\psi_{n_{CV}} - \psi_{n_S}\right) n_{CV} - B\left(\psi_{n_S} - \psi_{n_{CV}}\right) n_S\right] \tag{3.111}$$

Substituting equations (3.107), (3.109), (3.110) and (3.111) in equation (3.100), we obtain:

$$\beta_{n_{CV}} n_{CV} + \sum_i \beta_{n_i} n_i = F_n; \qquad i = E, W, N, S \tag{3.112}$$

where:

$$\begin{aligned}
\beta_{n_E} &= -(\mu_n)_e \frac{\Delta y_e}{\Delta x_E} B\left(\psi_{n_E} - \psi_{n_{CV}}\right) \\
\beta_{n_W} &= -(\mu_n)_w \frac{\Delta y_w}{\Delta x_W} B\left(\psi_{n_W} - \psi_{n_{CV}}\right) \\
\beta_{n_N} &= -(\mu_n)_n \frac{\Delta x_n}{\Delta y_N} B\left(\psi_{n_N} - \psi_{n_{CV}}\right) \\
\beta_{n_S} &= -(\mu_n)_s \frac{\Delta x_s}{\Delta y_S} B\left(\psi_{n_S} - \psi_{n_{CV}}\right) \\
\beta_{n_{CV}} &= (\mu_n)_e \frac{\Delta y_e}{\Delta x_E} B\left(\psi_{n_{CV}} - \psi_{n_E}\right) + (\mu_n)_w \frac{\Delta y_w}{\Delta x_W} B\left(\psi_{n_{CV}} - \psi_{n_W}\right) + \\
&\qquad (\mu_n)_n \frac{\Delta x_n}{\Delta y_N} B\left(\psi_{n_{CV}} - \psi_{n_N}\right) + (\mu_n)_s \frac{\Delta x_s}{\Delta y_S} B\left(\psi_{n_{CV}} - \psi_{n_S}\right)
\end{aligned}$$

$$F_n = (G - R)\Delta x \Delta y$$

Applying the same approach for discretizing the hole continuity equation (3.87), we get:

$$\beta_{p_{CV}} p_{CV} + \sum_i \beta_{p_i} p_i = F_p; \qquad i = E, W, N, S \tag{3.113}$$

where:

$$\begin{aligned}
\beta_{p_E} &= (\mu_p)_e \frac{\Delta y_e}{\Delta x_E} B\left(\psi_{p_{CV}} - \psi_{p_E}\right)\\
\beta_{p_W} &= (\mu_p)_w \frac{\Delta y_w}{\Delta x_W} B\left(\psi_{p_{CV}} - \psi_{p_W}\right)\\
\beta_{p_N} &= (\mu_p)_n \frac{\Delta x_n}{\Delta y_N} B\left(\psi_{p_{CV}} - \psi_{p_N}\right)\\
\beta_{p_S} &= (\mu_p)_s \frac{\Delta x_s}{\Delta y_S} B\left(\psi_{p_{CV}} - \psi_{p_S}\right)\\
\beta_{p_{CV}} &= -\Big((\mu_p)_e \frac{\Delta y_e}{\Delta x_E} B\left(\psi_{p_E} - \psi_{p_{CV}}\right) + (\mu_p)_w \frac{\Delta y_w}{\Delta x_W} B\left(\psi_{p_W} - \psi_{p_{CV}}\right) +\\
&\qquad (\mu_p)_n \frac{\Delta x_n}{\Delta y_N} B\left(\psi_{p_N} - \psi_{p_{CV}}\right) + (\mu_p)_s \frac{\Delta x_s}{\Delta y_S} B\left(\psi_{p_S} - \psi_{p_{CV}}\right) \Big)\\
F_p &= -(G - R)\Delta x \Delta y
\end{aligned}$$

3.4.4 Solving the discretized non-linear system

The discretization procedures in the previous sections lead to a set of non-linear equations that need to be solved in terms of our set of unknowns (ψ, n, p). The widely used methods to solve this set of equations are the fully coupled Newton's method and the decoupled Gummel's method [108], [109]. In this work, we decided to use Gummel's method even though Newton's method is usually chosen because of its quadratic convergence [110]. One of the advantages of Gummel's method is the insensitivity to the choice of the initial guess compared to Newton's method. This is important since getting a good initial guess is not trivial especially for our problem. One drawback of Gummel's method is that if the recombination term plays an important role, then the method will have a slow convergence rate and it will probably diverge. In the following, we will see how to generate a good initial guess and one way to overcome the recombination term problem by using the so called lagging approach [111], [112].

3.4.4.1 Equilibrium problem

For both methods, having a good initial guess will boost the convergence rate. One possible choice is the solution of the equilibrium problem. By enforcing vanishing current and assuming that the Fermi level is constant throughout the entire system, we will obtain the Poisson's equation at the thermodynamic equilibrium conditions as follows:

$$\nabla \cdot (\varepsilon_r \nabla \psi_{eq}) = N_C e^{(\psi_{eq}+\chi)} - N_V e^{(-\psi_{eq}-\chi-E_g)} - C \tag{3.114}$$

where ψ_{eq} is the electrostatic potential at thermodynamic equilibrium conditions. In equation (3.114), without loss of generality, we assumed that the Fermi level is equal to zero ($E_F = 0$). With suitable boundary conditions for ψ_{eq}, depending on the type of the contact, we solved the non-linear Poisson's equation. In the same way as in section 3.4.2, we used the fixed-point method to linearize equation (3.114):

$$\nabla \cdot (\varepsilon_r \nabla \psi_{eq}^{l+1}) - (n_{eq}^l - p_{eq}^l)\psi_{eq}^{l+1} = -(n_{eq}^l - p_{eq}^l)\psi_{eq}^l + n_{eq}^l - p_{eq}^l - C \tag{3.115}$$

where

$$n_{eq}^l = N_C e^{\left(\psi_{eq}^l+\chi\right)} \tag{3.116}$$

$$p_{eq}^l = N_V e^{\left(-\psi_{eq}^l-\chi-E_{\mathrm{g}}\right)} \tag{3.117}$$

are the electron and hole densities at thermodynamic equilibrium conditions and ψ_{eq}^l is the potential value from the previous iteration. With good initial guess, depending on the type of the contact, equation (3.115) is solved iteratively until convergence. The resulting solution (ψ_{eq}, n_{eq}, p_{eq}) will be the initial guess for Gummel's iteration.

3.4.4.2 Gummel's Iteration

Gummel [108], [109] developed an iterative approach to solve the coupled non-linear system of equations by decoupling scheme. Knowing the solution from the previous iteration (ψ^l, n^l, p^l) we can solve the linearized Poisson's equation (3.91) to obtain the value of the electrostatic potential ψ^{l+1} for the next step. After that, using the updated solution (ψ^{l+1}, n^l, p^l) we solve the continuity equation for electron (3.81) to update the value of the electron density n^{l+1}. Finally, we use (ψ^{l+1}, n^{l+1}, p^l) to evaluate the hole density p^{l+1} by solving the continuity equation for hole (3.82). This procedure is repeated until convergence is obtained.

Figure 3.5 illustrates the algorithm we used in our code to solve the non-linear system. We start by solving the equilibrium problem to obtain the initial guess (ψ_{eq}, n_{eq}, p_{eq}) for the out-of-equilibrium problem. We use that to solve the continuity equation for electron to update the electron density and then solving the continuity equation for hole to update the hole density. After that, we use the updated values to evaluate the electrostatic potential of the next step. In the continuity equation for electron and hole, we computed the recombination term depending on the previous step. When the recombination term is important, this will lead the system to diverge and to overcome this, we used the lagging approach.

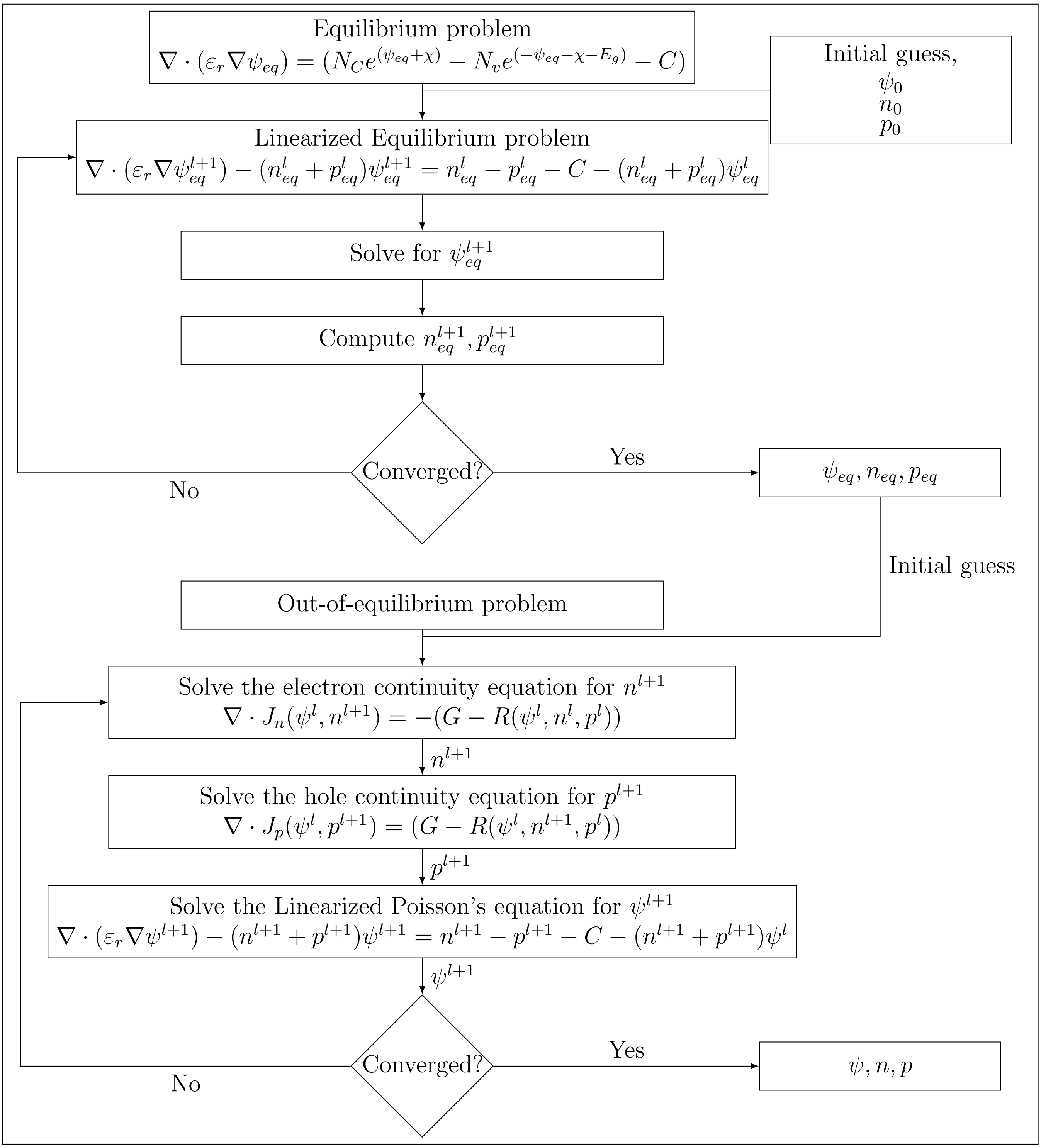

Figure 3.5: The algorithm used for our code.

3.4.4.3 Lagging approach

Seidman and Choo [111] suggested partial linearization of the recombination term by separating it into two terms. This implies an implicit treatment of the recombination rate in the continuity equation. In our model, we assumed having only the Shocley-Read-Hall recombination and it separates as follows:

$$R_n = \frac{p}{\tau_p(n+n_t)+\tau_n(p+p_t)}n - \frac{n_i^2}{\tau_p(n+n_t)+\tau_n(p+p_t)} \tag{3.118}$$

$$R_p = \frac{n}{\tau_p(n+n_t)+\tau_n(p+p_t)}p - \frac{n_i^2}{\tau_p(n+n_t)+\tau_n(p+p_t)} \tag{3.119}$$

where R_n and R_p are the separated recombination rate for electron and hole, respectively. This will require to update some coefficients in the discretized equations (3.112) and (3.113) as follows:

$$\begin{aligned}
\beta_{n_{CV}} = {} & (\mu_n)_e \frac{\Delta y_e}{\Delta x_E} B\left(\psi_{n_{CV}} - \psi_{n_E}\right) + (\mu_n)_w \frac{\Delta y_w}{\Delta x_W} B\left(\psi_{n_{CV}} - \psi_{n_W}\right) + \\
& (\mu_n)_n \frac{\Delta x_n}{\Delta y_N} B\left(\psi_{n_{CV}} - \psi_{n_N}\right) + (\mu_n)_s \frac{\Delta x_s}{\Delta y_S} B\left(\psi_{n_{CV}} - \psi_{n_S}\right) + \\
& \left(\frac{p}{\tau_p(n+n_t)+\tau_n(p+p_t)}\right) \Delta x \Delta y \\
F_n = {} & \left(G + \left(\frac{n_i^2}{\tau_p(n+n_t)+\tau_n(p+p_t)}\right)\right) \Delta x \Delta y
\end{aligned}$$

$$\begin{aligned}
\beta_{p_{CV}} = {} & -\Big((\mu_p)_e \frac{\Delta y_e}{\Delta x_E} B\left(\psi_{p_E} - \psi_{p_{CV}}\right) + (\mu_p)_w \frac{\Delta y_w}{\Delta x_W} B\left(\psi_{p_W} - \psi_{p_{CV}}\right) + \\
& (\mu_p)_n \frac{\Delta x_n}{\Delta y_N} B\left(\psi_{p_N} - \psi_{p_{CV}}\right) + (\mu_p)_s \frac{\Delta x_s}{\Delta y_S} B\left(\psi_{p_S} - \psi_{p_{CV}}\right) + \\
& \left(\frac{n}{\tau_p(n+n_t)+\tau_n(p+p_t)}\right) \Delta x \Delta y\Big) \\
F_p = {} & -\left(G + \left(\frac{n_i^2}{\tau_p(n+n_t)+\tau_n(p+p_t)}\right)\right) \Delta x \Delta y
\end{aligned}$$

3.4.5 Summary of section 3.4

The main choices made in this section were:

- To consider the system to be solved in its dimensionless form to avoid numerical overflow due to the important difference in the magnitude of the dimensioned unknowns.
- Linearization of Poisson's equation using the fixed-point method.
- Discretization of the equations using the cell centred finite volume method.
- Approximation of the current density at the interfaces of the control volumes based on the Scharfetter and Gummel numerically stable scheme.
- Resolution of the resulting non-linear system of equations by Gummel's method combined with the lagging approach.

3.5 Supplementary Results

In this section, we give supplementary results to the simulation results presented in section 3.2. We start with the validation of our simulator by comparing its results with that of Sesame software [113]. Then, the employment of Monte-Carlo simulation to obtain the XBIC generation rate is detailed. Finally, the effect of change of some material parameters on the XBIC signal is presented.

3.5.1 Validation

In this part, we compare the results of our simulator with the well established package Sesame. Sesame is a 2D python-based solar cell modelling tool developed in 2019 and it has been benchmarked against other software packages like Sentaurus [114], COMSOL [115], and SCAPS [116]. We report the results of two tests in this subsection considering a 2D p-n homojunction first and then a 2D p-n heterojunction.

We first considered the case of a 2D p-n homojunction with the material parameters given in table 3.2 and with the geometry shown in Figure 3.6. The system is square with sides of 4 µm with n-type material of 2 µm thickness with doping 10^{23} m^{-3} and p-type material with doping 10^{21} m^{-3}. At the vertical walls, we imposed periodic boundary conditions and assumed having Ohmic boundary conditions at the top and bottom contacts.

Parameter [units]	Value
N_C [m^{-3}]	8×10^{23}
N_V [m^{-3}]	1.8×10^{25}
E_g [eV]	1.5
χ [eV]	3.9
ε_r [-]	9.4
μ_n [m^{2}V^{-1}s^{-1}]	1×10^{-2}
μ_p [m^{2}V^{-1}s^{-1}]	1×10^{-2}
τ_n [s]	1×10^{-8}
τ_p [s]	1×10^{-8}

Table 3.2: Homojunction material parameters.

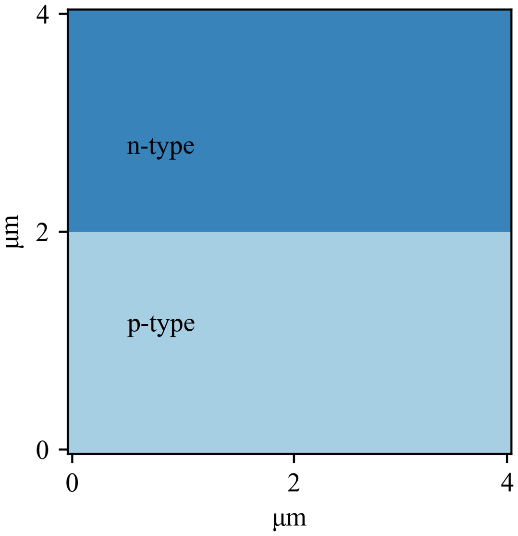

Figure 3.6: Homojunction geometry.

For the generation rate (G), we used a simple version of Lambert-Beer absorption model as follows:

$$G(y) = \alpha\phi e^{(-\alpha y)} \tag{3.120}$$

where $\alpha = 2.3\times10^6$ m^{-1} is the absorption coefficient and $\phi = 10^{21}$ m^{-2}s^{-1} is the incident flux.

Comparisons are made on the computed I-V curve (current-voltage characteristic curve) with our simulator and Sesame. The I-V curve is a graphical representation of the relationship between the applied voltage at the contacts and the current flowing through the device. It is one of the most common methods in characterizing solar cell devices. Key properties like short-circuit current (I_{SC}), open-circuit voltage (V_{OC}), maximum power point (mpp), fill factor (FF) and energy conversion efficiency (η) can be extracted and computed from the shape and details of the curve [117], [118]. Figure 3.7a shows the computed J-V curve (J here stands for current density) under illumination with our simulator and Sesame, while Figure 3.7b shows the computed band diagram under short circuit conditions. From Figure 3.7, we see good agreement between our simulator and Sesame software.

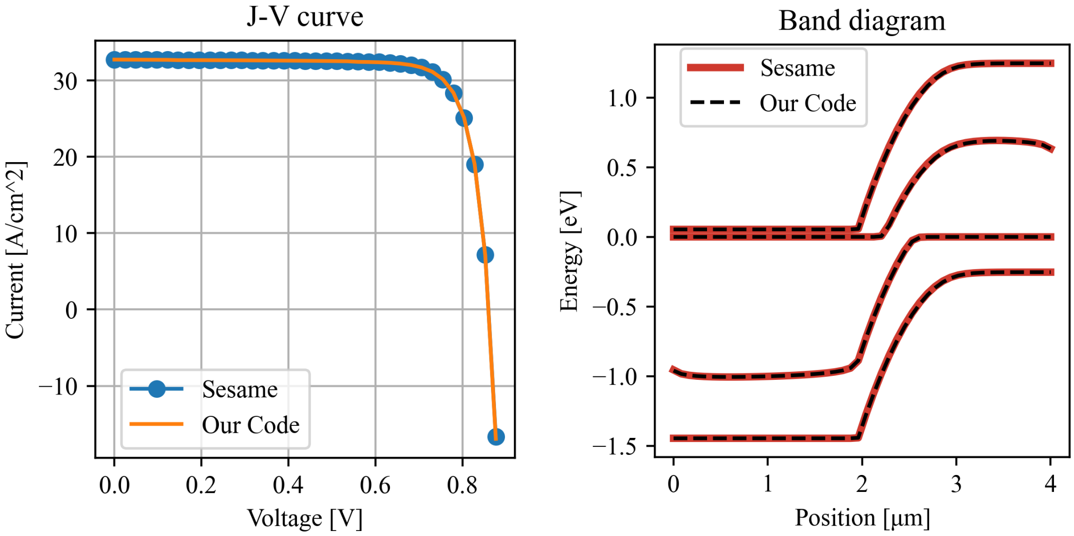

(a) (b)

Figure 3.7: Comparison between our simulator and Sesame for the homojunction test. (a) J-V curve. (b) Band diagram under short circuit conditions.

Next, we considered a 2D p-n heterojunction with the geometry shown in Figure 3.8. Material 1 was considered as p-type with doping 10^{21} m^{-3} and thickness of 1.85 µm while material 2 was considered as n-type with doping 10^{23} m^{-3} and thickness of 0.15 µm. Table 3.3 shows the materials parameters used in the simulations. In the same way as in the homojunction test, we assumed periodic boundary conditions at the vertical walls, Ohmic boundary conditions at the top and bottom contacts and used the same generation rate.

The illuminated J-V curve was computed with our simulator and Sesame, and the results are shown in Figure 3.9a. The band diagram under illumination was computed as well and the results are presented in Figure 3.9b. Similar to the homojunction test, we see a good agreement between our simulator and Sesame software for the heterojunction test.

From the tests we performed, a good agreement was found between our simulator and Sesame. The need for new simulator was due to the fact that the existent softwares deal only with virtual domains (samples). Our simulator was designed to take into account

Parameter [units]	Material 1	Material 2
N_C [m^{-3}]	8×10^{23}	2.2×10^{24}
N_V [m^{-3}]	1.8×10^{25}	1.8×10^{25}
E_g [eV]	1.5	2.4
χ [eV]	3.9	4
ε_r [-]	9.4	10
μ_n [m^{2}V^{-1}s^{-1}]	320×10^{-4}	1×10^{-2}
μ_p [m^{2}V^{-1}s^{-1}]	40×10^{-4}	1×10^{-2}
τ_n [s]	5×10^{-9}	1×10^{-8}
τ_p [s]	5×10^{-9}	1×10^{-13}

Table 3.3: Heterojunction materials parameters.

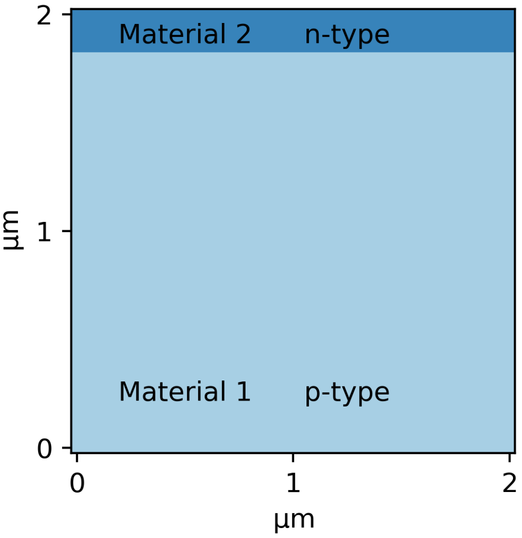

Figure 3.8: Heterojunction geometry description.

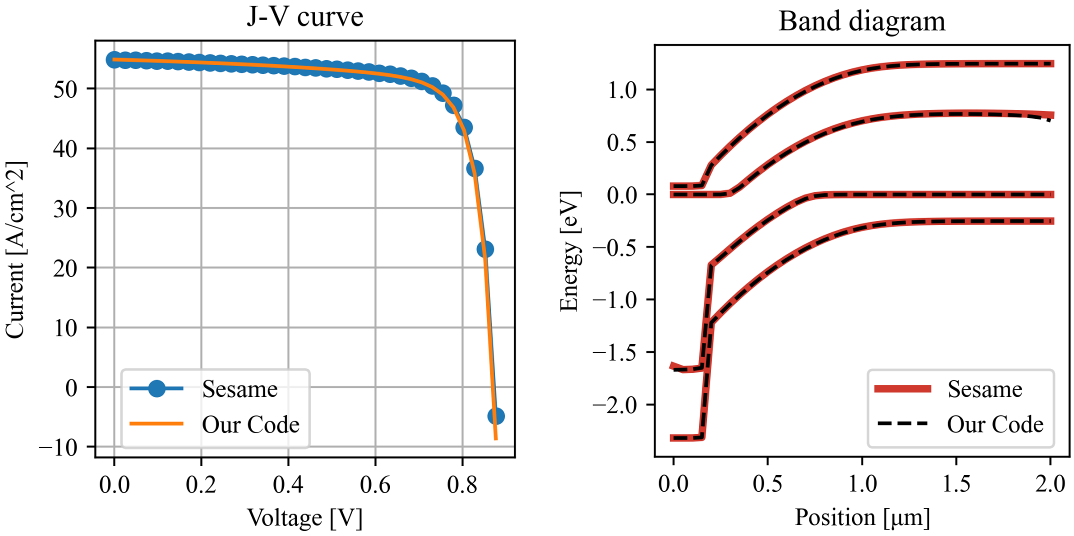

(a)

(b)

Figure 3.9: Comparison between our simulator and Sesame for the heterojunction test. (a) J-V curve. (b) Band diagram under short circuit conditions.

XBIC experiments output. The XRF data was used to generate the computation domain which reflects the real sample structure. Moreover, it was developed to take into account the Monte-Carlo simulations results and use them to produce the generation rates used in the simulations.

3.5.2 XBIC Generation rate

For the evaluation of the interaction volume of the X-ray beam with the solar cell layers, Monte-Carlo simulations have been performed based on the layer stack described in section 3.2. For each material, a cylinder of material was considered with a 1 µm thickness and a diameter of 1 cm large enough to include all scattering. Herein, the X-ray beam is considered as a perfect pencil beam hitting perpendicularly each cylinder at coordinates $(R, Z) = (0, 0)$. From this 3D simulation with 10^{12} incident photons, we have extracted the dose density, i.e., the energy deposited in the layer per unit volume as a function of the radial position R and the depth Z, see Figure 3.10a.

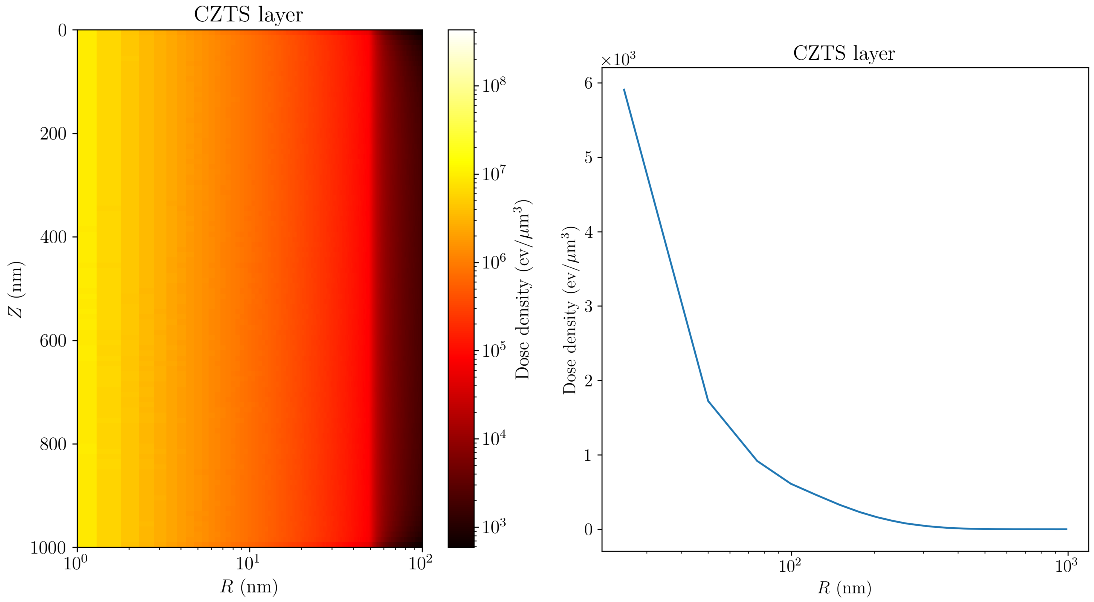

(a) (b)

Figure 3.10: Monte-Carlo based three-dimensional simulation of the dose distribution in CZTS layer for X-ray photons incident perpendicularly at depth $Z = 0$ and radial distance $R = 0$. (*a*) Radial dose density distribution with logarithmic color scale. (*b*) Depth integrated dose density as a function of R.

Figure 3.10b shows the depth integrated dose density as function of R. We used this data to build the generation profile for each pixel with the following assumptions: the photon scattering is allowed only in pixels of the same layer and, for the pixels at the lateral boundaries, we impose periodicity. The term G then is computed with the following formula:

$$G = \frac{\text{Dose density} \times \text{photons flux}}{W} \tag{3.121}$$

where W is the pair creation energy and it is approximately equal to $3E_\mathrm{g}$ [119]. For each pixel in the computation domain the generation rate was computed. Figure 3.11 shows three 2D examples for the generation rate in different layers. The sharp loss of the XBIC signal in the simulation results near the heterointerface, presented in section 3.2, might also be due to our simplified approach to include Monte Carlo simulations for each material separately, which will necessarily lead to inaccurate generation profiles at interfaces.

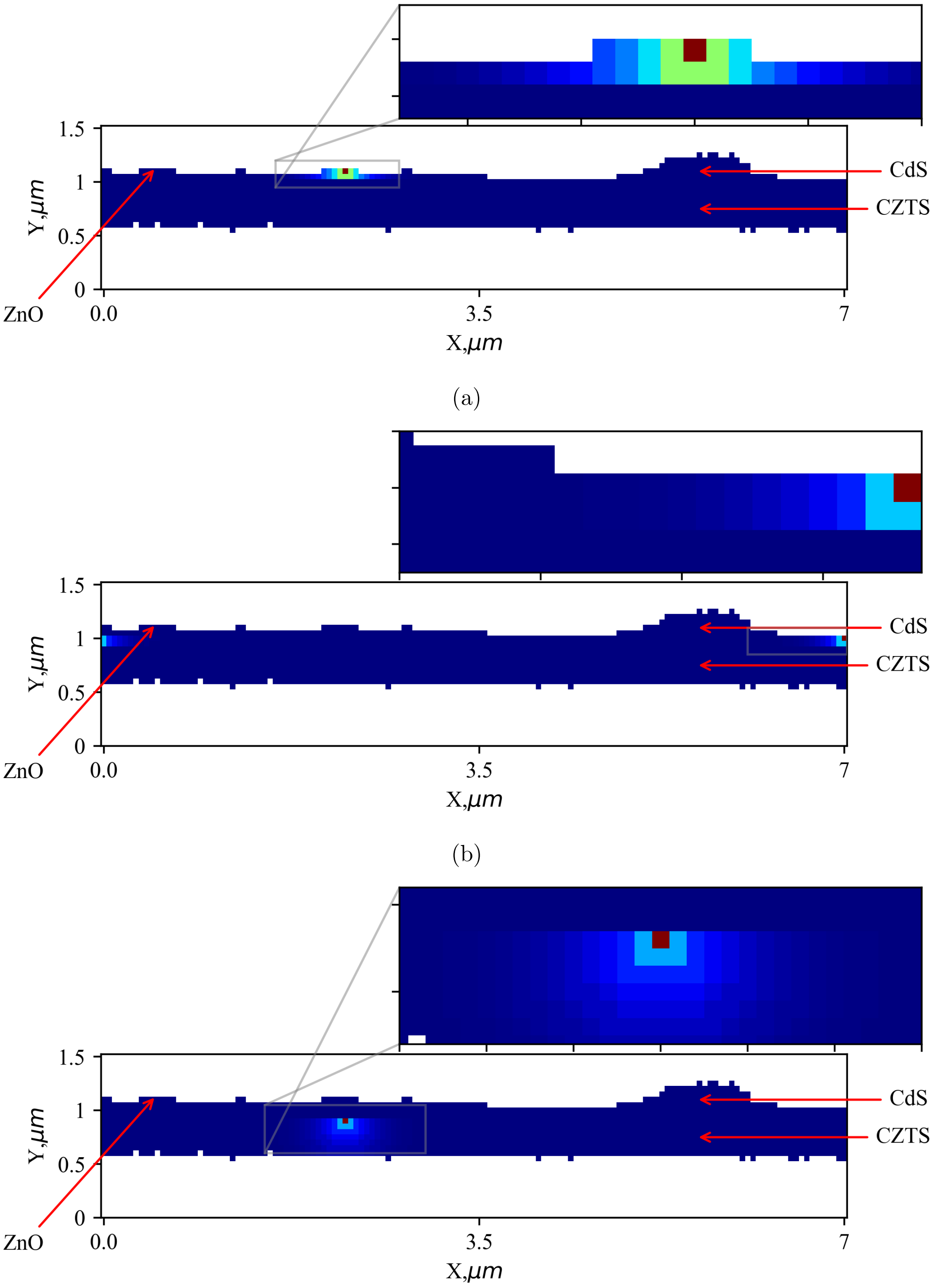

(a)

(b)

(c)

Figure 3.11: 2D generation profile examples in different layers with zoom: (a) In ZnO, (b) in CdS and (c) in CZTS.

3.5.3 Effects of the absorber layer parameters on the XBIC signal

From the XRF results (see Fig. 3 in section 3.2), compositional inhomogeneities within the CZTS layer can be seen (highlighted with white arrows). They are associated with relatively lower projected intensities of all elements composing the layer. This can be caused by voids between CZTS grains filled with CdS. At the nano scale the effects of such defects on the performance of the device can be seen by correlating the XRF data with the XBIC ones. Homogeneous layers with constant bulk parameters were assumed in our simulations. At this scale, this was an over simplification and material parameters taking into account the real material composition should be used. Normally, device design are done using ideal material parameters in order to meet the application requirements. Nevertheless, due to the manufacturing and deposition processes parameters variations are unavoidable [120]. The most common impacted parameters are band gap, acceptor density and carriers lifetime [121]–[123]. They will affect the performance of the device at the nano scale, which will impact the performance on the larger scale. In this section, the effect of these parameters for the absorber layer at the nano scale were investigated.

In the 2D sensitivity analysis, the results presented in Fig. 4(e)(section 3.2) were used as the simulation reference. We studied the effect of the band gap (energy gap E_g), acceptor densities (N_A) and carriers lifetime (τ_n and τ_p) for the absorber layer (CZTS) on the XBIC signal. Three different layer configurations are used to present the 2D sensitivity analysis as line profiles. These configurations, noted S1, S2 and S3, are localized in Figure 3.12. In S1, we have the complete layer structure ZnO/CdS/CZTS, in S2 and S3 the ZnO layer is lacking, and S3 is on the CdS defect.

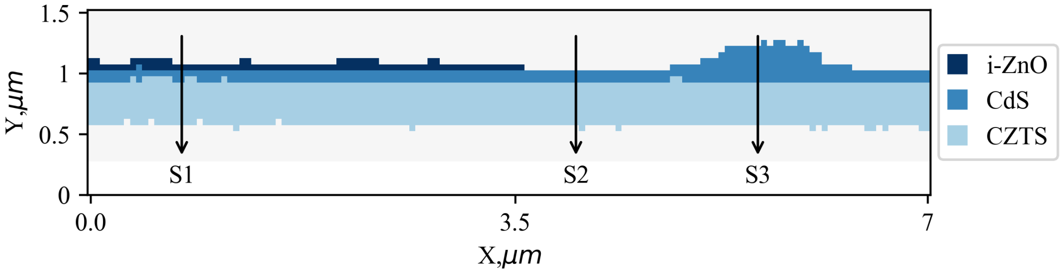

Figure 3.12: The computation domain with three distinct layer configurations S1, S2 and S3.

The influence of energy band gap of CZTS on the XBIC signal was investigated by varying the band gap from 1.3 eV to 1.5 eV (possible range according to [124], [125]) and simulation results are shown in Figure 3.13. It can be seen that by increasing the band gap of CZTS the XBIC signal decreases. This is mainly due to the direct dependence of the generation rate on the band gap as shown in equation 3.121. Large band gap means less electron-hole pair generation, resulting in less short circuit current (XBIC signal). Lacking ZnO is slightly reducing this effect as shown in Figures 3.13(b–c).

CZTS is a self-doped semiconductor with intrinsic defects formations. The resistivity and carrier densities are mainly coming from $Cu - Zn$ antisite defect and depends on the ratio of $Cu/(Zn + Sn)$ [126]. The effect of carrier density on the XBIC signal at the nano scale was studied by varying the ionized acceptor density (N_A) from 4×10^{20} m^{-3} to 6×10^{22} m^{-3} and the results are presented in Figure 3.14. It can be seen from Figure 3.14a that the XBIC signal remains nearly unchanged when the acceptor density is less than 4×10^{21} m^{-3}, however, beyond this value the XBIC signal is strongly affected and the peak

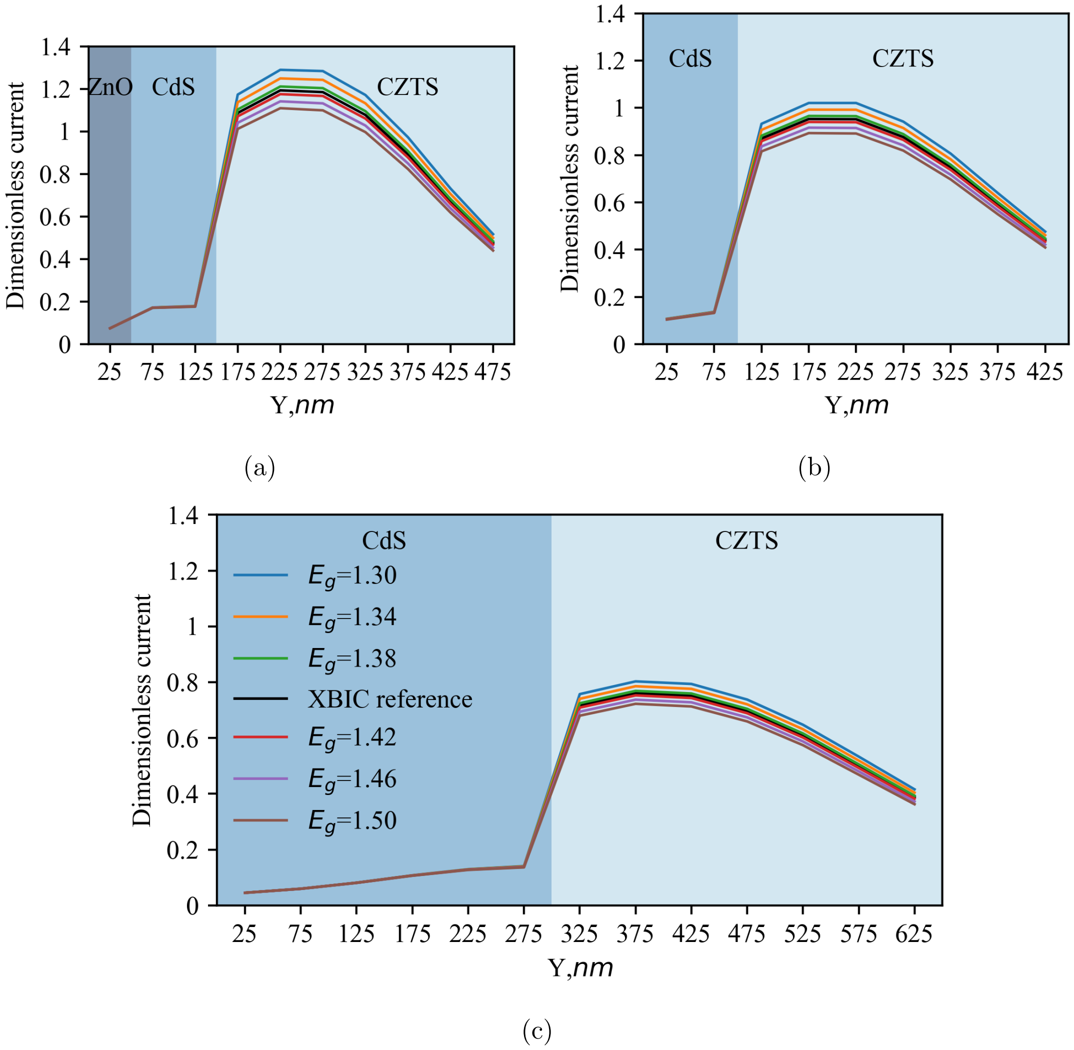

Figure 3.13: The effects of changing the CZTS band gap along S1 (a), S2 (b) and S3 (c). The legend displayed in panel (c) refers to all panels.

is shifted towards the CZTS/CdS interface. The decrease of the XBIC signal is probably due to the recombination process that is enhanced by increasing the acceptor density. This will reduce the minority carrier lifetime (electrons) and lower the possibility of collection of photon-generated electrons and thus lower the XBIC signal. Furthermore, increasing the acceptor concentration will decrease the depletion width towards the absorber layer and cause the XBIC peak to shift towards the CZTS/CdS interface. In principle, similar behaviour can be seen in Figures 3.14(b–c), but it mostly affects the electron-hole pairs generated deeply in the CZTS layer and decreases with the increase of the CdS thickness.

The carrier lifetime is one of the parameters which affects the solar cell performance. In CZTS, it is very short and is found to be lower than 1 ns [127]. The carrier lifetime is related to the diffusion length which inturn depends on the layer thickness [128], [129]. For the system we have, we studied the effect of the absorber carriers lifetime on the XBIC signal, see Figure 3.15. In Figure 3.15a we observe a saturation state for carriers lifetime larger than 1×10^{-9} s (1 ns), which indicates that for these values the diffusion length is larger than the thickness of the absorber layer. For shorter lifetime, the carriers

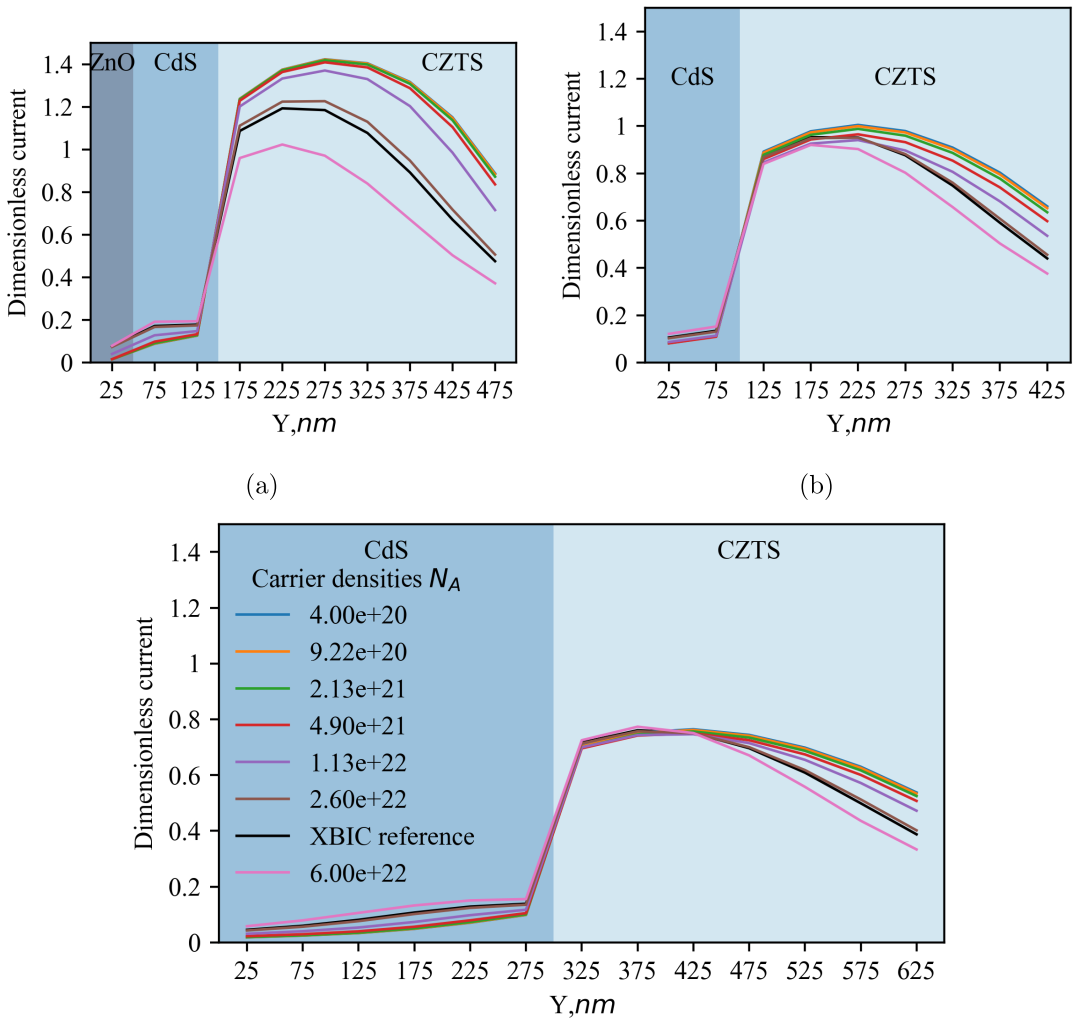

(a)

(b)

(c)

Figure 3.14: The 2D sensitivity analysis to evaluate the effects of changing the CZTS carriers density along S1 (a), S2 (b), and S3 (c). The legend displayed in figure (c) refers to all figures.

generated outside the depletion region are more likely to recombine before diffusion to the depletion region and being collected. This explains the decrease and the shift of XBIC signal with shorter carriers lifetime. Lacking ZnO in Figure 3.15(b–c) increases the effect of decreasing the carriers lifetime on the XBIC signal.

From the above 2D sensitivity analysis, we see that the performance of thin film solar cells is very sensitive to materials parameters at nano scale, and the functionalities are not only dependent on the geometry and the bulk properties. The presence of nano scale defects is highly affecting the performance of the device which impacts the performance in the application scale. The XBIC signal losses at the inhomogeneous composition defects are probably due to the variation of the band gap along the device with higher values along the defects. Moreover, these defects might create recombination centres which reduce the carriers lifetime and cause less charge collection.

The recorded data from a 2D projection with the present resolution did not allow the unambiguous assignment of chemical and morphological inhomogeneities in the sample.

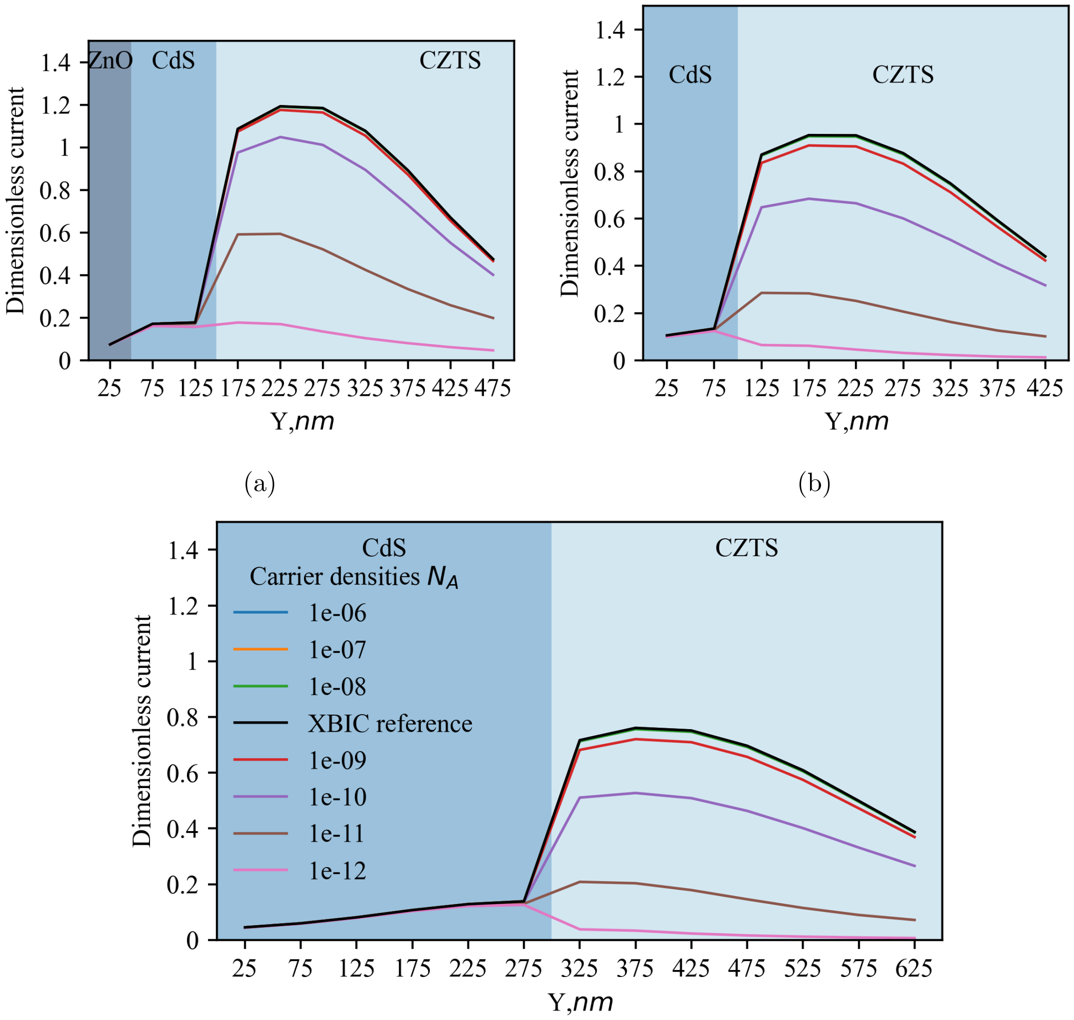

(a) (b) (c)

Figure 3.15: The effects of changing the CZTS carriers lifetime along S1 (a), S2 (b) and S3 (c). The legend displayed in panel (c) refers to all panels.

This makes the interpretation of such defects using 2D simulations tools limited.

3.6 Summary of chapter 3

In this chapter we presented our collaborative work in the framework of MUMMERING project. The experimental setup and the targeted sample along with the experimental and main simulation results were presented in section 3.2. The XBIC experiment was performed by the researchers from DTU and the Monte-Carlo simulations were performed in collaboration with Michael Stuckelberger from DESY.

Physical principles and assumptions we used for formulating the problem to be solved were presented. Poisson's equation with the drift-diffusion model were used to describe the charge collection in semiconductor devices.

We developed a simulator based on cell centred finite volume method combined with Scharfetter Gummel scheme. The simulator was designed to take into account:

- The real layer structure in the simulations by using 2D computation domain constructed from the XRF data.
- The Monte-Carlo simulations in the computation of the 2D generation profiles.

The developed simulator was compared with Sesame package, showing a good agreement for simple cases. 2D sensitivity analyses were performed to investigate some defects that appear from correlating the XRF data with the XBIC experimental results. In section 3.2, we studied the effect of the contact type and the effects of lacking ZnO layer on the device performance. In the supplementary results, the inhomogeneous composition defects were addressed by studying the effects of the absorber layer (CZTS) parameters on the XBIC signal at the nano scale.

To our best knowledge, this work can be considered as the first attempt to simulate XBIC measurements for a realistic sample geometry at the nanoscale.

3.7 Conclusions

In this chapter we presented the second example of multi-scale numerical modelling combined with synchrotron X-ray experiments. The interest of XBIC as a method of characterization of functional materials such as solar cells has been demonstrated as well as the benefits of combining it with numerical simulations to relate local defects to global performances.

We developed a multi-scale approach based on first-principles to simulate XBIC experiments. The conventional approach of modelling the performance of solar cells considers the nominal architecture of the device. However, structural variations resulting, e.g., from the inhomogeneous deposition of layers during fabrication, as well as various defects occurring in real devices are not considered. To overpass these limitations, we presented an approach in which material parameters can be associated with the local electrical performance based on the actual structure of the device. The approach consists of constructing a computational domain from X-ray fluorescence data used for first-principles modelling of the XBIC signal. The devolved model can then be used to interpret some aspects of the experimentally measured XBIC signal. Our approach shows that the electronic defects can be identified by XBIC, correlated with compositional and structural inhomogeneities from XRF and can be explained by simulations.

The 2D sensitivity analyses suggest that the XBIC loss at the regions lacking the ZnO layer was caused by the high barrier height at the CdS contact and the losses increase with the electronic defects. The presence of the ZnO layer was essential for the device under consideration. Furthermore, having suitable window layer with low barrier height will increase the performance in such devices. The inhomogeneous composition defects caused losses of the XBIC signal, from our supplementary results this might be explained by the variations of the band gap with high values along the defects and the creation of recombination centres which reduced the carriers lifetime.

The proposed simulator based on first-principles was precise enough to explain experimentally observed features. It has some limitations, but makes a significant step forward in the understanding of XBIC measurements by providing results at the nano scale. Acquiring material properties at the same nano scale is challenging, and even with advanced models producing accurate device description, if some material parameters are undetermined, the relevance of the results might be questionable.

To realize a better representation of the typically nano structured 3rd generation solar-cell devices, some challenging requirements should ideally be met: the material properties need to be determined at the same scale for the measurements and simulation, as they cannot be assumed to be representative of homogeneous materials. Furthermore, our simulator includes Monte Carlo simulations for each material separately, which will necessarily lead to approximate generation profiles at interfaces.

The 2D aspect of the problem could be extended to 3D by tomographic acquisition and accompanying extension of the model to 3D. This is important to handle the secondary phases and grain boundary issues in CZTS devices. Finally, a detailed and advanced treatment for heterointerface should be addressed to describe the heterojunction at CZTS/CdS interface.

Conclusions and Perspectives

In this thesis, we presented two examples of multi-scale numerical modelling combined with synchrotron X-ray experiments: (1) Multi-scale imaging and modelling for reactive transport at the pore scale, (2) Multi-modal characterization of Kesterite thin-film solar cells: experimental results and numerical interpretation. We showed the importance of multi-scale imaging techniques in the approximation of the effective properties and the advantages of combining it with multi-scale numerical modelling procedures. Furthermore, we illustrated the benefits of combining multi-scale numerical modelling with XBIC experiments to relate local defects to global performances.

In the first example, the proposed multi-scale imaging and modelling approach has been implemented successfully and various test cases of synthesized and real 3D volume were presented. The proposed grid coarsening approach and the spatial discretization were able to improve the computational aspects of the problem and to maintain a high global accuracy of the results, respectively. Using the multi-scale imaging approach in the local mesh refinement step, we were able to improve the quality of the results when computing the effective properties. Further investigation is needed to identify the critical regions at the local mesh refinement step.

The BiConjugate gradient method used to solve the nonsymmetric system, resulting from applying the spatial discretization on the NUCM, was one of the factors limiting the effects of the grid coarsening approach on the CPU time. Different methods to solve the nonsymmetric system can be investigated and their effect on the CPU time can be tested. Furthermore, the barycentric interpolation used to develop the spatial discretization causes the nonsymmetric system. To solve this problem, a symmetrical barycentric interpolation can be developed and tested.

The proposed NUCM with its benefits motivates the extension to reactive transport in porous media. Using the cell centred finite volume in the computation of, for instance, the effective permeability tensor will cause stability problems. Therefore, as future work, a suitable spatial discretization can be developed taking into account staggered grid structures.

Moreover, the artefacts associated with the acquired data sets can be investigated and suitable corrections can be applied. Then, more tests can be performed to study further the effects of the proposed multi-scale imaging and modelling approach on real data sets.

In the second example, we developed a 2D device simulator based on first principles, designed to handle 2D real device structures and to combine Monte-Carlo simulation in order to simulate XBIC experiments. Correlative scanning X-ray microscopy is a powerful tool for studies of functional materials such as solar cells, providing a spatially-resolved correlative characterization of the chemical composition and electrical performance at the nanoscale. XRF maps combined and correlated with XBIC measurements allow visualization of inhomogeneities in all the device layers and correlate them with local charge conversion efficiency. Then, the electronic defects identified from this combination can be explained by using the developed simulator.

The experiment's ultimate resolution was one of the factors limiting the scales at which the modelling was performed. Recent developments in X-ray optics can yield X-ray beams focused down to sub-10-nm [130]. Future experiments combining chemical mapping and electrical performance of thin film devices can differentiate layers with higher accuracy. Furthermore, in the presented 2D drift-diffusion model, a simple model at the heterointerface was used, advanced models can be used instead to improve the quality of the simulation results.

Finally, in this work, we demonstrated with two examples the benefits and advantages of the combination between multi-scale numerical modelling and synchrotron X-ray experiments. Advanced imaging tools provide very large volumes that need to be handled. The development of multi-scale numerical tools is of great importance to analyse and to extract valuable information from these volumes efficiently. On the other hand, the direct comparison between the experimental and the simulation results gives a step forward in the understanding of the functionality of advanced materials.

Bibliography

[1] "MUltiscale, Multimodal and Multidimensional imaging for EngineeRING". (2018), [Online]. Available: `https://cordis.europa.eu/project/id/765604`.

[2] S. Kamrava, M. Sahimi, and P. Tahmasebi, "Simulating fluid flow in complex porous materials by integrating the governing equations with deep-layered machines", *npj Computational Materials*, vol. 7, no. 1, p. 127, Dec. 2021, ISSN: 2057-3960. DOI: `10.1038/s41524-021-00598-2`.

[3] H.Darcy, *Les fontaines publiques de la ville de Dijon: exposition et application...* Victor Dalmont, 1865, p. 343.

[4] E. Sanchez-Palencia, "On the asymptotics of the fluid flow past an array of fixed obstacles", *International Journal of Engineering Science*, vol. 20, no. 12, pp. 1291–1301, Jan. 1982, ISSN: 00207225. DOI: `10.1016/0020-7225(82)90055-6`.

[5] S. Whitaker, "Flow in porous media I: A theoretical derivation of Darcy's law", *Transport in Porous Media*, vol. 1, no. 1, pp. 3–25, 1986, ISSN: 0169-3913. DOI: `10.1007/BF01036523`.

[6] U. D. Schiller and F. Wang, "Multiscale simulation of transport phenomena in porous media: from toy models to materials models", *MRS Communications*, vol. 8, no. 2, pp. 358–371, Jun. 2018, ISSN: 2159-6859. DOI: `10.1557/mrc.2018.29`.

[7] C. M. Marle, *Ecoulements monophasiques en milieux poreux*, 1967.

[8] S. Whitaker, "Diffusion and dispersion in porous media", *AIChE Journal*, vol. 13, no. 3, pp. 420–427, May 1967, ISSN: 0001-1541. DOI: `10.1002/aic.690130308`.

[9] S. Whitaker, *The Method of Volume Averaging* (Theory and Applications of Transport in Porous Media January 1999). Dordrecht: Springer Netherlands, 1999, vol. 13, ISBN: 978-90-481-5142-4. DOI: `10.1007/978-94-017-3389-2`.

[10] D. Ryan, R. Carbonell, and S. Whitaker, "Effective diffusivities for catalyst pellets under reactive conditions", *Chemical Engineering Science*, vol. 35, no. 1-2, pp. 10–16, 1980, ISSN: 00092509. DOI: `10.1016/0009-2509(80)80064-9`.

[11] J. Ochoa, P. Stroeve, and S. Whitaker, "Diffusion and reaction in cellular media", *Chemical Engineering Science*, vol. 41, no. 12, pp. 2999–3013, 1986, ISSN: 00092509. DOI: `10.1016/0009-2509(86)85036-9`.

[12] J.-H. Kim, J. Ochoa, and S. Whitaker, "Diffusion in anisotropic porous media", *Transport in Porous Media*, vol. 2, no. 4, pp. 327–356, Aug. 1987, ISSN: 0169-3913. DOI: `10.1007/BF00136440`.

[13] F. J. Valdés-Parada, D. Lasseux, and S. Whitaker, "Diffusion and Heterogeneous Reaction in Porous Media: The Macroscale Model Revisited", *International Journal of Chemical Reactor Engineering*, vol. 15, no. 6, pp. 1–24, Dec. 2017, ISSN: 1542-6580. DOI: `10.1515/ijcre-2017-0151`.

[14] D. Bernard, "3D Quantification of Pore Scale Geometrical Changes Using Synchrotron Computed", *Oil & Gas Science and Technology*, vol. 60, no. 5, pp. 747–762, Sep. 2005, ISSN: 1294-4475. DOI: `10.2516/ogst:2005053`.

[15] D. Bernard, Ø. Nielsen, L. Salvo, and P. Cloetens, "Permeability assessment by 3D interdendritic flow simulations on microtomography mappings of Al–Cu alloys", *Materials Science and Engineering: A*, vol. 392, no. 1-2, pp. 112–120, Feb. 2005, ISSN: 09215093. DOI: `10.1016/j.msea.2004.09.004`.

[16] L. Salvo, M. Suéry, A. Marmottant, N. Limodin, and D. Bernard, "3D imaging in material science: Application of X-ray tomography", *Comptes Rendus Physique*, vol. 11, no. 9-10, pp. 641–649, Nov. 2010, ISSN: 16310705. DOI: `10.1016/j.crhy.2010.12.003`.

[17] C. Noiriel, C. I. Steefel, L. Yang, and D. Bernard, "Effects of pore-scale precipitation on permeability and flow", *Advances in Water Resources*, vol. 95, pp. 125–137, Sep. 2016, ISSN: 03091708. DOI: `10.1016/j.advwatres.2015.11.013`.

[18] T. Rahman, H. L. Ramandi, H. Roshan, and S. Iglauer, "Representative Elementary Volume of Rock Using X-Ray Microcomputed Tomography: A New Statistical Approach", *Geofluids*, vol. 2020, pp. 1–13, Sep. 2020, ISSN: 1468-8115. DOI: `10.1155/2020/8866486`.

[19] M. Stuckelberger, B. West, T. Nietzold, *et al.*, "Review: Engineering solar cells based on correlative X-ray microscopy", vol. 32, no. 10, pp. 1825–1854, 2017. DOI: `10.1557/jmr.2017.108`.

[20] M. E. Stuckelberger, T. Nietzold, B. West, *et al.*, "Defect activation and annihilation in CIGS solar cells: an operando x-ray microscopy study", *J. Phys.: Energy*, vol. 2, p. 25 001, 2020. DOI: `10.1088/2515-7655/ab5fa6`.

[21] R. P. Winarski, M. V. Holt, V. Rose, *et al.*, "A hard X-ray nanoprobe beamline for nanoscale microscopy", *Journal of Synchrotron Radiation*, vol. 19, no. 6, pp. 1056–1060, Nov. 2012, ISSN: 09090495. DOI: `10.1107/S0909049512036783`.

[22] U. Johansson, D. Carbone, S. Kalbfleisch, *et al.*, "NanoMAX: the hard X-ray nanoprobe beamline at the MAX IV Laboratory", *Journal of Synchrotron Radiation*, vol. 28, no. 6, pp. 1935–1947, Nov. 2021, ISSN: 1600-5775. DOI: `10.1107/S1600577521008213`.

[23] G. Martínez-Criado, J. Villanova, R. Tucoulou, *et al.*, “Id16b: A hard x-ray nanoprobe beamline at the esrf for nano-analysis”, *Journal of synchrotron radiation*, vol. 23, no. 1, pp. 344–352, 2016. DOI: `10.1107/S1600577515019839`.

[24] A. Schropp, R. Döhrmann, S. Botta, *et al.*, “Ptynami: Ptychographic nano-analytical microscope”, *Journal of applied crystallography*, vol. 53, no. 4, pp. 957–971, 2020. DOI: `10.1107/S1600576720008420`.

[25] M. Trushin, O. Vyvenko, W. Seifert, *et al.*, “Combined XBIC/μ-XRF/μ-XAS/DLTS investigation of chemical character and electrical properties of Cu and Ni precipitates in silicon”, in *Physica Status Solidi (C) Current Topics in Solid State Physics*, vol. 6, 2009, pp. 1868–1873. DOI: `10.1002/pssc.200881430`.

[26] C. Ossig, T. Nietzold, B. West, *et al.*, “X-ray Beam Induced Current Measurements for Multi-Modal X-ray Microscopy of Solar Cells”, *Journal of Visualized Experiments*, vol. 2019, no. 150, Aug. 2019, ISSN: 1940-087X. DOI: `10.3791/60001`.

[27] A. Ulvestad, S. O. Hruszkewycz, M. V. Holt, *et al.*, “Multimodal x-ray imaging of grain-level properties and performance in a polycrystalline solar cell”, vol. 26, no. 4, pp. 1316–1321, Jul. 2019. DOI: `10.1107/S1600577519003606`.

[28] I. Calvo-Almazán, A. P. Ulvestad, E. Colegrove, *et al.*, “Strain mapping of CdTe grains in photovoltaic devices”, vol. 9, no. 6, pp. 1790–1799, 2019. DOI: `10.1109/JPHOTOV.2019.2942487`.

[29] C. Ossig, C. Strelow, J. Flügge, *et al.*, “Multi-modal X-ray microscopy measurements of a Cu(In,Ga)Se_2 solar cell”, *materials*, vol. 14, no. 1, p. 228, 2021. DOI: `10.3390/ma14010228`.

[30] C. Ossig, C. Strelow, J. Flügge, *et al.*, “Four-fold multi-modal x-ray microscopy measurements of a cu (in, ga) se2 solar cell”, *Materials*, vol. 14, no. 1, p. 228, 2021. DOI: `10.3390/ma14010228`.

[31] J. Maddox, “The sensational discovery of X-rays”, *Nature*, vol. 375, no. 6528, pp. 183–183, May 1995, ISSN: 0028-0836. DOI: `10.1038/375183a0`.

[32] C. G. BARKLA and J. NICOL, “X-Ray Spectra”, *Nature*, vol. 84, no. 2127, pp. 139–139, Aug. 1910, ISSN: 0028-0836. DOI: `10.1038/084139a0`.

[33] F. R. Elder, A. M. Gurewitsch, R. V. Langmuir, and H. C. Pollock, “Radiation from Electrons in a Synchrotron”, *Physical Review*, vol. 71, no. 11, pp. 829–830, Jun. 1947, ISSN: 0031-899X. DOI: `10.1103/PhysRev.71.829.5`.

[34] D. H. Tomboulian and P. L. Hartman, “Spectral and Angular Distribution of Ultraviolet Radiation from the 300-Mev Cornell Synchrotron”, *Physical Review*, vol. 102, no. 6, pp. 1423–1447, Jun. 1956, ISSN: 0031-899X. DOI: `10.1103/PhysRev.102.1423`.

[35] D. N. Supariasa, *Synchrotron Radiation* (Topics in Current Physics), C. Kunz, Ed. Berlin, Heidelberg: Springer Berlin Heidelberg, 1979, vol. 10, pp. 6–22, ISBN: 978-3-642-81299-6. DOI: `10.1007/978-3-642-81297-2`.

[36] D. J. Holder, P. D. Quinn, and N. G. Wyles, "The SRS at daresbury laboratory: A eulogy to the world's first dedicated high-energy synchrotron radiation source", *EPAC 2008 - Contributions to the Proceedings*, vol. 0806233, pp. 2133–2135, 2008.

[37] K. C. Cramer, "Lightening Europe: Establishing the European Synchrotron Radiation Facility (ESRF)", *History and Technology*, vol. 33, no. 4, pp. 396–427, Oct. 2017, ISSN: 0734-1512. DOI: `10.1080/07341512.2018.1489762`.

[38] P. Scherrer, *Swiss Light Source SLS*. Paul Scherrer Institut, 1999.

[39] Y. Cerenius, F. Hennies, and P. Fernandes Tavares, "Status of the MAX IV Laboratory", *Synchrotron Radiation News*, vol. 29, no. 1, pp. 34–38, Jan. 2016, ISSN: 0894-0886. DOI: `10.1080/08940886.2016.1124683`.

[40] P. Willmott, *An Introduction to Synchrotron Radiation*. Wiley, Jul. 2011, p. 352, ISBN: 9780470745793. DOI: `10.1002/9781119970958`.

[41] A. Balerna and S. Mobilio, "Introduction to Synchrotron Radiation", in *Synchrotron Radiation*, Berlin, Heidelberg: Springer Berlin Heidelberg, 2015, pp. 3–28, ISBN: 9783642553158. DOI: `10.1007/978-3-642-55315-8_1`.

[42] A. Gide, *Advanced Tomographic Methods in Materials Research and Engineering*, J. Banhart, Ed. Oxford University Press, Mar. 2008, pp. 5–24, ISBN: 9780199213245. DOI: `10.1093/acprof:oso/9780199213245.001.0001`.

[43] M. K. Bourbatache, T. D. Le, O. Millet, and C. Moyne, "Limits of Classical Homogenization Procedure for Coupled Diffusion-Heterogeneous Reaction Processes in Porous Media", *Transport in Porous Media*, vol. 140, no. 2, pp. 437–457, Nov. 2021, ISSN: 0169-3913. DOI: `10.1007/s11242-021-01683-2`.

[44] A. M. Tartakovsky, D. M. Tartakovsky, T. D. Scheibe, and P. Meakin, "Hybrid Simulations of Reaction-Diffusion Systems in Porous Media", *SIAM Journal on Scientific Computing*, vol. 30, no. 6, pp. 2799–2816, Jan. 2008, ISSN: 1064-8275. DOI: `10.1137/070691097`.

[45] I. Battiato and D. Tartakovsky, "Applicability regimes for macroscopic models of reactive transport in porous media", *Journal of Contaminant Hydrology*, vol. 120-121, no. C, pp. 18–26, Mar. 2011, ISSN: 01697722. DOI: `10.1016/j.jconhyd.2010.05.005`.

[46] T. Le, D. Lasseux, X. Nguyen, G. Vignoles, N. Mano, and A. Kuhn, "Multi-scale modeling of diffusion and electrochemical reactions in porous micro-electrodes", *Chemical Engineering Science*, vol. 173, pp. 153–167, Dec. 2017, ISSN: 00092509. DOI: `10.1016/j.ces.2017.07.039`.

[47] W. G. Gray, A. L. Dye, J. E. McClure, L. J. Pyrak-Nolte, and C. T. Miller, “On the dynamics and kinematics of two-fluid-phase flow in porous media”, *Water Resources Research*, vol. 51, no. 7, pp. 5365–5381, Jul. 2015, ISSN: 0043-1397. DOI: `10.1002/2015WR016921`.

[48] I. Battiato, P. T. Ferrero V, D. O’ Malley, *et al.*, “Theory and Applications of Macroscale Models in Porous Media”, *Transport in Porous Media*, vol. 130, no. 1, pp. 5–76, Oct. 2019, ISSN: 0169-3913. DOI: `10.1007/s11242-019-01282-2`.

[49] M. K. Bourbatache, O. Millet, and C. Moyne, “Upscaling diffusion–reaction in porous media”, *Acta Mechanica*, vol. 231, no. 5, pp. 2011–2031, May 2020, ISSN: 0001-5970. DOI: `10.1007/s00707-020-02631-9`.

[50] T. Le, D. Lasseux, L. Zhang, *et al.*, “Multiscale modelling of diffusion and enzymatic reaction in porous electrodes in Direct Electron Transfer mode”, *Chemical Engineering Science*, vol. 248, p. 117 157, Feb. 2022, ISSN: 00092509. DOI: `10.1016/j.ces.2021.117157`.

[51] J.-L. Auriault, C. Boutin, and C. Geindreau, *Homogenization of Coupled Phenomena in Heterogenous Media.* London, UK: ISTE, Jan. 2009, ISBN: 9781848211612.

[52] A. Mikelić, V. Devigne, and C. J. van Duijn, “Rigorous Upscaling of the Reactive Flow through a Pore, under Dominant Peclet and Damkohler Numbers”, *SIAM Journal on Mathematical Analysis*, vol. 38, no. 4, pp. 1262–1287, Jan. 2006, ISSN: 0036-1410. DOI: `10.1137/050633573`.

[53] C. T. Gray, William G and Miller, *Introduction to the thermodynamically constrained averaging theory for porous medium systems.* Springer, 2014, ISBN: 9783319040097.

[54] F. Valdes-Parada and J. Alvarez-Ramirez, “On the effective diffusivity under chemical reaction in porous media”, *Chemical Engineering Science*, vol. 65, no. 13, pp. 4100–4104, Jul. 2010, ISSN: 00092509. DOI: `10.1016/j.ces.2010.03.040`.

[55] F. J. Valdés-Parada, M. L. Porter, and B. D. Wood, “The Role of Tortuosity in Upscaling”, *Transport in Porous Media*, vol. 88, no. 1, pp. 1–30, May 2011, ISSN: 0169-3913. DOI: `10.1007/s11242-010-9613-9`.

[56] F. J. Valdés-Parada, D. Lasseux, and S. Whitaker, “Upscaling Reactive Transport Under Hydrodynamic Slip Conditions in Homogeneous Porous Media”, *Water Resources Research*, vol. 56, no. 1, Jan. 2020, ISSN: 0043-1397. DOI: `10.1029/2019WR025954`.

[57] P. Cloetens, W. Ludwig, E. Boller, F. Peyrin, M. Chlenker, and J. Baruchel, “3D IMAGING USING COHERENT SYNCHROTRON RADIATION”, *Image Analysis & Stereology*, vol. 21, no. 4, p. 75, May 2011, ISSN: 1854-5165. DOI: `10.5566/ias.v21.pS75-S85`.

[58] D. Bernard, D. Gendron, J.-M. Heintz, S. Bordère, and J. Etourneau, "First direct 3D visualisation of microstructural evolutions during sintering through X-ray computed microtomography", *Acta Materialia*, vol. 53, no. 1, pp. 121–128, Jan. 2005, ISSN: 13596454. DOI: `10.1016/j.actamat.2004.09.027`.

[59] S. Peng, Q. Hu, S. Dultz, and M. Zhang, "Using X-ray computed tomography in pore structure characterization for a Berea sandstone: Resolution effect", *Journal of Hydrology*, vol. 472-473, pp. 254–261, Nov. 2012, ISSN: 00221694. DOI: `10.1016/j.jhydrol.2012.09.034`.

[60] L. E. Beckingham, C. A. Peters, W. Um, K. W. Jones, and W. B. Lindquist, "2D and 3D imaging resolution trade-offs in quantifying pore throats for prediction of permeability", *Advances in Water Resources*, vol. 62, pp. 1–12, 2013, ISSN: 03091708. DOI: `10.1016/j.advwatres.2013.08.010`.

[61] N. Alyafei, A. Q. Raeini, A. Paluszny, and M. J. Blunt, "A Sensitivity Study of the Effect of Image Resolution on Predicted Petrophysical Properties", *Transport in Porous Media*, vol. 110, no. 1, pp. 157–169, Oct. 2015, ISSN: 0169-3913. DOI: `10.1007/s11242-015-0563-0`.

[62] M. P. Ortega Ramírez, L. Oxarango, and A. Gastelum Strozzi, "Effect of X-ray CT resolution on the quality of permeability computation for granular soils: definition of a criterion based on morphological properties", *Soil Research*, vol. 57, no. 6, p. 589, 2019, ISSN: 1838-675X. DOI: `10.1071/SR18189`.

[63] X. Feng, J. Zeng, H. Zhan, Q. Hu, Z. Ma, and S. Feng, "Resolution effect on image-based conventional and tight sandstone pore space reconstructions: Origins and strategies", *Journal of Hydrology*, vol. 586, no. January, p. 124 856, Jul. 2020, ISSN: 00221694. DOI: `10.1016/j.jhydrol.2020.124856`.

[64] K. M. Gerke, M. V. Karsanina, T. O. Sizonenko, X. Miao, D. R. Gafurova, and D. V. Korost, "Multi-Scale Image Fusion of X-Ray Microtomography and SEM Data to Model Flow and Transport Properties for Complex Rocks on Pore-Level", in *Day 2 Tue, October 17, 2017*, SPE, Oct. 2017, pp. 1–14. DOI: `10.2118/187874-MS`.

[65] L. C. Ruspini, G. Lindkvist, S. Bakke, L. Alberts, A. M. Carnerup, and P. E. Øren, "A Multi-Scale Imaging and Modeling Workflow for Tight Rocks", in *All Days*, SPE, May 2016, pp. 5–6, ISBN: 9781613994603. DOI: `10.2118/180268-MS`.

[66] Long H, Nardi C, Idowu N, *et al.*, "Multi-scale imaging and modeling workflow to capture and characterize microporosity in sandstone", *International Symposium of the Society of Core Analysts*, pp. 1–13, 2013.

[67] S. Shah, F. Gray, J. Crawshaw, and E. Boek, “Micro-computed tomography pore-scale study of flow in porous media: Effect of voxel resolution”, *Advances in Water Resources*, vol. 95, pp. 276–287, Sep. 2016, ISSN: 03091708. DOI: `10.1016/j.advwatres.2015.07.012`.

[68] “SUPREMATIM : SUPerREsolution of 3d MATerials IMages”. (2019), [Online]. Available: `https://www.math.u-bordeaux.fr/~jaujol/suprematim/`.

[69] G. T. Herman, *Image Reconstruction from Projections, The Fundamentals of Computerized Tomography by G. T. Herman*. New York: Academic Press, Jan. 1980, p. 316.

[70] R. Gordon, R. Bender, and G. T. Herman, “Algebraic Reconstruction Techniques (ART) for three-dimensional electron microscopy and X-ray photography”, *Journal of Theoretical Biology*, vol. 29, no. 3, pp. 471–481, 1970, ISSN: 10958541. DOI: `10.1016/0022-5193(70)90109-8`.

[71] M. Stampanoni, A. Groso, A. Isenegger, *et al.*, “Trends in synchrotron-based tomographic imaging: the SLS experience”, in *Developments in X-Ray Tomography V*, U. Bonse, Ed., vol. 6318, Aug. 2006, p. 63180M, ISBN: 0819463973. DOI: `10.1117/12.679497`.

[72] S. Vaucher, P. Unifantowicz, C. Ricard, *et al.*, “On-line tools for microscopic and macroscopic monitoring of microwave processing”, *Physica B: Condensed Matter*, vol. 398, no. 2, pp. 191–195, 2007, ISSN: 09214526. DOI: `10.1016/j.physb.2007.04.064`.

[73] J. Hertrich, D.-P.-L. Nguyen, J.-F. Aujol, *et al.*, “PCA reduced Gaussian mixture models with applications in superresolution”, *Inverse Problems & Imaging*, vol. 16, no. 2, p. 341, 2022, ISSN: 1930-8337. DOI: `10.3934/ipi.2021053`. arXiv: `2009.07520`.

[74] J. Hertrich. “Wasserstein Patch Prior for Image Superresolution”. (2021), [Online]. Available: `https://github.com/johertrich/Wasserstein_Patch_Prior`.

[75] E. O. Brenne, “Statistical Methods for Quantification and Segmentation of Material Microstructure from 3D X-ray Tomography Image Data”, PhD, Technical University of Denmark, 2021.

[76] D. Bernard and A. Chirazi, “Numerically Enhanced Microtomographic Imaging Method Using a Novel Ring Artefact Filter”, in *Advances in X-ray Tomography for Geomaterials*, London, UK: ISTE, 2010, pp. 117–124, ISBN: 1905209606. DOI: `10.1002/9780470612187.ch6`.

[77] B. Münch, P. Trtik, F. Marone, and M. Stampanoni, “Stripe and ring artifact removal with combined wavelet—Fourier filtering”, *Optics Express*, vol. 17, no. 10, p. 8567, May 2009, ISSN: 1094-4087. DOI: `10.1364/OE.17.008567`.

[78] N. T. Vo, R. C. Atwood, and M. Drakopoulos, “Superior techniques for eliminating ring artifacts in X-ray micro-tomography”, *Optics Express*, vol. 26, no. 22, p. 28 396, Oct. 2018, ISSN: 1094-4087. DOI: `10.1364/OE.26.028396`.

[79] P. A. Owusu and S. Asumadu-Sarkodie, “A review of renewable energy sources, sustainability issues and climate change mitigation”, *Cogent Engineering*, vol. 3, no. 1, S. Dubey, Ed., Apr. 2016, ISSN: 2331-1916. DOI: `10.1080/23311916.2016.1167990`.

[80] K. L. Chopra, P. D. Paulson, and V. Dutta, “Thin-film solar cells: an overview”, *Progress in Photovoltaics: Research and Applications*, vol. 12, no. 23, pp. 69–92, Mar. 2004, ISSN: 1062-7995. DOI: `10.1002/pip.541`.

[81] C. Ossig, T. Nietzold, B. West, *et al.*, “X-ray Beam Induced Current Measurements for Multi-Modal X-ray Microscopy of Solar Cells”, *Journal of Visualized Experiments*, vol. 2019, no. 150, pp. 1–20, Aug. 2019, ISSN: 1940-087X. DOI: `10.3791/60001`.

[82] F. Boutebakh, M. L. Zeggar, N. Attaf, and M. Aida, “Electrical properties and back contact study of CZTS/ZnS heterojunction”, *Optik*, vol. 144, pp. 180–190, Sep. 2017, ISSN: 00304026. DOI: `10.1016/j.ijleo.2017.06.080`.

[83] T. M. Friedlmeier, P. Jackson, A. Bauer, *et al.*, “High-efficiency Cu(In,Ga)Se2 solar cells”, *Thin Solid Films*, vol. 633, pp. 13–17, Jul. 2017, ISSN: 00406090. DOI: `10.1016/j.tsf.2016.08.021`.

[84] M. F. Islam, N. Md Yatim, and M. A. Hashim@Ismail, “A Review of CZTS Thin Film Solar Cell Technology”, *Journal of Advanced Research in Fluid Mechanics and Thermal Sciences*, vol. 81, no. 1, pp. 73–87, Mar. 2021, ISSN: 22897879. DOI: `10.37934/arfmts.81.1.7387`.

[85] M. Stuckelberger, B. West, S. Husein, *et al.*, “Latest developments in the x-ray based characterization of thin-film solar cells”, in *2015 IEEE 42nd Photovoltaic Specialist Conference (PVSC)*, IEEE, Jun. 2015, pp. 1–6, ISBN: 978-1-4799-7944-8. DOI: `10.1109/PVSC.2015.7355592`.

[86] O. F. Vyvenko, T. Buonassisi, A. A. Istratov, *et al.*, “X-ray beam induced current—a synchrotron radiation based technique for the in situ analysis of recombination properties and chemical nature of metal clusters in silicon”, *Journal of Applied Physics*, vol. 91, no. 6, pp. 3614–3617, Mar. 2002, ISSN: 0021-8979. DOI: `10.1063/1.1450026`.

[87] O. F. Vyvenko, T. Buonassisi, A. A. Istratov, and E. R. Weber, “X-ray beam induced current/microprobe x-ray fluorescence: synchrotron radiation based x-ray microprobe techniques for analysis of the recombination activity and chemical nature of metal impurities in silicon”, *Journal of Physics: Condensed Matter*, vol. 16, no. 2, S141–S151, Jan. 2004, ISSN: 0953-8984. DOI: `10.1088/0953-8984/16/2/017`.

[88] V. I. Orlov, O. V. Feklisova, and E. B. Yakimov, "A Comparison of EBIC, LBIC and XBIC Methods as Tools for Multicrystalline Si Characterization", *Solid State Phenomena*, vol. 205-206, pp. 142–147, Oct. 2013, ISSN: 1662-9779. DOI: `10.4028/www.scientific.net/SSP.205-206.142`.

[89] H. J. Leamy, "Charge collection scanning electron microscopy", *Journal of Applied Physics*, vol. 53, no. 6, R51–R80, Jun. 1982, ISSN: 0021-8979. DOI: `10.1063/1.331667`.

[90] R. R. Fahrtdinov, O. V. Feklisova, M. V. Grigoriev, D. V. Irzhak, D. V. Roshchupkin, and E. B. Yakimov, "X-ray beam induced current method at the laboratory x-ray source", *Review of Scientific Instruments*, vol. 82, no. 9, p. 093 702, Sep. 2011, ISSN: 0034-6748. DOI: `10.1063/1.3633948`.

[91] E. B. Yakimov, "Simulation of XBIC Contrast of Precipitates in Si", *Solid State Phenomena*, vol. 156-158, pp. 247–250, Oct. 2009, ISSN: 1662-9779. DOI: `10.4028/www.scientific.net/SSP.156-158.247`.

[92] Y. L. Shabel'nikova, E. B. Yakimov, M. V. Grigor'ev, R. R. Fahrtdinov, and V. A. Bushuev, "Calculating the extended defect contrast for the X-ray-beam-induced current method", *Technical Physics Letters*, vol. 38, no. 10, pp. 913–916, Oct. 2012, ISSN: 1063-7850. DOI: `10.1134/S1063785012100239`.

[93] L. Chayanun, G. Otnes, A. Troian, *et al.*, "Nanoscale mapping of carrier collection in single nanowire solar cells using X-ray beam induced current", *Journal of Synchrotron Radiation*, vol. 26, no. 1, pp. 102–108, Jan. 2019, ISSN: 1600-5775. DOI: `10.1107/S1600577518015229`.

[94] N. M. Kumar, A. R. Shaik, T. Walker, *et al.*, "Mapping current collection in cross section: The case of copper- doped cdte solar cells", in *2020 47th IEEE Photovoltaic Specialists Conference (PVSC)*, 2020, pp. 2178–2180. DOI: `10.1109/PVSC45281.2020.9300979`.

[95] T. Walker, M. E. Stuckelberger, T. Nietzold, *et al.*, "The nanoscale distribution of copper and its influence on charge collection in CdTe solar cells", *Nano Energy*, vol. 91, no. May 2021, p. 106 595, Jan. 2022, ISSN: 22112855. DOI: `10.1016/j.nanoen.2021.106595`.

[96] A. Saadaldin, A. Slyamov, M. E. Stuckelberger, *et al.*, "Multi-Modal Characterization of Kesterite Thin-Film Solar Cells: Experimental results and numerical interpretation", *Faraday Discussions*, 2022, ISSN: 1359-6640. DOI: `10.1039/D2FD00044J`.

[97] J. Nelson, *The Physics of Solar Cells*. Imperial college press, May 2003, ISBN: 978-1-86094-340-9. DOI: `10.1142/p276`.

[98] R. Scheer and H.-w. Schock, *Chalcogenide photovoltaics: physics, technologies, and thin film devices.* John wiley \& sons, 2011, ISBN: 9783527326471.

[99] Donald A Neamen, *Semiconductor Physics and Semiconductor Devices*. New York: McGraw-Hill, 2012, ISBN: 0072321075. DOI: 10.3169/itej1954.28.723.

[100] K. K. Sze, Simon M and Ng, *Physics of semiconductor devices*. John wiley \& sons, 2006.

[101] F. Salvat, J. Fernandez-Varea, J. Sempau, and OECD Nuclear Energy Agency., *PENELOPE 2006 : a code system for Monte Carlo simulation of electron and photon transport ; Workshop Proceedings, Barcelona, Spain, 4-7 July 2006*. Nuclear Energy Agency, Organisation for Economic Co-operation and Development, 2006, p. 281, ISBN: 9264023011.

[102] D. Schroeder, *Modelling of Interface Carrier Transport for Device Simulation* (Computational Microelectronics). Vienna: Springer Vienna, 1994, ISBN: 978-3-7091-7368-8. DOI: 10.1007/978-3-7091-6644-4.

[103] J. Slotboom, "Computer-aided two-dimensional analysis of bipolar transistors", *IEEE Transactions on Electron Devices*, vol. 20, no. 8, pp. 669–679, Aug. 1973, ISSN: 0018-9383. DOI: 10.1109/T-ED.1973.17727.

[104] P. A. Markowich, *The Stationary Semiconductor Device Equations* (Computational Microelectronics). Vienna: Springer Vienna, 1986, ISBN: 978-3-211-99937-0. DOI: 10.1007/978-3-7091-3678-2.

[105] D. Scharfetter and H. Gummel, "Large-signal analysis of a silicon Read diode oscillator", *IEEE Transactions on Electron Devices*, vol. 16, no. 1, pp. 64–77, Jan. 1969, ISSN: 0018-9383. DOI: 10.1109/T-ED.1969.16566.

[106] P. Farrell and E. Gartland Jr, *On the Scharfetter-Gummel discretization for drift-diffusion continutity equations*, 1991.

[107] S. J. Polak, C. Den Heijer, W. H. A. Schilders, and P. Markowich, "Semiconductor device modelling from the numerical point of view", *International Journal for Numerical Methods in Engineering*, vol. 24, no. 4, pp. 763–838, Apr. 1987, ISSN: 0029-5981. DOI: 10.1002/nme.1620240408.

[108] S. J. Polak, C. Den Heijer, W. H. A. Schilders, and P. Markowich, "Semiconductor device modelling from the numerical point of view", *International Journal for Numerical Methods in Engineering*, vol. 24, no. 4, pp. 763–838, Apr. 1987, ISSN: 0029-5981. DOI: 10.1002/nme.1620240408.

[109] A. Bortolossi, "3D Finite Element Drift-Diffusion Simulation of Semiconductor Devices", Master's thesis, Politecnico di Milano, 2014.

[110] W. Engl, H. Dirks, and B. Meinerzhagen, "Device modeling", *Proceedings of the IEEE*, vol. 71, no. 1, pp. 10–33, 1983, ISSN: 0018-9219. DOI: 10.1109/PROC.1983.12524.

[111] T. Seidman and S. Choo, "Iterative scheme for computer simulation of semiconductor devices", *Solid-State Electronics*, vol. 15, no. 11, pp. 1229–1235, Nov. 1972, ISSN: 00381101. DOI: `10.1016/0038-1101(72)90043-3`.

[112] J. W. Jerome, *TitleAnalysis of charge transport: a mathematical study of semiconductor devices*. Springer Science \& Business Media, 1996.

[113] B. Gaury, Y. Sun, P. Bermel, and P. M. Haney, "Sesame: A 2-dimensional solar cell modeling tool", *Solar Energy Materials and Solar Cells*, vol. 198, no. May 2018, pp. 53–62, Aug. 2019, ISSN: 09270248. DOI: `10.1016/j.solmat.2019.03.037`. arXiv: `1806.06919`.

[114] E. Guide, Sentaurus Device User and Version, "Synopsys inc", *Mountain View, CA, USA*, 2013.

[115] C. Multiphysics, "V. 5.4. cn. comsol. com", *COMSOL AB, Stockholm, Sweden*, 2017.

[116] M. Burgelman, P. Nollet, and S. Degrave, "Modelling polycrystalline semiconductor solar cells", *Thin Solid Films*, vol. 361-362, pp. 527–532, Feb. 2000, ISSN: 00406090. DOI: `10.1016/S0040-6090(99)00825-1`.

[117] T. Soga, "Fundamentals of Solar Cell", in *Nanostructured Materials for Solar Energy Conversion*, Elsevier, 2006, pp. 3–43, ISBN: 9780444528445. DOI: `10.1016/B978-044452844-5/50002-0`.

[118] T. Dittrich, "Basic Characteristics and Characterization of Solar Cells", in *Materials Concepts for Solar Cells*, WORLD SCIENTIFIC (EUROPE), Mar. 2018, pp. 3–43. DOI: `10.1142/9781786344496_0001`.

[119] R. C. Alig and S. Bloom, "Secondary-electron-escape probabilities", *Journal of Applied Physics*, vol. 49, no. 6, pp. 3476–3480, Jun. 1978, ISSN: 0021-8979. DOI: `10.1063/1.325257`.

[120] M. Huff, "Review—Important Considerations Regarding Device Parameter Process Variations in Semiconductor-Based Manufacturing", *ECS Journal of Solid State Science and Technology*, vol. 10, no. 6, p. 064 002, Jun. 2021, ISSN: 2162-8769. DOI: `10.1149/2162-8777/ac02a4`.

[121] T. Todorov, M. Kita, J. Carda, and P. Escribano, "Cu2ZnSnS4 films deposited by a soft-chemistry method", *Thin Solid Films*, vol. 517, no. 7, pp. 2541–2544, Feb. 2009, ISSN: 00406090. DOI: `10.1016/j.tsf.2008.11.035`.

[122] H. Katagiri and K. Jimbo, "Development of rare metal-free CZTS-based thin film solar cells", in *2011 37th IEEE Photovoltaic Specialists Conference*, IEEE, Jun. 2011, pp. 003 516–003 521, ISBN: 978-1-4244-9965-6. DOI: `10.1109/PVSC.2011.6186707`.

[123] X. Wu, W. Liu, S. Cheng, Y. Lai, and H. Jia, "Photoelectric properties of Cu 2 ZnSnS 4 thin films deposited by thermal evaporation", *Journal of Semiconductors*, vol. 33, no. 2, p. 022 002, Feb. 2012, ISSN: 1674-4926. DOI: `10.1088/1674-4926/33/2/022002`.

[124] A. D. Adewoyin, M. A. Olopade, and M. Chendo, "Prediction and optimization of the performance characteristics of CZTS thin film solar cell using band gap grading", *Optical and Quantum Electronics*, vol. 49, no. 10, p. 336, Oct. 2017, ISSN: 0306-8919. DOI: `10.1007/s11082-017-1176-3`.

[125] A. K. Singh, T. R. Rana, J. Kim, M. Shkir, and T.-C. Jen, "Impact on Structural and Optical Properties of CZTS Thin Films with Solvents and Ge Incorporation", *International Journal of Photoenergy*, vol. 2021, L. Palmisano, Ed., pp. 1–9, Mar. 2021, ISSN: 1687-529X. DOI: `10.1155/2021/1508469`.

[126] M. Jiang and X. Y, "Cu2ZnSnS4 Thin Film Solar Cells: Present Status and Future Prospects", in *Solar Cells - Research and Application Perspectives*, InTech, Mar. 2013. DOI: `10.5772/50702`.

[127] B. Shin, K. Wang, O. Gunawan, *et al.*, "High efficiency Cu2ZnSn(SxSe1-x)4 thin film solar cells by thermal co-evaporation", in *2011 37th IEEE Photovoltaic Specialists Conference*, vol. 1, IEEE, Jun. 2011, pp. 002 510–002 514, ISBN: 978-1-4244-9965-6. DOI: `10.1109/PVSC.2011.6186456`.

[128] I. L. Repins, H. Moutinho, S. G. Choi, *et al.*, "Indications of short minority-carrier lifetime in kesterite solar cells", *Journal of Applied Physics*, vol. 114, no. 8, p. 084 507, Aug. 2013, ISSN: 0021-8979. DOI: `10.1063/1.4819849`.

[129] M. Djinkwi Wanda, S. Ouédraogo, and J. Ndjaka, "Theoretical analysis of minority carrier lifetime and Cd-free buffer layers on the CZTS based solar cell performances", *Optik*, vol. 183, no. February, pp. 284–293, Apr. 2019, ISSN: 00304026. DOI: `10.1016/j.ijleo.2019.02.058`.

[130] H. Yan, X. Huang, Y. S. Chu, A. Pattammattel, E. Nazaretski, and P. Ill, "Hard x-ray nanoprobe: a scanning hard x-ray microscopy beamline offering multi-modal imaging capabilities at 10 nm", in *X-Ray Nanoimaging: Instruments and Methods IV*, B. Lai and A. Somogyi, Eds., International Society for Optics and Photonics, vol. 11112, SPIE, 2019, p. 1 111 202. DOI: `10.1117/12.2531196`.

Appendix A

Change of scale by volume averaging

A.0.1 Change of scale by volume averaging

In volume averaging technique we use the information at the local scale (the pore scale here) to derive volume averaged equations that are valid at the global scale (the continuous porous medium scale here). We start by dividing the averaging volume $\mathscr{V}$ into two parts; V_f represents the volume of the F phase contained within the averaging volume and V_s represents the volume of the S phase.

$$\mathscr{V} = V_f + V_s \tag{A.1}$$

We can define the porosity as the volume fraction of the F phase, as follows,

$$\varepsilon = \frac{V_f}{\mathscr{V}} \tag{A.2}$$

The idea is to rewrite the equations (2.6) and (2.7) in terms of averaged quantities, so we introduce the superficial average of C as:

$$\langle C \rangle = \frac{1}{\mathscr{V}} \int\limits_{V_f} C dV \tag{A.3}$$

Integrating equation (2.6) over the domain V_f and dividing by $\mathscr{V}$ we obtain:

$$\frac{1}{\mathscr{V}} \int\limits_{V_f} \frac{\partial C}{\partial t} dV = \frac{1}{\mathscr{V}} \int\limits_{V_f} \nabla \cdot \nabla C \tag{A.4}$$

Using the general transport theorem [9] to express the left hand side, we can rewrite equation (A.4) as follows:

$$\frac{\partial \langle C \rangle}{\partial t} = \frac{1}{\mathscr{V}} \int\limits_{V_f} \nabla \cdot \nabla C \tag{A.5}$$

In fact, the superficial average concentration is not a good representation of the concentration in the F phase and it is more convenient to rewrite equation (A.5) in terms of the intrinsic average concentration which defined by:

$$\langle C \rangle^f = \frac{1}{V_f} \int\limits_{V_f} C dV \tag{A.6}$$

These two averaged concentrations are related by:

$$\langle C \rangle = \varepsilon \langle C \rangle^f \tag{A.7}$$

and we can use equation (A.7) in equation (A.5) to obtain:

$$\varepsilon\frac{\partial\langle C\rangle^f}{\partial t} = \frac{1}{\mathscr{V}}\int\limits_{V_f} \nabla\cdot\nabla C \tag{A.8}$$

In equation A.8 we assumed that the porosity is constant. Now we should express the right hand side of equation (A.8) in terms of the intrinsic average concentration. For that we decompose the concentration according to GRAY's decomposition as:

$$C = \langle C\rangle^f + \tilde{C} \tag{A.9}$$

where $\tilde{C}$ is the concentration perturbation due to the presence of the solid phase. Using the spatial averaging theorems [9] and equation (2.7) we can rewrite equation (A.8) as follows:

$$\varepsilon\frac{\partial\langle C\rangle^f}{\partial t} = \nabla\cdot\left[\varepsilon\nabla\langle C\rangle^f + \frac{1}{\mathscr{V}}\int\limits_{\mathrm{A_{fs}}} n_{\mathrm{fs}}\tilde{C}dA\right] - \mathrm{a}_v k_R(\langle C\rangle^f - C^*) \tag{A.10}$$

where a_v is the specific reactive surface. it represents the reactive surface area per unit volume, which is given by:

$$\mathrm{a}_v = \frac{\mathrm{A_{fsr}}}{\mathscr{V}} \tag{A.11}$$

In equation, (A.10) we assumed that the concentration perturbation due to the presence of the solid phase is much smaller than the intrinsic average concentration and the reaction rate k_R is constant in the averaging volume. The right hand side of equation (A.10) is still containing microscopic term that has to be modified. In the same way as [9] we can represent the concentration perturbation by the following expression:

$$\tilde{C} = \mathbf{B}\cdot\nabla\langle C\rangle^f + s(\langle C\rangle^f - C^*) \tag{A.12}$$

where the vector $\mathbf{B}$ and the scalar s are the closure variables. Both are solution of partial differential problems, called the closure problems, which have to be solved at the local scale:

$$\nabla^2\mathbf{B} = 0 \tag{A.13}$$

$$-n_{\mathrm{fs}}\cdot\nabla\mathbf{B} = n_{\mathrm{fs}}, \quad \text{at} \quad \mathrm{A_{fs}} \tag{A.14}$$

$$\mathbf{B}(r + l_i) = \mathbf{B}(r), \quad i = 1, 2, 3 \tag{A.15}$$

with

$$\langle\mathbf{B}\rangle^f = 0 \tag{A.16}$$

for the vector $\mathbf{B}$ and for the scalar s we have:

$$\nabla^2 s = -\bar{k} \tag{A.17}$$

$$-n_{\mathrm{fs}} \cdot \nabla s = k_R, \quad \text{at} \quad \mathrm{A}_{\mathrm{fsr}} \tag{A.18}$$

$$s(r + l_i) = s(r), \quad i = 1, 2, 3 \tag{A.19}$$

with

$$\langle s \rangle^f = 0 \tag{A.20}$$

equations (A.15) and (A.19) represent periodic boundary conditions, where r is position vector and l_i is the lattice vector. The term $\bar{k}$ is defined by the following equation:

$$\bar{k} = \frac{1}{V_f} \int\limits_{\mathrm{A}_{\mathrm{fsr}}} k_R dA \tag{A.21}$$

and with the assumption that k_R is constant on the reactive fluid-solid interface, we have:

$$\bar{k} = k_R \frac{\mathrm{A}_{\mathrm{fsr}}}{V_f} \tag{A.22}$$

The vector $\mathbf{B}$ mainly takes into account the effects of the micro-geometry on diffusion and the scalar s takes into account the same effects and the effects of the chemical reactions on the fluid-solid interface. Introducing the variable s^* defined as $\frac{s}{k_R}$, we can rewrite equations (A.17), (A.18), (A.19) and (A.20) in the following form:

$$\nabla^2 s^* = -\frac{\mathrm{A}_{\mathrm{fsr}}}{V_f} \tag{A.23}$$

$$-n_{\mathrm{fs}} \cdot \nabla s^* = 1, \quad \text{at} \quad \mathrm{A}_{\mathrm{fsr}} \tag{A.24}$$

$$s^*(r + l_i) = s^*(r), \quad i = 1, 2, 3 \tag{A.25}$$

with

$$\langle s^* \rangle^f = 0 \tag{A.26}$$

This new form only depends on the micro-geometry and the effect of the reaction rate is taken into account by the factor k_R in the macroscopic equation. Substituting equation (A.12) in equation (A.10) we obtain the dimensionless macroscopic equation as follows:

$$\varepsilon \frac{\partial \langle C \rangle^f}{\partial t} = \nabla \cdot \left[\varepsilon \left(\mathbf{I} + \frac{1}{V_f} \int\limits_{\mathrm{A}_{\mathrm{fs}}} (n_{\mathrm{fs}} \mathbf{B}) dA \right) \cdot \nabla \langle C \rangle^f \right] + \nabla \cdot \left[\varepsilon \left(\frac{k_R}{V_f} \int\limits_{\mathrm{A}_{\mathrm{fs}}} (n_{\mathrm{fs}} s^*) dA \right) (\langle C \rangle^f - C^*) \right] - \varepsilon k_R \frac{\mathrm{A}_{\mathrm{fsr}}}{V_f} (\langle C \rangle^f - C^*) \tag{A.27}$$

Introducing the dimensionless effective diffusion tensor:

$$D_{\mathrm{eff}} = I + \frac{1}{V_f} \int\limits_{\mathrm{A}_{\mathrm{fs}}} (n_{\mathrm{fs}} \mathbf{B}) dA \tag{A.28}$$

and the dimensionless vector:

$$U = \frac{1}{V_f} \int\limits_{\mathrm{A_{fs}}} (n_{\mathrm{fs}} s^*) dA \tag{A.29}$$

we can rewrite equation (A.27) in the following closed form:

$$\varepsilon \frac{\partial \langle C \rangle^f}{\partial t} = \nabla \cdot \left[\varepsilon D_{\mathrm{eff}} \cdot \nabla \langle C \rangle^f \right] + \nabla \cdot \left[\varepsilon k_R U (\langle C \rangle^f - C^*) \right] - \varepsilon k_R \frac{\mathrm{A_{fsr}}}{V_f} (\langle C \rangle^f - C^*) \tag{A.30}$$

Appendix B

Spatial discretization: Cases 2.1.2-2.1.11

Case 2.1.2, AC$_k$ is of level l and sharing the part 2 of face 4 (North) of AC$_j$, AC$_h$ is of level $l+1$ and sharing face 6 (Top) of AC$_j$. The localized points involved in the interpolation are shown in Figure B.1 and summarized in Table B.1. using equation (2.37) we have,

	X	Y	Z
p_i	$\frac{1}{2}$	$\frac{1}{2}$	$\frac{1}{2}$
p_j	-1	0	0
p_k	$-\frac{1}{2}$	$\frac{3}{2}$	$\frac{1}{2}$
p_h	-1	0	2
p_n	$-\frac{5}{6}$	$\frac{1}{2}$	$\frac{1}{2}$
p_{j1}	$-\frac{1}{2}$	$\frac{1}{2}$	$\frac{1}{2}$

Table B.1: The points involved in the interpolation case 2.1.2.

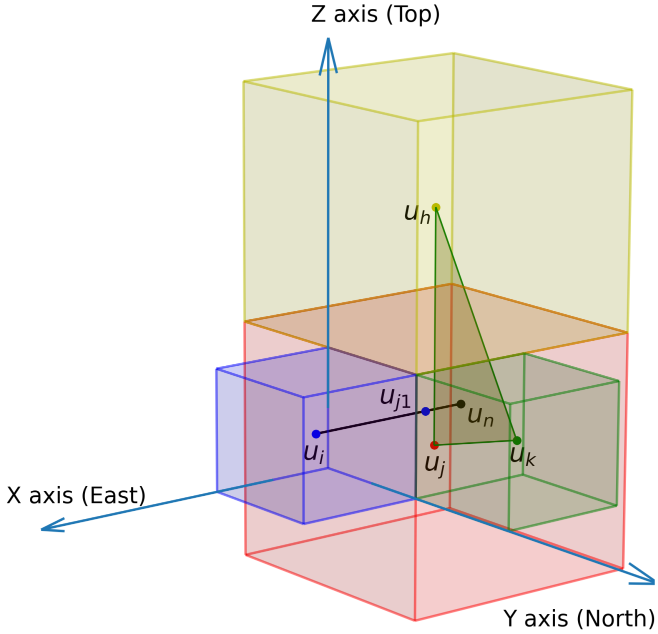

Figure B.1: Case 2.1.2 schematic diagram.

$$u_n = \frac{3u_j + 2u_k + u_h}{6} \tag{B.1}$$

and applying equation (2.39) we get,

$$u_{j1} = \frac{u_i + 3u_n}{4} = \frac{2u_i + 3u_j + 2u_k + u_h}{8} \tag{B.2}$$

Finally, the term $(\nabla u \cdot n)_{c\Gamma_1}\Gamma_1$ is approximated using equation (2.43).

Case 2.1.3, AC$_k$ is of level l and sharing the part 2 of face 4 (North) of AC$_j$, AC$_h$ is of level $l+2$ and sharing part 1 of its face 5 (Bottom) with face 6 (Top) of AC$_j$. Because AC$_i$ and AC$_k$ are of level 1, this is the only conflagration with AC$_h$ of level $l+2$. The localized points involved in the interpolation are shown in Figure B.2 and summarized in Table B.2. using equation (2.37) we have,

$$u_n = \frac{5u_j + 4u_k + u_h}{10} \tag{B.3}$$

and applying equation (2.39) we get,

$$u_{j1} = \frac{2u_i + 5u_n}{7} = \frac{4u_i + 10u_j + 4u_k + u_h}{14} \tag{B.4}$$

	X	Y	Z
p_i	$\frac{1}{2}$	$\frac{1}{2}$	$\frac{1}{2}$
p_j	-1	0	0
p_k	$-\frac{1}{2}$	$\frac{3}{2}$	$\frac{1}{2}$
p_h	-2	-1	3
p_n	$-\frac{9}{10}$	$\frac{1}{2}$	$\frac{1}{2}$
p_{j1}	$-\frac{1}{2}$	$\frac{1}{2}$	$\frac{1}{2}$

Table B.2: The points involved in the interpolation case 2.1.3.

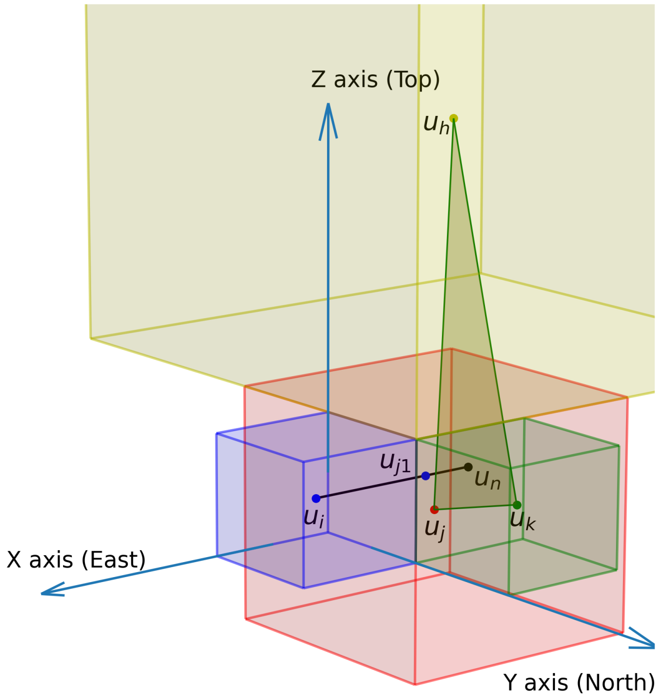

Figure B.2: Case 2.1.3 schematic diagram.

Finally, the term $(\nabla u \cdot n)_{c\Gamma_1}\Gamma_1$ is approximated using equation (2.43).

Case 2.1.4, AC$_k$ is of level $l+1$ and sharing face 4 (North) of AC$_j$, AC$_h$ is of level l and sharing the part 2 of face 6 (Top) of AC$_j$. The localized points involved in the interpolation are shown in Figure B.3 and summarized in Table B.3. using equation (2.37) we have,

$$u_n = \frac{3u_j + u_k + 2u_h}{6} \tag{B.5}$$

and applying equation (2.39) we get,

$$u_{j1} = \frac{u_i + 3u_n}{4} = \frac{2u_i + 3u_j + u_k + 2u_h}{8} \tag{B.6}$$

Finally, the term $(\nabla u \cdot n)_{c\Gamma_1}\Gamma_1$ is approximated using equation (2.43).

Case 2.1.5, AC$_k$ is of level $l+1$ and sharing face 4 (North) of AC$_j$, AC$_h$ is of level $l+1$ and sharing face 6 (Top) of AC$_j$. The localized points involved in the interpolation are shown in Figure B.4 and summarised in Table B.4. using equation (2.37) we have,

$$u_n = \frac{2u_j + u_k + u_h}{4} \tag{B.7}$$

and applying equation (2.39) we get,

$$u_{j1} = \frac{u_i + 2u_n}{3} = \frac{2u_i + 2u_j + u_k + u_h}{6} \tag{B.8}$$

	X	Y	Z
p_i	$\frac{1}{2}$	$\frac{1}{2}$	$\frac{1}{2}$
p_j	-1	0	0
p_k	-1	2	0
p_h	$-\frac{1}{2}$	$\frac{1}{2}$	$\frac{3}{2}$
p_n	$-\frac{5}{6}$	$\frac{1}{2}$	$\frac{1}{2}$
p_{j1}	$-\frac{1}{2}$	$\frac{1}{2}$	$\frac{1}{2}$

Table B.3: The points involved in the interpolation case 2.1.4.

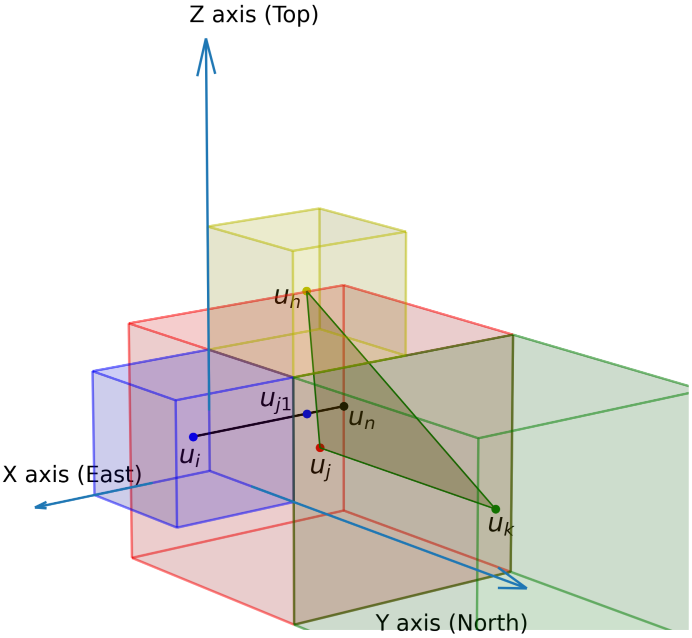

Figure B.3: Case 2.1.4 schematic diagram.

	X	Y	Z
p_i	$\frac{1}{2}$	$\frac{1}{2}$	$\frac{1}{2}$
p_j	-1	0	0
p_k	-1	2	0
p_h	-1	0	2
p_n	-1	$\frac{1}{2}$	$\frac{1}{2}$
p_{j1}	$-\frac{1}{2}$	$\frac{1}{2}$	$\frac{1}{2}$

Table B.4: The points involved in the interpolation case 2.1.5.

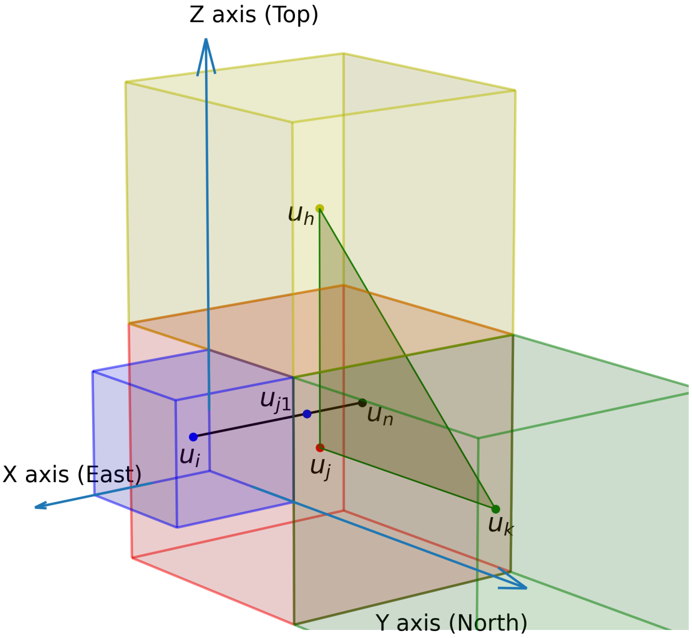

Figure B.4: Case 2.1.5 schematic diagram.

Finally, the term $(\nabla u \cdot n)_{c\Gamma_1}\Gamma_1$ is approximated using equation (2.43).

Case 2.1.6, AC$_k$ is of level $l+1$ and sharing face 4 (North) of AC$_j$, AC$_h$ is of level $l+2$ and sharing part 2 of its face 5 (bottom) with face 6 (Top) of AC$_j$. The localized points involved in the interpolation are shown in Figure B.5 and summarised in Table B.5. using equation (2.37) we have,

	X	Y	Z
p_i	$\frac{1}{2}$	$\frac{1}{2}$	$\frac{1}{2}$
p_j	-1	0	0
p_k	-1	2	0
p_h	-2	1	3
p_n	$-\frac{7}{6}$	$\frac{1}{2}$	$\frac{1}{2}$
p_{j1}	$-\frac{1}{2}$	$\frac{1}{2}$	$\frac{1}{2}$

Table B.5: The points involved in the interpolation case 2.1.6.

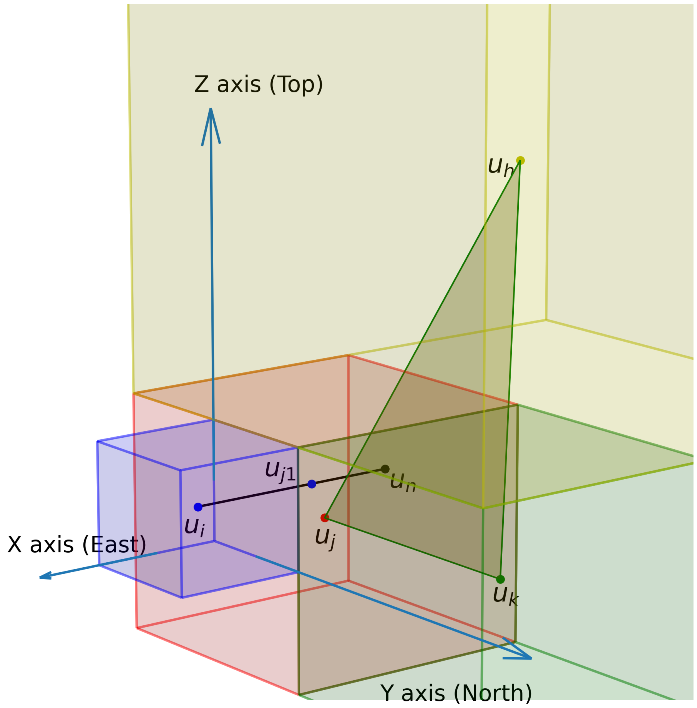

Figure B.5: Case 2.1.6 schematic diagram.

$$u_n = \frac{4u_j + u_k + u_h}{6} \tag{B.9}$$

and applying equation (2.39) we get,

$$u_{j1} = \frac{2u_i + 3u_n}{5} = \frac{4u_i + 4u_j + u_k + u_h}{10} \tag{B.10}$$

Finally, the term $(\nabla u \cdot n)_{c\Gamma_1}\Gamma_1$ is approximated using equation (2.43).

Case 2.1.7, AC$_k$ is of level $l+1$ and sharing face 4 (North) of AC$_j$, AC$_h$ is of level $l+2$ and sharing part 1 of its face 5 (bottom) with face 6 (Top) of AC$_j$. The localized points involved in the interpolation are shown in Figure B.6 and summarised in Table B.6. using equation (2.37) we have,

$$u_n = \frac{3u_j + 2u_k + u_h}{6} \tag{B.11}$$

and applying equation (2.39) we get,

$$u_{j1} = \frac{2u_i + 3u_n}{5} = \frac{4u_i + 3u_j + 2u_k + u_h}{10} \tag{B.12}$$

Finally, the term $(\nabla u \cdot n)_{c\Gamma_1}\Gamma_1$ is approximated using equation (2.43).

	X	Y	Z
p_i	$\frac{1}{2}$	$\frac{1}{2}$	$\frac{1}{2}$
p_j	-1	0	0
p_k	-1	2	0
p_h	-2	-1	3
p_n	$-\frac{7}{6}$	$\frac{1}{2}$	$\frac{1}{2}$
p_{j1}	$-\frac{1}{2}$	$\frac{1}{2}$	$\frac{1}{2}$

Table B.6: The points involved in the interpolation case 2.1.7.

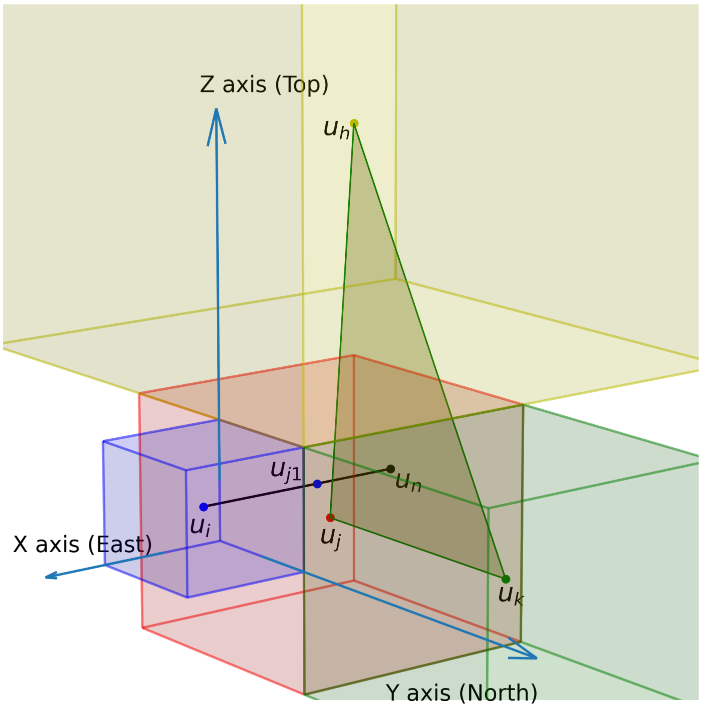

Figure B.6: Case 2.1.7 schematic diagram.

Case 2.1.8, AC$_k$ is of level $l+2$ and sharing part 1 of its face 3 (South) with face 4 (North) of AC$_j$, AC$_h$ is of level l and sharing part 2 of face 6 (Top) of AC$_j$. The localized points involved in the interpolation are shown in Figure B.7 and summarised in Table B.7. using equation (2.37) we have,

$$u_n = \frac{5u_j + u_k + 4u_h}{10} \tag{B.13}$$

and applying equation (2.39) we get,

$$u_{j1} = \frac{2u_i + 5u_n}{7} = \frac{4u_i + 5u_j + u_k + 4u_h}{14} \tag{B.14}$$

Finally, the term $(\nabla u \cdot n)_{c\Gamma_1}\Gamma_1$ is approximated using equation (2.43).

Case 2.1.9, AC$_k$ is of level $l+2$ and sharing part 1 of its face 3 (South) with face 4 (North) of AC$_j$, AC$_h$ is of level $l+1$ and sharing face 6 (Top) of AC$_j$. The localized points involved in the interpolation are shown in Figure B.8 and summarised in Table B.8. using equation (2.37) we have,

$$u_n = \frac{3u_j + u_k + 2u_h}{6} \tag{B.15}$$

	X	Y	Z
p_i	$\frac{1}{2}$	$\frac{1}{2}$	$\frac{1}{2}$
p_j	-1	0	0
p_k	-2	3	-1
p_h	$-\frac{1}{2}$	$\frac{1}{2}$	$\frac{3}{2}$
p_n	$-\frac{9}{10}$	$\frac{1}{2}$	$\frac{1}{2}$
p_{j1}	$-\frac{1}{2}$	$\frac{1}{2}$	$\frac{1}{2}$

Table B.7: The points involved in the interpolation case 2.1.8.

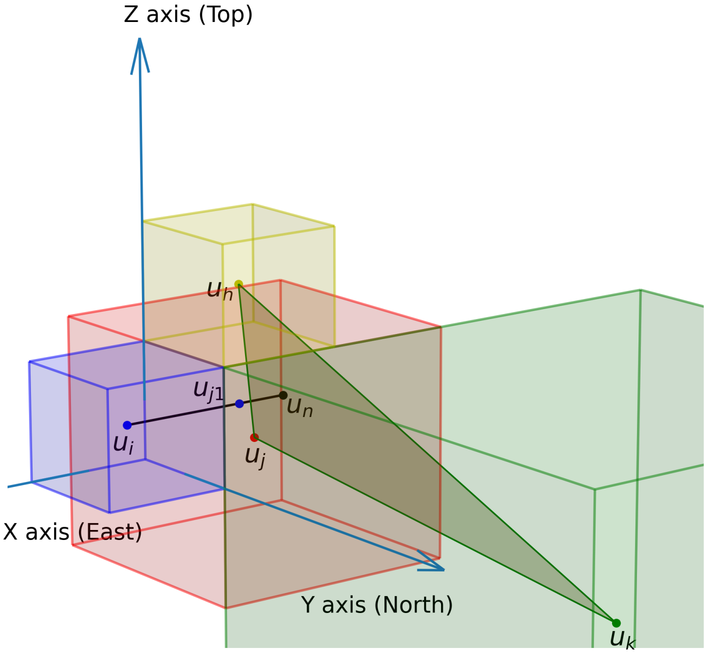

Figure B.7: Case 2.1.8 schematic diagram.

	X	Y	Z
p_i	$\frac{1}{2}$	$\frac{1}{2}$	$\frac{1}{2}$
p_j	-1	0	0
p_k	-2	3	-1
p_h	-1	0	2
p_n	$-\frac{7}{6}$	$\frac{1}{2}$	$\frac{1}{2}$
p_{j1}	$-\frac{1}{2}$	$\frac{1}{2}$	$\frac{1}{2}$

Table B.8: The points involved in the interpolation case 2.1.9.

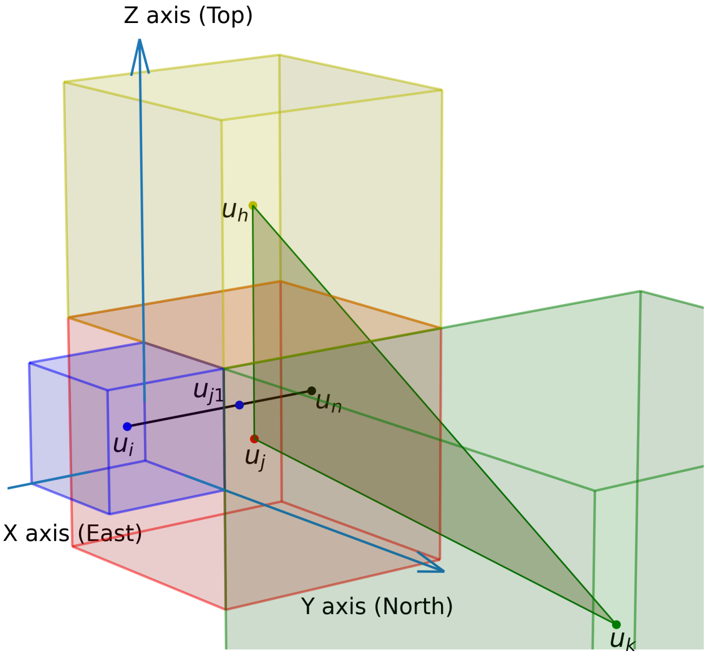

Figure B.8: Case 2.1.9 schematic diagram.

and applying equation (2.39) we get,

$$u_{j1} = \frac{2u_i + 3u_n}{5} = \frac{4u_i + 3u_j + u_k + 2u_h}{10} \tag{B.16}$$

Finally, the term $(\nabla u \cdot n)_{c\Gamma_1}\Gamma_1$ is approximated using equation (2.43).

Case 2.1.10, AC$_k$ is of level $l+2$ and sharing part 4 of its face 3 (South) with face 4 (North) of AC$_j$, AC$_h$ is of level $l+1$ and sharing face 6 (Top) of AC$_j$. The localized points involved in the interpolation are shown in Figure B.9 and summarised in Table B.9. using equation (2.37) we have,

	X	Y	Z
p_i	$\frac{1}{2}$	$\frac{1}{2}$	$\frac{1}{2}$
p_j	-1	0	0
p_k	-2	3	1
p_h	-1	0	2
p_n	$-\frac{7}{6}$	$\frac{1}{2}$	$\frac{1}{2}$
p_{j1}	$-\frac{1}{2}$	$\frac{1}{2}$	$\frac{1}{2}$

Table B.9: The points involved in the interpolation case 2.1.10.

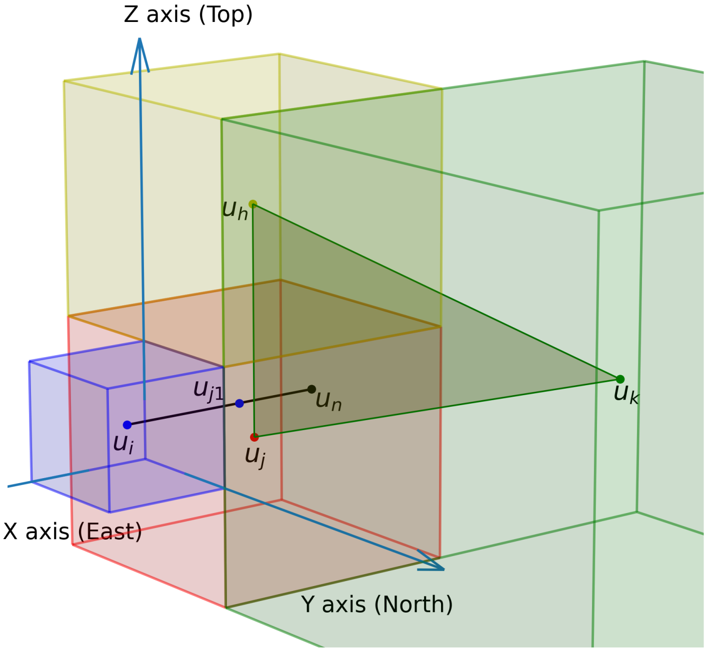

Figure B.9: Case 2.1.10 schematic diagram.

$$u_n = \frac{4u_j + u_k + u_h}{6} \tag{B.17}$$

and applying equation (2.39) we get,

$$u_{j1} = \frac{2u_i + 3u_n}{5} = \frac{4u_i + 4u_j + u_k + u_h}{10} \tag{B.18}$$

Finally, the term $(\nabla u \cdot n)_{c\Gamma_1}\Gamma_1$ is approximated using equation (2.43).

Case 2.1.11, AC$_k$ is of level $l+2$ and sharing part 1 of its face 3 (South) with face 4 (North) of AC$_j$, AC$_h$ is of level $l+2$ and sharing part 1 of its face 5 (Bottom) with face 6 (Top) of AC$_j$. The localized points involved in the interpolation are shown in Figure B.10 and summarised in Table B.10. using equation (2.37) we have,

$$u_n = \frac{2u_j + u_k + u_h}{4} \tag{B.19}$$

	X	Y	Z
p_i	$\frac{1}{2}$	$\frac{1}{2}$	$\frac{1}{2}$
p_j	-1	0	0
p_k	-2	3	-1
p_h	-2	-1	3
p_n	$-\frac{3}{2}$	$\frac{1}{2}$	$\frac{1}{2}$
p_{j1}	$-\frac{1}{2}$	$\frac{1}{2}$	$\frac{1}{2}$

Table B.10: The points involved in the interpolation case 2.1.11.

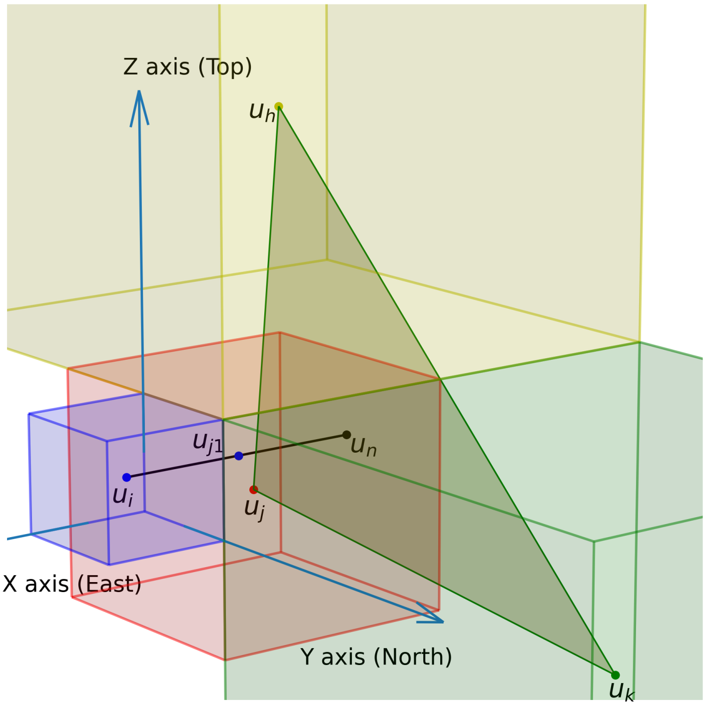

Figure B.10: Case 2.1.11 schematic diagram.

and applying equation (2.39) we get,

$$u_{j1} = \frac{u_i + u_n}{2} = \frac{4u_i + 2u_j + u_k + u_h}{8} \tag{B.20}$$

Finally, the term $(\nabla u \cdot n)_{c\Gamma_1}\Gamma_1$ is approximated using equation (2.43).

Titre : Deux exemples de modelisation numerique multi-echelle combinee avec des experiences avancees utilisant les rayons X : l'imagerie multi-echelle du transport reactif en milieu poreux et le courant induit par rayon X (XBIC)

Résumé :

Dans ce travail, nous présentons deux exemples d'expériences basées sur le rayonnement synchrotron et comment, en combinant modélisation et simulations, les résultats obtenus peuvent être interprétés en tenant compte des applications visées. Nous rapportons une étude multimodale des propriétés électriques, chimiques et structurelles d'une cellule solaire en couche mince en kestérite en combinant les techniques d'imagerie à résolution spatiale de courant induit par faisceau de rayons X (XBIC) et de fluorescence (XRF) pour l'évaluation d'un dispositif entièrement fonctionnel en géométrie de section transversale. Nous soutenons les données expérimentales avec la modélisation en volume fini du signal XBIC en résolvant l'équation de Poisson et les équations de continuité pour les électrons et les trous dans le domaine de calcul 2D construit à partir des données XRF. Les données ont permis de corréler la composition chimique, les défauts aux interfaces et le dépôt inhomogène des couches avec l'efficacité locale de collecte des charges du dispositif. Nous présentons également une procédure d'imagerie et de modélisation multi-échelle pour le transport réactif dans les milieux poreux. Pour les problèmes que nous considérons, les réactions hétérogènes sont dominantes, ce qui signifie que la partie réactive de l'interface fluide/solide doit être décrite précisément à l'échelle locale. D'autre part, la distribution spatiale globale du solide doit également être caractérisée précisément car elle détermine la représentativité des propriétés moyennes de transport. Dans ce travail, nous utilisons une grille cartésienne non uniforme résultant d'une double approche : d'abord, un grossissement de la grille visant à améliorer les aspects de calcul, et ensuite un raffinement local de la géométrie de l'interface visant à améliorer la précision des résultats. Dans l'approche d'imagerie multi-échelle, nous utilisons à la fois des images à basse résolution (pertinentes à l'échelle globale) et à haute résolution (pertinentes à l'échelle locale) dans le processus d'affinement. Cela améliore la qualité des résultats pour les propriétés effectives. Pour les grands volumes, l'approche du grossissement de la grille est capable de réduire le temps du CPU de 35 à 50 % sans perdre la précision de la solution.

Mots clés :

Rayon X synchrotron, Cellule solaire CZTS, courant induit par faisceau de rayons X (XBIC), milieux poreux, moyenne volumique, imagerie multi-échelle, grossissement de la grille, raffinement du maillage local, Imagerie 3D.

ICMCB-CNRS

[Institut de Chimie de la Matière Condensée de Bordeaux, UMR5026, 87 Avenue du Dr Albert Schweitzer, 33600 Pessac]

Title : Two examples of multi-scale numerical modelling combined with advanced X-ray based experiments: multi-scale imaging for reactive transport in porous media and X-ray beam induced current (XBIC)

Abstract :

In this work, we present two examples of synchrotron X-ray based experiments and how, combining modelling and simulations, the obtained results can be interpreted taking into account the targeted applications. We report a multi-modal study of electrical, chemical, and structural properties of a kesterite thin-film solar cell by combining the spatially resolved X-ray beam induced current (XBIC) and fluorescence (XRF) imaging techniques for the evaluation of a fully functional device in cross-section geometry. We support experimental data with the finite volume modelling of the XBIC signal by solving the Poisson equation and the continuity equations for electrons and holes within the 2D computation domain constructed from the XRF data. Data allowed correlating chemical composition, defects at interfaces, and inhomogeneous deposition of the layers with the local charge collection efficiency of the device. We also present a multi-scale imaging and modelling procedure for reactive transport in porous media. For the problems we consider, heterogeneous reactions are dominant, meaning that the reactive part of the fluid/solid interface must be precisely described at the local scale. On the other hand, the global spatial distribution of the solid must also be precisely characterized because it determines the representativeness of the average transport properties. In this work, we use a non-uniform Cartesian grid resulting from a twofold approach: first, a grid coarsening aiming in improving the computational aspects, and second a local refining of the interface geometry aiming in improving the accuracy of the results. In the multi-scale imaging approach we use both low-resolution (relevant to the global scale) and high-resolution (relevant to the local scale) images in refinement process. This improves the quality of the results for the effective properties. For large volumes, the grid coarsening approach is able to reduce the CPU time by 35-50% without losing the accuracy of the solution.

Keywords :

Synchrotron X-ray, CZTS solar cell, X-ray beam induced current (XBIC), Porous media, Volume averaging, Multi-scale imaging, Grid coarsening, Local mesh refinement, 3D imaging.

ICMCB-CNRS

[Institut de Chimie de la Matière Condensée de Bordeaux, UMR5026, 87 Avenue du Dr Albert Schweitzer, 33600 Pessac]